Novel Functionalised, Nanoarrays of DNA Binding Supramolecular Helicates

UNIVERSITY OF BIRMINGHAM

Jenifer Christine White

A thesis submitted to the University of Birmingham for the degree of Doctor of Philosophy

School of Chemistry
University of Birmingham
September 2015

Abstract

Work described in this thesis shows the design, synthesis, DNA binding activity and gold nanoparticle interaction of functionalised triple stranded supramolecular helicates.

DNA structures and the way molecules recognise and bind to them are reviewed, with specific emphasis on supramolecular compounds. Supramolecular helicates are discussed in detail with consideration of how they may be used as anticancer agents. Nanoparticles, specifically gold nanoparticles are studied, with specific reference to how they are able to enhance anticancer properties of drug molecules and how they may be used to develop potent anticancer therapies.

The design and synthesis of novel functionalised supramolecular helicate structures is presented. Through the use of click chemistry, the supramolecular cylinder, $[Fe_2(L_P)_3]^{4+}$ (L_P= $C_{25}H_{20}N_4$), is successfully functionalised with ester, piperidine and thioacetate moieties to form the three new iron helicates $[Fe_2(L_{Ester})_3]Cl_4$, $[Fe_2(L_{Piperidine})_3]Cl_4$ and $[Fe_2(L_{Thioacetate})_3][BF_4]_4$. Each new structure is found to interact with ct-DNA and induce a structural change, through analysing DNA interactions with the use of circular and linear dichroism. The formation of DNA three-way junctions and these cylinder structures is also investigated, with the use of polyacrylamide gel electrophoresis. It is shown that such junction structures are stabilised by each of the three tetra-cationic compounds to varying degrees, $[Fe_2(L_{Thioacetate})_3][BF_4]_4$ > $[Fe_2(L_{Ester})_3]Cl_4$ > $[Fe_2(L_{Piperidine})_3]Cl_4$, showing the diversity of this class of compound.

As well as DNA interactions, cell toxicity of the novel functionalised supramolecular helicates is investigated using human alveolar adenocarcinoma and breast cancer cell lines. It is found that these structures are able to enter such cell lines and induce cell death at concentrations <50 μM.

Attempts at attaching supramolecular helicates to gold nanoparticles is also described, via electrostatic interactions and covalent bonding. Stabilisation of the nanoparticles using a surfactant coating, allows for the tetra-cationic species to be attached successfully. Studies show that nanoparticles functionalised with the ruthenium helicate, $[Ru_2(L_P)_3]Cl_4$, and newly synthesised thioacetate functionalised iron helicate, $[Fe_2(L_{Thioacetate})_3][BF_4]_4$ are able to interact with DNA structures and enter cancerous cell lines, to induce cell death. It is observed using circular and linear dichroism that these functionalised nanoparticles are able to interact with ct-DNA and induce a structural change, however, are they are not as active as the 'free' compounds. TEM images show that these functionalised gold nanoparticles are able to enter cancerous cells, and through the use of MTT assays it is shown that they cause cell death at nanomolar concentrations after 72 hours incubation.

With the formation of three novel supramolecular iron helicates and the incorporation of supramolecular chemistry and nanotechnology, foundations of work in this area is discussed, showing promising results for future research.

Acknowledgements

Firstly I would like to thank my supervisor Professor Mike Hannon for the opportunity he has given me to be part of the Hannon group, and to work on such a challenging and interesting project. I would like to express my gratitude for the assistance and guidance he gave throughout my PhD.

I would also like to convey my appreciation to Hannon group members, past and present, who I had the pleasure of working with. Specifically Jenna, Natalia and Hannah, for welcoming me into the group and passing on their knowledge. And to Lindsey, Lois, Ashleigh and Pete for all the cake and support they provided through my years of research.

I am grateful to Professor Zoe Pikramenou for her guidance and knowledge working with nanoparticles and Sam Adams for his time and hard work helping me with gold surface experiments. I am also grateful to Dr Nik Hodges for his help and use of facilities for cell studies. I would like to thank all members of the analytical facilities within the School of Chemistry, for their advice and hard work.

I would like to express my gratitude to the University of Birmingham, the EPSRC and COST for funding, allowing me to part take in this research and allowing me to explore the subject further through conference attendance.

Finally, I must express my heartfelt appreciation to my family. For the love and support they have given me over the years and blessing me with my gorgeous nieces and nephew throughout my time in Birmingham. I could not have got through this time without you.

Contents

Abbreviations

3WJ	three way junction
4WJ	four way junction
δ	chemical shift (NMR)
ε	molar absorption coefficient ($mol^{-1}dm^3cm^{-1}$)
λ	wavelength
λmax	wavelength maximum
A	adenine (DNA base)
AuNPs	gold nanoparticles
BF_4	tetrafluoroborate
bpy	2,2'-bipyridine
br	broad (in NMR and IR data)
C	cytosine (DNA base)
CD	circular dichroism
CDCl3	deuterated chloroform
CD3CN	deuterated acetonitrile
CD_3OD	Methyl-d_3 alcohol-*d*
cm	centimetre
^{13}C NMR	carbon nuclear magnetic resonance (spectroscopy)
ct-DNA	calf thymus deoxyribonucleic acid
COSY	two dimensional correlation spectroscopy (NMR)
d	doublet (NMR)
DCM	dichloromethane
dd	doublet of doublets (NMR)
DLS	dynamic light scattering
DMEM	dulbecco's modified eagle's medium
DMSO	dimethyl sulfoxide
DNA	deoxyribonucleic acid
dppz	dipyridyl[3,2-a:2'3'-c]phenazine
ESI	electrospray ionisation (mass spectrometry)
EtBr	ethidium bromide

EtOAc	ethyl acetate
EtOH	ethanol
FBS	foetal bovine serum
G	guanine (DNA base)
glygly	glycylglycine
^{1}H NMR	proton nuclear magnetic resonance (spectroscopy)
HRMS	high resolution mass spectrometry
hrs	hours
HSQC	heteronuclear single quantum coherence
h-Telo	human telomeric
Hz	hertz
IC_{50}	half maximal inhibitory concentration
ICD	induced circular dichroism
ILD	induced linear dichroism
IR	infra-red (spectroscopy)
J	coupling constant (NMR)
K	Kelvin
LD	linear dichroism
m	medium (in IR data)
m	multiplet (in NMR data)
M	molar (mol dm^{-3})
NIR	near infrared
μM	micromolar
mdeg	millidegrees
MeCN	acetonitrile
MeOH	methanol
MHz	megahertz
MLCT	metal to ligand charge transfer
mM	millimolar
mmol	millimole
MS	mass spectrometry
MTT	3-(4,5-dimethylthiazol-2-yl)-2,5-diphenyltetrazolium bromide

m/z	mass to charge ratio
nm	nanometre
nM	nanomolar
NMR	nuclear magnetic resonance (spectroscopy)
^{32}P	phosphorus-32 (isotope)
PAGE	polyacrylamide gel electrophoresis
PBS	phosphate buffered saline
PF_6	hexafluorophosphate
phen	phenanthroline
ppm	parts per million
PyTA	2,4-diamino-6-(2′-pyridyl)-1,3,5-triazine
PzTA	2,4-diamino-6-(2′-pyrazino)-1,3,5-triazine)
RNA	ribonucleic acid
RPMI	roswell park memorial institute medium
s	strong (in IR data)
s	singlet (in NMR data)
SPR	surface plasmon resonance
T	thymine (DNA base)
t	triplet (NMR)
tBu	tert-Butyl
td	triplet of doublets (NMR)
TEM	transmission electron microscopy
UV	ultraviolet (light/spectroscopy)
UV-Vis	Ultraviolet-visible (spectroscopy)
w	weak (IR)
ZAuNPs	zonyl (surfactant) coated gold nanoparticles

Chapter 1

Introduction

Deoxyribonucleic acid, DNA, encodes for all information essential to life in biological systems. For this reason, its structure and function are important to understand when developing new drug treatments. It plays a vital role within cellular processes, to maintain the cell function, for example within gene expression and DNA replication. As such, DNA can be a target for treatment of disease. A variety of natural and synthetic molecules are able to bind to DNA and affect the biological activity, resulting in therapeutic agents. Developing new drug molecules that have a high affinity to DNA or attaching therapeutic molecules to the surface of nanoparticles in order to direct delivery of compounds in high concentrations to DNA, may inhibit DNA replication, and as a result generate a potent anticancer therapy.

1.1 DNA Structure

The structure of B-DNA was discovered in 1953 [1] and consists of a sugar phosphate backbone, with interlinking base pairs, Figure 1. These four bases form complimentary pairings between a purine (adenine and guanine) and pyrimidine (thymine and cytosine) respectively. This results in a double helical structure which has both a major and minor groove, which is the most common form of DNA in *vivo* [2]. The major groove of DNA is 22 Å wide and the minor, 12 Å wide [3]. Due to the minor groove being narrow, the major groove is more susceptible to interactions occurring with biomolecules due to the accessibility of the bases [4].

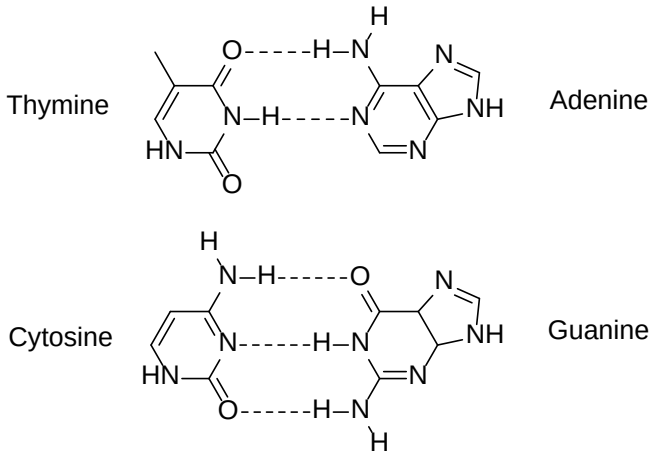

Figure 1: Watson-Crick DNA base pairings, with corresponding hydrogen bonding interactions (dotted lines)

DNA also exists in other forms; including A and Z conformations which are present in living organisms, Figure 2 [5-7]. A-DNA occurs in dehydrated samples of DNA [8]; like B-DNA it is a right-handed double helix, but is flatter and wider giving it a deep major groove and shallow minor groove [9]. Z-DNA is a left-handed double helix with a zigzag backbone, resulting in no distinct major groove. It is not a stable conformation, and is formed via B-Z DNA transitions through biological activity [10].

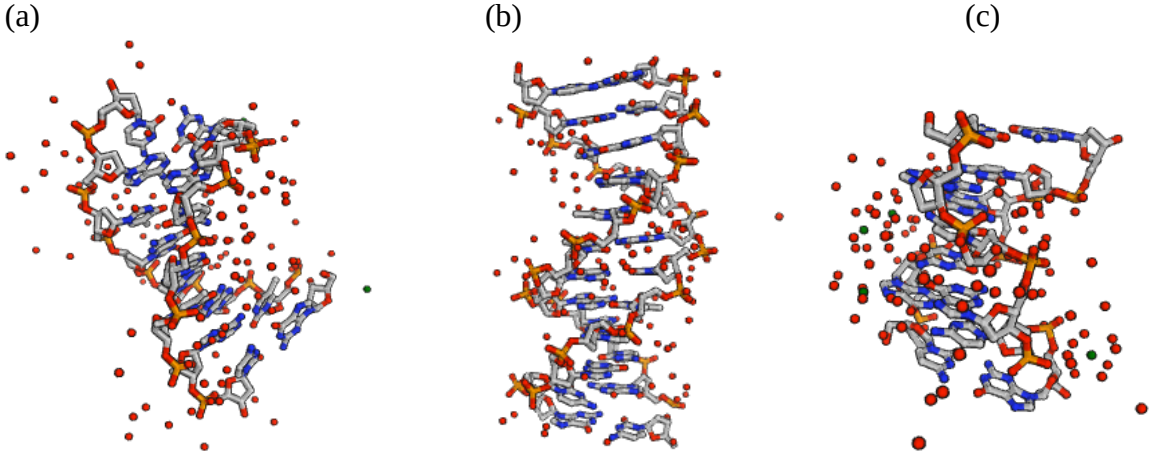

Figure 2: DNA conformations (a) A-DNA (PDB 5ANA) [5], (b) B-DNA (PDB 1BNA) [6], (c) Z-DNA (PDB 1DCB) [7]

Other DNA structures also occur in *vivo*, such as DNA junctions [11] and DNA tetraplex [12] which are important structures for gene expression, Figure 3. DNA junctions are intermediate structures formed by recombination events [11]. Three-way DNA junctions (3WJ) are formed during DNA replication [13]. Four-way DNA junctions are formed through homologous genetic recombination, a process which is important when repairing double-stranded DNA [11].

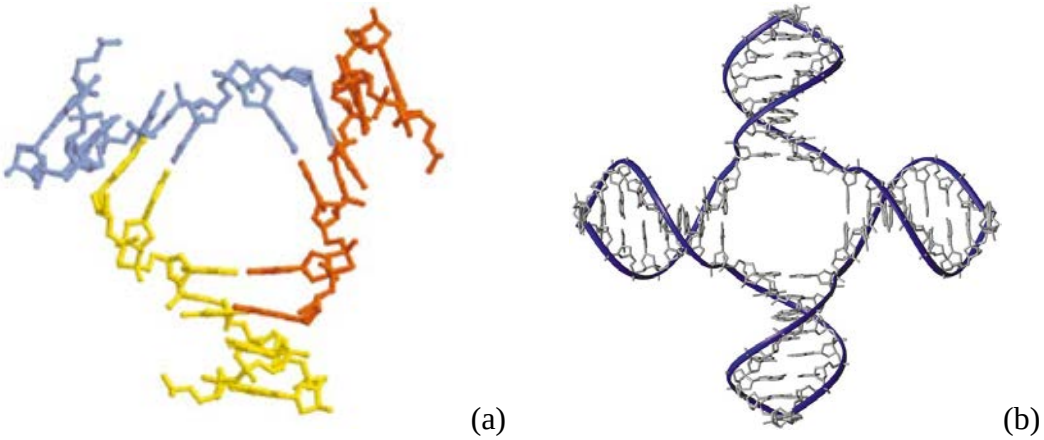

(a) (b)

Figure 3: (a) DNA three-way junction [reproduced from ref[13]], (b) DNA 4-way junction [reproduced from ref[11]]

Tetraplex or G-quadruplex DNA is a four stranded helix structure consisting of stacked G-quartets, Figure 4 [14, 15]. Each quartet involves the planar association of four guanine bases in a cyclic hydrogen bonding arrangement, from one, two or four guanine rich DNA sequences interacting. Such structures are found at the end of eukaryotic chromosomes [14].

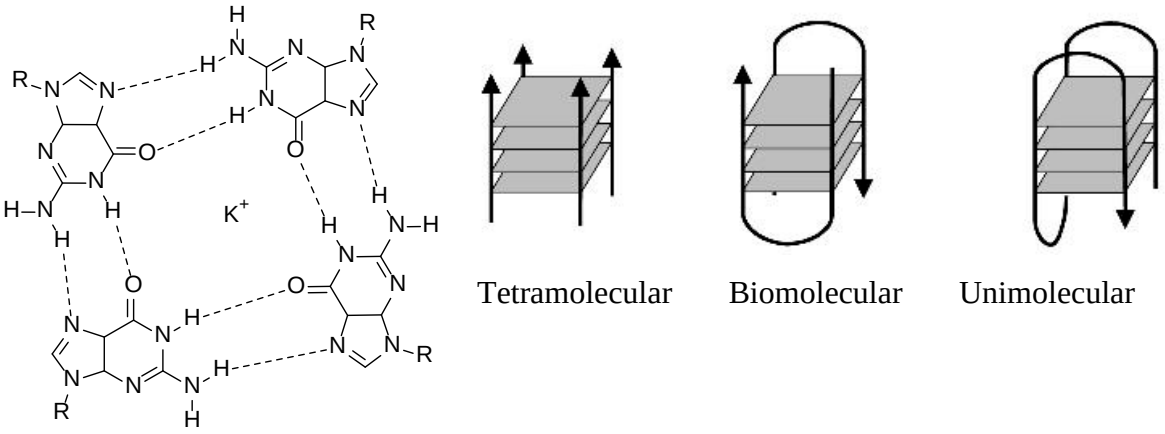

Figure 4: Guanine quartet showing hydrogen bonding interactions (left) [14] and the possible conformers of G-quandruplexes (right) [adapted from ref[15]]

1.2 DNA Recognition

Interactions with DNA have been explored for many years to develop drug molecules. Natural and synthetic small molecules are able to interact with DNA via a range of binding modes, categorically: major groove binders, minor groove binders, intercalators, sugar-phosphate backbone binders and through coordinative binding. Such interactions may effect the biological function of DNA, resulting in potential therapeutic agents.

1.2.1 Major Groove Binders

The major groove of B-DNA is prone to interactions with biological macromolecules, as the edge of the DNA bases are exposed due to the width of the groove (22 Å) [3, 4]. Zinc fingers are common motifs found on DNA-binding proteins which invoke a structural change on binding to DNA. They bind to the major groove of DNA, Figure 5, resulting in a globular structure as a result of the DNA being coordinated to a zinc centre [16]. Multiple zinc fingers interact with the DNA in a sequence-specific manner, to invoke structural changes. Such proteins are usually involved in gene transcription processes and as such have been targeted for use in new gene regulation [17] and HIV therapies [18].

Figure 5: Zinc finger interaction with the major groove of DNA (PDB 2GLI) [16]

Other small synthetic molecules have also been found to bind to the major groove of DNA. For example Numistine, Figure 6, a derivative of nitrosourea acts as a major groove directed alkylating anticancer agent. Through interactions with specific bases in the major groove, the compound acts a therapeutic agent for glioma treatment [19].

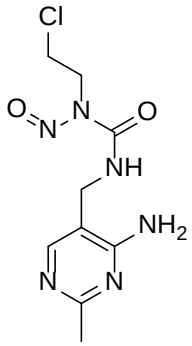

Figure 6: Structure of Numistine [19]

1.2.2 Minor Groove Binders

The minor groove of DNA is deeper and narrower than the major, being only 12 Å wide. As such, it partakes in fewer interactions with biological molecules, making it an ideal target for synthetic molecules.

Hoechst 33258 is a fluorescent DNA stain which binds in the minor groove of B-DNA, Figure 7 [20, 21]. Research shows that the molecule binds preferentially to A-T rich DNA sequences, commonly found in the minor groove region [21]. On binding to DNA, the compound fluoresces and so is commonly used as a nuclear stain within cell studies to identify viable cells [22]. It can be used to investigate whether a new compound binds to the minor groove of DNA, via Hoechst displacement [23]. With reduction in fluorescence of the Hoechst/DNA conjugate on the addition of a new compound, it is possible to conclude that Hoechst is being displaced from the minor groove and being substituted for the new compound [23].

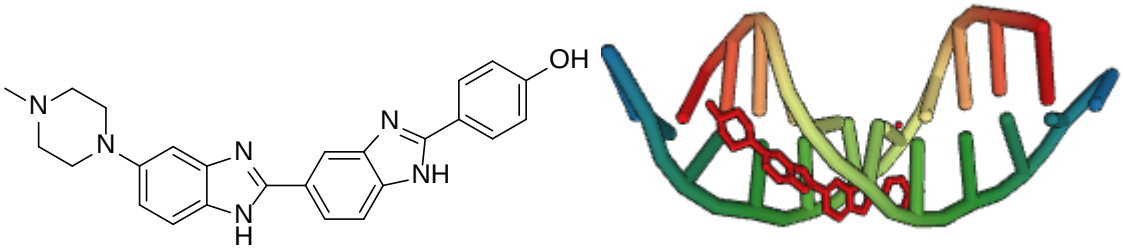

Figure 7: Structure of Hoechst 33258 (left) and the crystal structure of Hoechst binding to the minor groove of B-DNA (PDB 8BNA) [20]

Metal complexes are also able to bind in the minor groove of DNA. It has been shown that the copper complexes, $[Cu(glygly)(PyTA)]ClO_4.1.5H_2O$ and $[Cu(glygly)\text{-}(PzTA)]ClO_4.1.5H_2O$, selectively bind to the minor groove, where they are able to partake in DNA cleavage through an oxidative mechanism [24]. They are able to act as nucleic acid probes and as such, can be utilised as chemotherapeutic agents.

1.2.3 Intercalators

Intercalation normally occurs through insertion of planar polycyclic aromatic compounds between the stacked base pairs with DNA. The overlapping π systems of the intercalator and nucleobases stabilise the interaction [25].

Positively charged compounds favour intercalation as the electrostatic interaction of the negatively charged phosphate backbone on the DNA and the positive compound stabilise DNA-drug interactions [26]. A well-studied intercalating agent is Ethidium Bromide (EtBr), Figure 8 [27, 28]. This cationic compound forms a fluorescent complex on binding with DNA and so can be used, like Hoechst 33258, to establish whether new drug molecules interact with DNA, in this case via intercalation. Through displacement of EtBr, fluorescence of the solution will decrease as a result of DNA/EtBr dissociation [28].

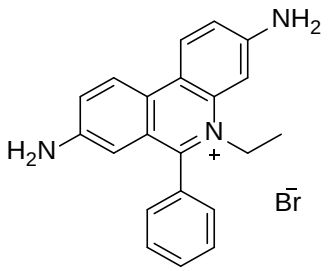

Figure 8: Structure of Ethidium Bromide (EtBr) [27]

By introducing metal centres into the design of intercalating compounds, a range of geometries can be achieved compared to solely organic compounds as a result of multiple binding sites [25]. By altering these metal centres, it has been found that binding affinities between DNA and complexes can be altered [26]. Ruthenium complexes formed with planar polycyclic organic ligands have been shown to intercalate with DNA [25, 29, 30]. $[Ru(phen)_2dppz]^{2+}$ for example, Figure 9 [29], exhibits luminescent properties on interacting with DNA [30]. In aqueous solution, emission of the compound is quenched, however on intercalation with DNA, luminescence is enhanced, providing positive indication that an interaction is occurring [30].

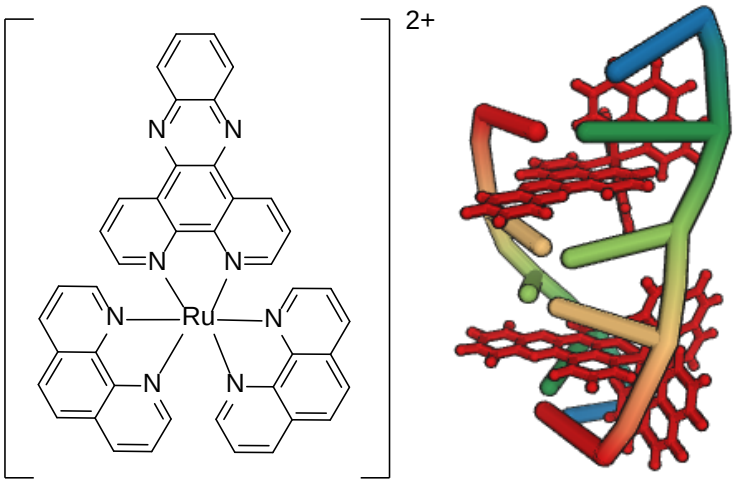

Figure 9: Structure of rac-[Ru(phen)$_2$dppz]$^{2+}$ (left), intercalation of rac-[Ru(phen)$_2$dppz]$^{2+}$, showing enantiomer orientation (PDB 4JD8) (right) [29]

1.2.4 Sugar-phosphate Backbone Binders

The sugar-phosphate backbone of DNA comprises of alternating sugar and phosphate units. The phosphate groups are negatively charged and the oxygen rich structure is hydrophilic in nature [31]. As such, interactions with cationic species are favourable.

There are few examples of compounds which exclusively bind to the sugar-phosphate backbone of DNA. However, a trinuclear platinum complex has been developed which interacts with the backbone, Figures 10 and 11 [32, 33].

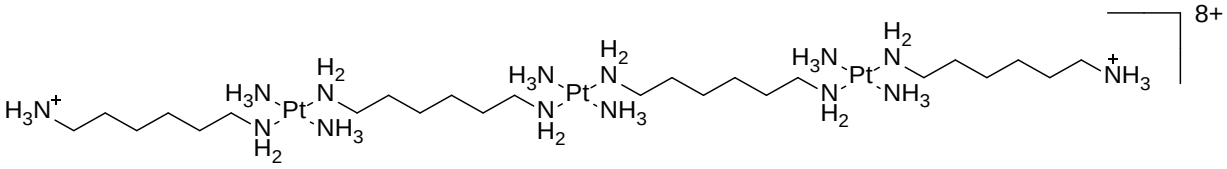

Figure 10: Farrell's trinuclear platinum compound [32]

This compound contains three square planar platinum atoms which are unable to participate in covalent bonding with DNA. As such, this long cationic molecule can span across the sugar-phosphate backbone of DNA, spanning the minor groove, Figure 11.

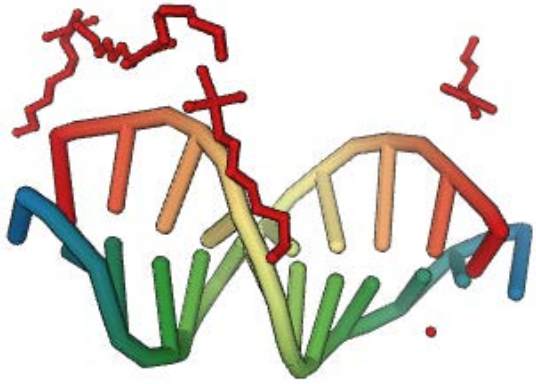

Figure 11: Crystal structure of Farrell's trinuclear platinum drug binding to the sugar-phosphate backbone of DNA (PDB 2DYW) [33]

1.2.5 Coordinative Binding

Some molecules are able to bind directly to DNA, often selectively for a specific nucleotide or binding mode. The most celebrated metallodrug, cisplatin, is an example of a simple molecule which is capable of binding with DNA, resulting in distortion of the structure, Figure 12 [34]. By coordinating specifically to two adjacent guanines in the double helix, it is able to manipulate the structure, generating kinks; so acting as an anticancer treatment by inducing apoptosis as a result of the cell cycle being terminated in the G2 phase [34, 35].

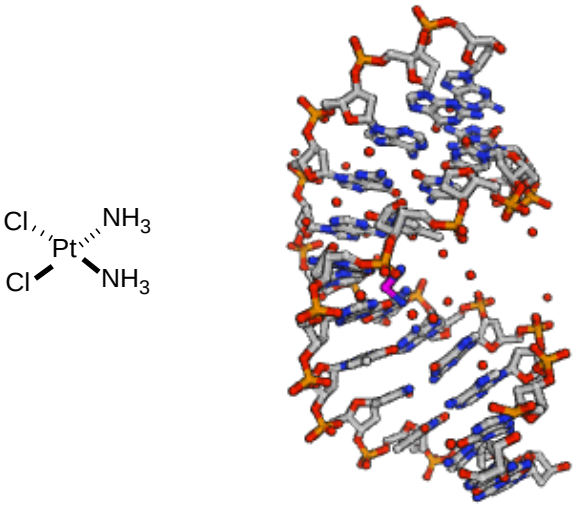

Figure 12: Structure of cisplatin (left), structure of cisplatin bound to DNA (right), demonstrating the kinking effect inflicted on the DNA structure (PDB 1AIO) [34]

This molecule plays an important role in treatment for a range of cancers including testicular, ovarian and bladder. Severe side-effects are produced by this drug, including vomiting, kidney toxicity and bone marrow suppression [25]. Consequently, many variations on this molecule have been developed in an attempt to enhance the drug properties and reduce side-effects [36]. Compounds such as oxaliplatin and carboplatin, Figure 13, have been developed to target cancer cell lines which are cisplatin resistant and to reduce side-effects, respectively [37, 38]. On producing libraries of cisplatin analogues, research continues to build on and develop current cancer treatments [39].

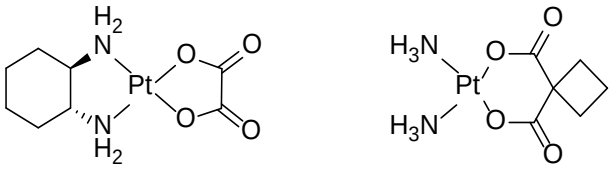

Figure 13: Structure of oxaliplatin (left) and carboplatin (right) [37]

Based on the success of cisplatin, further research into the use of metal complexes in anticancer therapy has been carried out [40-42]. A variety of metal centres including iron, ruthenium and gold, have been used to create new therapeutic agent, Figure 14.

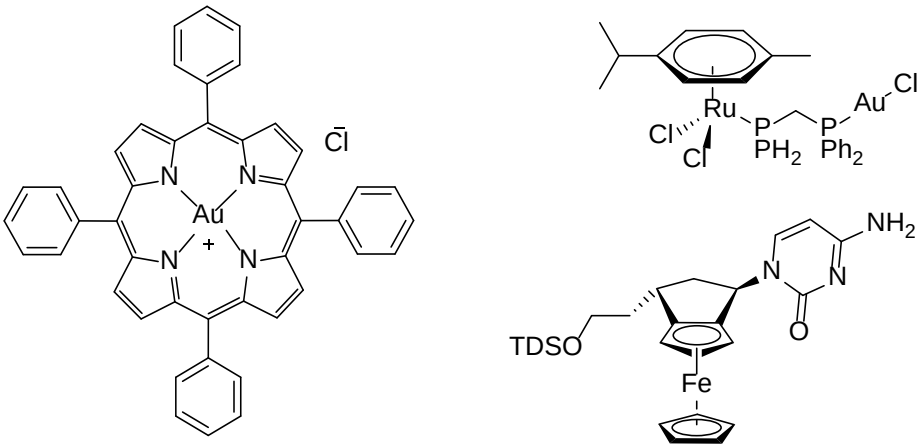

Figure 14: Representative metallodrug compounds being investigated for anticancer treatment [40, 42]

1.2.6 Drug Recognition of Other DNA Structures

As well as duplex DNA, other DNA structures are present within cells, resulting from processes which occur in *vivo*, such as DNA replication, recombination and transcription. As such, these structures are also targets for new therapeutic agents.

1.2.6.1 DNA Junctions

DNA three-way junctions (3WJ) are Y-shaped DNA structures which contain a cavity where there is no helix stacking [43]. Such structures form during DNA rearrangements and so can be targeted by drug molecules. It has been found that such structures can be stabilised with the use of metal ions, forming stable structures within the junction [44]. On modifying DNA strands with bpy, it is possible to form stable 3WJs in the presence of Ni(II). Formation of $[Ni(bpy)_3]^{2+}$ within the centre of the cavity results in a stable junction formation [44].

Holliday junctions are also an important structure to consider when designing drug molecules. These four-way junctions (4WJ) are intermediate structures formed during homologous genetic recombination [45]. This exchange in nucleotide sequences may occur during meiosis or during DNA repair. As such, this has become a target of interest to develop new drug molecules.

A bis-acridine compound has been developed which is able to bind noncovalently to the cross over region of a Holliday junction, Figure 15 [46]. The positively charged compound is able to neutralise the high charge density of DNA, allowing for the negatively charged DNA strands to come together in this fashion.

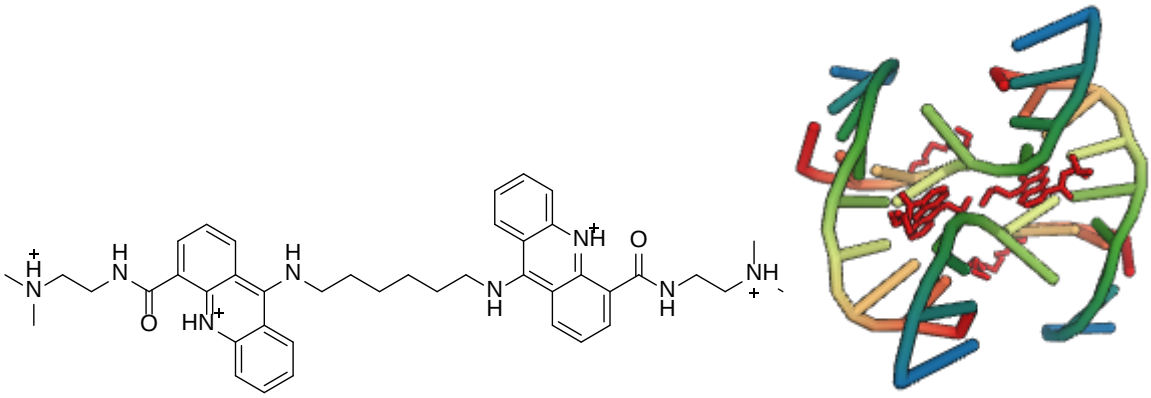

Figure 15: Structure of bis-acridine (left) and bis-acridine binding in a Holliday junction (right) (PDB 2GWA) [46]

1.2.6.2 G-Quadruplex Structures

Telomeric DNA is used within DNA replication and cell division. The ability of this replication to occur is determined by telomere length, if the sequence is too short then the cell will instigate apoptosis [47]. G-Quadruplex structures form at the terminals of telomeric DNA, and so pose a potential target to inhibit telomerase, the protein used in cancerous cells to maintain telomere length and as a result cell division [47, 48].

Metallodrugs have been developed in an attempt to target G-quadruplex structures to inhibit telomerase, so acting as anticancer agents. Due to the planar guanine quartet formed within such DNA structures, cationic planar systems have been developed to bind to the top of a G-quadruplex, so blocking the protein. Such compounds as CuGGHK-Acr [47] and the pentacationic manganese(III) porphyrin shown in Figure 16 [48] are able to stabilise these DNA structures and show potential as anticancer agents.

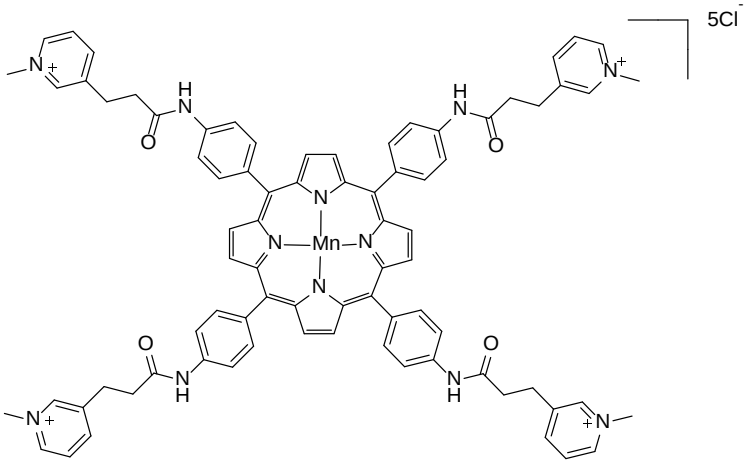

Figure 16: Pentacationic manganese(III) porphyrin G-quadruplex stabiliser [48]

1.3 Supramolecular Chemistry

Supramolecular chemistry is defined as 'the chemistry of molecular assemblies and of the intermolecular bond' [49]. It uses self-assembly of two or more molecules to form an array of structures such as helicates, catenanes, rotaxanes and molecular knots. These highly organised structures are bound by intramolecular interactions including; hydrogen bonding, metal coordination, pi-pi interactions, electrostatic effects and van der Waals forces [50]. Often metal centres are used to connect organic molecules via non-covalent bonds, bridging the gap between organic and inorganic chemistry.

1.3.1 Supramolecular Helicates

One class of supramolecular structure are supramolecular helicates. These self-assembled structures are formed using organic ligands containing several binding sites which interact with metallic cations, Figure 17. One or more ligand coordinates to one or more metal ion, with the resulting structure dependant on the metal coordination number and position of binding sites on the ligand [51]. If the same ligand strands coordinate, the resultant helicate is deemed

homotopic, whereas if different strands are coordinated a heterotopic helicate is formed, Figure 17 [51].

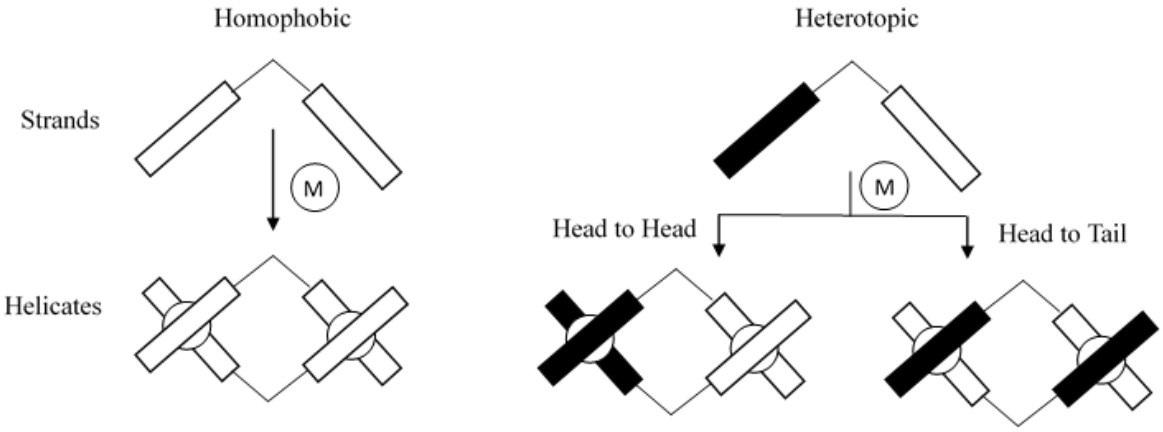

Figure 17: Schematic representation of homophobic and heterophobic helicate formation (adapted from ref[51])

Each metal centre within a helicate is stereogenic, being either Δ or Λ configurations, which correspond to P and M enantiomers respectively, of the corresponding helicate, Figure 18 [52]. When achiral ligands are bound to the metal centres, a racemic mixture is formed. To obtain predominantly one enantiomer, stereogenic motifs may be attached to the ligand to encourage only one conformer to form [52], or the enantiomer may be separated through chiral chromatography [53].

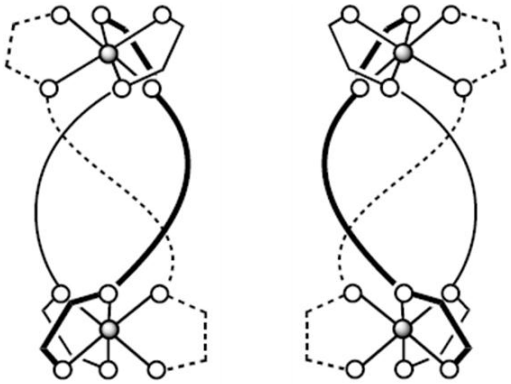

Figure 18: P (left) and M (right) enantiomers of dinuclear helicates [reproduced from ref[52]]

1.4 Fe(II) Cylinder

The iron based supramolecular cylinder $[Fe_2L_3]^{4+}$ (L= $C_{25}H_{20}N_4$), Figure 19, is a triple stranded helicate with octahedral environments around two Fe(II) centres. It is prepared with three bis-pyridyl-imine ligand strands being wrapped around the two metal centres [54, 55].

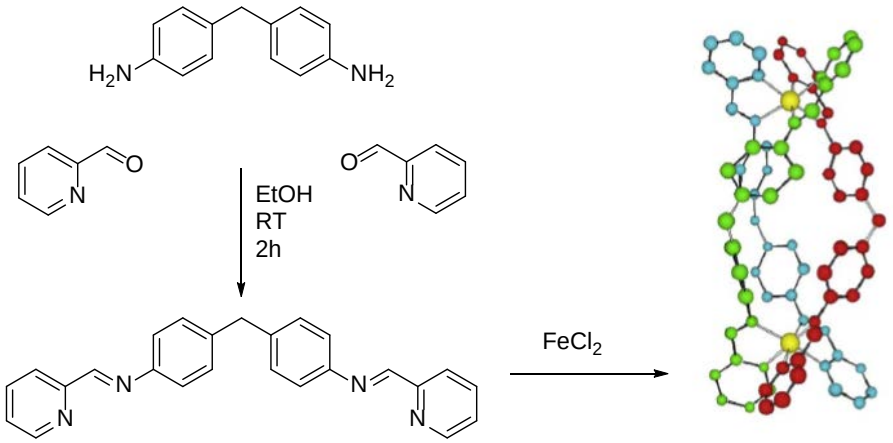

Figure 19: The molecular structure of the ligand and the tetracationic triple helical supramolecular cylinder $[Fe_2(C_{25}H_{20}N_4)_3]Cl_4$ [reproduced from ref[54]]

The size and shape of this supramolecular helicate, are comparable to that of zinc fingers [54, 56]. Consequently, it is able to fit into the major groove of B-DNA and induce a structural change, thus acting as a potent apoptotic and cytostatic agent [54, 57, 58].

The cationic nature of the cylinder allows a strong interaction with DNA [54, 59]. The major and minor grooves in DNA are flexible and have been found to respond to cationic binding [59]. This iron cylinder has a 4+ charge, so the attraction to negatively charged DNA is very strong, with the binding constant being in excess of 10^7 M^{-1} at 20 mM NaCl [60-62]. It is considered that a strong interaction between metallo-intercalators and ct-DNA when the binding constant is $>10^6$ M^{-1} [63]. As a result of the helicate interacting with the major groove of DNA, intramolecular coiling of DNA strands is induced, Figure 20, as well as DNA unwinding [54, 61].

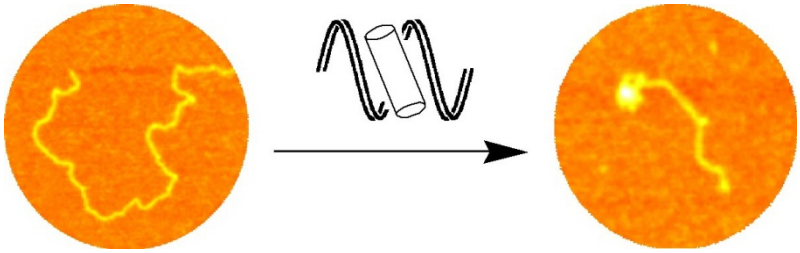

Figure 20: AFM images showing dramatic intra-molecular coiling induced by the cylinders (reproduced from ref[54])

This supramolecular molecule is chiral, so present in the right handed (P, ΔΔ) and left handed (M, ΛΛ) forms, Figure 21 [61, 62]. During synthesis, a racemic mixture is formed, with both enantiomers being *rac* isomers, as the stereochemistry around each metal centre is the same [64].

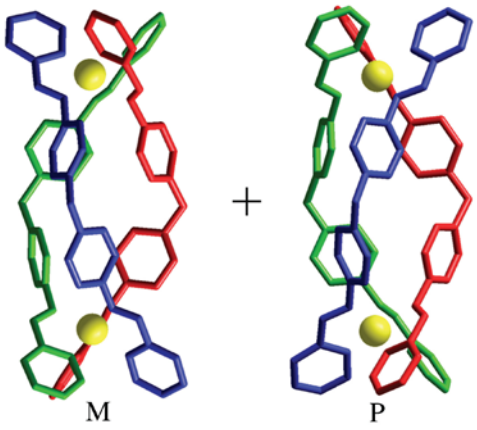

Figure 21: 3D structures of M-$[Fe_2L_3]^{4+}$ and P-$[Fe_2L_3]^{4+}$ (reproduced from ref[61])

The racemic mixture causes intramolecular bending when interacting with DNA whereas the individual enantiomers invoke different structural effects [62]. It is possible to separate these enantiomers through the simple use of paper chromatography [53].

The M enantiomer is proficient at unwinding DNA [61]. This may be the result of different binding modes as it has been proposed that the M enantiomer favours major groove binding and that the P possibly sits along the minor groove, across two phosphate backbones [62].

This metallo compound has been shown to act as a potent cytostatic and apoptotic agent [57, 65]. This water soluble complex is able to enter cancer cell lines, inducing cytostasis at low micromolar concentrations, and with slightly increased concentrations, apoptosis is reached in a number of cancer cells lines [57]. $[Fe_2(C_{25}H_{20}N_4)_3]Cl_4$ has also been shown to exhibit antimicrobial activity against *E. coli* and *B. subtilis*, demonstrating the diverse applications of this helicate [66].

1.4.1 Three-Way Junction Binding

The same metallo-supramolecular cylinder is also able to bind to DNA within a three-way junction (3WJ), Figure 22. The helicate inhabits a Y-shaped junction of branched DNA, which has a trigonal hydrophobic cavity [60, 67, 68]. The palindromic duplex of DNA, Figure 22 (left), allows for this structure to form on addition of the tetracationic complex. This 3WJ interaction has been fully characterised by NMR and X-ray crystallography [60].

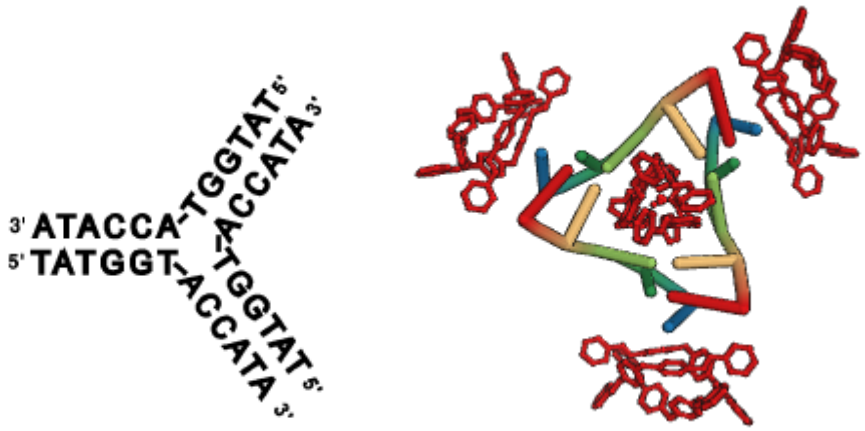

Figure 22: Schematic of the 3WJ (left) and 3D structure of the $[Fe_2L_3]^{4+}$ interacting with the DNA 3WJ (PDB 2ET0) (right) [67]

One example of a Y-shaped junction is that of the DNA replication fork, formed during transcription [65]. Blocking the replication pathway can result in cytostasis and apoptosis, depending on concentration [65, 68].

The binding of this metallo-complex to an RNA-3WJ was also investigated, as junction structures are common in RNA. It was found that the cylinder stabilises and promotes 3WJ formation with RNA strands, with similar binding affinity to the nucleic acid analogue [69].

1.4.2 Cylinder Analogues

Spurred from the success of the 'parent' cylinder $[Fe_2(C_{25}H_{20}N_4)_3]^{4+}$, variations of the helicate have been developed, with the aim of enhancing binding interactions currently observed with DNA and to improve the selectivity of the complex [55, 61, 64, 70-72].

1.4.2.1 Ligand Alteration

By altering the ligand of this supramolecular cylinder, a number of properties of the resulting helicate can be changed.

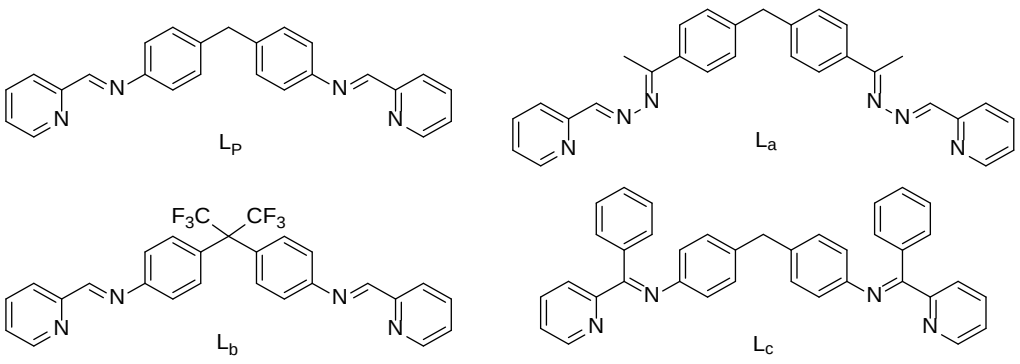

Figure 23: Example analogues of parent ligand, L_P [61, 64]

For example (L_a), Figure 22, has been made bulky compared to the parent ligand (L_P). This addition to the ligand results in the *meso* isomer (ΔΛ) of helicate being the dominant species, which was thought to be due to the lack of CH···π interactions in the complex [64].

The addition of CF_3 (L_b) and phenyl groups (L_c) also resulted in the ligand becoming bulkier. It was observed that the bulkier cylinders did not induce DNA unwinding, thought to be due to the ligands being the incorrect dimensions to fit into the major groove of B-DNA [61, 64]. Size and shape of the cylinder are thought to be crucial to the binding activity observed with DNA [61].

The ligand has also been altered with the addition of chiral arginine residues, Figure 24. This was found to enhance recognition of the DNA 3WJ, resulting in an increased cytotoxic activity against cancer cell lines [72]. Such alterations to the parent cylinder can enhance properties exhibited by this class of compound.

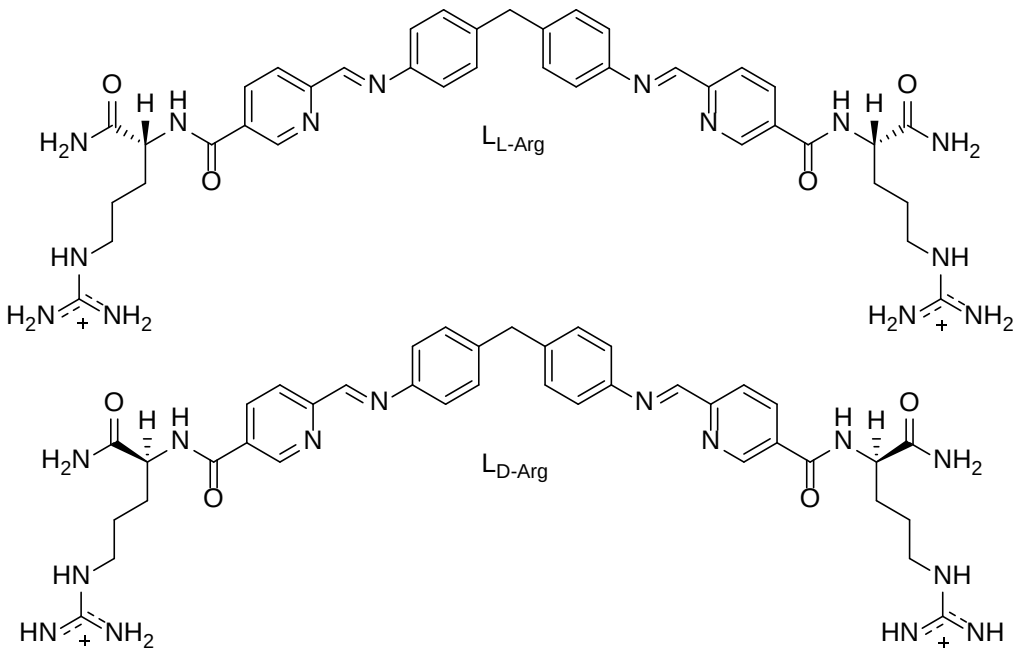

Figure 24: Structure of ligands modified with the addition of arginine residues, $L_{L\text{-}Arg}$ and $L_{D\text{-}Arg}$ [72]

1.4.2.2 Metal Alteration

The compound, $[M_2L_3]^{4+}$ where L = $C_{25}H_{20}N_4$ and the parent metal centre is Fe(II), has been investigated using alternative metal centres. Research has been carried out on cylinders containing ruthenium [73], nickel [74] and copper [75] centres.

By altering the metal centres of the helicate to ruthenium, the size and charge of the cylinder remain virtually unchanged [73]. Synthesis of this complex however, requires intense heating to encourage the inert metal to form the triple stranded helicate and after purification by column chromatography a very low yield is achieved [73].

Unlike the iron parent cylinder, this $[Ru_2L_3]^{4+}$ compound is luminescent [73] and due to the photoredox and photophysical properties of ruthenium, it is capable of causing single-strand breaks in DNA when irradiated with UVA or visible light [55]. Studies show that the ruthenium complex unwinds DNA markedly less than the iron analogue [55], yet due to the high stability of the complex at 94 ºC, PCR studies could be performed to investigate whether the complex could interfere with DNA amplification, which was not possible for the iron cylinder [65]. It was found that the supramolecular cylinder inhibits binding of DNA polymerase, demonstrating the potential of this complex to inhibit DNA transcription and hence cell replication [65].

The nickel analogue of the metallo-supramolecular cylinder has also been studied and found to stabilise G-quadruplex DNA, with chiral selectivity, Figure 25 [74]. Research showed that the P-enantiomer was able to stabilise human telomeric (h-Telo) G-quadruplex DNA, increasing the melting temperature of the 1:1 [complex]/[DNA] species, whereas the M-enantiomer did not, even at higher ratios [74]. Comparison with different, longer flanking DNA sequences, showed the same chiral selectivity of the P-enantiomer, as it was able to bind to the end of the G-quartet by external stacking, unlike the M-enantiomer, Figure 25 [74].

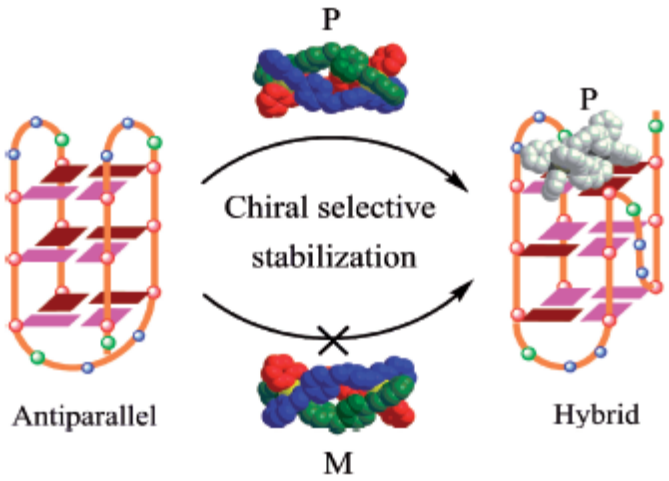

Figure 25: Representative illustration of chiral supramolecular complex selective recognition of human telomeric G-quadruplex DNA [reproduced from ref[74]]

1.5 Nanoparticles

Nanoparticles range in size, between 1 to 100 nm, making them a similar size to many biomolecules such as membrane receptors, proteins and nucleic acids [76, 77]. Nanoparticles are of great interest within medicine as they are anticipated to eradicate limitations of conventional treatments such as toxicity and bioavailability due to their unique properties of: nano size, high solubility, large surface area: volume ratio and varying geometries [77, 78]. Hence, nanomedicine is an exciting area of research being applied in many fields including drug delivery, therapeutics, biomedical imaging and biodiagnostics [76, 79].

There are a vast range of nanostructures being used to develop drug treatments including; quantum dots, carbon nanotubes, magnetic nanoparticles and gold nanoparticles [77]. The chemical composition and shape of nanoparticles influence both their chemical and physical properties [77].

Nanoparticles have some limitations, primarily that the long term side effects and toxicological risks are unknown [77]. It is thought that the properties of nanoparticles which make them

distinctive may also be the cause of their toxicity. A number of studies have been performed regarding the risks of exposure, with inconclusive results [76, 77, 80].

1.5.1 Gold Nanoparticles (AuNPs)

Gold has been utilized in medicine for many years; ancient cultures used gold for treating diseases such as measles, small pox and syphilis [81]. It is an inert metal and as a result is non-toxic, making it an ideal material to use in medicine [82]. Organogold compounds have been developed for antimicrobial, antitumour and anti-HIV treatments [78, 83].

Gold also exhibits the unique optical property, whereby electrons on the surface oscillate in the presence of incident photons hitting the metal surface, resulting in surface plasmon resonance (SPR). This resonance can be used to investigate materials adsorbing onto a gold surface and results in solutions of gold nanoparticles being a characteristic deep red/purple colour [76, 84-89].

Gold nanoparticles, AuNPs, are the most stable metallic nanoparticle [84, 85]. They can have many geometries including nanorods, nonocages and nanospheres, which are usually less than 50 nm in size [77]. The size of nanoparticle can be adjusted by varying synthetic conditions. One common method of forming AuNPs is using the Turkevich method, where gold salts are reduced in the presence of a stabilizing agent to form spherical, monodispersed particles in aqueous solution [86, 87]. Altering the ratio of ligand to gold during synthesis affects the nanoparticle size, with a larger ligand molar ratio giving a smaller core size of AuNP [85, 88, 89]. This method commonly uses a citrate salt in AuNP formation, as it acts as both a reducing agent and capping agent, stabilising the nanoparticles through electrostatic interactions between the lone pair on the oxygen and the metal surface [90]. The composition of this monolayer

coating the particles governs their chemical behaviour, whereas the core dictates their physical behaviour [91].

The size and surface charge of AuNPs greatly effects the cellular interaction they partake in. For example it has been shown that negatively charged AuNPs are able to accumulate in different organs size dependently, with smaller nanoparticles tending to accumulate in higher quantities [92, 93]. In comparison with positively charged AuNPs, the positive particles accumulated less within organs, and show higher levels of toxicity [92]. This difference in toxicity is likely due to the interactions between AuNPs and the cell membrane. Mammalian cell membranes are typically negatively charged, and so cationic AuNPs have a greater affinity to cellular structures than anionic particles [80, 94]. As such, it is proposed that such particles are able to enter cells through direct diffusion, and induce cell death [94].

1.5.2 Applications in Medicine

AuNPs can be used in a range of medical applications including drug delivery, biosensing, therapeutics, and diagnostic imaging [76, 78, 92]. They have many unique characteristics which make them useful, including their electrical and optical properties [76].

1.5.2.1 Drug Delivery

AuNPs provide an ideal scaffold for the targeted delivery of drugs, as it has previously been shown that nanosystems can accumulate within cells at high concentrations, potentially enhancing bioavailability for targeted sites [78, 82, 96-98].

Delivery systems can be formed through functionalising AuNP surfaces, to form a monolayer of drug molecules via thiol-linkers [82, 97]. The thiol groups are mobile and exchangeable on

the gold surface [99] and can stabilise AuNPs, resulting in air and thermally stable particles [85]. The binding mode of sulphur to gold is usually via a thiolate linkage (RS^-) [100].

Compared to free drugs, AuNPs have been shown to improve the biodistribution and solubility of drug molecules on binding, providing sustained and controlled release [82].

For example, by tethering oxaliplatin to the surface of AuNPs via coordination of the platinum to carboxylate functionalised AuNPs, activity towards cancerous cells can be increased up to 6-fold compared to the free drug [98]. This increase in potency was thought to have resulted from increased cellular uptake of the nanoparticles and hence the drug molecule [98].

Other potential drug compounds have successfully been delivered into cells with the use of AuNPs, including Pt(IV) prodrugs [101] which exhibit no cytotoxicity without being delivered into cell lines with the use of AuNPs and Ru(II) compounds [102] which can be released from the surface of AuNPs once within cells, to induce cell death through exposure to light .

It is also possible to use AuNPs to deliver other biomolecules [97], including nucleic acids and proteins [103]. AuNPs are diverse nanocarriers which can hold large biomolecules without any hindrance to their function [77, 82]. The addition of DNA to AuNPs can also stabilise particles in solution [104] and enhance cellular uptake of the AuNPs [103-105]. It is possible to visualise such DNA/AuNP hybrids within cells [103] and can be characterised using circular dichroism [106].

Such research demonstrates how AuNPs can be utilised to increase drug potency, by ensuring drug molecules enter the cell as a result of proficient uptake of the nanoparticle vehicles. Due to the liable nature of the thiol linkers binding compounds to the nanoparticle surface, evidence suggests that the mode of action the drug molecules would take to induce cell death are not hindered as a result of being initially bound to a gold surface. As such, this is a stimulating area of research, which will be explored further within this thesis.

1.5.2.2 Gene Therapy

Another use of AuNPs is in gene therapy, where they are able to act as non-viral system for gene delivery [77]. Viruses are a well-known medium for gene therapy; however they have safety concerns. Due to the number of barriers being encountered (blood-retinal, blood-brain etc.) the efficiency of non-viral gene delivery systems has been found to be poor [77, 82]. Nanoparticles, however, have been shown to cross these same barriers [77, 96] and due to their large surface to volume ratio, the payload to carrier ratio is optimised, making them an ideal alternative to viral treatments [82].

1.5.2.3 Sensors

Through selectively functionalising the surface of AuNPs with specific analytes, it is possible to utilise them as sensors. For example, by attaching a chelating ligand to the surface, lanthanide ions can be incorporated into the surface monolayer, resulting in phosphorescent nanoparticles which can detect the presence of other metal cations [107]. It has been shown that G-quadruplex functionalised particles can also be used as sensors, specifically detecting the presence of Pb^{2+} through changes in LSPR absorbance [108]. By immobilising organoruthenium(II) complexes onto AuNPs, an effective electrochemical system has been developed with the capability to detect iodate and nitrite in solution [109]. As such it is possible to dramatically alter the properties of AuNPs through their functionalisation, making them an adaptive platform to utilise.

1.5.3 Gold Nanoparticles in Cancer Treatment

One area of research under continual development, is the use of AuNPs for treatment and detection of cancer. It has been shown that AuNPs have the great advantage of accumulating in cancerous cells, increasing cell stress and hindering cell growth [98, 110, 111]. Consequently, the use of AuNPs may potentially decrease toxicity levels seen with other treatment methods and are hoped to reduce limitations of dosage levels and drug resistance to certain cancer types. By tethering known drug molecules to AuNPs, it is possible for drug potency to be increased. The potent anticancer metallo-drug cisplatin has successfully been attached to AuNPs, in an attempt to enhance the selectivity of drug administration [112]. The functionalised nanoparticles were able to enter cancerous cells and exhibit enhanced in *vitro* anticancer activity, comparable to free cisplatin [112].

A cisplatin Pt(IV) prodrug, which is reduced to Pt(II) in cells to give active cisplatin has also been attached to AuNPs [113]. In its prodrug form, attached to AuNPs, it can successfully be delivered to prostate cancer, resulting in reduction of tumour size, at significantly reduced concentrations compared to the free drug [110]. By combining this technology with protein recognition on cell surfaces, delivery can be targeted specifically to prostate cancer cells, using the prostate specific membrane antigen, PSMA [113].

As well as prostate cancer, breast [114], lung [115] and head and neck cancer [110] have also been targeted by AuNP treatments, showing the diverse capability of these nanostructures. Early-phase clinical trials and single-dose pilot studies have been performed with AuNP therapies, showing some positive results, indicating that nanoparticles could be a treatment option in the future.

AuNPs have been used in radiotherapy studies. Nanoparticles capped with glucose, function by accelerating the G1/S cell cycle phase, leaving cells in the G2/M phase, sensitising cancer cells

to radiotherapy. This treatment process has been found to be affective in prostate cancer cells [116].

AuNPs can also be used for the detection of cancer. The intense scattering of large AuNPs allows for imaging of cancerous cells. It is possible to label cancer cells using immunotargeting. By attaching particular antibodies to the AuNP surface, specific cells are targeted and detected [117].

Photothermal cancer therapy can also be used with AuNPs. Research has been carried out on nanoparticles which aggregate in acidic conditions, similar to those found in cancerous cells. As such, an absorbance shift to far-red and NIR is observed for the aggregate species, which can be exploited for photothermal therapy, demonstrated within in *vivo* models [118]. Breast cancer can be targeted via this treatment, using doxorubicin-loaded DNA wrapped gold nanorods [119]. It was found that cell apoptosis was induced by these nanosystems, and on laser irradiation, growth of primary breast tumours were reduced and distant metastasis inhibited [119]. By attaching prodrugs the surface of AuNPs, it is possible to photoactivate the drug molecule with near infrared light, so controlling the activity of the drug molecule until it has accumulated in cancerous cells as a result of being nanoparticle bound [120]. Such photothermal therapy can also be used with clusters of AuNPs, resulting in high ablation temperatures, shown to be effective towards breast cancer cell lines [121].

By combing nanotechnology and supramolecular chemistry, it is therefore proposed to imitate some of the success described with respect to combining therapies to produce an effective anticancer agents, through delivery of supramolecular complexes to the desired cancerous cells.

1.5.4 Metal Compound Functionalised Nanoparticles

As described with the platinum anticancer compounds oxaliplatin and cisplatin, inorganic molecules can be attached to the surface of nanoparticles via ligand displacement, to enhance drug delivery. Through the diverse nature of metallic complexes, it has also been possible to attach compounds to AuNPs with a variety of metal centres. For example, ruthenium compounds have successfully been attached to AuNPs in order to form luminescent particle for use in cellular imaging, Figure 26 [120]. Through attaching the complex via long alkyl chains, the luminescent properties of the complex remain unquenched by the nanoparticle surface, resulting in a system which can be used for imaging in cells [120].

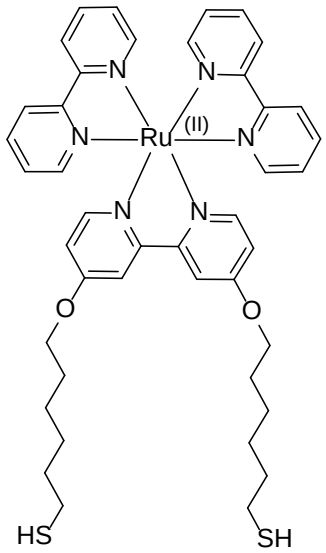

Figure 26: Structure of the ruthenium(II) polypyridyl complex developed in the Pikramenou group [125]

Nickel [121] and iron complexes [122] have also be attached to AuNPs, for use as protein sensors and for the adsorption of microbes respectively.

Nanoparticles can be used to hold lanthanide ions, for use in phosphorescent and fluorescence applications [107, 126-128]. Eu(III) complexes can be attached to AuNPs, to give water soluble luminescent particles [125]. When combined with peptide coated AuNPs, it is possible to

monitor peptide interactions from the red luminescent properties generated on lanthanide binding [126]. The advantage of using AuNPs is that a high concentration of material can be obtained without affecting emission properties. This produces efficient sensors for metal cations and is thought could be utilized in other areas such as in biomolecular and optoelectronic systems [107]. It has been shown therefore, that a range of metal complexes can be bound to the surface of AuNPs, without the properties of the compounds being jeopardised as a result.

1.5.5 Reactions on Gold Nanoparticles

To functionalise the surface of AuNPs, ligands on the surface can be displaced or reactions can be performed on the surface monolayer to attached desired functionality, Figure 27. The latter enables nanoparticles to be functionalised with a variety of compounds, not just those with a thiol/sulphur containing moiety.

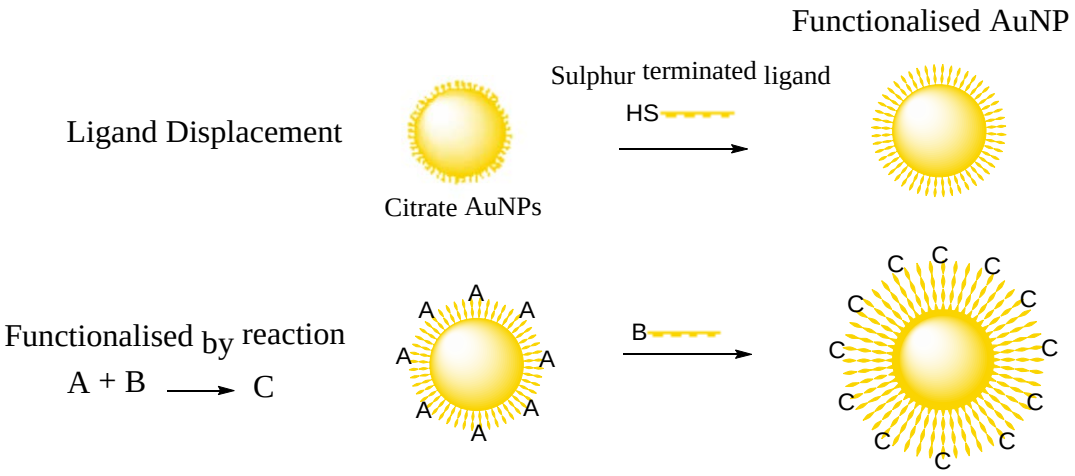

Figure 27: Schematic representation of AuNPs being functionalised through ligand displacement and through reactions on the surface monolayer

By attaching one reactant to the AuNP surface, reactions can be carried out on the monolayer using similar reaction conditions to those used without nanoparticles present.

For example, ‘click’ reactions have been performed on nanoparticles as a method to attach metal complexes to the surface [128] and as a method of detecting Cu^{2+} in solution, through the binding and aggregation of complementary crosslinking nanoparticles [129]. This versatile coupling technique has also been used to functionalise AuNPs for use as an electrochemical aptasensor [130]. Using this technique allowed for self-assembly of the nanoparticle coating, which was able to detect the presence of lysozyme [130].

Another coupling technique which has been used on AuNPs is peptide coupling [131]. The reaction between carboxylate coated nanoparticles and a peptide chain with amine terminal, allows for peptide structure to be easily bound to AuNPs [131]. Such systems are then able to go on to further react in reactions such as oxidative coupling [132], showing the diverse capabilities of functionalising AuNPs for a desired purpose.

1.6 Summary and Thesis Aims

Vast amounts of research has been conducted to understand the varying DNA structures and target sites for drug recognition. Previous research has been carried out to use supramolecular structures to target these biomolecules to induce a structural change, and the use of AuNPs has become profound in resent year as a method of directing the delivery of drug molecules and enhancing the potency of a range of drug molecules through a range of means.

The work described in this thesis, aims to synthesise novel supramolecular helicate structures which are able to bind to a range of DNA structure to induce structural change. By adding new functionality to the known class of triple stranded iron helicate, it is aimed to enhance the kinking and coiling observed when interacting with ct-DNA, with a view to producing highly potent cytotoxic compounds. It is also aimed that these novel compounds will stabilise and encourage the formation of DNA 3WJs, and as a result, create compounds which can interact

with DNA via multiple binding modes, to enhance the ability of this class of compound to inhibit DNA replication.

It is also aimed to combine this supramolecular chemistry with nanotechnology. Through the addition of new functionality to the supramolecular helicate $[Fe_2L_3]^{4+}$ (L= $C_{25}H_{20}N_4$), it is hoped to increase the DNA recognition and cytotoxicity properties of the complex. By then attaching this iron cylinder to the surface of gold nanoparticles, it is hoped to enhance interactions currently observed with DNA. By attaching multiple cylinders to the AuNP surface, it is hypothesised that higher concentrations of the compound can be used to treat cells and as such an increased number of interactions will occur with DNA, increasing potency of the complex. Ultimately the aim being to increase the kinking and coiling effect on binding with DNA, causing hindrance to replication, producing a potentially potent anticancer therapy.

By attaching this class of compound to the surface of AuNPs it is also anticipated that this will direct delivery of the complex to cancerous cell lines. As AuNPs accumulate within cancerous cells, it is hoped that this too will increase the cytotoxic nature of the helicates, as well as minimise possible side effects from the compound entering non-cancerous cells. Ultimately, it will be aimed to synthesise multi-functionalised nanoparticles, containing a supramolecular drug molecule and targeting agent on the AuNP monolayer, in order to target delivery to a specific cancer cell line through targeted recognition.

By exploring interactions of the developed helicates and AuNPs with DNA and cells, using the DNA binding techniques; circular dichroism, linear dichroism and polyacrylamide gel electrophoresis, and cell toxicity studies such as MTT assays, it is hoped to show that supramolecular chemistry and nanotechnology can be combined to produce exciting results within this area of research.

1.7 References

1. J. D. Watson and F. H. C. Crick, *Nature*, 1953, **171**, 737-738
2. X-L. Yang and A. H-J. Wang, *Pharmacology & Therapeutics*, 1999, **83**, 181–215
3. R. Wing, H. Drew, T. Takano, C. Broka, S. Tanaka, K. Itakura and R. E. Dickerson, *Nature*, 1980, **287**, 755-758
4. C. O. Pabo and R. T. Sauer, *Ann. Rev. Biochem.*, 1984, **53**, 293-321
5. F. Takusagawa, *J. Biomol. Struct. Dyn.*, 1990, **7**, 795-809
6. H. R. Drew, R. M. Wing, T. Takano, C. Broka, S. Tanaka, K. Itakura and R. E. Dickerson, *Proc. Natl. Acad. Sci. USA*, 1981, **78**, 2179-2183
7. R. V. Gessner, C. A. Frederick, G. J. Quigley, A. Rich and A. H. Wang, *J. Biol. Chem.*, 1989, **264**, 7921-7935
8. A. K. Mazur, *J. Am. Chem. Soc.*, 2003, **125**, 7849-7859
9. M. Trieb, C. Rauch, B. Wellenzohn, F. Wibowo, T. Loerting and K. R. Liedl, *J. Phys. Chem. B*, 2004, **108**, 2470-2476
10. M. A. Fuertes, V. Cepeda, C. Alonso and J. M. Pérez, *Chem. Rev.*, 2006, **106**, 2045-2064
11. D. M. J. Lilley, *Q. Rev. Biophys.*, 2000, **33**, 109-159
12. H. Mita, T. Ohyama, Y. Tanaka and Y. Yamamoto, *Biochemistry*, 2006, **45**, 6765-6772
13. K. C. Woods, S. S. Martin, V. C. Chu and E. P. Baldwin, *J. Mol. Biol.*, 2001, **313**, 49-69
14. K. Suntharalingham, A. J. P. White and R. Vilar, *Inorg. Chem.*, 2009, **48**, 9427-9435
15. G. Songab and J. Ren, *Chem. Commun.*, 2010, **46**, 7283–729
16. N. P. Pavletich and C. O. Pabo, *Science*, 1993, **261**, 1701-1707
17. C. A. Gersbach, T. Gaj and C. F. Barbas, *Acc. Chem. Res*., 2014, **47**, 2309−2318
18. L. Reynolds, C. Ullman, M. Moore, M. Isalan, M. J. West, P. Clapham, A. Klug and Y. Choo, *Proc. Natl. Acad. Sci. USA*, 2003, **100**, 1615-1620
19. S. Agarwal1, D. K. Jangir1, R. Mehrotra1, N. Lohani and M. R. Rajeswari, *PLOS ONE*, 2014, **9**, 1-8
20. P. E. Pjura, K. Grzeskowiak and R. E. Dickerson, *J. Mol. Biol.*, 1987, **197**, 257-271
21. J. A. Parkinson, J. Barber, K. T. Douglas, J. Rosamond and D. Sharples, *Biochemistry*, 1990, **29**, 10181-10190

22. Y. Teng, M. Gao, J. Wang, Q. Kong, H. Hua, T. Luo and Y. Jiang, *Cell Death Dis.*, 2014, **5**, 1-12
23. N. Shahabadi, S. Hadidi and A. Taherpour, *Appl. Biochem. Biotechnol.*, 2014, **172**, 2436-2454
24. X.-B. Fu, D.-D. Liu, Y. Lin, W. Hu, Z.-W. Maoa and X-Y Le, *Dalton Trans.*, 2014, **43**, 8721–8737
25. J. C. García-Ramos, R. Galindo-Murillo, F. Cortés-Guzmán and L. Ruiz-Azuara, *J. Mex. Chem. Soc.*, 2013, **57**, 245-259
26. G. Baronea, A. Terenzi, A. Lauriaa, A. M. Almericoa, J. M. Leal, N. Bustoc and B. Garcíac, *Coord. Chem. Rev.*, 2013, **257**, 2848-2862
27. J.-B. Lepecq and C. Paoletti, *J. Mol. Biol.*, 1967, **27**, 87-106
28. J. Zhu, L. Chen, Y. Dong, J. Li and X. Liu, *Spectrochim. Acta. Mol. Biomol. Spectrosc.*, 2014, **124**, 78-83
29. J. P. Hall, D. Cook, S. R. Morte, P. McIntyre, K. Buchner, H. Beer, D. J. Cardin, J. A. Brazier, G. Winter, J. M. Kelly and C. J. Cardin, *J. Am. Chem. Soc.*, 2013, **135**, 12652-12659
30. F. Pierand and A. Kirsch-De Mesmaeker, *Inorg. Chem. Commun*., 2006, **9**, 111-126
31. M. J. Hannon, *Chem Soc Rev*, 2007, **36**, 280-295
32. M. B. G. Kloster, J. C. Hannis, D. C. Muddiman and N. Farrell, *Biochemistry*, 1999, **38**, 14731-14737
33. S. Komeda, T.Moulaei, K. Kruger Woods, M. Chikuma, N. P. Farrell and L. Dean Williams, *J. Am. Chem. Soc*., 2006, **128**, 16092-16103
34. P. M. Takahara, A. C. Rosenzweig, C. A. Frederick and S. J. Lippard, *Nature*, 1995, **377**, 649-652
35. G. Chu, *J. Biol. Chem.*, 1994, **269**, 787-790
36. A. Pashi and F. Zunino, *Angew. Chem. lnt. Ed. Engl*., 1987, **26**, 615-624
37. E. R. Jamieson and S. J. Lippard, *Chem. Rev*., 1999, **99**, 2467-2498
38. M. J. Hannon, *Pure Appl. Chem.*, 2007, **79**, 2243-2261
39. M. M. Misic, V. L. Jakovljevic, Z. D. Bugarcic, V. I. Zivkovic, I. M. Srejovic, N. S. Barudzic, D. M. Djuric and S. S. Novokmet, *Cardiovasc. Toxicol*., 2015, **15**, 261–268
40. P. C. Bruijnincx and P. J. Sadler, *Curr. Opin. Chem. Biol.*, 2008, **12**, 197-206
41. F. R. Keene, J. A. Smith and J. G. Collins, *Coord. Chem. Rev*, 2009, **253**, 2021-2035

42. L. Massai, J. Fernández-Gallardo, A. Guerri, A. Arcangeli, S. Pillozzi, M. Contel and L. Messori, *Dalton Trans.*, 2015, **44**, 11067–11076
43. D. R. Duckett and D. M. J. Lilley, *EMBO J.*, 1990, **9**, 1659-1664
44. J.-L. H. A. Duprey, Y. Takezawa and M. Shionoya, *Angew. Chem. lnt. Ed.*, 2013, **52**, 1212-1216
45. D. R. Duckett, A. I. H. Murchie, S. Diekmann, E. von Kitzing, B. Kemper and D. M. J. Lilley, *Cell*, 1988, **55**, 79-89
46. A. L. Brogden, N. H. Hopcroft, M. Searcey and C. J. Cardin, *Angew. Chem. lnt. Ed. Engl*., 2007, **46**, 3850-3854
47. Z. Yu, M. Han and J. A. Cowan, *Angew. Chem. lnt. Ed.*, 2015, **54**, 1901-1905
48. A. Ali and S. Bhattacharya, *Bioorg. Med. Chem.*, 2014, **22**, 4506-5621
49. J. M. Lehn, *Pure & Appli. Chem*., 1978, **50**, 871—892
50. J. M. Lehn, *Angew Chem. Int. Ed. Engl.*, 1988, **27**, 89-112
51. C. Piguet, G. Bernardinelli and G. Hopfgartner, *Chem. Rev.*, 1997, **97**, 2005-2062
52. J. J. Jodry and J. Lacour, *Chem. Eur. J.*, 2000, **6**, 4297-4304
53. M. J. Hannon, I. Meistermann, C. J. Issac, C. Blomme, J. R. Aldrich-Wright and A. Rodger, *Chem. Commun*., 2001, **12**, 1078-1079
54. M. J. Hannon, V. Moreno, M. J. Prieto, E. Moldrheim, E. Sletten, I. Meistermann, C. J. Isaac, K. J. Sanders and A. Rodger, *Angew. Chem. Int. Ed*., 2001, **40**, 879- 884
55. J. Malina, M. J. Hannon and V. Brabec, *Chem. Eur. J.*, 2008, **14**, 10408-10414
56. H. Yu, X. Wang, M. Fu, J. Ren and X. Qu, *Nucleic Acids Res.*, 2008, **36**, 5695–5703
57. A. C. G. Hotze, N. J. Hodges, R. E. Hayden, C. Sanchez-Cano, C. Paines, N. Male, M-T. Tse, C. M. Bunce, J. K. Chipman and M. J. Hannon, *Chem. Biol.*, 2008, **15**, 1258-1267
58. S. Khalid, M. J. Hannon, A. Rodger and P. M. Rodger, *Chem. Eur. J.*, 2006, **12**, 3493-3506
59. N. V. Hud and M. Polak, *Curr. Opin. Struct. Biol.*, 2001, **11**, 293–301
60. L. Cerasino, M. J. Hannon and E. Sletten, *Inorg. Chem.*, 2007, **46**, 6245-6251
61. J. Malina, M. J. Hannon and V. Brabec, *Nucleic Acids Res.*, 2008, **36**, 3630-3638
62. I. Meistermann, V. Moreno, M. J. Prieto, E. Moldrheim, E. Sletten, S. Khalid, P. M. Rodger, J. C. Peberdy, C. J. Isaac, A. Rodger and M.J. Hannon, *Proc. Natl. Acad. Sci., USA*, 2002, **99**, 5069–5074

63. S. Kemp, N. J. Wheate, D. P. Buck, M. Nikac, J. G. Collins, J. R. Aldrich-Wright, *J. Inorg. Biochem.*, 2007, **101**, 1049-1058
64. C. Uerpmann, J. Malina, M. Pascu, G. J. Clarkson, V. Moreno, A. Rodger, A. Grandas and M. J. Hannon, *Chem. Eur. J.*, 2005, **11**, 1750-1756
65. C. Ducani, A. Leczkowska, N. J. Hodges and M. J. Hannon, *Angew. Chem. Int. Ed*., 2010, **49**, 8942-8945
66. A. D. Richards, A. Rodger, M. J. Hannon and A. Bolhuis, *Int. J. Antimicrob. Ag.*, 2009, **33**, 469-472
67. A. Oleksi, A. G. Bianco, R. Boer, I. Uson, J. Aymami, A. Rodger, M. J. Hannon and M. Coll, *Angew Chem. Int. Ed. Engl.*, 2006, **45**, 1227-1231
68. D. R. Boer, J. M. C. A. Kerckhoffs, Y. Parajo, M. Pascu, I. Uson, P. Lincoln, M. J. Hannon and M. Coll, *Angew. Chem. Int. Ed*., 2010, **49**, 2336 –2339
69. S. Phongtongpasuk, S. Paulus, J. Schnabl, R. K. O. Sigel, B. Spingler, M. J. Hannon and E. Freisinger, *Angew. Chem. Int.l Ed.*, 2013, **52**, 11513-11516
70. S. E. Howson, A. Bolhuis, V. Brabec, G. J. Clarkson, J. Malina, A. Rodger and P. Scott, *Nat. Chem.*, 2012, **4**, 31-36
71. F. Cui, S. Li, C. Jia, J. S. Mathieson, L. Cronin, X-J. Yang and B. Wu, *Inorg. Chem.*, 2012, **51**, 179-187
72. L. Cardo, V. Sadovnikova, S.Phongtongpasuk, N. J. Hodges and M. J. Hannon, *Chem. Commun.*, 2011, **47**, 6575–6577
73. G. I. Pascu, A. C. G. Hotze, C. Sanchez-Cano, B. M. Kariuki and M. J. Hannon, *Angew. Chem. Int. Ed*., 2007, **119**, 4452-4456
74. H. Yu, X. Wang, M. Fu, J. Ren and X. Qu, *Nucleic Acids Res.*, 2008, **36**, 5695–5703
75. A. D. Richards, A. Rodger, M. J. Hannon and A. Bolhuis, *Int. J. Antimicrob. Agents*, 2009, **33**, 469-472
76. W. E. Bawarski, E. Chidlowsky, D. J. Bharali and S. A. Mousa, *Nanomed. Nanotechnol.*, 2008, **4**, 273–282
77. N. Sanvicens and M. P. Marco, *Trends Biotechnol.*, 2008, **26**, 425-433
78. P. C. Chen, S. C. Mwakwari and A. K. Oyelere, *Nanotechnol Science Appl.*, 2008, **1,** 45-66
79. N. L. Rosi and C. A. Mirkin, *Chem. Rev.*, 2005, **105**, 1547-1562

80. C. M. Goodman, C. D. McCusker, T. Yilmaz and V. M. Rotello, *Bioconjug. Chem.*, 2004, **15**, 897-900
81. M. Rai, A. Gade and A. Yadav, *Metal Nanoparticles in Microbiology*, Springer, Heidelburg, 2011
82. P. Ghosh, G. Han, M. De, C. K. Kim and V. M. Rotello, *Adv. Drug Deliv. Rev.*, 2008, **60**, 1307–1315
83. M. Gielen and E. R. T. Tiekink, *Metallotherapeutic Drugs and Metal-Based Diagnostic Agents: The use of metals in medicine*; Wiley & Sons, West Sussex (England), 2005, p516
84. R. Bhattacharya, C. R. Patra, A. Earl, S. Wang, A. Katarya, L. Lu, J. N. Kizhakkedathu, M. J. Yaszemski, P. R. Greipp, D. Mukhopadhyay and P.Mukherjee, *Nanomed. Nanotechnol.*, 2007, **3**, 224–238
85. M.-C. Daniel and D. Astruc, *Chem. Rev.*, 2004, **104**, 293-346
86. J. Turkevich, P. C. Stevenson and J. Hillier, *Discuss. Faraday Soc.*, 1951, **11**, 55-75
87. J. Kimling, M. Maier, B. Okenve, V. Kotaidis, H. Ballot an A. Plech, *J. Phys. Chem. B.*, 2006, **110**, 15700-15707
88. F. Westerlund and T. Bjørnholm, *Curr. Opin. Colloid In.*, 2009, **14**, 126–134
89. J. C. Love, L. A. Estroff, J. K. Kriebel, R. G. Nuzzo and G. M. Whitesides, *Chem. Rev.*, 2005, **105**, 1103-1169
90. J.-W. Park and J. S. Schumaker-Parry, *J. Am. Chem. Soc.*, 2014, **136**, 1907-1921
91. R. Arvizo, R. Bhattacharya and P.Mukherjee, *Expert Opin. Drug Deliv.*, 2010, **7**, 759-763
92. S. Hirn, M. Semmler-Behnke, C. Schleh, A. Wenk, J. Lipka, M. Schäffler, S. Takenaka, W. Möller, G. Schmid, U. Simon and W. G. Kreyling, *Eur. J. Pharm. Biopharm.*, 2011, **77**, 407-416
93. G. Sonavane, K. Tomoda and K. Makino, *Colloids Surf., B*, 2008, **66**, 274-280
94. E. E. Connor, J. Mwamuka, A. Gole, C. J. Murphy and M. D. Wyatt, *Small*, 2005, **1**, 325-327
95. J. Lin, H. Zhang, Z. Chen and Y. Zheng, *ACS Nano*, 2010, **4**, 5421-5429
96. B. Duncan, C. Kim, V. M. Rotello, *J. Control. Release*, 2010, **148**, 122-127
97. S. Rana, A. Bajaj, R. Mout and V. M. Rotello, *Adv. Drug Deliv. Rev.*, 2012, **64**, 200-216

98. S. D. Brown, P. Nativo, J-A. Smith, D. Stirling, P. R. Edwards, B. Venugopal, D. J. Flint, J. A. Plumb, D. Graham and N. J. Wheate, *J. Am. Chem. Soc*., 2010, **132**, 4678–4684

99. P. D. Jadzinsky, G. Calero, C. J. Ackerson, D. A. Bushnell and R. D. Kornberg, *Science*, 2007, **318**, 430-433

100. A. Badia, L. Demers, L. Dickinson, F. G. Morin, R. B. Lennox and L. Reven, *J. Am. Chem. Soc.*, 1997, **119**, 11104-11105

101. A. Garaikoetxea Arguinzoniz, N. Gómez Blanco, P. Ansorena Legarra and J. C. Mareque-Rivas, *Dalton Trans*., 2015, **44**, 7135-7138

102. M. Martínez-Calvo, K. N. Orange, R. B. P. Elmes, B. la Cour Poulsen, D. C. Williams and T. Gunnlaugsson, *Nanoscale*, 2016, **8**, 563-574

103. Y. Ding, Z. Jiang, K. Saha, C. S. Kim, S. T. Kim, R. F. Landis and V. M. Rotello, *Molecular Therapy*, 2014, **22**, 1075-1083

104. R. Gill, K. Göeken and V. Subramaniam, *Chem. Commun.*, 2013, **49**, 11400-11402

105. D. A. Giljohann, D.S. Seferos, P. C. Patel, J. E. Millstone, N. L. Rosi and C. A. Mirkin, *Nano Lett.*, 2007, **7**, 3818-3821

106. A. Azizi and B. Ranjbar, *Plasmonics*, 2014, **9**, 273-281

107. B. I. Ipe, K. Yoosaf and K. G. Thomas, *J. Am. Chem. Soc.*, 2006, **128**, 1907-1913

108. S. Cheng, B. Zheng, M. Wang, X. Ge, Q. Zhao, W. Liu and M. H.-W. Lam, *Biosens. Bioelectron*., 2014, **53**, 479-483

109. A. Azadbakht, A. R. Abbasi, Z. Derikvand and S. Amraei, *Mater. Sci. Eng. C*, 2015, **48**, 270-278

110. S. Jain, D. G. Hirst and J. M. O'sullivan, *Brit. J. Radiol.*, 2012, **85**, 101-113

111. H. K. Patra, S. Banerjee, U. Chaudhuri, P. Lahiri and A. K. Dasgupta, *Nanomedicine*, 2007, **3**, 111-119

112. E. C. Gryparis, M. Hatziapostolou, E. Papadimitriou and K. Avgoustakis, *Eur. J. Pharmaceut. Biopharmaceut.*, 2007, **67**, 1-8

113. S. Dhar, N. Kolishetti, S. J. Lippard and O. C. Farokhzad, *Proc. Natl. Acad. Sci., USA*, 2011, **108**, 1850-1855

114. J. Lee, D. K. Chatterjee, M. H. Lee and S. Krishnan, *Cancer Lett.*, 2014, **347**, 46-53

115. M. Sathishkumar, S. Pavagadhi, A. Mahadevan and R. Balasubramanian, *Ecotox. Environ. Safe.*, 2015, **114**, 232-240

116. W. Roa, X. Zhang, L. Guo, A. Shaw, X. Hu, Y. Xiong, S. Gulavita, S. Patel, X. Sun, J. Chen, R. Moore and J. Z. Xing, *Nanotechnol.*, 2009, **20**, 1-9

117. E. Boisselier and D. Astruc, *Chem. Soc. Rev.*, 2009, **38**, 1759-1782

118. J. Nam, N. Won, H. Jin, H. Chung and S. Kim, *J. Am. Chem. Soc.*, 2009, **131**, 13639-13645

119. D. Wang, Z. Xu, H. Yu, X. Chen, B. Feng, Z. Cui, B. Lin, Q. Yin, Z. Zhang, C. Chen, J. Wang and W. Zheng, *Biomaterials*, 2014, **35**, 8374-8384

120. E. Ruggiero, J. Hernández, J. C. Mareque-Rivas and L. Salassa, *Chem. Commun.*, 2015, **51**, 2091-2094

121. C. Iodice, A. Cervadoro, A. L. Palange, J. Key, S. Aryal, M. R. Ramirez, C. Mattu, G. Ciardelli, B. E. O'Neill and P. Decuzzi, *Opt. Laser. Eng.*, 2016, **76**, 74-81

122. N. J. Rogers, S. Claire, R. M. Harris, S. Farabi, G. Zikeli, I. B. Styles, N. J. Hodges and Z. Pikramenou, *Chem. Commun.*, 2014, **50**, 617-619

123. C. Pezzato, S. Maiti, J. L.-Y. Chen, A. Cazzolaro, C. Gobbo and L. J. Prins, *Chem. Commun.*, 2015, **51**, 9922-9931

124. T. Inomata, T. Murase, H. Ido, T. Ozama and H. Masuda, *Chem. Lett.*, 2014, **43**, 1146-1148

125. D. J. Lewis, T. M. Day, J. V. Macpherson and Z. Pikramenou, *Chem. Commun.*, 2006, **13**, 1433-1435

126. A. C. Savage and Z. Pikramenou, *Chem. Commun.*, 2011, **47**, 6431-6433

127. H. T. Khuyen, P. T. Thu, T. T. Huong, D. K. Tung, N. T. Binh, W. Strek, L. Q. Minh and T. K. Anh, *J. Lumin.*, 2015, **166**, 67-70

128. Y. Song, X. Xu, K. W. MacRenaris, X.-Q. Zhang, C. A. Mirkin and T. J. Meade, *Angew. Chem. Int. Ed.*, 2008, **48**, 9143-9147

129. Y. Zhou, S. Wang, K. Zhang and X. Jiang, *Angew. Chem.*, 2008, **120**, 7564-7566

130. D. Xie, C. Li, L. Shangguan, G. Qi, D. Xue and Q. Gao, *Sensor. Actuat. B-Chem.*, 2014, **192**, 558-564

131. D. Bartczak and A. G. Kanaras, *Langmuir*, 2011, **27**, 10119-10123

132. S. L. Capehart, A. M. ElSohly, A. C. Obermeyer and M. B. Francis, *Bioconjugate Chem.*, 2014, **25**, 1888-1892

Chapter 2

Novel Functionalised Triple Stranded Helicates

2.1 Introduction and Aims

Within the Hannon group, the iron supramolecular helicate $[Fe_2L_3]^{4+}$ (L= $C_{25}H_{20}N_4$), has been developed [1]. This cylindrical structure interacts with a variety of DNA structures, including the major groove of B-DNA and within the heart of three way junctions, 3WJ, to induce structural changes, Figure 1 [1-3]. Consequently, this complex is able to prevent DNA transactions in *vitro* [4], resulting in a potent apoptotic and cytostatic agent [5].

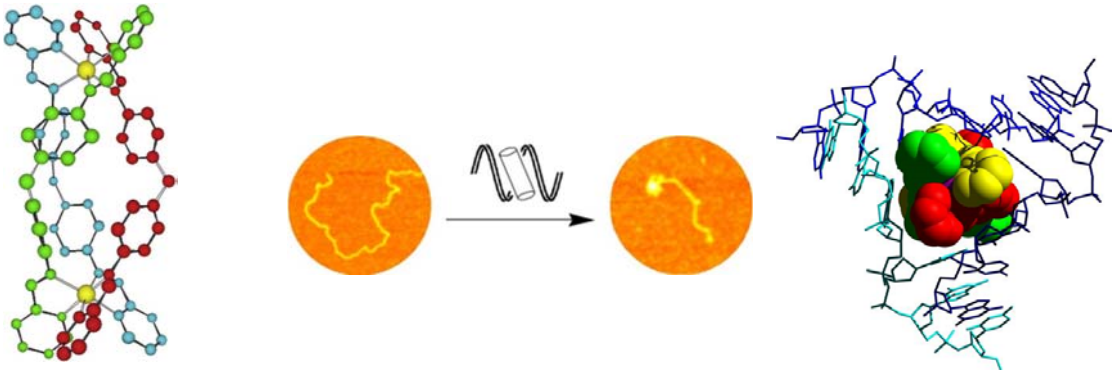

Figure 1: Structure of triple stranded supramolecular cylinder $[Fe_2(C_{25}H_{20}N_4)_3]Cl_4$ [reproduced from ref[1]] (left); AFM images showing intra-molecular coiling induced by the cylinders [reproduced from ref[1]] (middle); Model structure of cylinder bound in the heart of a DNA three-way junction [reproduced from ref[2]] (right)

Research has previously been carried out in an attempt to improve and tune the DNA binding interaction and cytotoxicity effects of this compound, through altering the ligand and metal centres of the helical structure [6-10].

The 'parent' bis-pyridyl-imine ligand is formed through a 2:1 condensation reaction between 2-pyridine carboxaldehyde and 4,4'-methylenedianiline. Three ligands are then coordinated around two metal centres, forming a triple stranded helicate [1]. The iron complex and ligand

are sensitive to a range of reaction conditions, specifically acidic environments. As such, most structural alterations are performed during ligand synthesis, commonly to the aldehyde, prior to forming the potentially labile imine bond by reaction with 'spacer' 4,4'-methylenedianiline. Reactions such as peptide coupling [6] and Suzuki couplings [7] have previously been used to add a range of functionality to the ligand, Figure 2.

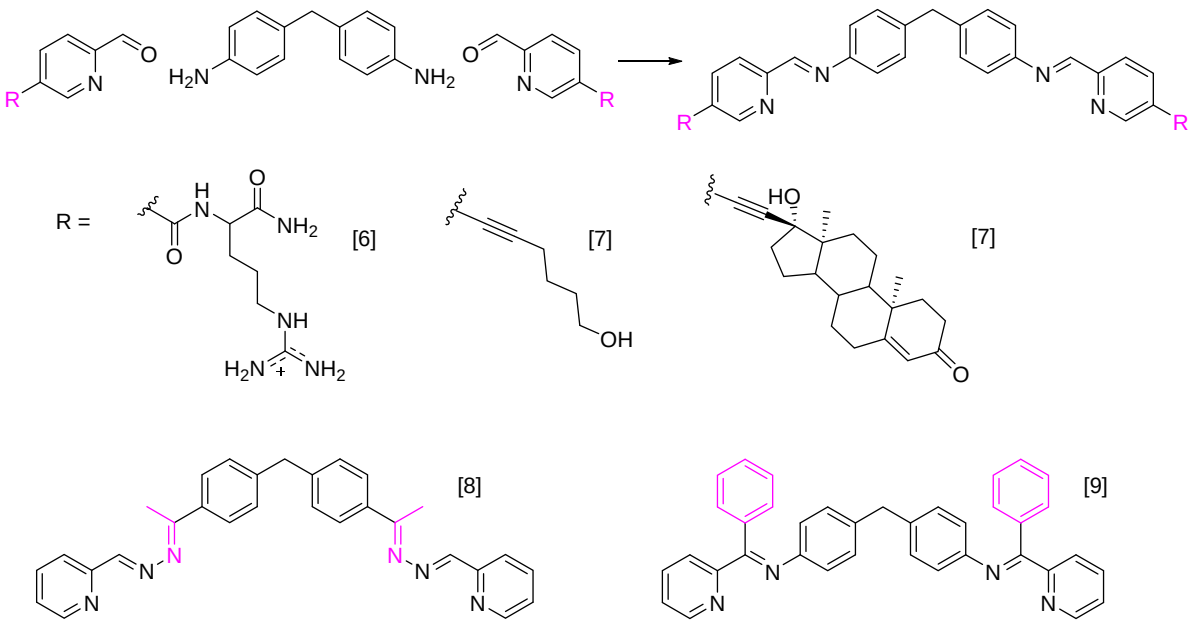

Figure 2: Example modifications previously made to the 'parent' complex, $[Fe_2(C_{25}H_{20}N_4)_3]Cl_4$ [6-9]

Inspired by the success of the iron helicate, and with a view to explore the capabilities of the supramolecular complex further, in this thesis click chemistry will be used as a novel method to functionalise the cylindrical structure. As such it is hoped to probe and potentially improve the DNA binding properties of this class of supramolecular helicate. Subsequently, it is hoped to establish an easy and reproducible method of attaching useful functionality to the helicate, whilst maintaining the solubility and cytotoxic nature of the compounds.

Alongside this, the ability and viability of attaching such helicate structures to the surface of gold nanoparticles (AuNPs) will be investigated. By attaching many cylinders to the gold

surface, it is hoped numerous interactions will occur with DNA at one time, as occurs with multiple zinc fingers on a protein surface [11]. As such, it is anticipated that the intramolecular coiling effect previously seen when the helicate interacts with B-DNA [1], would be enhanced in confined areas of binding. Consequently, this may boost activity inhibiting DNA replication, resulting in potential a potent anticancer treatment.

In order to achieve this, the parent cylinder $[Fe_2(L_P)_3]^{4+}$ (L_P= $C_{25}H_{20}N_4$), will be attached to AuNPs via sulfide linkers, as has previously been demonstrated for other inorganic drug molecules [12, 13]. Once synthesised, the cylinder coated nanoparticles will be tested for their binding effects on DNA (see *Chapter 4*). It is hoped that the cylinder is still able to bind to the major groove of DNA and, as many cylinders will be attached to the gold surface, it is anticipated enhanced intramolecular coiling will be induced, resulting in highly cytotoxic nanoparticles.

2.2 Novel Functionalisation Route

2.2.1 Click Chemistry

In order to add new functionality to the triple stranded iron helicate, a simple coupling reaction was used to combine new moieties with the original bis-pyridyl-imine ligand. Click chemistry is a widely used reaction, where azide and alkyne functional groups are coupled together with the aid of a copper(I)-catalyst, Scheme 1. This 1,3-dipolar cycloaddition, results in the formation of a 1,4-disubstituted 1,2,3-triazole [14].

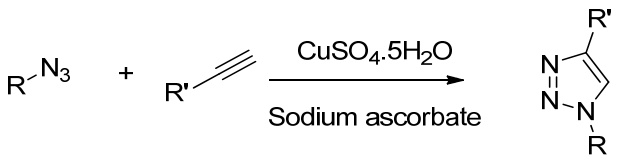

Scheme 1: General reaction scheme for a click reaction using a copper catalyst

Within the Hannon Group, the triple stranded iron helicate has previously been functionalised with alkyne groups, $[Fe_2(L_{ALK})_3][BF_4]_4$, Figure 3 [7].

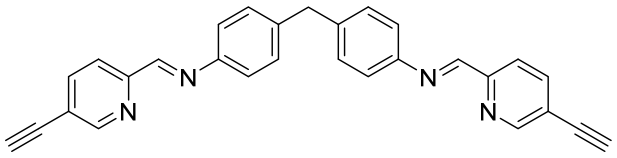

Figure 3: Structure of L_{ALK} ligand present in complex, $[Fe_2(L_{ALK})_3][BF_4]_4$, *previously synthesised by Jenna Norman* [7]

This alkyne cylinder is known to be soluble in a variety of water miscible solvents, and has shown promising results in DNA binding studies [7]. It is simply synthesised using the commercially available iron source, $Fe(BF_4)_2.6H_2O$, 'spacer' 4,4'-methylenedianaline and an aldehyde functionalised with an alkyne group, aldehyde **1**.

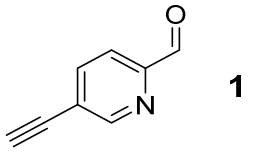

1

It was therefore decided to investigate the reactivity of this compound, and explore whether click chemistry could be used as a novel way to functionalise the cylinder, Scheme 2.

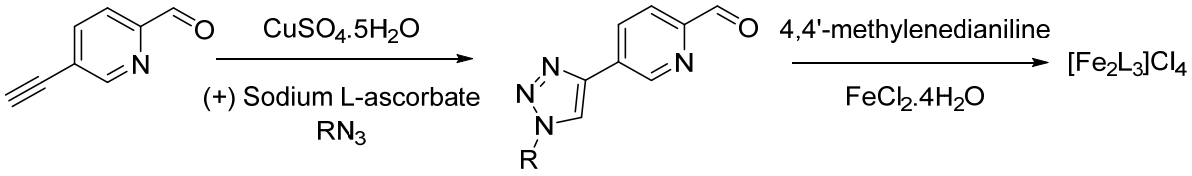

Scheme 2: Proposed cylinder functionalisation using click-chemistry

2.2.2 Sulphur Functionality

Due to the strong affinity of sulphur to gold [15] a large amount of research has previously been carried out with the connection of molecules to AuNPs via sulphur linkages [13, 16-18]. Therefore it was decided to attach a sulphur moiety to the parent ligand (L_P), in order to

subsequently attach it to the surface of AuNPs. With this addition to the parent cylinder, it was hoped that only the physical properties would be altered and not the ability of the complex to interact with DNA.

As discussed, numerous coupling reactions have previously been utilised in the Hannon group to add functionality to the triple stranded iron helicate [6, 7]. In this instance, the novel use of click chemistry will be investigated, as well as peptide coupling which has previously been used to successfully functionalise the cylinder, whilst maintaining the characteristic DNA binding properties [6], in order to attach the desired sulphur moieties to the complex.

2.2.2.1 Click Chemistry

As demonstrated in *section 2.2.1*, an alkyne group has previously been attached to the ligand system [7], making this the ideal starting material for a click reaction. By reacting aldehyde **1** with an azide, containing a sulphur moiety, it is proposed that sulphur can be incorporated into the ligand system as demonstrated in Scheme 3. The subsequent helicate structure will then contain six sulphur linkers able to interact with the surface of AuNPs.

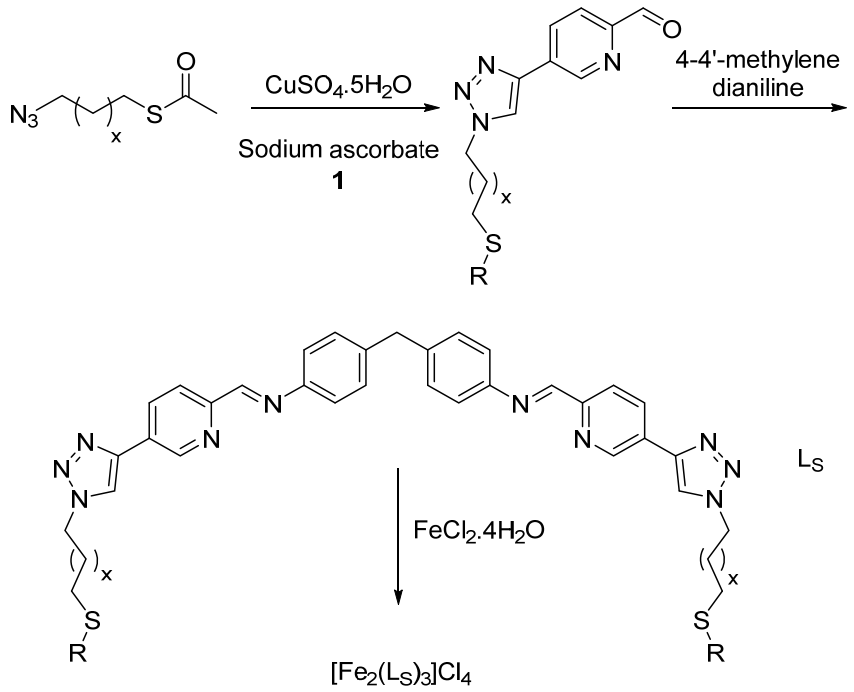

Scheme 3: Proposed synthetic route to functionalise an iron helicate with a sulphur moiety by click chemistry

2.2.2.2 Peptide Coupling

Peptide coupling is a proven technique of adding functionality to these triple stranded helicates, enhancing the binding activity of the cylinders with DNA structures [6].

Scheme 4: General peptide coupling reaction scheme, where X=activating group [19]

The amide bond generated during this coupling reaction between an amine and acid, does not adversely affect complex solubility in water miscible solvents, or how the complex interacts with biological systems [6]. As such, it was theorised that this technique could be used to add sulphur functionality to the complex, Scheme 5, which may result in biologically active complexes, able to bind to AuNPs and be cytotoxic in nature.

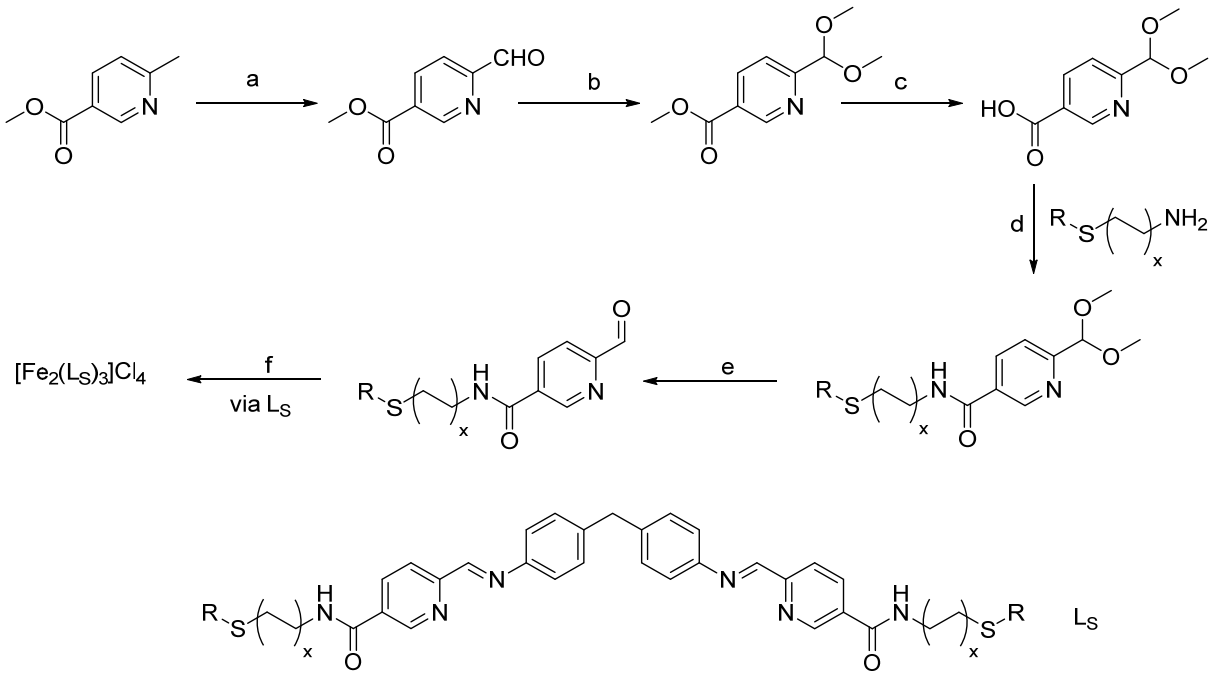

Scheme 5: Proposed synthetic route to functionalise the iron helicate with a sulphur moiety by peptide coupling

(a) I_2, DMSO (b) Trimethyl orthoformate, formic acid, sulphuric acid (c) MeOH, 1M NaOH, (d) EDC, HOBt, DMF (e) 1M HCl, THF (f) 6 equiv. aldehyde, 3 equiv. 4,4'-methylenedianiline, 2 equiv. $FeCl_2.4H_2O$.

2.3 Iron Cylinder Synthesis

2.3.1 Parent Cylinder

The iron based supramolecular cylinder $[Fe_2(L_P)_3]^{4+}$ (L_P= $C_{25}H_{20}N_4$), is a triple stranded helicate with two Fe(II) centres. It is easily prepared from three bis-pyridyl-imine ligand strands being wrapped around the two metal centres. This 'parent' complex has previously been synthesised and characterised within the Hannon group, so the synthetic route followed was from the literature [1]. This complex was synthesised in order to compare results from DNA binding and cytotoxicity studies of new complexes with those of the original structure, *Chapter 3*.

Firstly the ligand (L_P) was formed in a high yielding reaction, 92 %, by mixing 4,4'-methylenedianiline and 2-pyridine carboxaldehyde in 1:2 stoichiometry, Scheme 6. On

refluxing this ligand in a methanolic solution of iron(II) chloride, in 3:2 equivalents, a purple solution was formed, indicating that the iron complex had been synthesised. On purification of the product through counterion exchange from $[Fe_2(L_P)_3]Cl_4$ to $[Fe_2(L_P)_3][PF_6]_4$ and isolation of the product through re-precipitation, $[Fe_2(L_P)_3]Cl_4$ was obtained as a purple solid (87 %).

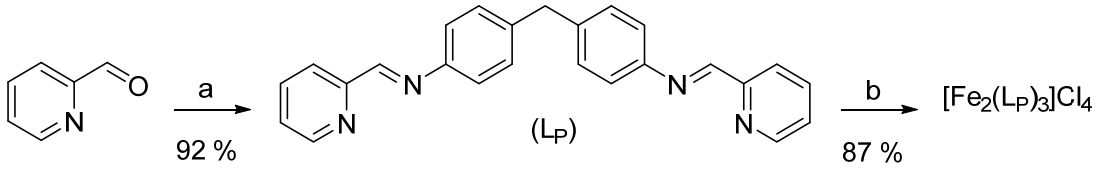

Scheme 6: Synthetic route for preparation of $[Fe_2(L_P)_3]Cl_4$, parent cylinder
a) 0.5 equiv. 4,4'-methylenedianiline, EtOH, rt., 2 hr; b) $FeCl_2.4H_2O$, MeOH

^{1}H NMR of the complex, Figure 4, has a peak corresponding to the imine proton (H_{im}), showing that the ligand has remained intact as the complex has been formed. On binding to the metal centres, the four phenyl protons in the ligand give rise to two broad peaks in the spectrum, due to rotation of the phenylene rings at room temperature. Only one peak is seen for the phenyl protons in the ligand ^{1}H NMR, giving a strong indication that the complex has formed.

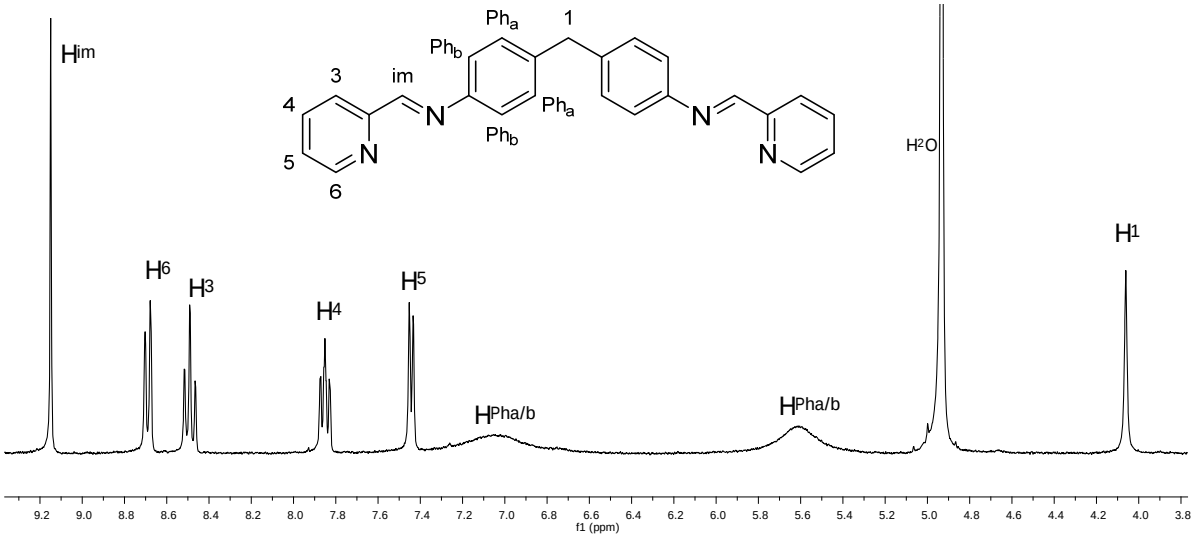

Figure 4: ^{1}H NMR (300 MHz, CD_3OD, 298 K) of $[Fe_2(L_P)_3]Cl_4$

The compound is purple in colour, which is characteristic to this class of triple stranded helicate, due to metal-ligand charge transfer, MLCT, which occurs between the iron centres and the ligands. This generates a peak in the UV-Vis spectrum at 574 nm as a result of the MLCT, giving a strong indication that the triple stranded iron complex has formed.

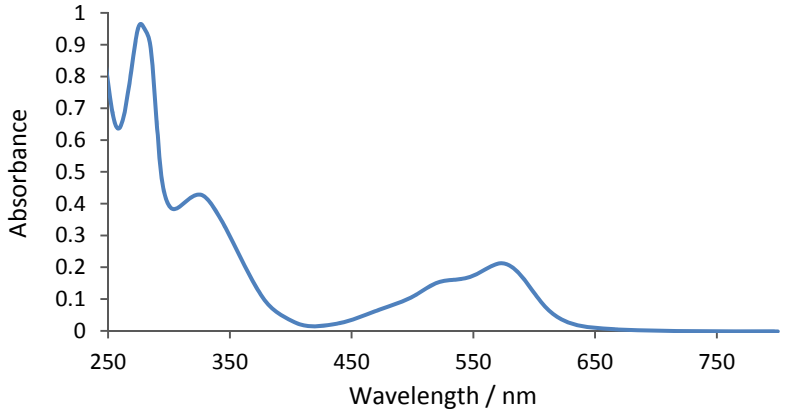

Figure 5: UV-Vis spectrum of the $[Fe_2(L_P)_3]Cl_4$ (17 µM, H_2O)

2.3.2 Alkyne Functionalisation

As discussed in *section 2.2.1*, aldehyde **1** has previously been synthesised within the Hannon group [7]. This structure contains the key alkyne functionality to participate in a click reaction, and so was re-synthesised using the known route, to use in new experimental procedures.

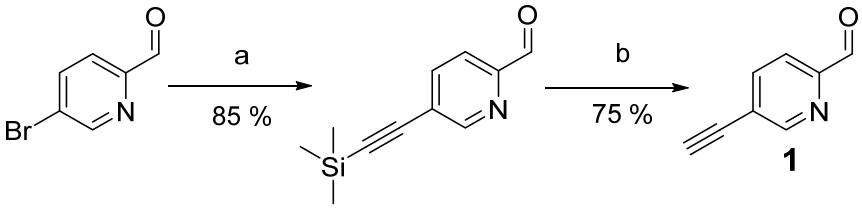

Scheme 7: Synthetic route for the preparation of aldehyde **1**

a) $Pd(PPh_3)_2Cl_2$, CuI, PPh_3, NEt_3, THF, Trimethylsilylacetylene b) K_2CO_3, MeOH

Aldehyde **1**, was formed through a two-step reaction from 5-bromopyridine-2-carboxaldehyde, Scheme 7. The first step uses the palladium catalysed Sonogashira reaction, to replace the bromide with a protected alkyne at the C5 position. This is a high yielding reaction (85 %)

which is then followed by deprotection of the alkyne (H_5) to give aldehyde **1** as a cream solid (75 %).

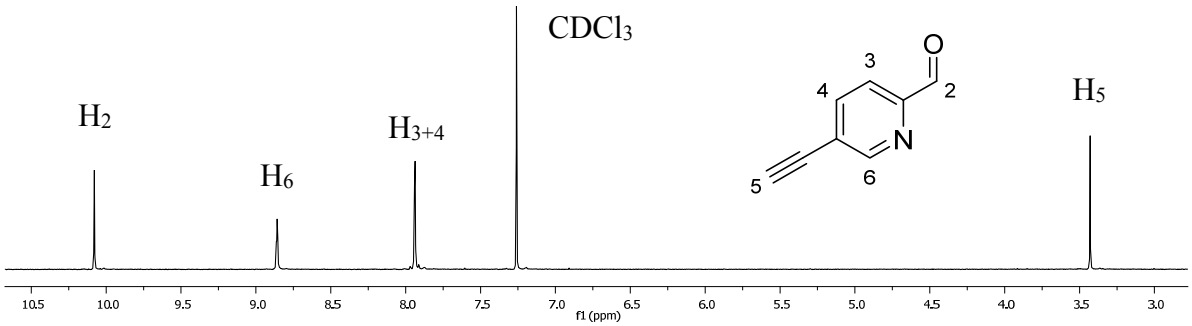

Figure 6: ^{1}H NMR (300 MHz, $CDCl_3$, 298 K) of 5-ethynylpicolinaldehyde, aldehyde **1**

The additional functionality is placed at position five on the aromatic ring, as it has previously been found that this location maintains the binding activity of the subsequent iron helicates towards DNA [20, 21]. It is apparent that retaining the linear shape of the 'cylinders' is a key attribute to the binding action of this class of compound.

By adding an alkyne moiety to the pyridine carboxaldehyde, six additional groups can be added to the subsequent triple stranded helicate structure via click chemistry. Functionalisation of aldehyde **1** will be carried out prior to ligand formation, ensuring that the imine bond formed during ligand synthesis is not affected by click chemistry reaction conditions.

2.3.3 Click Reactions

2.3.3.1 Ester Cylinder

It was decided to investigate the reactivity of aldehyde **1** in a click reaction, by first using the simple, commercially available, cheap azide: 5-ethynylpicolinaldehyde. This was used to form aldehyde **2**, and the subsequent iron helicate structure, Scheme 8.

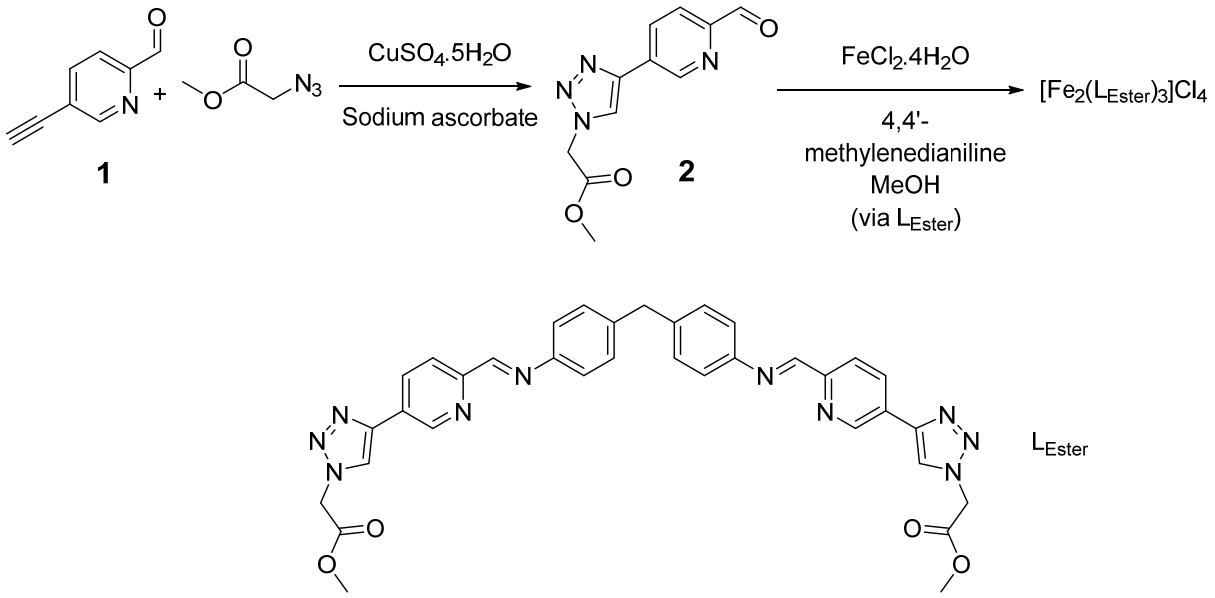

Scheme 8: Synthetic route for the preparation of supramolecular helicate $[Fe_2(L_{Ester})_3]Cl_4$ via aldehyde **2**

The click reaction was performed in a 1:1 mixture of H_2O/*t*-butanol with the Cu(I)- catalyst, formed *in situ* through reduction of copper(II) sulphate with sodium ascorbate. This 1,3-dipolar cycloaddition was a high yielding reaction (76 %) which produced the peach solid, aldehyde **2**. There were many advantages to using click chemistry to incorporate functionality into this system. The key aldehyde moiety needed to form the imine bonds with the diamine 'spacer' of the ligand did not need protecting under these click chemistry conditions. As a result, this method of adding functionality is more efficient than those which have previously been used [6]. Aldehyde **2** was isolated by extraction from the H_2O/*t*-butanol mixture with DCM and after washing with water, no further purification was required. The ^1H NMR shows that the click reaction was successful, through the presence of a proton from the triazole ring, H_7. Both the aromatic aldehyde, H_6 and ester functionality H_{8+9} are present in the structure, Figure 7 (*2D NMR in Appendix A.1.1*).

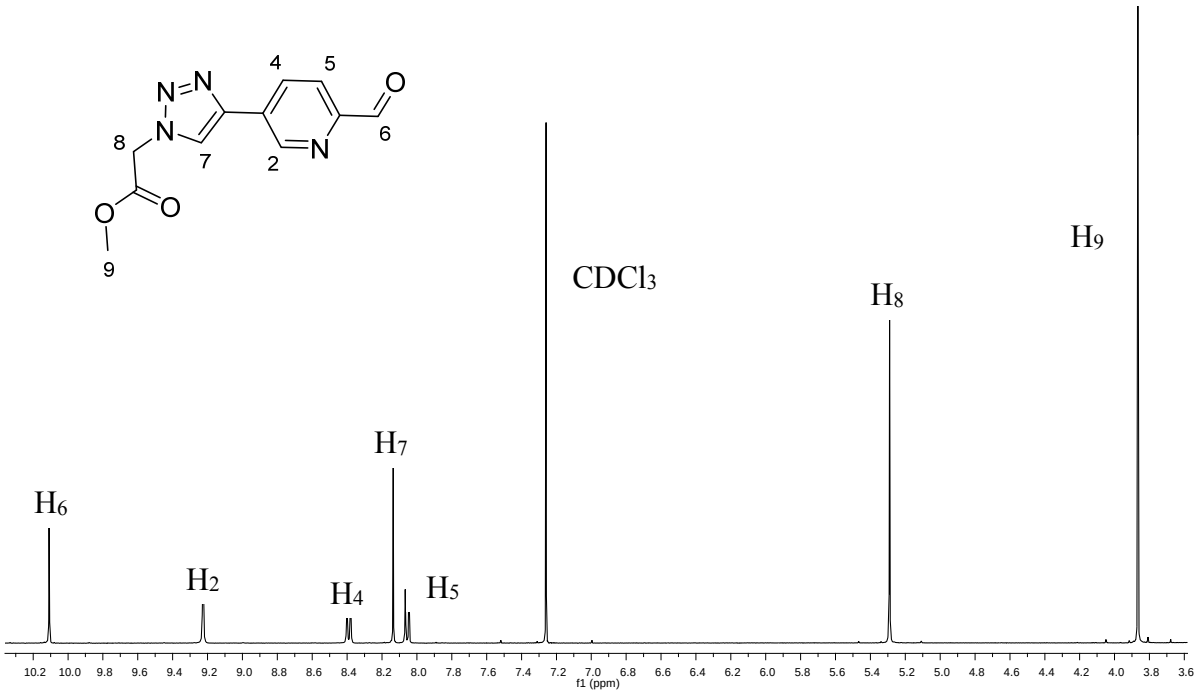

Figure 7: ^{1}H NMR (400 MHz, $CDCl_3$, 298 K) of 2-(4-(6-formylpyridin-3-yl)-1H-1,2,3-triazol-1-yl)acetate: ester aldehyde **2,** assignment based on 2D-NMR spectroscopy

Aldehyde **2** was then used to form L_{Ester} in a 2:1 reaction with 4,4'-methylenedianiline (94 %). The two functionalised aldehydes bound to the 'spacer' group via imine bonds. The product of this reaction was a brown solid, isolated by filtration and purified with copious washing with MeOH.

The ligand was only soluble in DMSO, which is known to breakdown these helicate complexes as it is able to coordinate to the iron centres, consequently the helicate was synthesised using a one-pot reaction from aldehyde **2** [7]. The chloride salt of the helicate was therefore synthesised in a 6:3:2 reaction mixture of aldehyde **2**/4,4'-methylenedianiline/$FeCl_2.4H_2O$. The aldehyde and spacer were first stirred in MeOH followed by a methanolic solution of the Fe(II) source. On addition of the iron, the solution immediately started to turn from yellow to purple in colour, indicating that despite the ligand not being pre-formed, the helicate is a favourable conformation for the substituents to form. This complex was soluble in MeOH and so was

isolated by precipitation with diethyl ether and collected by filtration. Copious washing with diethyl ether yielded a purple solid (83 %).

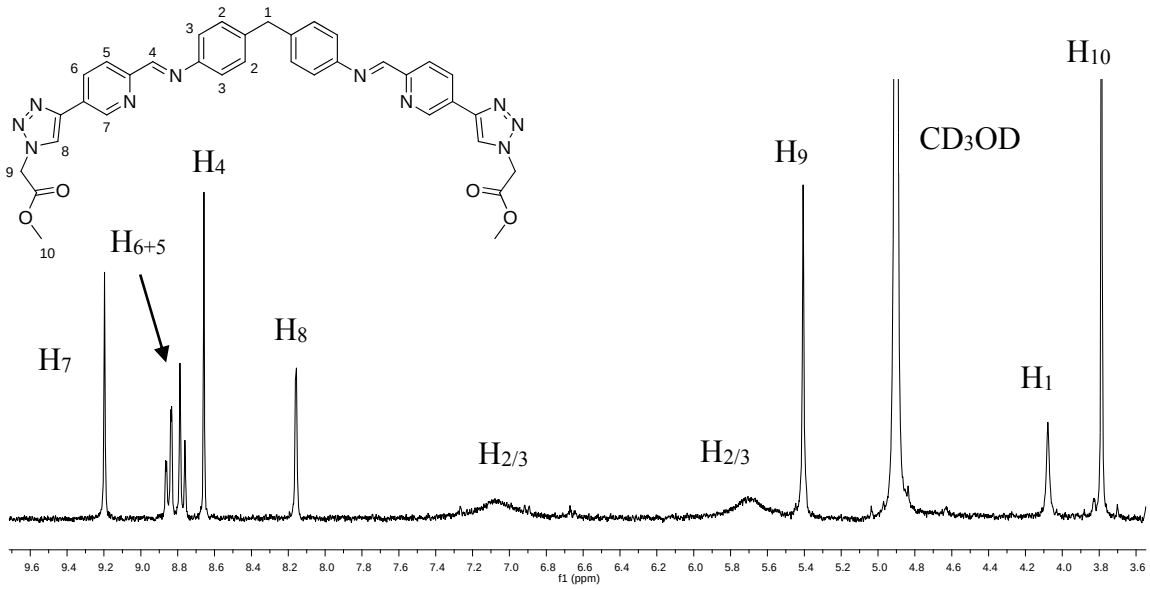

Figure 8: ^{1}H NMR (300 MHz, CD_3OD, 298 K) of $[Fe_2(L_{Ester})_3]Cl_4$, assignment based on 2D-NMR spectroscopy

The presence of the characteristic imine (H_4), split phenyl ($H_{2/3}$) and spacer (H_1) protons in the ^{1}H NMR, Figure 8, at expected integrations and chemical shifts were found. The presence of ester functionality could be identified by peaks from H_{9+10}, joined to the structure through the formation of a 1,4-disubstituted triazole, indicated by H_8 (*2D NMR in Appendix A.1.2*).

The distinctive deep purple colour of the product indicated that the triple stranded helicate had been formed. The expected MLCT absorption at 590 nm, gives the complex its colour and indicates that the triple stranded helicate has been synthesised, Figure 9. Through use of mass spectrometry, complex formation was confirmed by the presence of peaks at 519 m/z corresponding to the 4+ charged species $[Fe_2(L_{Ester})_3]^{4+}$ and at 698 m/z corresponding to the 3+ charged species $[Fe_2(L_{Ester})_3]^{3+}$ (*Appendix A.1.2*).

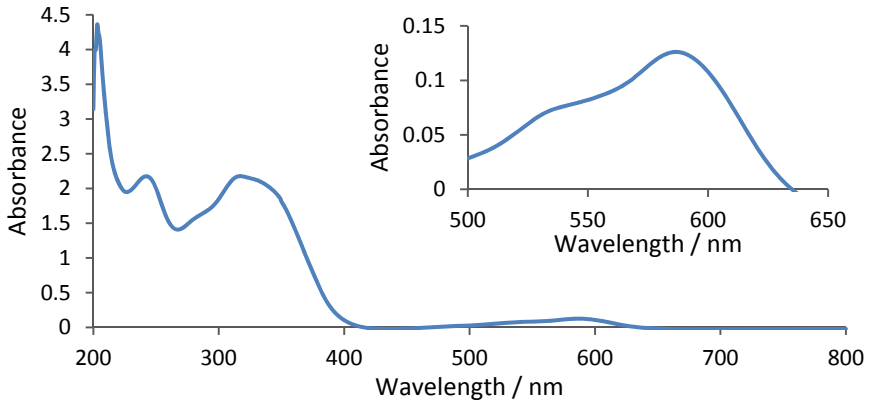

Figure 9: UV-Vis spectrum of the $[Fe_2(L_{Ester})_3]Cl_4$ (25 µM, MeOH)

Click chemistry appeared to be a simple, efficient and high yielding method of functionalising the parent cylinder. This method was therefore used to functionalise the cylinder with functional groups which may enhance the DNA binding properties of the helicate.

2.3.3.2 Piperidine Cylinder

Piperidine structures have been found to interact with the phosphate backbone of B-DNA when protonated [22]. It was hypothesised that this interaction could potentially enhance the binding affinity observed between the iron helicate and DNA. It was therefore attempted to attach this functionality to the cylinder via addition to the precursor aldehyde, with click chemistry, Scheme 9.

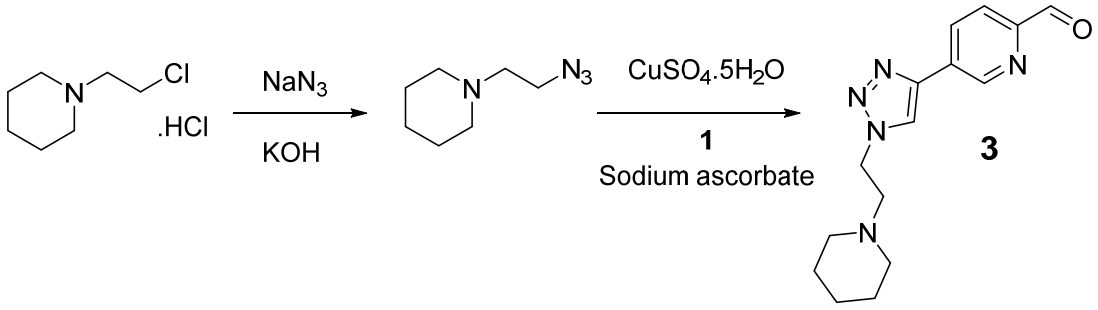

Scheme 9: Synthetic route for the preparation of aldehyde **3** using click chemistry

1-(2-chloroethyl)piperidine hydrogenchloride was first converted into an azide using sodium azide, in an overnight reflux to give a yellow oil (91 %). This was then attached to the alkyne functionalised aldehyde **1**, via a click reaction to produce aldehyde **3** as a yellow solid (59 %). As with the formation of aldehyde **2**, catalytic quantities of $CuSO_4.5H_2O$ and sodium ascorbate were used to form a Cu(I) catalyst *in situ*. A 1,4-disubstituted 1,2,3-triazole was formed through the reaction between stoichiometric quantities of the azide and alkyne. The reaction was complete after reacting at room temperature overnight, so no further purification was required after extraction of the product from the reaction mixture with DCM. The catalytic species were retained in the aqueous layer, making addition of the piperidine group easily achieved.

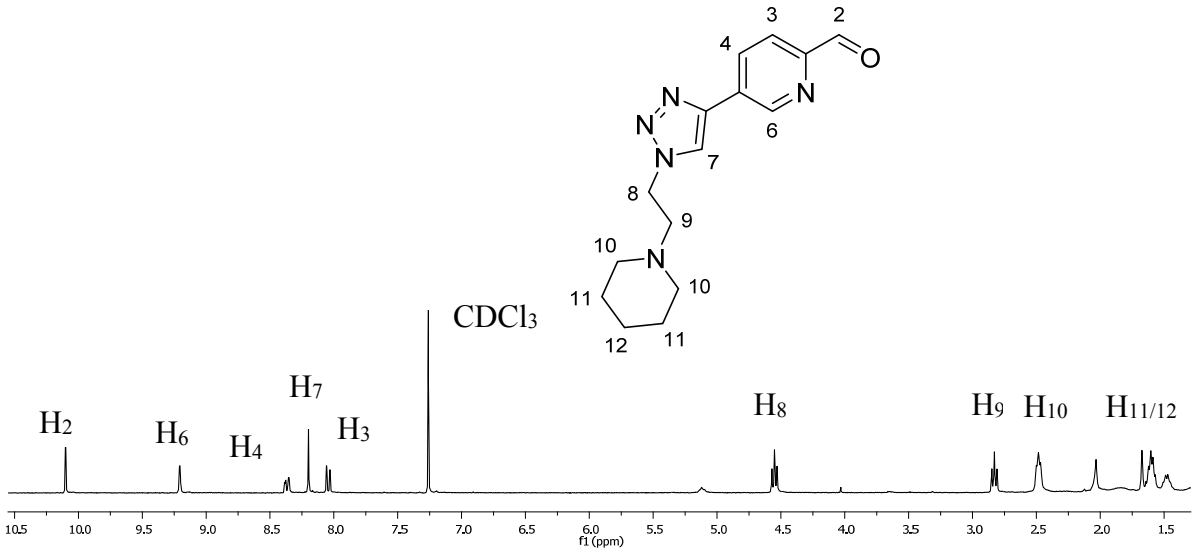

Figure 10: ^1H NMR (300 MHz, $CDCl_3$, 298 K) of 5-(1-(2-(piperidin-1-yl)ethyl)-1H-1,2,3-triazol-4-yl)picolinaldehyde: piperidine aldehyde **3,** assignment based on 2D-NMR spectroscopy

Presence of the proton within the triazole ring (H_7) and absence of the alkyne peak at 3.4 ppm in the ^1H spectrum, Figure 10, indicate that the click reaction was successful. Both the aromatic species from the aldehyde >7.5 ppm and piperidine functionality <5.0 ppm are present in the resulting structure (*2D NMR in Appendix A.1.3*).

Aldehyde **3** was converted into the ligand via a 2:1 reaction with 4,4'-methylenedianiline (30 %). On formation of the ligand, a cream solid precipitated out of methanolic solution, allowing for collection and purification by filtration and washing with excess methanol.

The triple stranded helicate was then synthesised in a 3:2 reaction of the ligand and $FeCl_2.4H_2O$ (41 %), Scheme 10. The reaction was performed in EtOH, as it was known from the previous reaction step, that the ligand was insoluble in MeOH. The iron complex was formed at room temperature overnight, producing a purple compound which was partially soluble in EtOH. The product was isolated from the reaction mixture via precipitation with diethyl ether and collected by suction filtration. The yield of this reaction was less than that previously observed for complex formation, so it was attempted to synthesise this complex straight from aldehyde **3** using the 'one-pot' method described in *section 2.3.3.1*. However, using this method gave rise to side products from the reaction, which could not be separated from the desired product. As a result, it was concluded that this technique could not be used to synthesise the piperidine helicate.

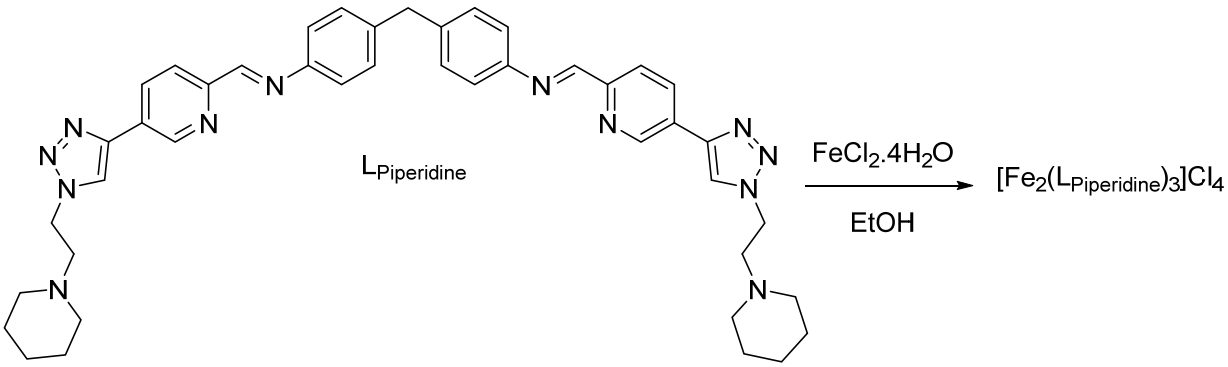

Scheme 10: Synthetic route for the preparation of the piperidine functionalised iron cylinder, $[Fe_2(L_{Piperidine})_3]Cl_4$

Within the ^1H NMR spectrum, Figure 11, characteristic imine (H_2) and spacer (H_7) protons, appear at expected integrations and chemical shifts. The fact that the phenyl protons ($H_{1a/b}$) have split into two broad signals in the spectrum, highly indicates that the ligand is coordinated

to iron centres, since this effect is also seen with the parent ligand on helicate formation. The piperidine functionality could be identified from peaks corresponding to $H_{10\text{-}12}$, linked to the aromatic structure through the formation of a 1,4-disubstituted triazole, indicated by H_5 (*2D-NMR in Appendix A.1.4*).

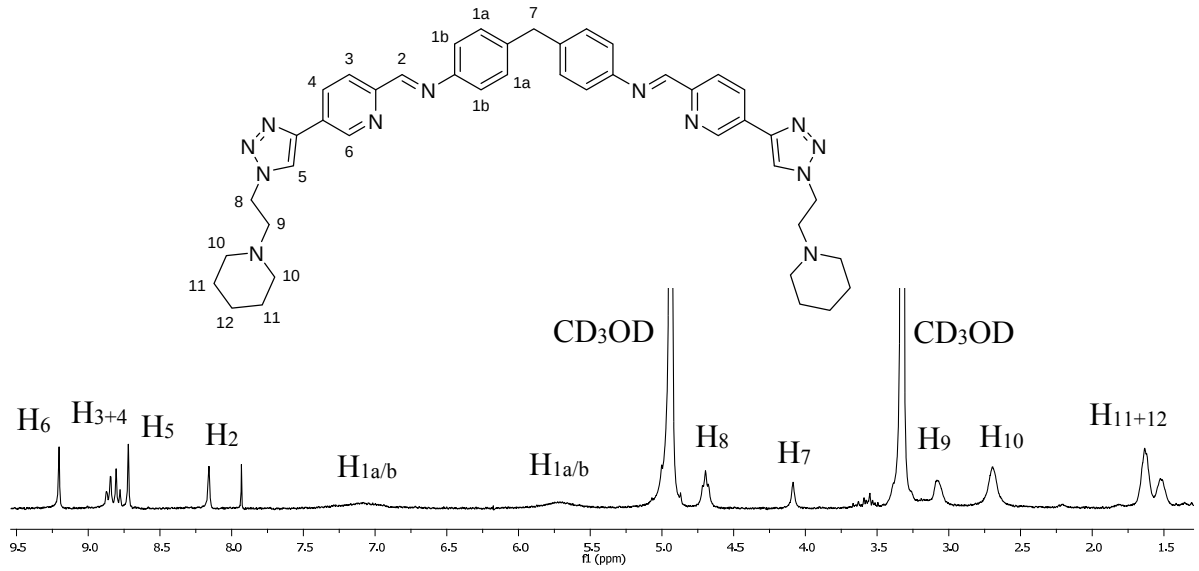

Figure 11: ^{1}H NMR (300 MHz, CD_3OD, 298 K) of $[Fe_2(L_{Piperidine})_3]Cl_4$, assignment based on 2D-NMR spectroscopy

The product formed from this reaction was a purple coloured compound, which strongly indicated that a triple stranded iron helicate was formed upon reaction of $L_{Piperidine}$ with an iron(II) source. UV-Vis spectroscopy, Figure 12, confirmed presence of the characteristic MLCT absorbance expected at 589 nm, showing that the metal is present within the resulting structure. Further analysis from mass spectrometry confirmed that the triple stranded iron complex was formed, through the presence of peaks at 577 m/z corresponding to the 4+ charged species $[Fe_2(L_{Piperidine})_3]^{4+}$ and at 782 m/z corresponding to the 3+ charged species $[Fe_2(L_{Piperidine})_3]Cl^{3+}$ (*Appendix A.1.4*).

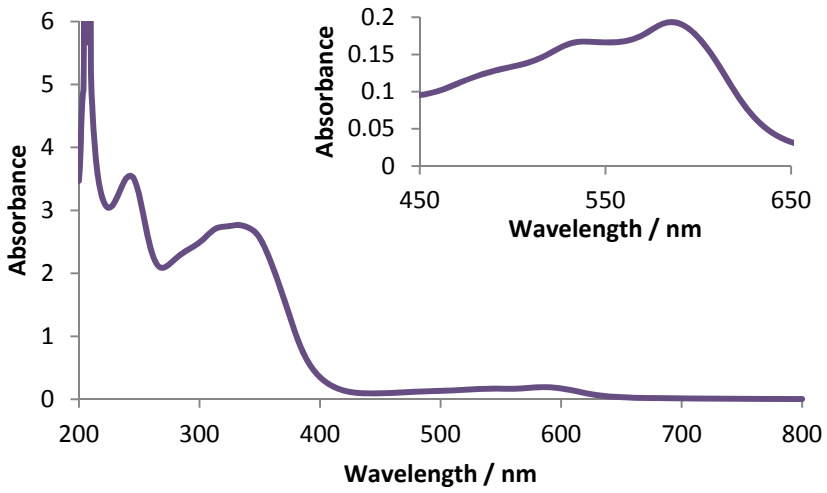

Figure 12: UV-Vis spectrum of $[Fe_2(L_{Piperidine})_3]Cl_4$ (25 µM, MeOH)

Addition of piperidine functionality to the helicate complex, shows that click chemistry is an easy and reproducible method of functionalising this class of compound. The addition of a triazole ring to the ligand structure, does not dramatically affect the solubility properties of the complex. Both complexes functionalised through click chemistry were soluble in MeOH when in the chloride salt forms. Additional solubility in MeCN was also achieved by converting the counterion to PF_6^-. As such, these 'clicked' helicates are soluble in water miscible solvents, allowing studies into their DNA binding and cell toxicity to be performed (*Chapter 3*).

2.3.3.3 Sulphur Functionalised Helicates for Gold Nanoparticle Attachment

As described in *section 2.1*, an aim of this research is to attach sulphide linkers to the parent cylinder $[Fe_2(L_P)_3]^{4+}$ (L_P= $C_{25}H_{20}N_4$), in order to attach the helicate structure to AuNPs.

Click reactions have been performed on the surface of AuNPs, by various research groups, as a means to detect polymers [23] and Cu(II) in solution [24]. 1-azidoundecan-11-thiol has been used to coat nanoparticles with azide functionality, to subsequently react with an alkyne moiety [24, 25]. It was therefore considered whether a cylinder structure might be attached to AuNPs

via a simple click reaction, between the alkyne functionalised cylinder, $[Fe_2(L_{ALK})_3][BF_4]_4$ Figure 3, and an azide coated nanoparticle.

When the alkyne cylinder was tested for its stability under click reaction conditions, it was found that the helicate structure was not retained; indicated by loss of the purple colour, characteristic of the complex. This was most likely due to interference in metal coordination from the catalytic copper present in the reaction mixture.

To circumvent this an alternative strategy was employed, where the sulphur moieties were attached by click reaction to the cylinder during ligand synthesis, with the formed cylinder then attached to the nanoparticle surface by thiol displacement (*Chapter 4*).

2.3.3.3.1 Undecyl-thioacetate Cylinder

As stated, 1-azidoundecan-11-thiol has previously been attached to AuNPs, functionalising them with azide which can subsequently participate in click reactions [24, 25]. Research indicates that having a long linker between the nanoparticle surface and bound substituent can be advantageous in maintaining desired properties of the bound compound [26, 27]. In this case, it will beneficial to have distance between the nanoparticle and cylinder, to ensure the iron complex is still able to interact and bind with DNA structures when nanoparticle bound.

As such, it was proposed to synthesise a new cylinder with 1-azidoundecan-11-thiol as addition to the parent structure. Using the alkyne functionality on aldehyde **1,** this sulphur linker can be clicked onto the ligand, to be incorporated into the helicate structure.

Synthesis began with the formation of 1-azidoundecan-11-thioacetate from $Br(CH_2)_{11}OH$ in a three step reaction, Scheme 11.

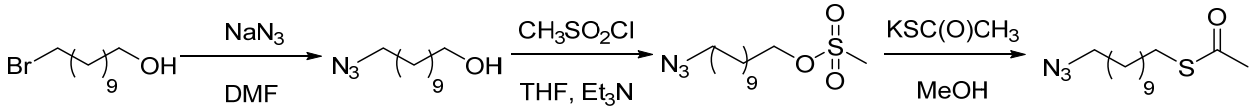

Scheme 11: Synthetic route of the protected thiol functionalised azide: 1-azidoundecan-11-thioacetate

The first reaction step introduced azide functionality into the compound, through nucleophilic substitution of the bromide, forming a yellow oil in stoichiometric quantities (100 %). The alcohol was then converted into a methyl sulfonate leaving group; in a high yielding reaction step, to give a pale yellow oil (98 %). Finally sulphur was introduced into the compound, through displacement of the methyl sulfonate group with a thioacetate (19 %). This step was low yielding as a result of multiple chromatography columns required to purify the compound. At this stage in the synthesis, the thiol was left protected with an acetate group, so as not to react in forthcoming reaction conditions, specifically with the copper catalyst present in the click reaction.

This azide was then clicked onto aldehyde **1**, so incorporating a sulphur moiety into the aromatic aldehyde structure, forming aldehyde **4**, Scheme 12.

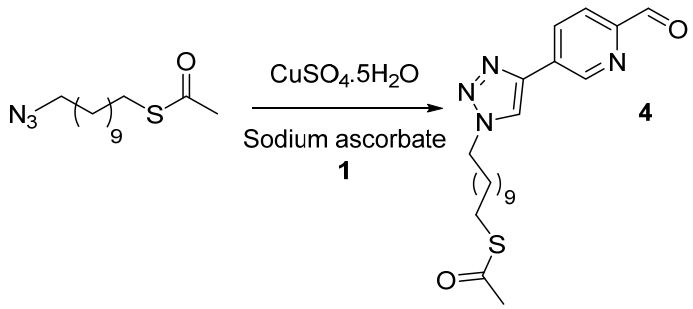

Scheme 12: Preparation of aldehyde **4** via click reaction

5-ethynylpicolinaldehyde was reacted with 1-azidoundecan-11-thioacetate in 1:1 ratio over six days. The click reaction was catalysed with a Cu(I) catalyst formed *in situ* from the reduction of $CuSO_4.5H_2O$ with sodium ascorbate. On formation of aldehyde **4**, the product precipitated

out of solution, so was collected by filtration and purified by washing with copious quantities of water, methanol and diethyl ether, to yield a light brown solid (189 mg, 94 %).

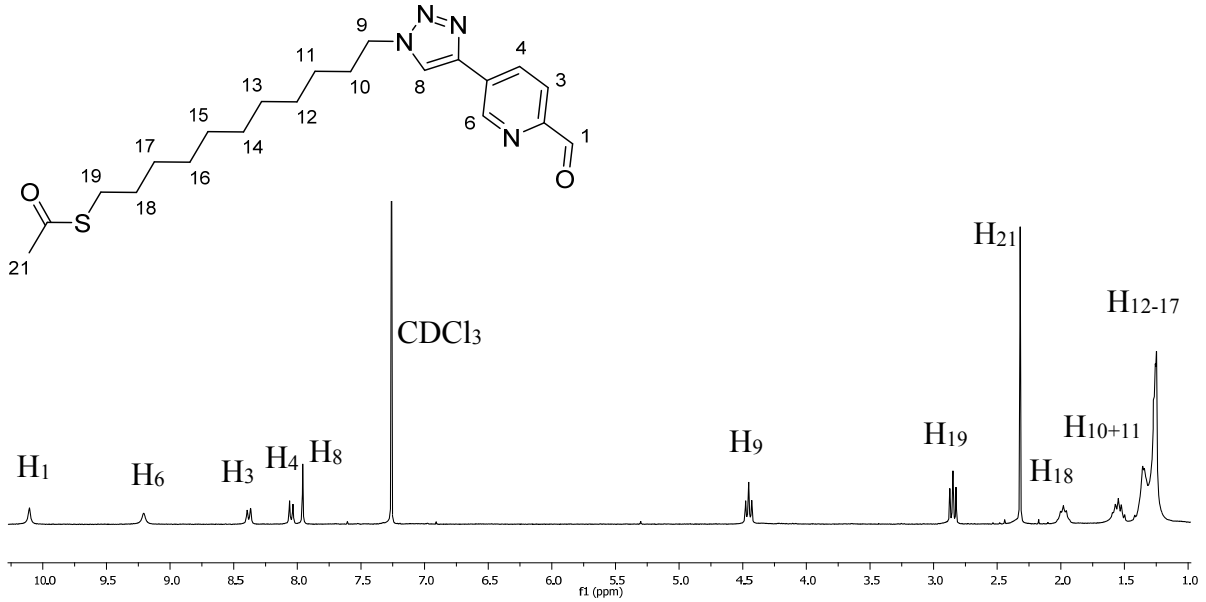

Figure 13: ^{1}H NMR (300 MHz, $CDCl_3$, 298 K) of aldehyde **4,** assignment based on 2D-NMR spectroscopy

It was then attempted to convert aldehyde **4** into the subsequent ligand and triple stranded iron helicate, Scheme 13.

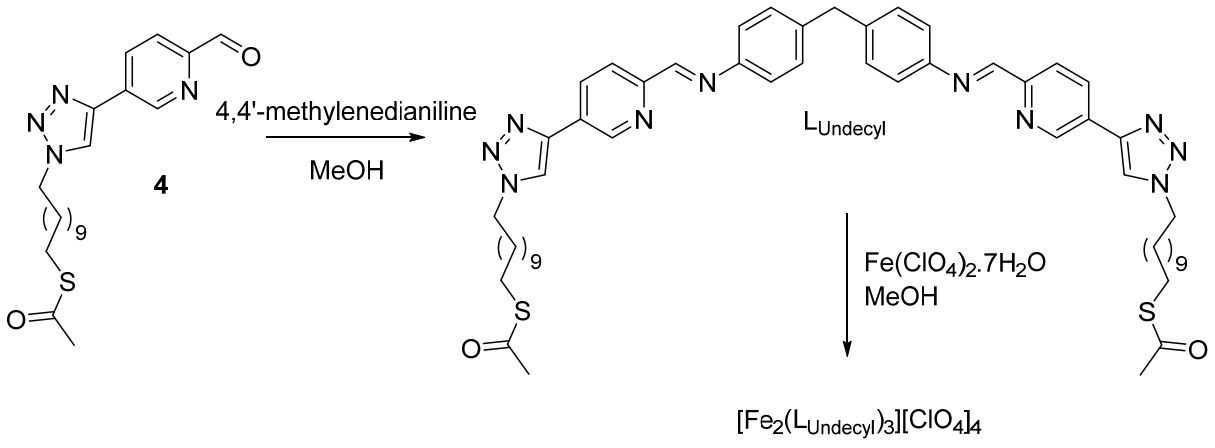

Scheme 13: Preparation of ligand ($L_{Undecyl}$) and cylinder ($[Fe_2(L_{Undecyl})_3][ClO_4]_4$ from aldehyde **4**

On mixing aldehyde **4** with 4,4'-methylenedianiline overnight in a 2:1 ratio, a product precipitated out of methanolic solution, and so was collected by filtration and purified through washing with methanol and diethyl ether (52 %). However, this suspected ligand, $L_{Undecyl}$, was highly insoluble, resulting in limited characterisation analysis being able to be performed.

On reacting this solid with $Fe(ClO_4)_2.7H_2O$, it was suspected an iron helicate was synthesised due to the purple solid formed. This reaction was low yielding (12 %) and required heating due to the insoluble nature of the 'ligand'.

Syntheses of the triple stranded helicate with chloride, hexafluorophosphate and tetrafluoroborate counterions were attempted, yet were unsuccessful, deemed from lack of colour change in the reaction mixture over time. Synthesis was also attempted using the 'one-pot' method described in *section 2.3.3.1*, however this gave rise to a black insoluble solid which could not be analysed. Using the perchlorate counterion seemed to promote solubility, resulting in a purple solid which could be partially dissolved in MeOH.

The ^1H NMR was obtained for this compound, showing the expected ratio of peaks for the iron complex, suggesting it was formed during the reaction. However, the phenyl protons ($H_{Pha/b}$) do not appear as broad or shifted into different environments as previously witnessed with the iron complexes, possibly a result of insolubility in CD_3OD. Due to the insoluble nature of the compound, full characterisation of the complex was not accomplished.

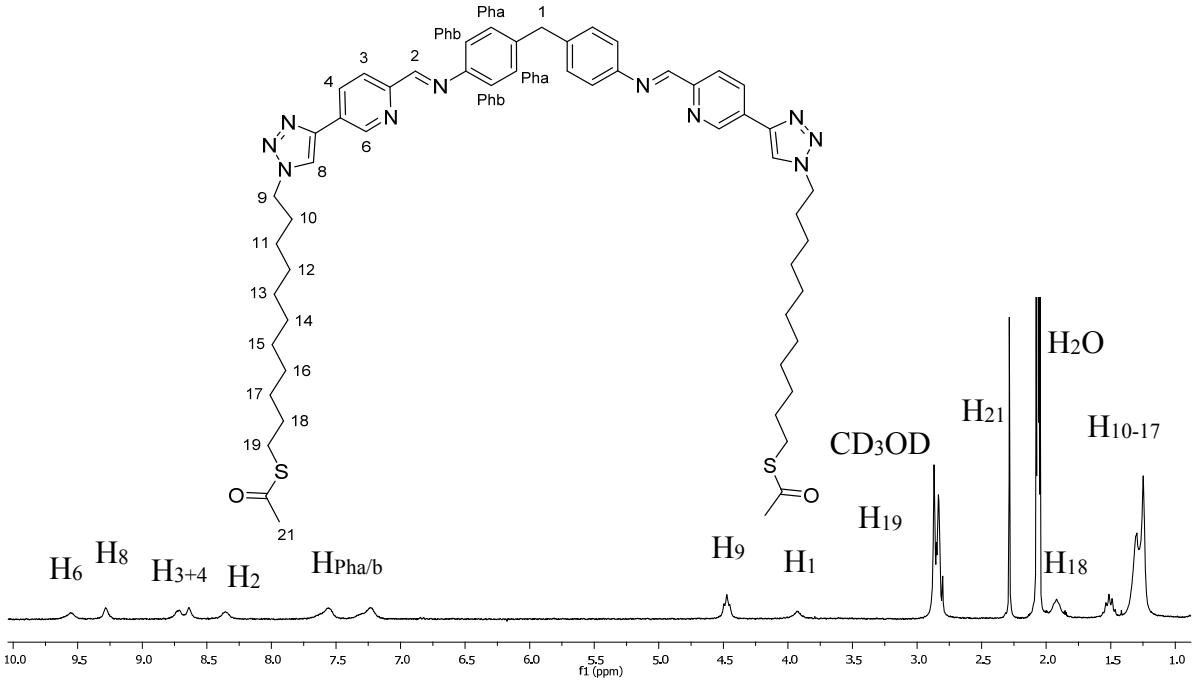

Figure 14: ^{1}H NMR (300 MHz, CD_3OD, 298 K) of $[Fe_2(L_{Undecyl})_3][ClO_4]_4$

Consequently, likely due the aliphatic chain from the attached azide, the complex was highly insoluble in water miscible solvents, making it inappropriate for the desired application. When combined with ct-DNA in buffer solution, it immediately precipitated out of solution. As such it would not be possible to combine with AuNPs suspended in water or interact with cells in media without precipitating out of solution. As a result, synthesis of a more soluble complex was investigated.

2.3.3.3.2 Thioacetate Cylinder

In order to create a more water compatible complex, a polyethylene glycol, PEG, chain was used in the linker between the azide and sulphur moieties. Oxygen atoms within the PEG chains promote water solubility, due to the formation of hydrogen bonds [28].

An azide was therefore synthesised which contained a PEG chain and sulphur containing moiety. This was achieved over three reaction steps to form S-(2-(2-(2-azidoethoxy)ethoxy)ethyl) ethanethioate, Scheme 14.

A slightly shorter linker length was also used in an attempt to promote solubility, making the resulting iron complex slightly smaller and less bulky.

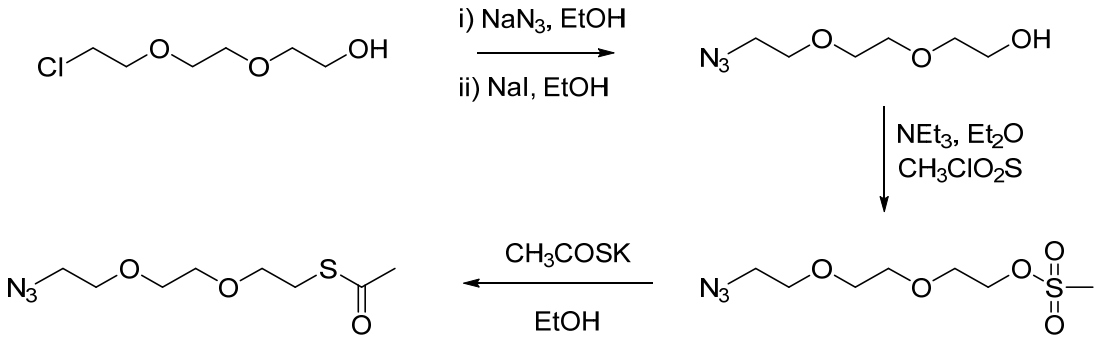

Scheme 14: Preparation route of S-(2-(2-(2-azidoethoxy)ethoxy)ethyl) ethanethioate

Firstly 2-(2-(2-chloroethoxy)ethoxy)ethan-1-ol was converted into an azide through substitution of the chloride using sodium azide. On refluxing overnight, conversion of the starting material was complete to yield a colourless oil (76 %). The alcohol was then converted into a methyl sulfonate leaving group; in a high yielding reaction step, to give a pale yellow oil (74 %). Finally, sulphur was introduced into the compound, through displacement of the methyl sulfonate group with a thioacetate. This overnight reaction requiring purification of the product by column chromatography, to yield a yellow/orange oil (93 %). The sulphur atom was kept protected for subsequent click reaction and complex formation steps, to avoid side reactions occurring between the thiol, copper catalyst and iron source.

S-(2-(2-(2-azidoethoxy)ethoxy)ethyl) ethanethioate was then reacted with aldehyde **1** in a copper catalysed click reaction to produce aldehyde **5**, Scheme 15. Stoichiometric quantities of the azide and alkyne were reacted overnight with a Cu(I) catalyst, formed *in situ* from reduction

of $CuSO_4.5H_2O$ with sodium ascorbate. After purification by column chromatography, the product was obtained as a yellow solid (68 %).

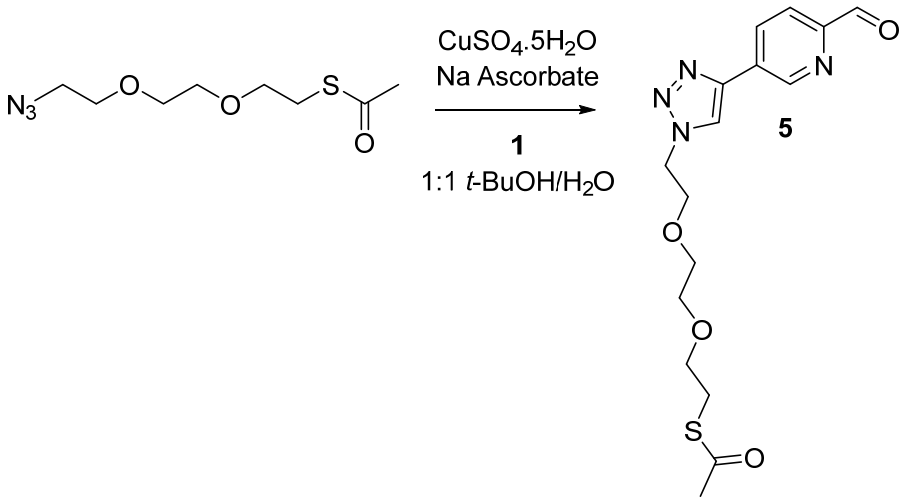

Scheme 15: Preparation of aldehyde **5** through a click reaction

Presence of the proton produced from the newly formed triazole ring (H_7) and absence of the alkyne peak at 3.4 ppm in the ^1H spectrum, Figure 15, indicate the click reaction was successful. Aromatic protons from the aldehyde >8.0 ppm, as well as those from the PEG chain and thioacetate protons <5.0 ppm, were also present in the spectra (*2D NMR in Appendix A.1.5*). Through mass spectrometry and infra-red analysis, the structure was confirmed through the presence of signals corresponding to the aldehyde (2893 cm^{-1}), carbonyl (1694 cm^{-1}) and C-N (1354 cm^{-1}) functionalities.

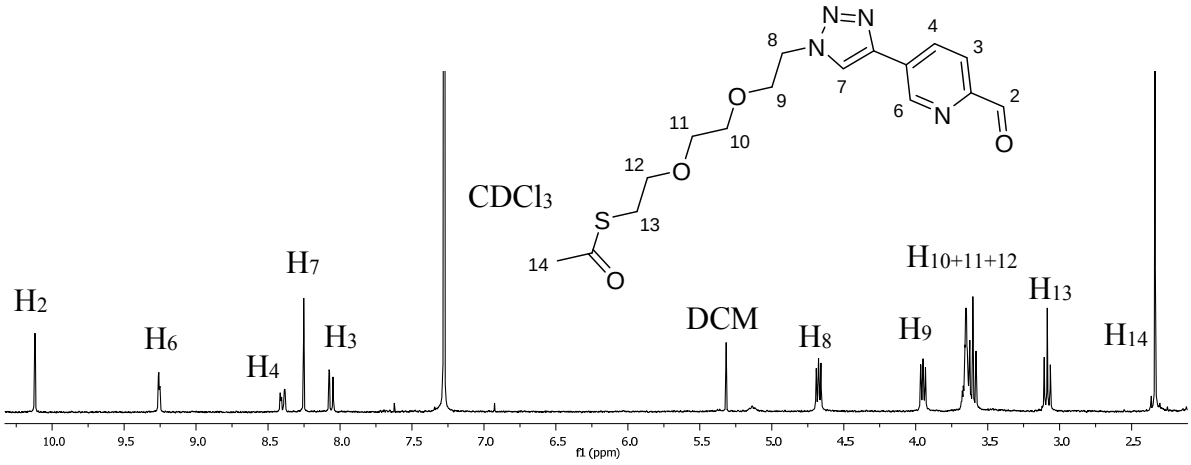

Figure 15: ^{1}H NMR (400 MHz, $CDCl_3$, 298 K) of S-(2-(2-(2-(4-(6-formylpyridin-3-yl)-1H-1,2,3-triazol-1-yl)ethoxy)ethoxy) ethyl) ethanethioate: aldehyde **5,** assignment based on 2D-NMR spectroscopy

Aldehyde **5** was then converted to the ligand and iron complexes, Scheme 16. On reacting aldehyde **5** with 4,4'-methylenedianiline (spacer) in 2:1 stoichiometry, the ligand, $L_{Thioacetate}$, was formed and precipitated out of methanolic solution to form a pale brown solid (86 %). This was isolated by filtration and purified by washing with methanol and diethyl ether. This ligand was not very soluble in an alcohol solution, so formation of the cylinder was performed through a 'one-pot' reaction containing 6:3:2 aldehyde **5**/4,4'-methylenedianiline/$Fe(BF_4)_2.6H_2O$. The aldehyde and spacer were first stirred in MeOH followed by a methanolic solution of the iron source. On addition of Fe(II), the solution immediately started to turn purple and was left for the reaction to complete overnight. The product was partially soluble in MeOH, so was precipitated out of solution using diethyl ether, collected by filtration and washed with copious quantities of diethyl ether. The tetraborofluorate salt form of this complex was synthesised, as attempted synthesis using the more commonly used chloride or hexafluorophosphate salts, resulted in green, insoluble precipitates forming, thought to be either double stranded helicates

or polymer species. The tetraborofluorate product, $[Fe_2(L_{Thioacetate})_3][BF_4]_4$, was formed in high yield (94 %) and was highly soluble in MeCN.

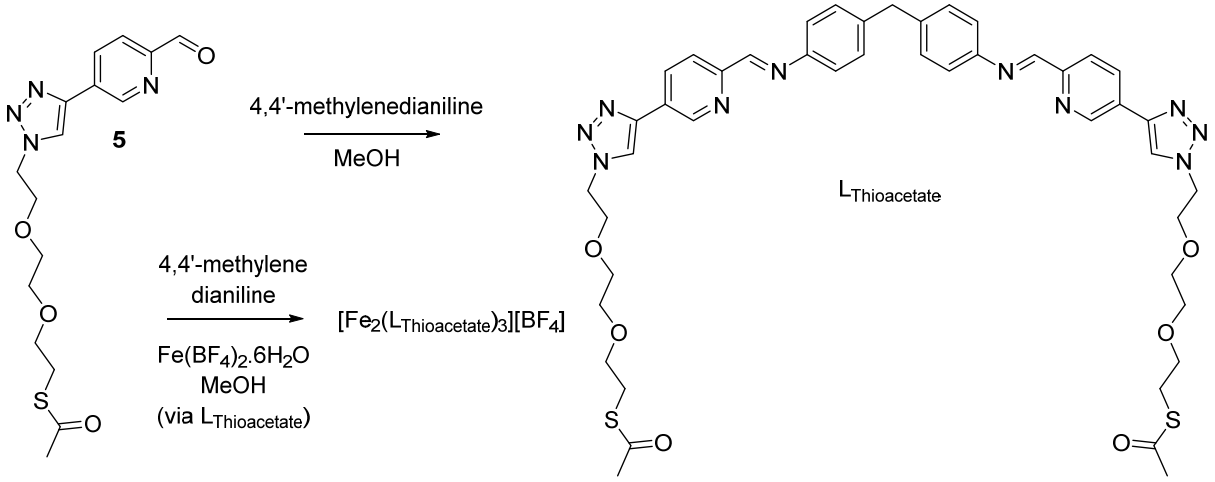

Scheme 16: Preparation of the ligand ($L_{Thioacetate}$) and cylinder $[Fe_2(L_{Thioacetate})_3][BF_4]_4$ from aldehyde **5**

The structure of the complex was confirmed through analysis.

Presence of the characteristic imine (H_2), split phenyl ($H_{15/16}$) and spacer (H_{17}) protons in the ^1H NMR, Figure 16, at expected integrations and chemical shifts indicated the presence of a cylinder species. The new side chain functionality could be identified from peaks corresponding to $H_{8\text{-}14}$, linked to the aromatic structure through the formation of a 1,4-disubstituted triazole, indicated by H_7.

The presence of ester functionality could be identified by peaks from H_{9+10} (*2D NMR in Appendix A.1.6*).

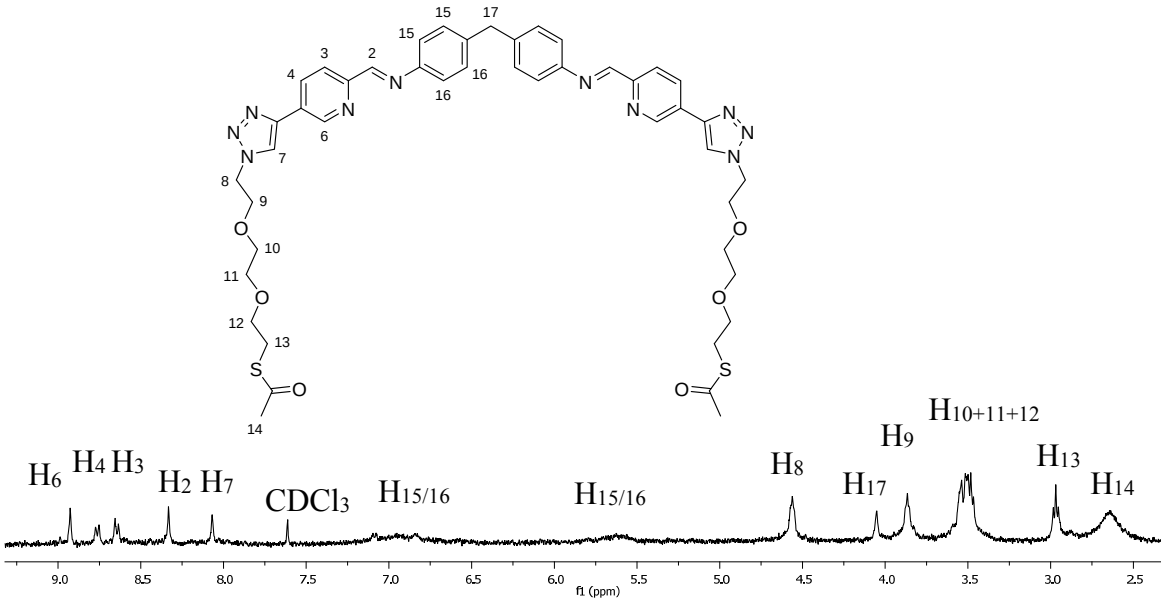

Figure 16: ^{1}H NMR (400 MHz, CD_3CN, 298 K) of $[Fe_2(L_{Thioacetate})_3][BF_4]_4$. Assignment based on 2D-NMR spectroscopy

The distinct purple colour of the product indicated that the triple stranded helicate has been formed. Within the UV spectrum of the complex, Figure 17, there is a MLCT band at 589 nm which gives rise to this colour and shows that the metal is present within the resulting structure. Through used of mass spectrometry and elemental analysis, it was confirmed that the triple stranded iron complex was formed, through the presence of peaks at 696 m/z corresponding to the 4+ charged species $[Fe_2(L_{Thioacetate})_3]^{4+}$, 956 m/z corresponding to the 3+ charged species $([Fe_2(L_{Thioacetate})_3][BF_4]_3)^{3+}$ and at 1497 m/z corresponding to the 2+ charged species $([Fe_2(L_{Thioacetate})_3][BF_4]_2)^{2+}$ (*Appendix A.1.6*).

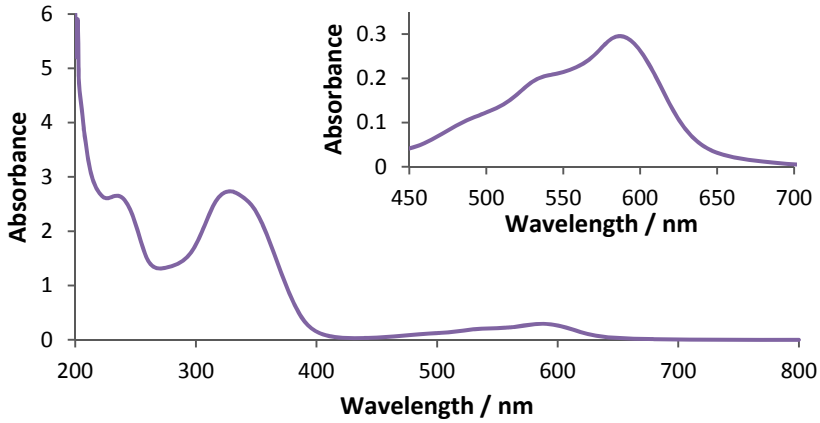

Figure 17: UV spectra of $[Fe_2(L_{Thioacetate})_3][BF_4]_4$ (25 μM, MeCN)

Through the use of click chemistry, a triple stranded iron helicate was synthesised, containing sulphur moieties. This thioacetate cylinder is soluble in water miscible solvents, and so can be analysed within DNA binding studies as to whether it can bind and manipulate different DNA structures and whether the complex is toxic towards cancer cell lines (*Chapter 3*). The iron helicate is functionalised with a sulphur containing moiety and as such, it can be investigated whether the structure binds to AuNPs, with the view to enhancing DNA binding and cell toxicity activity through directed delivery of the compound to cancerous cells (*Chapter 4*).

2.3.4 Peptide Coupling Reactions

Peptide coupling is a known method of adding functionality to the triple stranded iron helicates described, enhancing the binding activity of the cylinders with DNA [6]. This coupling method was therefore used to attach sulphur moieties to the ligand structure, in an attempt to produce a stable, water soluble complex able to interact with DNA and bind to AuNPs.

2.3.4.1 Lipoic Acid Cylinder

A common linker used to attach molecules to the surface of AuNPs is lipoic acid [16, 29, 30]. This compound contains two sulphur atoms capable of binding to a gold surface, so is the ideal

addition to a molecule. Lipoic acid also contains an acid group capable of participating in a peptide coupling reaction [19], so was subsequently added to the 2-pyridine carboxaldehyde structure used within ligand synthesis, Scheme 17.

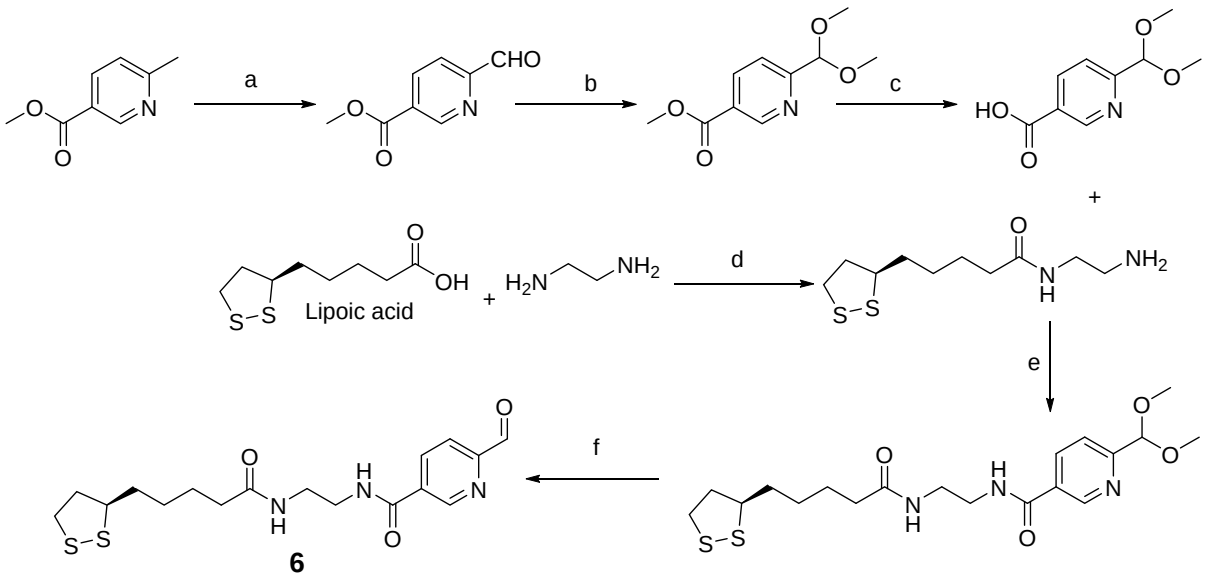

Scheme 17: Synthesis scheme for formation of and reactions with aldehyde **6**
(a) I_2, DMSO (b) Trimethyl orthoformate, formic acid, sulphuric acid (c) MeOH, 1M NaOH (d) CDI, $CHCl_3$, ethylenediamine (e) EDC, HOBt, DMF (f) 1M HCl, THF.

Synthesis began with commercially available methyl 6-methylnicotinate. The pyridine ring was functionalised at the C2 and C5 positions which are the sites of substitution for the designed ligand.

An aldehyde was first introduced at the C2 position to allow binding of spacer, 4,4'-methylenedianiline, during ligand formation. Through reacting the methyl group with iodine and DMSO, the key aldehyde functionality was produced, yielding a cream/yellow solid (37 %). This was subsequently protected with an acetal group (50 %), ensuring that the C5 position could be functionalised in successive reaction steps, without the newly formed aldehyde being destroyed. The ester was then hydrolysed overnight to give an acid group (84 %), which could be utilised in a peptide coupling reaction.

(±)-α-Lipoic acid was first aminated with ethylenediamine in a peptide coupling reaction. This diamine linker allows for the sulphur moiety and pyridine carboxaldehyde to be combined, providing a long linker to separate the cylinder structure from the intended AuNP surface [26, 27].

The acid group on the pyridine ring was then utilised in a peptide coupling reaction with this aminated lipoic acid, in a low yield (17 %). This poor yield was thought to be due to the aminated lipoic acid being only partially soluble in the reaction solvent and the fact that some product may have been lost through purification by column chromatography.

This product was then converted to the desire aldehyde **6**, via acid deprotection of the acetal over six days to give a cream solid (72 %).

Presence of peaks corresponding to the amide protons (H_5 and H_8) in the ^1H NMR, Figure 18, indicate that the peptide coupling reactions were successful. A peak corresponding to the aldehyde (H_1) shows that deprotection was achieved, allowing for ligand synthesis to be conducted. Both, aromatic protons ($H_{2\text{-}4}$) and lipoic acid functionality ($H_{9\text{-}15}$) are present in the resulting structure.

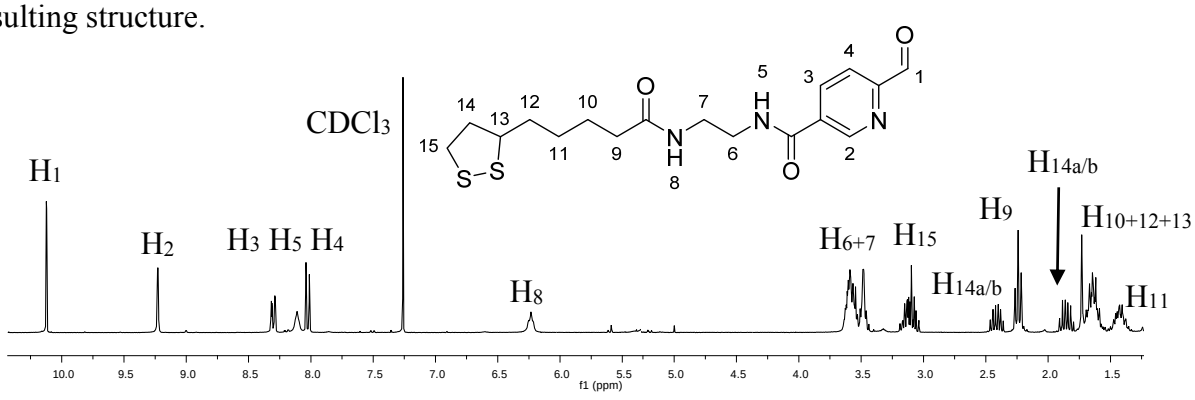

Figure 18: ^1H NMR (300 MHz, $CDCl_3$, 298 K) of aldehyde **6**, assignment based on 2D-NMR spectroscopy

Aldehyde **6** was converted into the ligand structure, L_{Lipoic}, via a 2:1 reaction with 4,4'-methylenedianiline. This reaction formed an insoluble pale cream solid which was collected by

filtration (94 %). The solid product was attempted to be dissolved in a variety of solvents: $CDCl_3$, CH_3CN, H_2O, CH_3OH and DMSO, however despite sonication and being left for long periods of time in the various solvents, the compound did not dissolve into solution. As such, full analysis to characterise the structure could not be achieved. Yet due to the change in solubility and appearance of the product, it was concluded that aldehyde **6** had reacted with the dianiline to yield the desired ligand product.

Due to the insoluble nature of L_{Lipoic}, the iron helicate, $[Fe_2(L_{Lipoic})_3][BF_4]_4$, was synthesised using a 'one-pot' reaction where the ligand was formed *in situ*, Scheme 18.

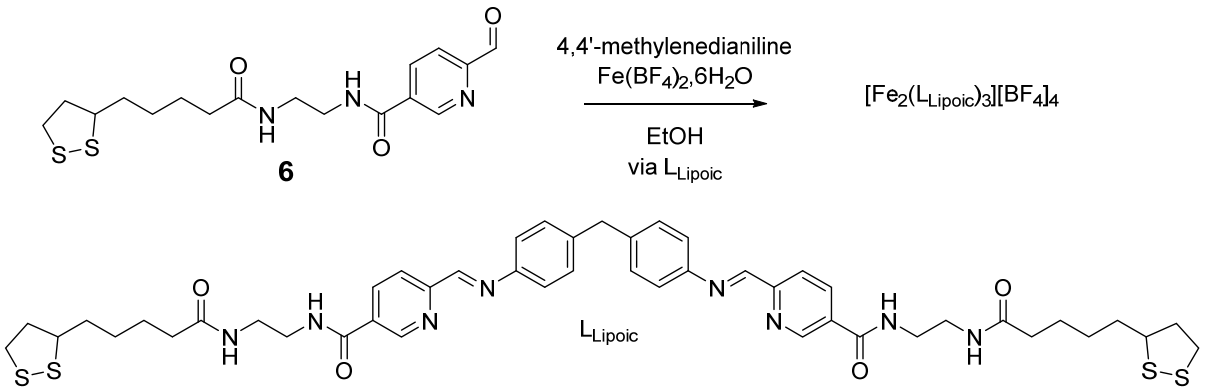

Scheme 18: Preparation of the lipoic acid cylinder $[Fe_2(L_{Lipoic})_3][BF_4]_4$ from aldehyde **6**, via ligand (L_{Lipoic})

Reaction of aldehyde **6**/4,4'-methylenedianiline/$Fe(BF_4)_4.6H_2O$ in a 6:3:2 mixture yielded a blue/purple solid (71 %). On formation, this purple product precipitated out of ethanolic solution, so was isolated by filtration and washed with copious quantities of EtOH and diethyl ether.

Again, this reaction formed a highly insoluble compound, meaning analytical data could not be obtained. The colour of the product was typical of a triple stranded iron helicate, indicating that the iron complex had formed. It was attempted to form the complex in different salt forms to

aid solubility. Yet, when using the Cl^- and PF_6^- iron salts, the triple stranded helicates did not form under the same reaction conditions, indicated by the green precipitate.

As a result, it was concluded that this sulphur functionalised cylinder would not be appropriate to bind to DNA structures or AuNPs due to its insolubility in water miscible solvents. Despite work previously performed using peptide coupling [6], it appeared that for the purpose of this project, 'click' functionalised cylinders gave the best results.

2.4 Asymmetric Ligand Synthesis

The aim of introducing sulphur into the ligand structure was to bind the subsequent helicates structures to AuNPs. Through the 2:1 reaction between the functionalised aldehyde and spacer compound 4,4'-methylenedianiline, both ends of the helicate become functionalised with sulphur and so can go on to bind to the gold surface. It was anticipated that this double functionalisation of the helicate may result in aggregation of the AuNPs on binding, as one cylinder molecule is capable of forming multiple interactions with nanoparticles [31]. As such, an asymmetrical ligand was attempted to be synthesised, with only one sulphur residue per ligand.

2.4.1 Parent Half Ligand, L_{Half}

Within the Hannon group a 'half' ligand has previously been developed [32], where the spacer molecule is functionalised, on only one side, Scheme 19. Addition of a pyridine ring, through an azo bond, leaves a free amine to react with an aldehyde, as in the formation of parent ligand. Preparation of this compound had previously been performed, but was replicated in order to further react with new aldehydes synthesised within this research.

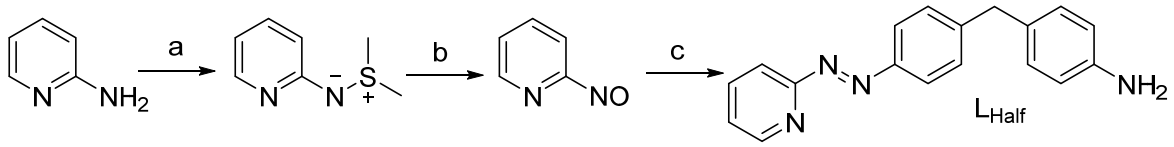

Scheme 19: Preparation of half ligand, L_{Half}

(a) *N*-chlorosuccinimide, dimethyl sulfilimine, sodium methoxide (b) *m*-chloroperoxybenzoic acid, DMSO, dimethyl sulfide (c) 4,4'-methylenedianiline (excess), glacial acetic acid

Synthesis began with commercially available 2-aminopyridine, where a nitro group was introduced at the C2 position by a two-step process. Firstly a dimethyl sulfilimine group was formed (48 %) which was then oxidised with *m*-chloroperoxybenzoic acid to give the nitro moiety (31 %). Both products were purified by recrystallisaton, resulting in yellow crystals which were then reacted with to form the half ligand.

Through using a 4:1 ratio of 4,4'-methylenedianaline : 2-nitrosopyridine, L_{Half} was formed. Using an excess of the spacer molecule, encouraged the half ligand to form, as opposed to the full ligand where both amine groups react to form azo bonds. It was attempted to purify the ligand by flash column chromatography, but this was unsuccessful as a result of the large excess of 4,4'-methylenedianaline being carried through with the product. Recrystallisation of the product was achieved from methanol giving an orange solid (22%).

It was clear from the ^{1}H NMR spectrum, Figure 19, that the symmetrical ligand was not formed as there is a peak relating to the unreacted amine (H_{NH2}). The aromatic protons of the spacer have different chemical shifts, showing that they are in different environments. If the molecule was symmetrical, both aromatic rings would give the same NMR shifts.

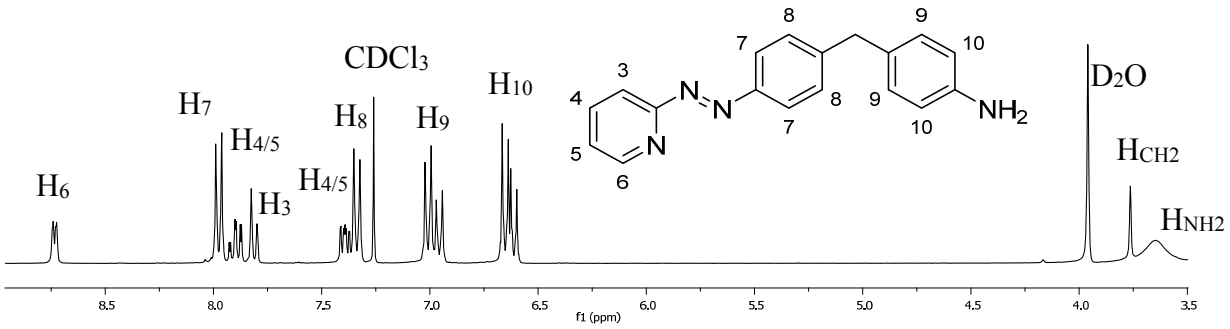

Figure 19: ^{1}H NMR (300 MHz, $CDCl_3$, 298 K) of L_{Half}

2.4.2 Asymmetric Lipoic Acid Ligand: $L_{Asym\text{-}Lipoic}$

It was attempted to react aldehyde **6** with this half ligand, in an attempt to synthesise asymmetric ligand, $L_{Asym\text{-}Lipoic}$, Scheme 20. However, from past research within the Hannon group, it has been shown that it can be difficult to form the subsequent asymmetrical ligands from this half ligand [32].

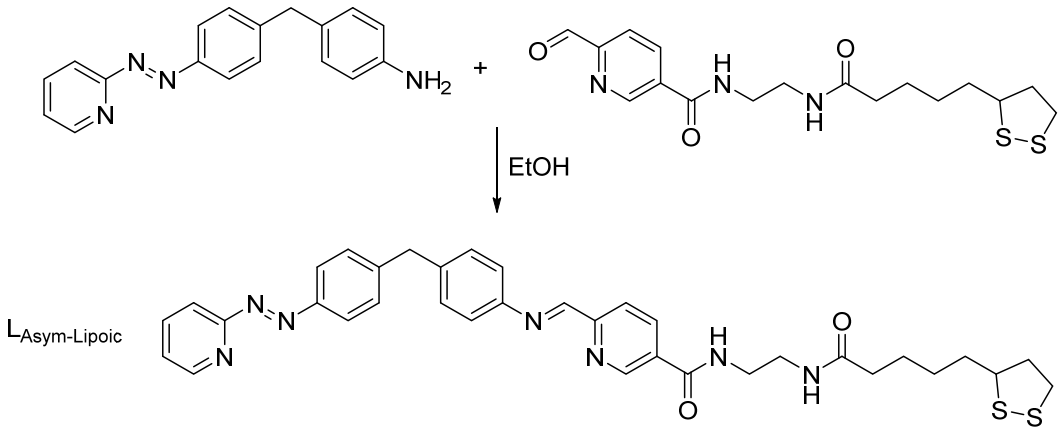

Scheme 20: Preparation of asymmetric ligand $L_{Asym\text{-}Lipoic}$

Figure 20 shows ^{1}H NMR spectra from the reaction mixture after four days, compared to the corresponding starting materials. After four days it was clear from TLC and NMR analysis that unreacted L_{Half} was still present within the reaction mixture, Figure 20. The reaction mixture did, however, show absence of the aldehyde peak above 10 ppm, indicating that some asymmetric ligand may have been synthesised.

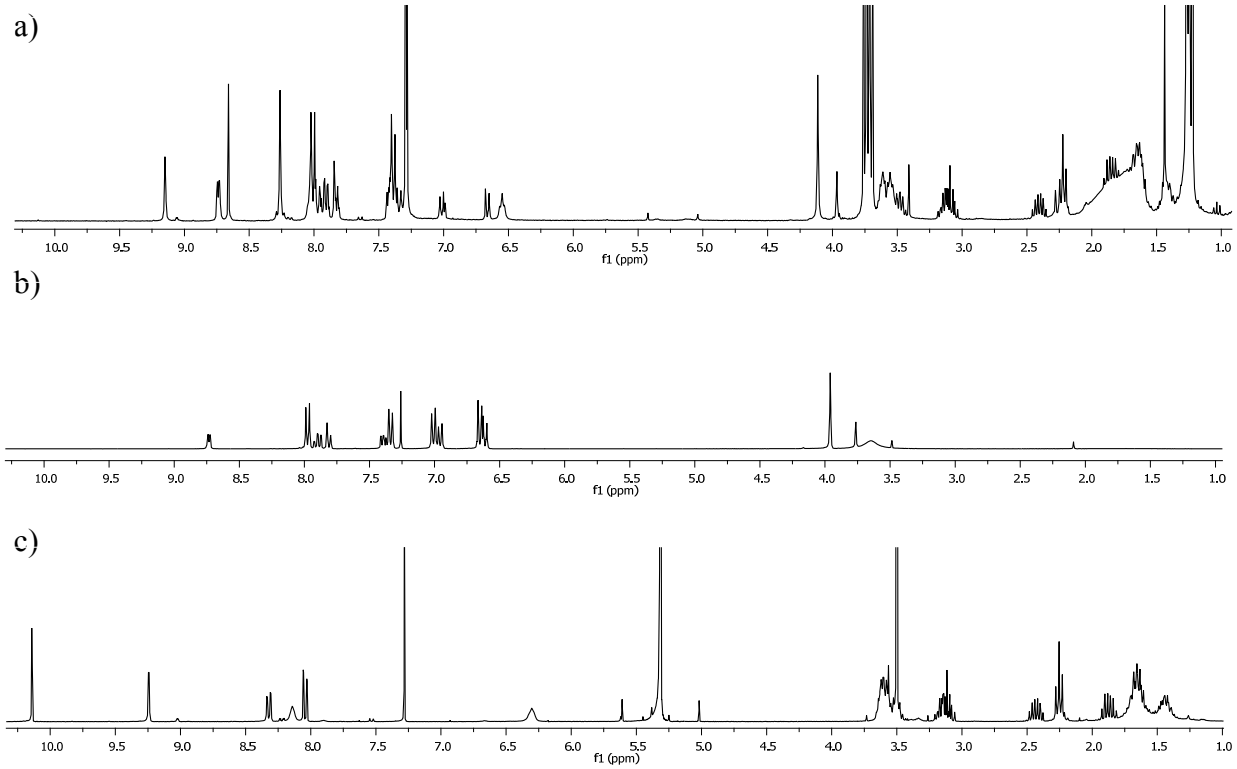

Figure 20: Figure 19: ^{1}H NMR (300 MHz, $CDCl_3$, 298 K) of (a) reaction mixture after 4 days (b) L_{Half} (c) aldehyde **6**

The impure ligand could not be purified by column chromatography due to the labile nature of the imine bond, so it was attempted to purify the reaction mixture through recrystallization, in order to identify compounds present. As such it became apparent that the aldehyde may have degraded over time, as only starting materials were present in the mass spectrum, with no peaks relating to the asymmetric product.

Different reaction conditions were attempted in order to get the reaction to reach completion. Firstly glacial acetic acid was added to the reaction mixture which can catalyse imine formation. 3Å molecular sieves were also added, to remove water made during imine bond formation, in an attempt to force the reaction to continue as per Le Chatelier's principle [33]. However, results from using these reaction conditions showed similar outcomes to that demonstrated by Figure 20.

An insoluble dark orange/red product was also formed from the reaction, showing that some reaction had occurred between the yellow and orange starting materials, although due to the insoluble nature of this solid, analysis of this product was inconclusive.

2.4.3 Asymmetric Thioacetate Ligand: $L_{Asym\text{-}Thioacetate}$

It was also attempted to form an asymmetric ligand with the thioacetate aldehyde **5**. This too was functionalised with sulphur, yet was successfully converted into a ligand and triple stranded helicate structures, *section 2.3.3.3.2*.

As with $L_{Asym\text{-}Lipoic}$, aldehyde **5** was reacted in a 1:1 mixture with L_{Half} in the presence of glacial acetic acid and molecular sieves, Scheme 21.

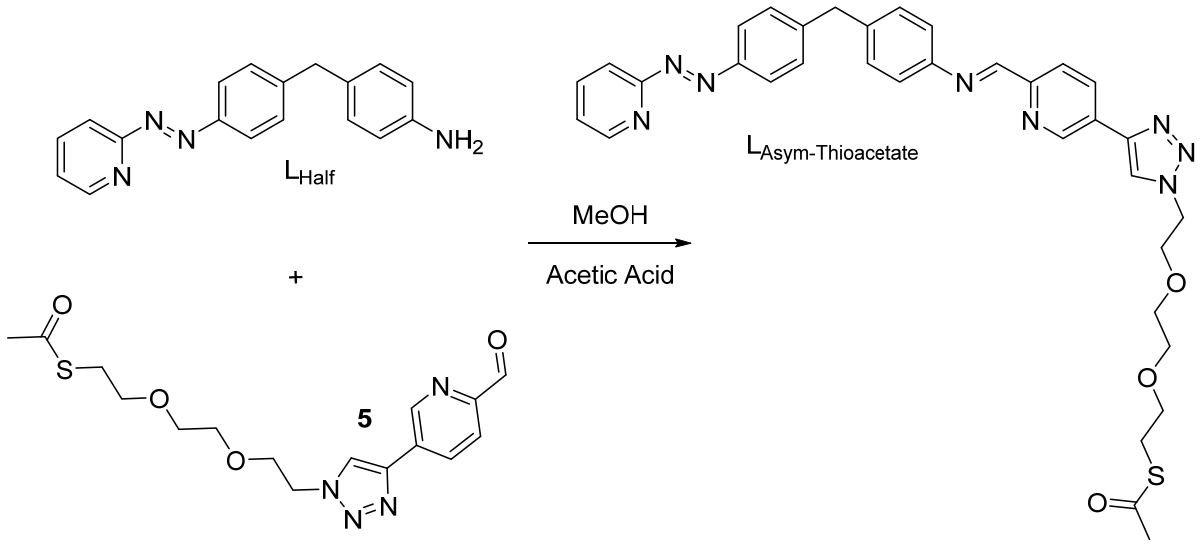

Scheme 21: Attempted preparation of $L_{Asym\text{-}Thioacetate}$, from L_{Half} and aldehyde **5**

After a week of reacting, the reaction had not reached completion, despite the addition of excess aldehyde **5**, and heating the reaction mixture to 50 ˚C. As such, it was not possible to isolate any asymmetric ligand which may have been formed.

It was therefore concluded that synthesis an asymmetric ligand via this method was unlikely.

2.5 Ruthenium Cylinder Synthesis

The ruthenium analogue of the original unsubstituted helicate described in *section 2.1*, has previously been synthesised within the Hannon group [34, 35]. It shows different chemical properties to the iron complex, exhibiting higher stability due to the inert Ru(II) centres. The ruthenium triple stranded helicate is however more difficult to synthesise than the iron complex, requiring high temperatures and increased reaction time to form. Microwave reactor synthesis can be used to synthesise this complex, allowing equivalent yields to be achieved within a fraction of the time required by conventional thermal heating chemistry techniques [36]. Consequently, it was also hoped to synthesise stable ruthenium structures, with the view to bind them with the surface of AuNPs.

2.5.1 Parent Ruthenium Cylinder

The parent ruthenium complex, $[Ru_2(L_P)_3]Cl_4$, has previously been synthesised [34-36], however it was hoped to replicate this synthesis in order to interact the complex with AuNPs, to investigate whether the DNA binding interactions currently observed could be enhanced.

This ruthenium cylinder was synthesised from L_P (synthesis described in *section 2.3.1*) over four hours in the microwave reactor with $Ru(DMSO)_4Cl_2$, Scheme 22. The reaction was performed at 200 ºC, forming a deep orange/red solution characteristic of ruthenium complexes.

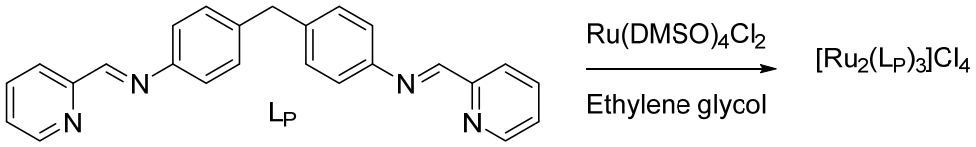

Scheme 22: Preparation of the parent ruthenium cylinder via microwave reactor synthesis

In order to isolate the product from the reaction mixture, the ruthenium complexes were precipitated out of solution with a methanolic solution of ammonium hexafluorophosphate.

This converted the counterion to PF_6^-, allowing it to be collected by suction filtration and washed with copious quantities of H_2O.

The major products of this reaction, were the double stranded complex and polymer species. The desired triple stranded helicate was formed in very low yield, meaning purification and isolation of $[Ru_2(L_P)_3][PF_6]_4$ was difficult. However, through multiple purification columns on alumina (20:1:1 MeCN/ H_2O/$KNO_{3(aq)}$) the complex was isolated as a dark orange solid (1 %). ^1H NMR spectrum of the complex, Figure 21, shows a corresponding spectra to that seen for the iron parent cylinder, Figure 4, having similar chemical shifts for the respective protons. For the ruthenium complex, the phenyl proton signals are less broad compared to the iron complex, likely due to the inert nature of the ruthenium centres the ligands are coordinated to.

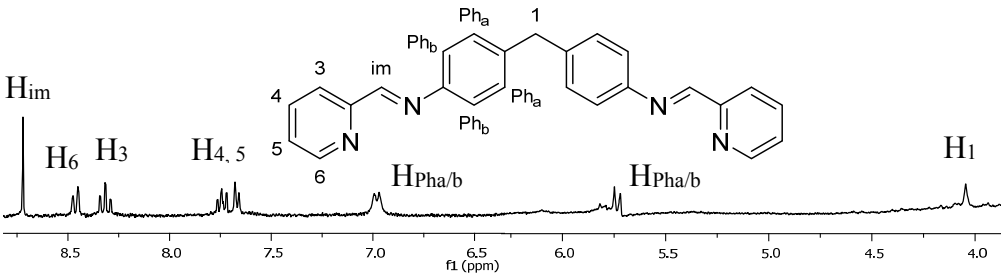

Figure 21: ^1H NMR (300 MHz, CD_3CN, 298 K) of $[Ru_2(L_P)_3][PF_6]_4$

The ruthenium complex, $[Ru_2(L_P)_3]Cl_4$, is dark orange in colour and so λ_{max} appears at a lower wavelength within the UV-Vis spectrum, compared to the iron analogue, Figure 22.

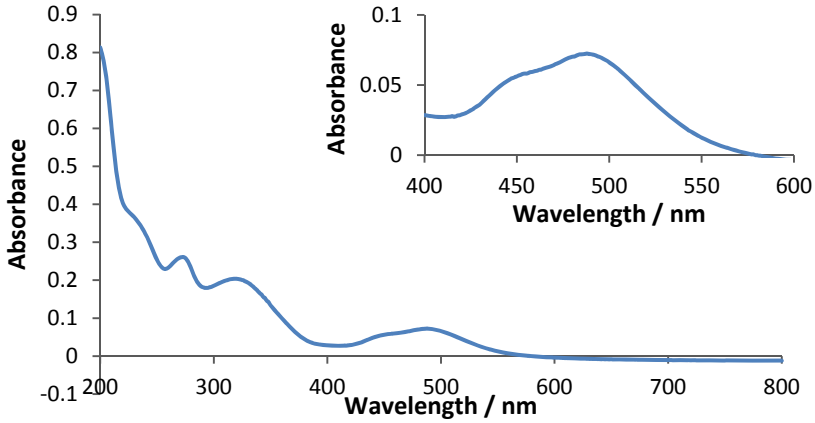

Figure 22: UV spectra of $[Ru_2(L_P)_3]Cl_4$ (10 µM, H_2O)

2.5.2 Thioacetate Ruthenium Cylinder

It was also attempted to form the ruthenium analogue of the thioacetate complex, synthesised in *section 2.3.3.3.2*. This new cylinder structure contains key sulphur moieties required to attach such a complex to AuNPs. Through forming the ruthenium analogue of the complex, it was hoped to form a highly stable, water soluble compound, capable of binding to AuNPs and maintain the DNA binding activity.

As such, the ruthenium complex was synthesised within the microwave reactor, as per $[Ru_2(L_P)_3]Cl_4$. On reacting the thioacetate functionalised ligand, $L_{Thioacetate}$ with $Ru(DMSO)_4Cl_2$ a dark orange/red solution was formed, Scheme 23. As with the parent complex, the ruthenium species were precipitated out of solution using methanolic hexafluorophosphate, to give a dark orange solid.

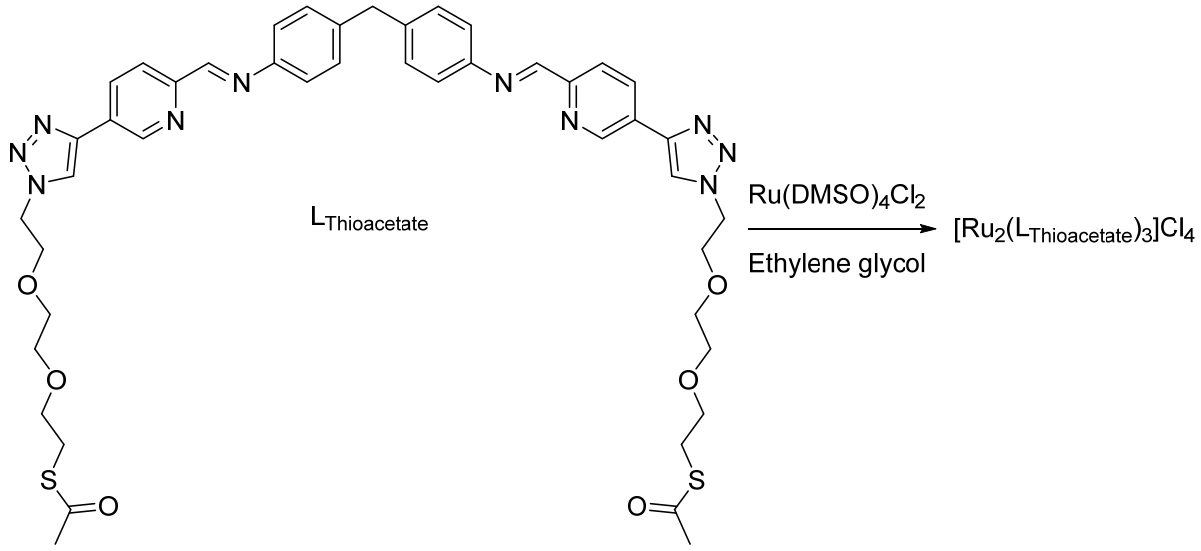

Scheme 23: Attempted preparation of $[Ru_2(L_{Thioacetate})_3]Cl_4$ within a microwave reactor

It was attempted to purify the product of this reaction through column chromatography (on silica, alumina and cellulose) and through recrystallization, in an attempt to isolate the product from its impurities. However, this was to no avail as pure product was not attained. From

previous research, it was found that such metal complexes are retained on HPLC columns [36], so this technique was not used in an effort to purify the thioacetate ruthenium complex.

The ^{1}H NMR of the product, Figure 23, demonstrates that purification of the triple stranded helicate was not achieved. The peaks appear broad and undefined, indicating that some paramagnetic Ru(III) species are present in the sample solution, and as such the compound was not pure. This was also confirmed through mass spectrometry which showed peaks in the spectra corresponding to impurities.

It did however appear that in the ^{1}H NMR there were peaks corresponding to the ligand in solution, with aromatic protons and those corresponding to the thioacetate functionalised side chain of the compound being present. This indicates that the triple stranded complex may have formed in low yield, and that a more proficient purification technique is required to isolate the complex.

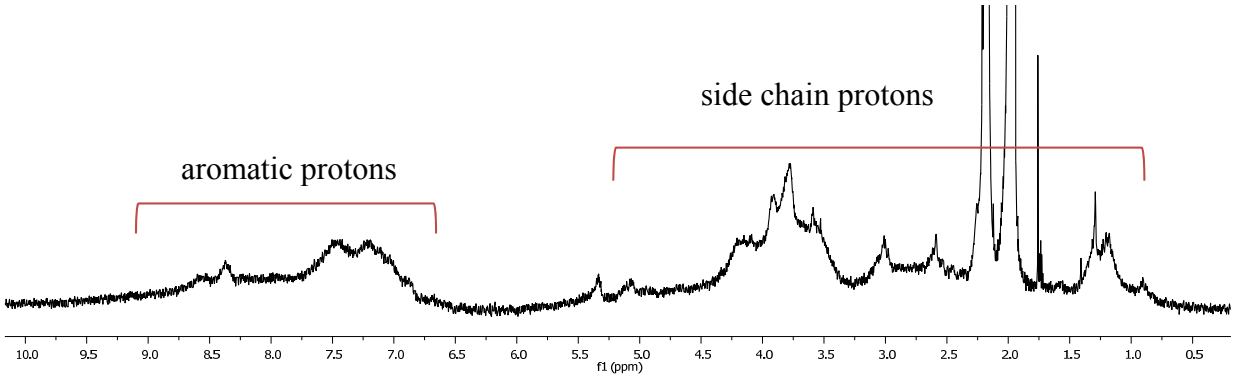

Figure 23: ^{1}H NMR (300 MHz, CD_3CN, 298 K) of $[Ru_2(L_{Thioacetate})_3][PF_6]_4$

2.6 Conclusions

In this chapter, the novel use of click chemistry was employed to end functionalise the bis-pyridyl-imine ligand present within $[Fe_2(L_P)_3]^{4+}$ (L_P= $C_{25}H_{20}N_4$). These functionalised ligands were subsequently synthesised into triple stranded iron helicates.

Three new Fe(II) cylinders were successfully functionalised with the use of click chemistry, outlined in *section 2.2.1*. Firstly an ester moiety was conjugated to the cylinder structure via four reaction steps, with an overall yield of 40 %. This produced a purple compound, soluble in MeOH. Through addition of these ester groups, it is hoped that enhanced DNA binding activity will be observed compared to the parent cylinder, as a result of additional hydrogen bonding between oxygen atoms in the ester and the DNA structure. The complex is not water soluble, yet can be dissolved into a water miscible solvent, allowing for DNA binding and cell toxicity studies to be performed (*Chapter 3*).

The second new complex formed was a piperidine functionalised cylinder. Through six reactions steps, piperidine groups were incorporated into the ligand structure, adding an additional six groups to the resulting helicate, with overall yield of 4 %. It is hoped that the additional piperidine moieties will interact with the backbone of DNA, resulting in a more potent anticancer agent as a result of inhibiting DNA replication on binding, compared to the parent cylinder.

The third new complex synthesised was functionalised with thioacetate groups, over seven reaction steps, with an overall yield of 21 %. This cylinder is also soluble in a water miscible solvent, allowing for subsequent DNA binding and cell toxicity studies to be performed with it. Through addition of thioacetate terminated side chains, it is hoped that additional hydrogen bonding interactions will occur between the oxygen atoms in the side chains and DNA, resulting in an enhanced coiling and kinking effect to the DNA as compared with the parent complex (*Chapter 3*). This cylinder also contains sulphur moieties able to interact and functionalise the surface of AuNPs (*Chapter 4*). On addition to nanoparticles, it is anticipated that high concentrations of the cylinder compounds will interact with DNA, resulting in a structural change which may inhibit DNA replication and hence result in a potent anticancer therapy.

The iron and ruthenium centred parent cylinders were also synthesised within this chapter, in order to compare activity of the new complexes with DNA, cancer cell lines and AuNPs, with the original structures (*Chapters 3 and 4*).

Other sulphur functionalised cylinders were also synthesised, however due to insolubility, it was not possible to fully characterise the structures and as a result, were deemed inappropriate structures for the purpose of this research.

It was also attempted to form asymmetric ligands through use of the half ligand formerly synthesised within the Hannon group, *section 2.4*. However, due to an inability to purify the structures, it was not possible to fully characterise the compounds, or form the subsequent iron(II) helicate structures.

As such the three new helicate structures functionalised via click chemistry will be investigated further, with respect to their DNA binding, cell toxicity and AuNP functionalising abilities (*Chapters 3 and 4*).

2.7 References

1. M. J. Hannon, V. Moreno, M. J. Prieto, E. Moldrheim, E. Sletten, I. Meistermann, C. J. Isaac, K. J. Sanders and A. Rodger, *Angew. Chem. Int. Ed.*, 2001, **40**, 879- 884
2. A. Oleksy, A. G. Blanco, R. Boer, I. Usón, J. Aymamí, A.Rodger, M. J. Hannon and M. Coll, *Angew. Chem. Int. Ed.*, 2006, **45**, 1227-31
3. L. Cerasino, M. J. Hannon and Einar Sletten, *Inorg. Chem.*, 2007, **46**, 6245-6251
4. C. Ducani, A. Leczkowska, N. J. Hodges and M. J. Hannon, *Angew. Chem. Int. Ed.*, 2010, **49**, 8942 –8945
5. A. C. G. Hotze, N. J. Hodges, R. E. Hayden, C. Sanchez-Cano, C. Paines, N. Male, M-K. Tse, C. M. Bunce, J. K. Chipman and M. J. Hannon, *Chem. Biol.*, 2008, **15**, 1258-1267
6. L. Cardo, V. Sadovnikova, S.Phongtongpasuk, N. J. Hodges and M. J. Hannon, *Chem. Commun.*, 2011, **47**, 6575–6577
7. J. Norman, *PhD Thesis*, U. Birmingham, 2012
8. C. Uerpmann, J. Malina, M. Pascu, G. J. Clarkson, V. Moreno, A. Rodger, A. Grandas and M. J. Hannon, *Chem. Eur. J.*, 2005, **11**, 1750-1756
9. J. Malina, M. J. Hannon and V. Brabec, *Nucleic Acids Res.*, 2008, **36**, 3630-3638
10. J. Malina, M. J. Hannon and V. Brabec, *Chem. Eur. J.*, 2008, **14**, 10408-10414
11. N. P. Pavletich and C. O. Pabo, *Science*, 1993, **261**, 1701-1707
12. X. Li, R. Li, X. Qian, Y. Ding, Y. Tu, R. Guo, Y. Hu, X. Jiang, W. Guo and B. Liu, *Eur. J. Pharmaceut. Biopharmaceut.*, 2008, **70**, 726-734
13. A. C. Savage and Z. Pikramenou, *Chem. Commun.*, 2011, **47**, 6431-6433
14. F. Himo, T. Lovell, R. Hilgraf, V. V. Rostovtsev, L. Noodleman, B. Sharpless and V. V. Fokin, *J. Am. Chem. Soc.*, 2005, **127**, 210-216
15. L. H. Dubois, *Annu. Rev. Phys. Chem.*, 1992, **43**, 437-463
16. P. Ghosh, G. Han, M. De, C. K. Kim and V. M. Rotello, *Adv. Drug Deliv. Rev.*, 2008, **60**, 1307–1315
17. S. Rana, A. Bajaj, R. Mout and V. M. Rotello, *Adv. Drug Deliv. Rev.*, 2012, **64**, 200-216
18. D. J. Lewis, P. B. Glover, M. C. Solomons and Z. Pikramenou, *J. Am. Chem. Soc.*, 2011, **133**, 1033-1045
19. C. A. G. N. Montalbetti and V. Falque, *Tetrahedron*, 2005, **61**, 10827-10852

20. J. C. Peberdy, J. Malina, S. Khalid, M. J. Hannon and A. Rodger, *J. Inorg. Biochem.*, 2007, **101**, 1937-1945.
21. S. Khalid, M. J. Hannon, A. Rodger and P. M. Rodger, *J. Mol. Graphics Modell.*, 2007, **25**, 794 – 800
22. Y. Najajreh, Y. Ardeli-Tzaraf, J. Kasparkova, P. Heringova, D. Prilutski, L. Balter, S. Jawbry, E. Khazanov, J. M. Perez, Y. Barenholz, V. Brabec and D. Gibson, *J. Med. Chem.*, 2006, **49**, 4674-4683
23. Y. He, Y. Liang and D. Wang, *Chem. Commun.*, 2015, **51**, 12092-12094
24. Y. Zhou, S. Wang, K. Zhang and X. Jiang, *Angew. Chem.*, 2008, **120**, 7564-7566
25. Z. Lin, S. Gao, J. Lin, W. Lin, S. Qui, L. Guo, B. Qiu and G. Chen, *Anal. Methods*, 2012, **4**, 612-615
26. P. Bertoncello, E. T. Kefalas, Z. Pikramenou, P. R. Unwin and R. J. Forster, *J. Phys. Chem. B*, 2006, **110**, 10063-10069
27. N. J. Rogers, S. Claire, R. M. Harris, S. Farabi, G. Zikeli, I. B. Styles, N. J. Hodges and Z. Pikramenou, *Chem. Commun.*, 2014, **50**, 617-619
28. Z. Liu, X. Sun, N. Nakayama-Ratchford and H. Dai, *ACS Nano.*, 2007, **1**, 50-56
29. J. Nam, N. Won, H. Jin, H. Chung and S. Kim, *J. Am. Chem. Soc.*, 2009, **131**, 13639-13645
30. S. D. Brown, P. Nativo, J-A. Smith, D. Stirling, P. R. Edwards, B. Venugopal, D. J. Flint, J. A. Plumb, D. Graham and N. J. Wheate, *J. Am. Chem. Soc.*, 2010, **132**, 4678-4684
31. E. Sugata and S. Kobatake, *RSC Adv.*, 2015, **5**, 34704-34708
32. L. J. Childs, *PhD Thesis*, U. Warwick, 2002
33. H. Le Chatelier, *Compt. Rend.*, 1884, **99**, 786
34. G. I. Pascu, A. C. G. Hotze, C. Sanchez-Cano, B. M. Kariuki and M. J. Hannon, *Angew. Chem. Int. Ed.*, 2007, **46**, 4374-4378
35. J. Malina, M. J. Hannon and V. Brabec, *Chem. Eur. J.*, 2008, **14**, 10408-10414
36. A. Leczkowska , *PhD Thesis*, U. Birmingham, 2010

Chapter 3

DNA and Cell Interactions of Helicate Complexes

The triple stranded helicates developed within the Hannon group are known to interact with a variety of DNA structures. Due to the size, shape and charge of these complexes they have the capability to interact with the grooves found in duplex DNA as well as Y-shaped and three way junction (3WJ) structures present when DNA is in a replication state [1, 2]. More recently, the interactions with quadruplex DNA [3] have been investigated, showing that these cylindrical structures have the ability to bind to a diverse range of DNA structures.

As a result of these interactions, the iron helicates are capable of inhibiting DNA replication and are able to do so *in vitro* [4]. Consequently, those helicates functionalised with additional groups described in *Chapter 2* will in this chapter, be tested for DNA interactions and cell toxicity using a variety of techniques including; circular and linear dichroism, hoechst and ethidium bromide displacement studies, polyacrylamide gel electrophoresis and MTT assays.

3.1 Circular Dichroism

Circular dichroism (CD) is a technique used to investigate interactions between proteins or DNA with other molecules. Specifically it is the difference in absorption of left and right circularly polarised light [5]. CD is used for studying chiral molecules as they exhibit a CD signal, due to enantiomers absorbing left and right handed circularly polarised light in different quantities. In this case, calf thymus DNA (ct-DNA) will be investigated as a long 'genomic' DNA. Due to the helical structure of duplex DNA, it is a chiral species exhibiting a characteristic CD spectrum, Figure 1.

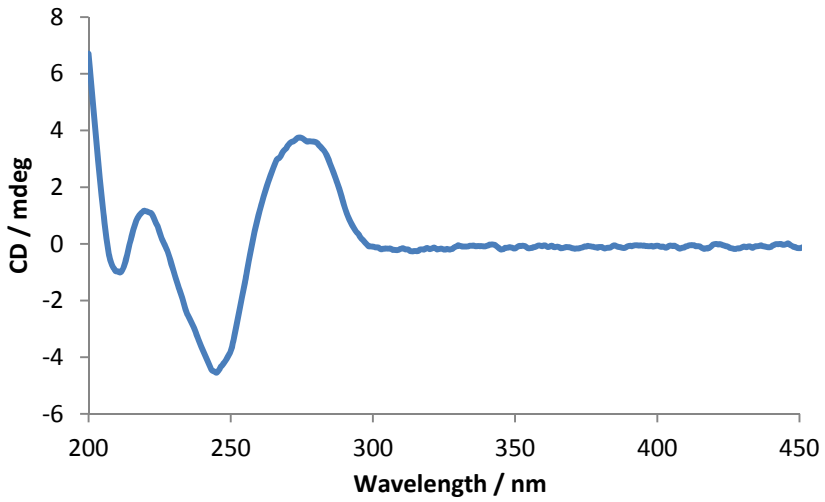

Figure 1: Spectra of 100 μM ct-DNA (B conformation)

When an achiral ligand or a racemic mixture, in this case racemic iron(II) helicate complexes, bind to DNA, an induced CD signal (ICD) may arise. This ICD can be used to determine that a binding interaction has occurred as the compound is now in a fixed chiral environment, and can indicate what kind of interactions are occurring between the ligand and DNA [5].

Each chiral molecule has a characteristic CD spectrum, so any variation from this on addition of an achiral compound can be used to confirm that an interaction between the two species is occurring. Different forms of DNA structures have alternative CD spectra, Figure 2. As a result, it may be possible to determine how DNA is being manipulated on binding.

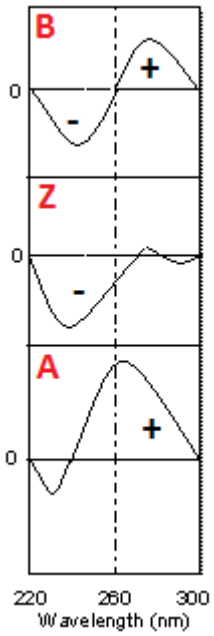

Figure 2: Characteristic CD spectrum for B, Z and A type DNA between 220-300 nm [reproduced from ref[6]]

The cylinder compounds discussed in *Chapter 2* are formed in a racemic mixture consisting of equal quantities of M and P enantiomers. These complexes do not therefore exhibit a CD signal unless the enantiomers are isolated [7].

It is known that these iron helicates are able to interact with B-DNA, resulting in induced chirality from the formation of complex-DNA conjugates. Figure 3 demonstrates this for the 'parent' cylinder, $[Fe_2(L_P)_3]^{4+}$ ($L_P = C_{25}H_{20}N_4$), showing increasing interactions with ct-DNA, with an increasing ratio of DNA bases to complex in solution.

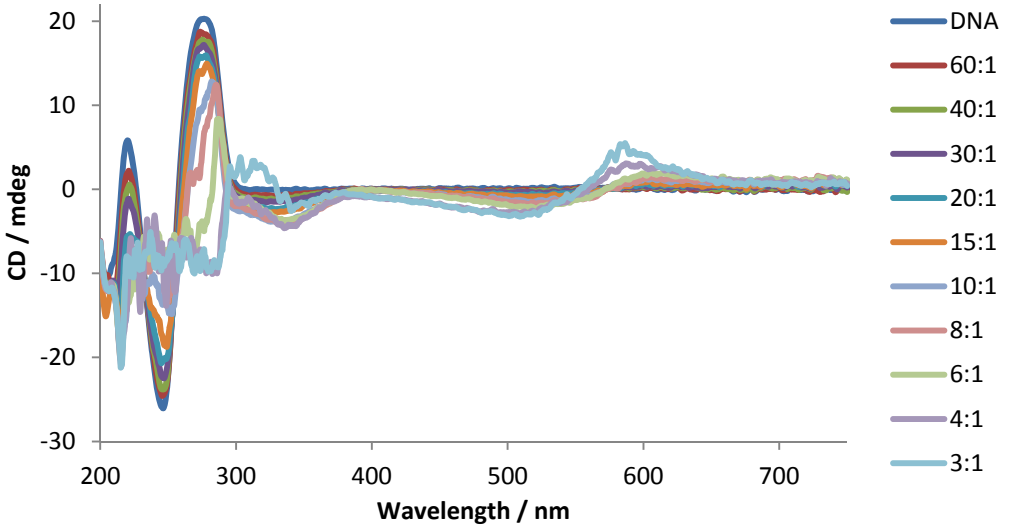

Figure 3: CD of 300 µM ct-DNA in 20 mM NaCl and 1 mM $(CH_3)_2AsO_2Na.3H_2O$ (pH 6.8) with increasing concentrations of parent cylinder. Legend shows ct-DNA : $[Fe_2(L_P)_3]Cl_4$ ratios

Figure 3 shows results consistent with those previously observed by Meistrmann *et al.* [7]. The generation of ICD signals around 340 nm and 590 nm indicate that the cylinder is binding to ct-DNA, producing signals from the complex's ligand and MLCT bands. These peaks increase in intensity with increased loading of the cylinder into a solution of ct-DNA maintained at 300 µM.

Below 300 nm there appear to be competing ICD signals from the DNA and complex, though the B-form signal is retained. Reduction in the magnitude of the characteristic B-DNA peaks does not necessarily mean that the form of DNA is being altered on addition of the complex, but may indicate that a structural change is occurring as a result of the cylinder interacting with ct-DNA.

The same experiment was performed for each of the functionalised cylinder, to compare whether the additional functional groups altered how the helicates interact with DNA.

3.1.1 Stability in Solvent

In order to test the click functionalised cylinders synthesised in *Chapter 2*, on their ability to interact with ct-DNA, it was necessary to make them soluble in an aqueous solution. Due to their high insolubility in water, it was necessary to mix these complexes with a water miscible organic solvent, MeOH or MeCN, to dissolve them into aqueous buffer. In doing so, it was important to ensure that the effects observed in the CD experiments, were caused from only the addition of the respective compounds and not the solvents they are being administered with. Solutions of MeOH and MeCN (20 % in water) corresponding to the levels used to dissolve the click cylinders in future experiments, where titrated into a solution of ct-DNA (100 µM) to observe if the organic solvent altered the ct-DNA characteristic spectra.

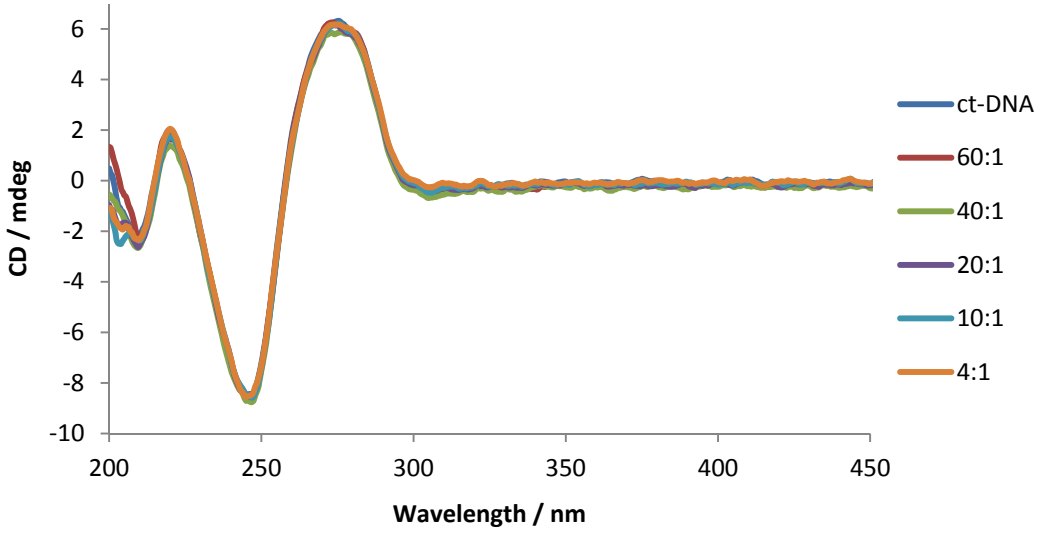

Figure 4: CD of 100 µM ct-DNA in 20 mM NaCl and 1 mM $(CH_3)_2AsO_2Na.3H_2O$ (pH 6.8) with increasing concentrations of MeOH. Legend shows ct-DNA:20 % MeOH solution ratios

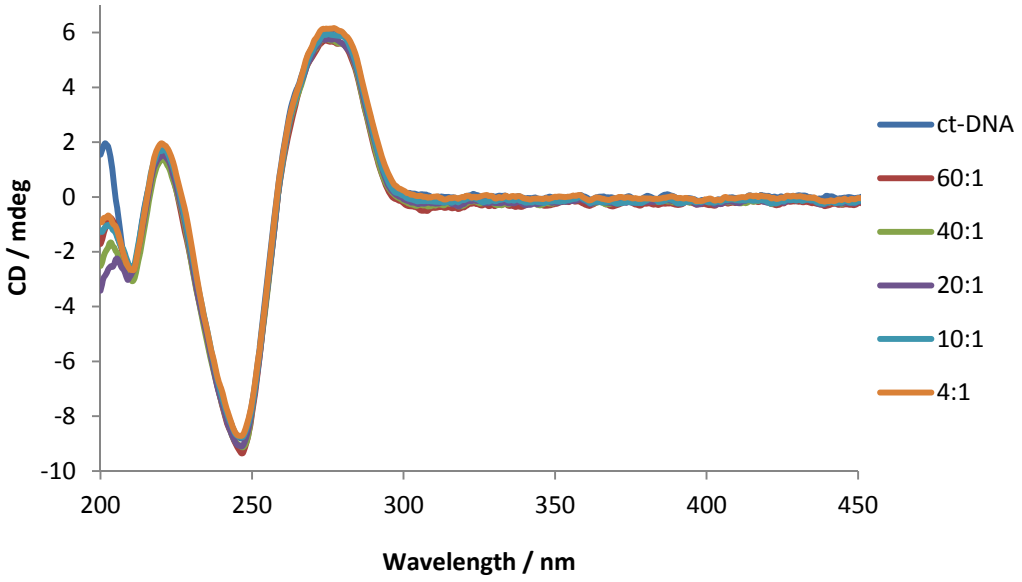

Figure 5: CD of 100 µM ct-DNA in 20 mM NaCl and 1 mM $(CH_3)_2AsO_2Na.3H_2O$ (pH 6.8) with increasing concentrations of MeCN. Legend shows ct-DNA:20 % MeCN solution ratios

On addition of solutions of $MeOH/H_2O$ and $MeCN/H_2O$, the maximum volumes of solvent added to the ct-DNA solutions was 6 %. The same ratios as those tested with the complex solutions were added, producing no observable alteration to the ct-DNA. As a result, it was concluded that any effects observed to the CD signal from addition of a complex solution to ct-DNA, are the result of complex-DNA interactions, and not an effect of the experimental procedure.

3.1.2 Ester Cylinder, $[Fe_2(L_{Ester})_3]Cl_4$

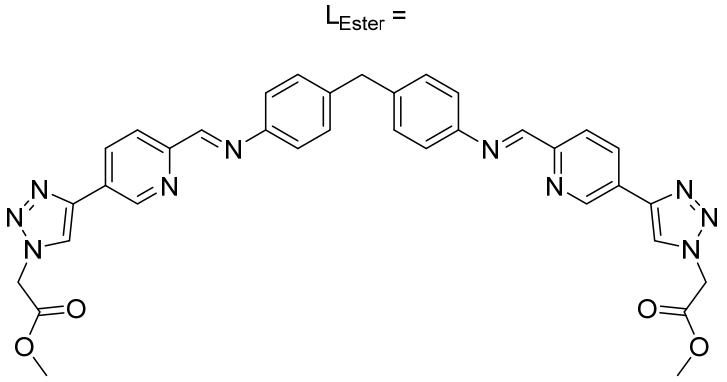

Figure 6: Structure of ligand present in $[Fe_2(L_{Ester})_3]Cl_4$

CD experiments were performed with $[Fe_2(L_{Ester})_3]Cl_4$, Figure 6, to investigate whether this new complex interacted with ct-DNA, and how addition of the ester group by click chemistry may have altered the properties of such a complex. $[Fe_2(L_{Ester})_3]Cl_4$ does not give a CD signal itself as it exists as a racemic mixture, so this complex was titrated into a solution of ct-DNA to investigate if any interactions between the complex and DNA occur, evident from induced and altered signals.

CD experiments were performed with a constant concentration of ct-DNA (300 μM) in aqueous buffer with increasing ratios of complex. The concentration of ct-DNA stated, corresponds to the concentration of bases in solution based on UV calculations using ε= 6600 $moldm^{-3}$ at 260 nm. Experiments were carried out in a 1 cm cuvette to allow for visualisation of weaker signals in the MLCT region (450-750 nm), Figure 7, and a 1 mm cuvette to avoid signal saturation between 200-450 nm, Figure 8, which can occur at high concentrations of the loaded complex.

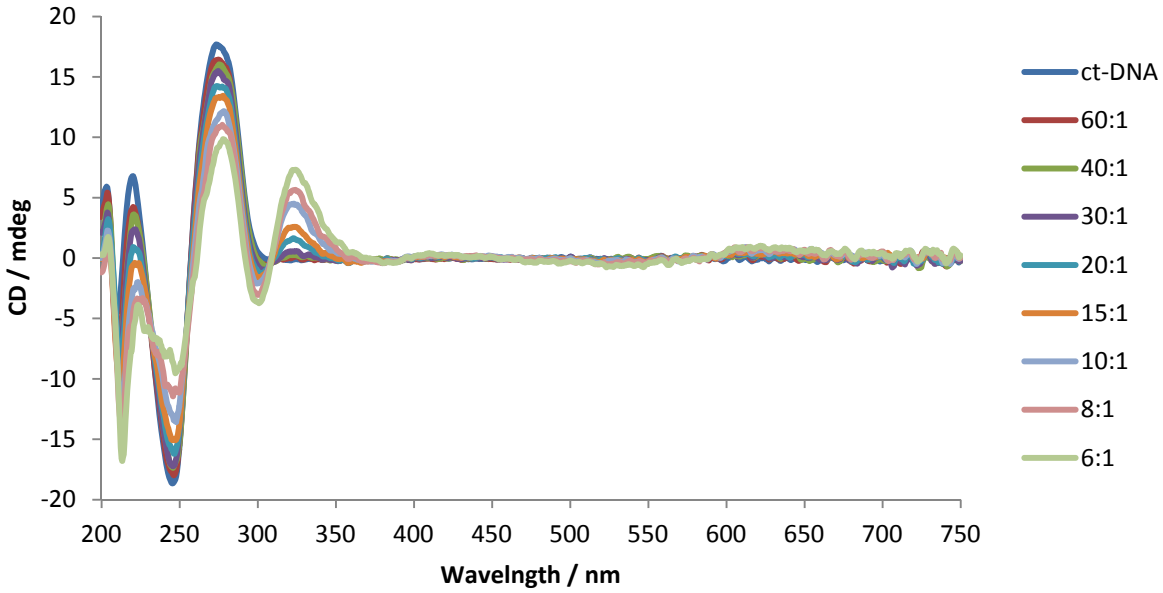

Figure 7: CD of 300 µM ct-DNA in 20 mM NaCl and 1 mM $(CH_3)_2AsO_2Na.3H_2O$ (pH 6.8) with increasing concentrations of ester cylinder. Legend shows ct-DNA: $[Fe_2(L_{Ester})_3]Cl_4$ ratios. UV region (200-750 nm) was analysed in 1 cm cuvette

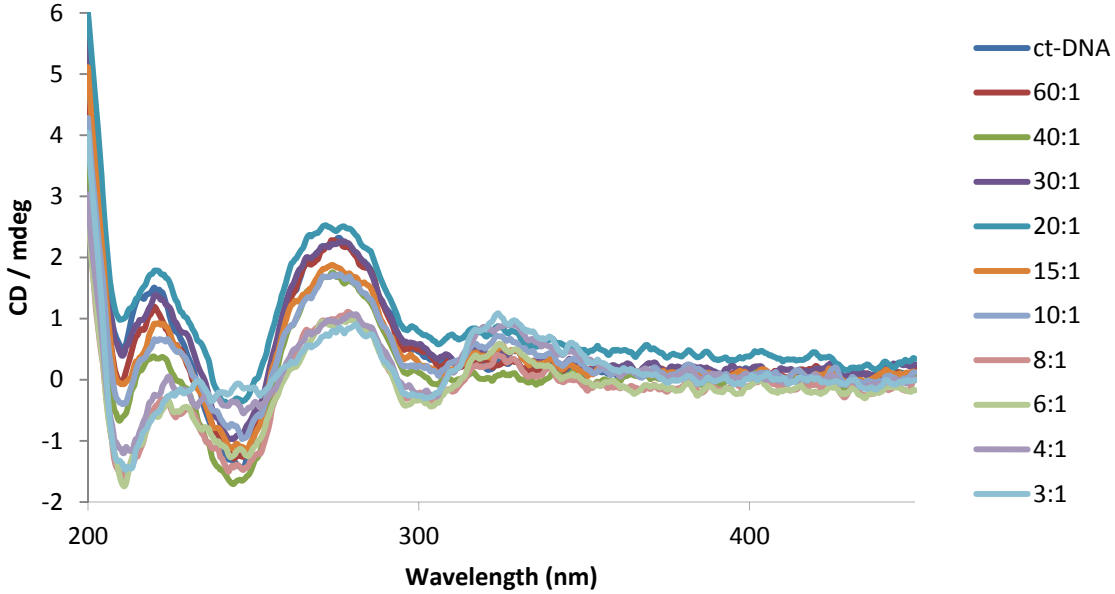

Figure 8: CD of 300 µM ct-DNA in 20 mM NaCl and 1 mM $(CH_3)_2AsO_2Na.3H_2O$ (pH 6.8) with increasing concentrations of ester cylinder. Legend shows ct-DNA: $[Fe_2(L_{Ester})_3]Cl_4$ ratios. UV region (200-450 nm) was analysed in 0.1 cm cuvette

The CD spectra shows ICD signals being produced on increasing concentration of complex at 301 nm (negative) and 322 nm (positive) which correspond to transitions from the ligand. There is also a weak peak observed at 615 nm, corresponding to the MLCT of the complex. These induced signals endorse that the iron(II) helicate is binding to ct-DNA. The intensity of the characteristic DNA bands are altered through addition of the complex, with both peaks between 220-300 nm decreasing in magnitude on addition of complex. This change in spectra does not correspond to the characteristic CD signals of A or Z-DNA, Figure 2, therefore it is likely that a B-DNA conformation is retained, and that as a result of competing induced signals from the helicate and DNA, the intensity of the curve is reduced.

These experiments are performed in an aqueous buffer solution to stabilise the DNA. It is therefore essential that complexes investigated using this technique, dissolve in such a solution. In order to dissolve $[Fe_2(L_{Ester})_3]Cl_4$ in aqueous solution, it was necessary to add 20 % MeOH to the starting complex solution, corresponding to a maximum of 6 % MeOH in the resulting DNA/complex mixtures. The effect of this level of organic solvents in such an experiment was shown to have no observable effect on the DNA, *section 3.1.1* [8].

However, when using the conditions stated above, the complex was seen to precipitate out of solution at high DNA/complex ratios. Consequently, the results shown in Figures 7 and 8 do not reflect the true complex concentrations interacting with DNA. A less concentrated solution of DNA (100 μM) was investigated, allowing for a lower concentration of complex to be added to the buffered solution, decreasing the chance of precipitation. Only a 1 cm path length was used to investigate the lower concentrated solutions, Figures 9 and 10.

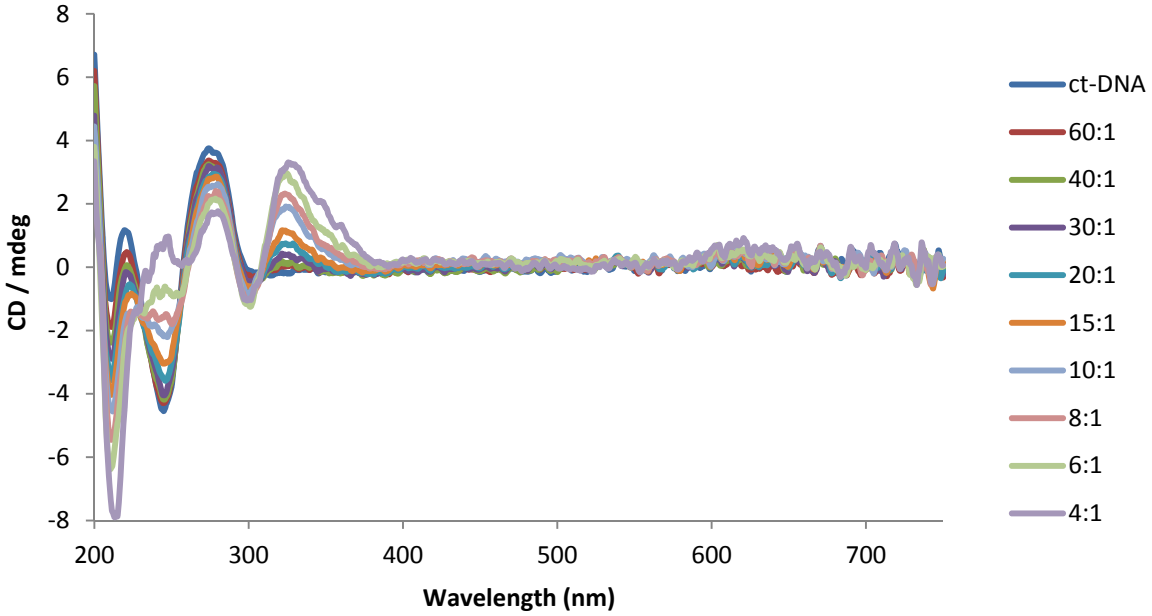

Figure 9: CD of 100 µM ct-DNA in 20 mM NaCl and 1 mM $(CH_3)_2AsO_2Na.3H_2O$ (pH 6.8) with increasing concentrations of ester cylinder. Legend shows ct-DNA: $[Fe_2(L_{Ester})_3]Cl_4$ ratios. UV region (200-750 nm)

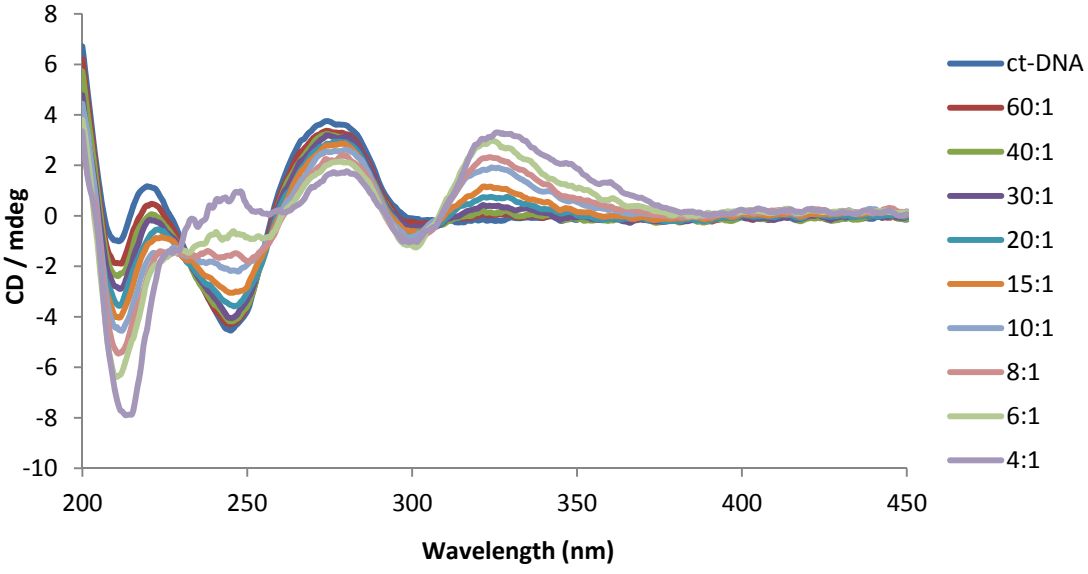

Figure 10: CD of 100 µM ct-DNA in 20 mM NaCl and 1 mM $(CH_3)_2AsO_2Na.3H_2O$ (pH 6.8) with increasing concentrations of ester cylinder. Legend shows ct-DNA: $[Fe_2(L_{Ester})_3]Cl_4$ ratios. UV region (200-450 nm)

An ICD signal was observed at 326 nm, corresponding to that seen at higher concentration, corresponding to transitions from the ligand. The magnitude of this ICD peak is greater than that previously detected, with the induced peak being almost the same magnitude as the characteristic DNA peak at 274 nm. In the previous experiment, Figure 7, only half of this response was observed, corresponding to an increased water solubility of the complex at lower concentration, ensuring the complex is able to interact with the DNA. A weak ICD signal at 613 nm is observed, corresponding to MLCT signals, suggesting that the iron cylinder is binding to ct-DNA.

The characteristic B-conformation signals are altered on addition of the iron(II) helicate, as the binding sites become occupied by complex, the intensity of these peaks reduces in magnitude. The negative peak between 220-260 nm decreases in intensity, possibly resulting from competing ICD signals from the complex and DNA, or it may correspond to the DNA being manipulated to a more A-DNA like structure, Figure 2. A-DNA is more compact and shorter than B-DNA, with the base pairs no longer being perpendicular to the helical axis [9], an effect which could have occurred, consequence of the new complex binding to the ct-DNA.

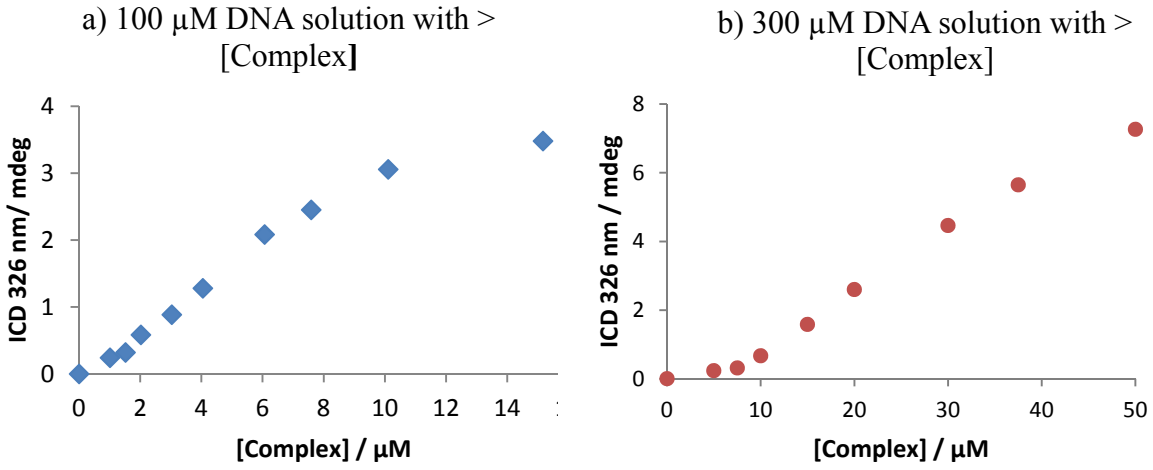

Figure 11: Intensity of ICD signals at 326 nm with increasing concentration of $[Fe_2(L_{Ester})_3]Cl_4$ for a) 100 µM ct-DNA (60:1-6:1) and b) 300 µM ct-DNA (60:1-6:1)

On addition of the ester cylinder to ct-DNA, ICD signals were observed at 326 nm, demonstrated by Figure 11. The magnitude of this ICD signal increased in intensity with increasing complex concentration. The curve of the graph, Figure 11 (a), starts to level off at 10 μM $[Fe_2(L_{Ester})_3]Cl_4$ (10:1 DNA/complex). This implies that there is an interaction of ~5:1 DNA base pairs/cylinders. This value reflects results observed for the parent cylinder, which is known to span over five base pairs [4]. The addition of ester groups to the cylinder would have increased the length of the complex by ~1 nm. It was therefore expected that the binding ratio observed would be lower than 5:1, through poor fit of the complex into ct-DNA binding sites. However, this result suggests that the binding constant of this complex is likely lower than that of the parent cylinder, allowing for a similar overall ratio.

3.1.3 Piperidine Cylinder, $[Fe_2(L_{Piperidine})_3]Cl_4$

$L_{Piperidine}$=

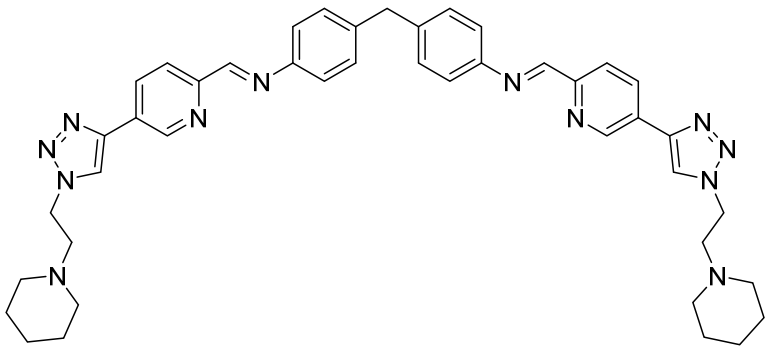

Figure 12: Structure of ligand in $[Fe_2(L_{Piperidine})_3]Cl_4$

Due to results found in *section 3.1.2*, all future CD experiments were performed with 100 µM solutions of ct-DNA in order to get the maximum loading of complexes, whilst maintaining solubility in buffer solution.

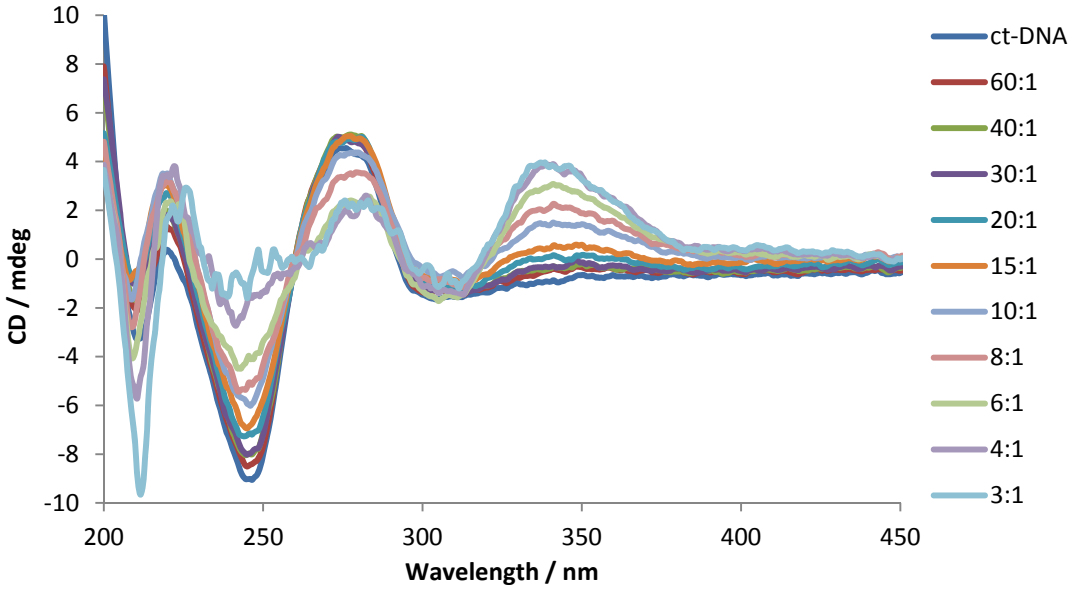

Figure 13: CD of 100 µM ct-DNA in 20 mM NaCl and 1 mM $(CH_3)_2AsO_2Na.3H_2O$ (pH 6.8) with increasing concentrations of $[Fe_2(L_{Piperidine})_3]Cl_4$. Legend shows ct-DNA:complex ratios. Maximum 4% MeOH in titration solution

Consequence of using lower concentrations of ct-DNA and complex, no ICD signal were observed corresponding to the MLCT of the complex. Spectra are therefore shown up to 450 nm, despite the full scan to 750 nm being run, as no useful information was gained from the higher wavelengths.

The characteristic B-DNA conformation signals are again altered on addition of the iron(II) helicate, similar interactions as seen with the ester cylinder were observed for the piperidine complex. With increasing concentration of complex, the magnitude of the DNA signals decreased. This could be the result of competing ICD signals from the complex and DNA, or

could show the DNA structure being manipulated into a different form, shortening and distorting the DNA as a consequence of complex-DNA interactions.

On addition of the piperidine complex to ct-DNA, a large ICD at 338 nm is generated, corresponding to transitions from the ligand. The relationship between intensity of the peak and complex concentration is shown in Figure 14.

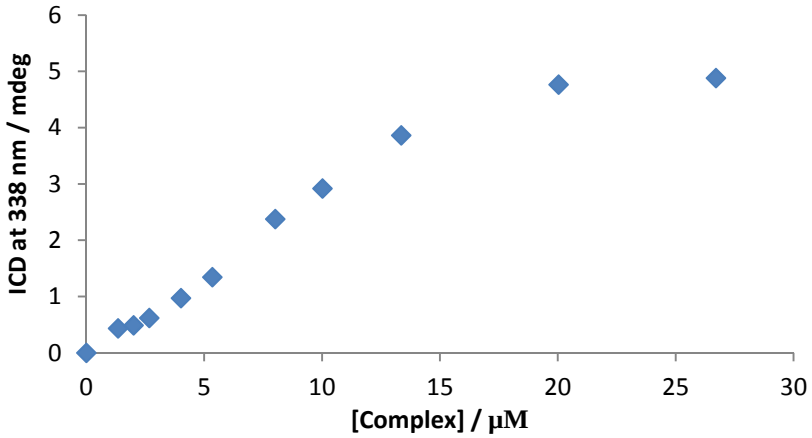

Figure 14: Intensity of ICD signal at 338 nm with increasing concentration of $[Fe_2(L_{Piperidine})_3]Cl_4$ in 100 µM ct-DNA (60:1-4:1 ct-DNA/complex)

The signal at 338 nm increases in magnitude until ~ 17 µM, indicating that there is an interaction of 3:1 base pairs to cylinders. This increase in binding ratio for the piperidine cylinder, may be the result of the piperidine functionality being able to interact with the DNA backbone [10]. If the cylinder is able to wrap around the DNA, an increased number of interactions may be able to occur. It may also suggest that the binding strength is weaker for this functionalised cylinder compared to the parent, meaning not every complex in solution is bound to the DNA.

3.1.4 Thioacetate Cylinder, $[Fe_2(L_{Thioacetate})_3][BF_4]_4$

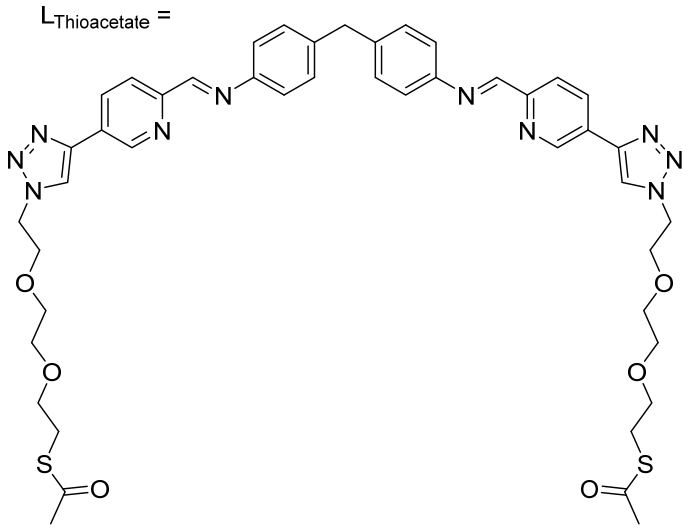

Figure 15: Structure of ligand in $[Fe_2(L_{Thioacetate})_3][BF_4]_4$

Solubility of the thioacetate cylinder was different to that of the previously functionalised helicates. The longer chain, despite being a polyethylene glycol (PEG) chain makes the complex insoluble in water and MeOH. As a result, MeCN was used to solubilise the complex in water, to allow addition to buffered DNA solution.

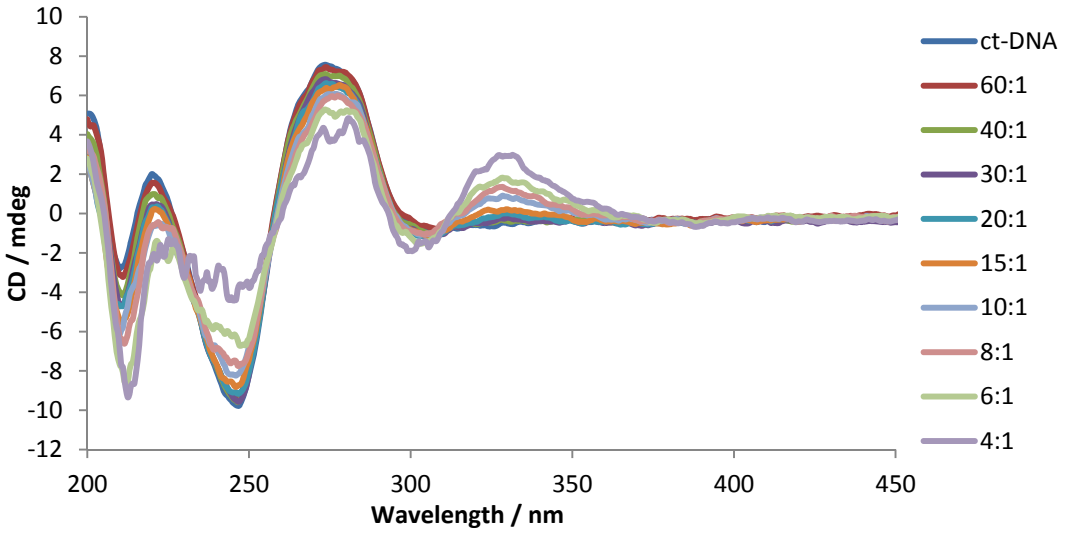

Figure 16: CD of 100 µM ct-DNA in 20 mM NaCl and 1 mM $(CH_3)_2AsO_2Na.3H_2O$ (pH 6.8) with increasing concentrations of $[Fe_2(L_{Thioacetate})_3][BF_4]_4$. Legend shows ct-DNA:complex ratios. Maximum 3% MeCN in titration solution

On addition of increasing concentrations of thioacetate cylinder, an ICD signal is observed at 328 nm, corresponding to transitions from the ligand. This indicates that the cylinder is binding to the ct-DNA as chirality of the complex is induced. The characteristic B-DNA conformation signals are reduced in magnitude on addition of the iron(II) helicate. Both the negative and positive peaks between 220-300 nm decrease as binding sites become occupied through complex binding. This could be the result of competing ICD signals from the complex and DNA, or the result of the DNA being manipulated into another conformation as a result of the complex binding.

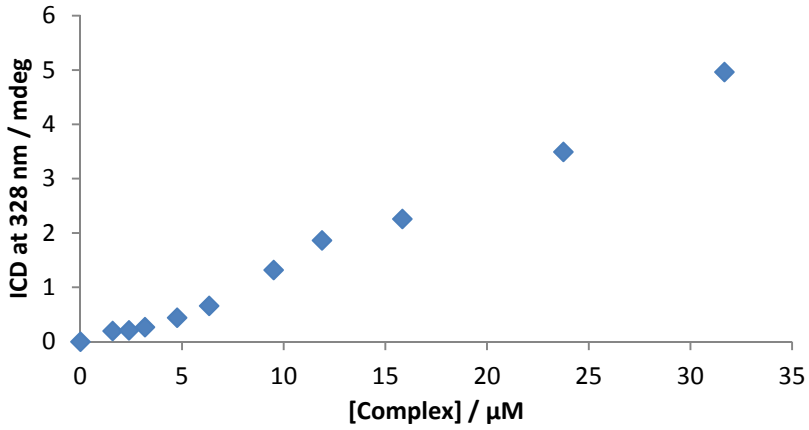

Figure 17: Intensity of ICD signal at 328 nm with increasing concentration of $[Fe_2(L_{Thioacetate})_3][BF_4]_4$ in 100 µM ct-DNA (60:1-4:1 ct-DNA/complex)

With addition of increasing thioacetate cylinder concentrations to ct-DNA, an ICD signal is produced at 328 nm. When a complex/DNA ratios of 4:1 is reached, an increased binding affinity is observed, compared to the ester and piperidine cylinders. A linear relationship is observed between the ICD peak intensity and complex concentration, indicating that the ct-DNA has a higher affinity of this complex than seen previously. Due to solubility issues, it was not possible to increase the ratio of DNA:complex tested by CD titration, and so from these

results it can be estimated that there is an ~5:3 interaction between DNA bases and thioacetate cylinder. This increased ratio compared with the ester and piperidine cylinders may be the result of many factors. For example: it could be due to the new sulphur containing moieties attached to the complex, the increased length of the linker arm between the triazole formed during the click reaction, the fact there are now oxygen atoms in the structure thanks to the PEG chain linker or that the binding constant is much lower than the other cylinders due to the increased size, so not all of the cylinders in solution are on the DNA. These modifications have resulted in slightly altered effects to those seen with the ester and piperidine functionalised cylinders, the interaction between this complex and DNA structures will be further investigated.

3.2 Linear Dichroism

Linear dichroism is a technique used to monitor the interactions between bio-macromolecules and ligands [5], as with circular dichroism, however this technique uses linearly polarised light. In this instance the interaction between iron(II) helicate complexes with ct-DNA are being investigated.

Linear Dichroism uses an orientated sample to measure the difference between light absorbed which has been polarized parallel and perpendicular to the axis of orientation [5, 11].

$$LD = A\| - A \perp [12]$$

In order to orientate the sample, a couette cell, Figure 18 [13], is used which spins the sample solution, resulting in the sample becoming orientated at velocity. Small molecules are unable to be orientated in this manner, so no LD signal is observed. Due to the molecular size of ct-DNA, it is possible to orientate in solution, producing a characteristic LD signal, Figure 19.

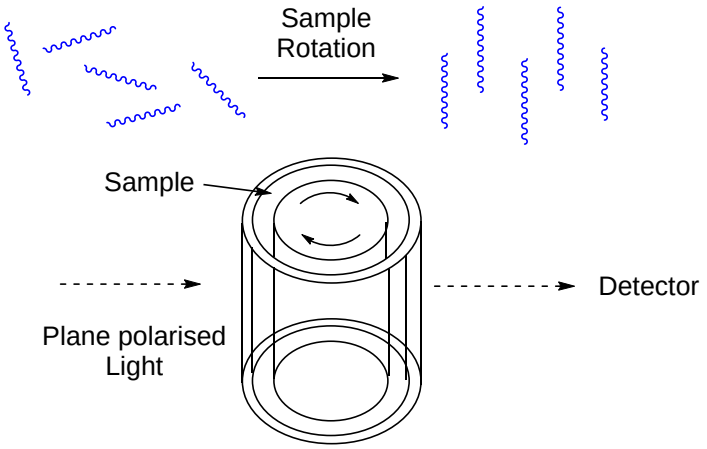

Figure 18: Schematic diagram of a Couette flow cell [reproduced from ref[13]]

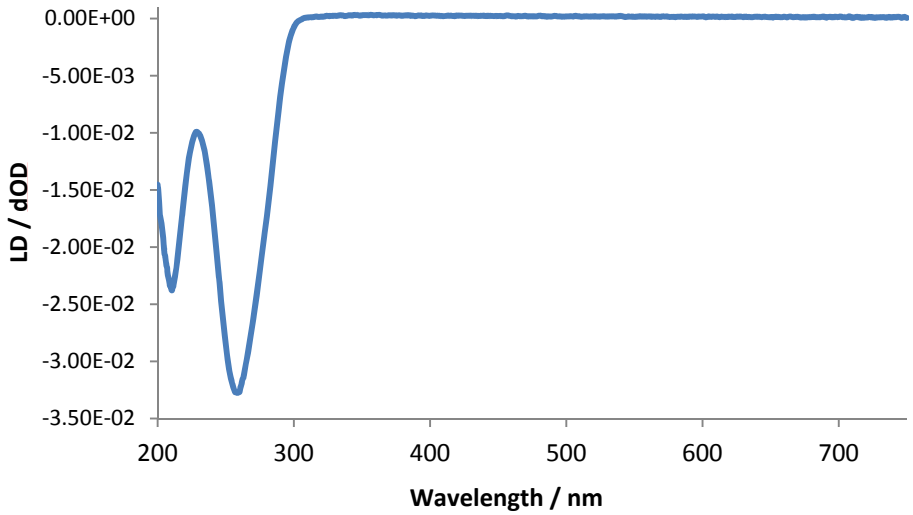

Figure 19: Spectrum of 100 µM ct-DNA (B conformation)

The iron(II) helicates being discussed are nanoscale, resulting in no LD signals, through lack of orientation. As ct-DNA has a characteristic LD spectrum, Figure 19, it is possible to monitor compounds interacting with the structure, by looking at alterations in the LD signal. These alterations can then be rationalised to identify what type of interaction and effect the addition of complexes can have on the orientation and hence structure of the DNA.

It is known through previous research that the parent cylinder is able to alter the structure of ct-DNA on binding [7]. This activity was reproduced through titrating increasing concentrations of cylinder with a consistent concentration of ct-DNA, Figure 20.

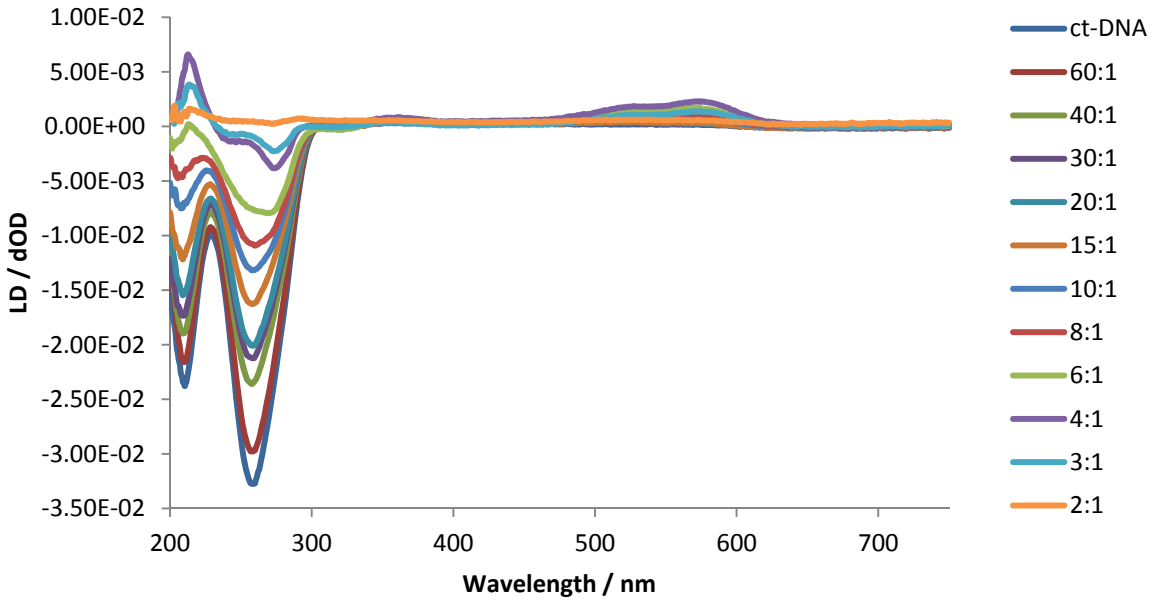

Figure 20: LD of 300 µM ct-DNA in 20 mM NaCl and 1 mM $(CH_3)_2AsO_2Na.3H_2O$ (pH 6.8) with increasing concentrations of $[Fe_2(L_P)_3]Cl_4$. Legend shows ct-DNA:complex ratios

On addition of increasing ratios of the parent cylinder, the characteristic DNA peaks at 210 nm and 260 nm continually decrease in magnitude. This is due to the cylinder binding in the major groove of the helical DNA, causing kinking and coiling of the structure [1]. As a result the DNA strands become less orientated in solution and hence the LD signal decreases.

Induced LD signals (ILD) are also produced on addition of the complex. The growth of peaks at 212 nm and between 500-600 nm show that the cylinder is becoming orientated in solution. As a result it can be concluded that the complex is binding in a specific manner to the DNA [1]. As the ratio of ct-DNA:complex reaches above 4:1, these induced signals decrease, perhaps reflecting the reduced orientation of the DNA.

3.2.1 Stability of ct-DNA in Solvent

As with the CD experiments performed in *section 3.1*, a portion of water miscible organic solvents had to be used in LD experiments in order to get the newly functionalised cylinder complexes into aqueous buffer solution. Equivalent portions of solvent were therefore tested with ct-DNA to ensure that the quantities used within these experiments had no effect on the DNA, and that changes in LD spectra observed were as a result of the complexes only.

On addition of equivalent ratios of MeOH, as used in the experimental procedure, no observable alteration to the LD signal of ct-DNA was detected, Figure 21. Slight alterations to the intensity of the peaks appear, likely due to pipetting error.

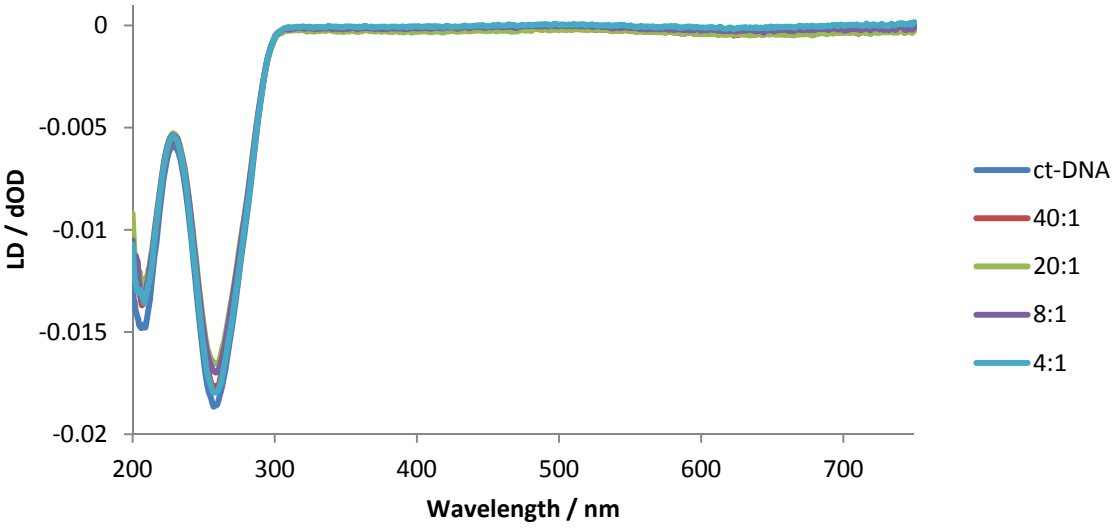

Figure 21: LD of 100 µM ct-DNA in 20 mM NaCl and 1 mM $(CH_3)_2AsO_2Na.3H_2O$ (pH 6.8) with increasing concentrations of MeOH. Legend shows ct-DNA:20 % MeOH solution ratios

When aliquots of MeCN/H_2O were titrated into a solution of ct-DNA, Figure 22, little effect on the LD spectrum of ct-DNA was observed. The ratios analysed were equivalent to those used when analysing the thioacetate cylinder, indicating that any observations made from future experiments, were as a result of the functionalised cylinder and not due to the solvent it was

administered in. The intensity of the characteristic peak at 260 nm decreases slightly on addition of MeCN, likely due to pipetting error.

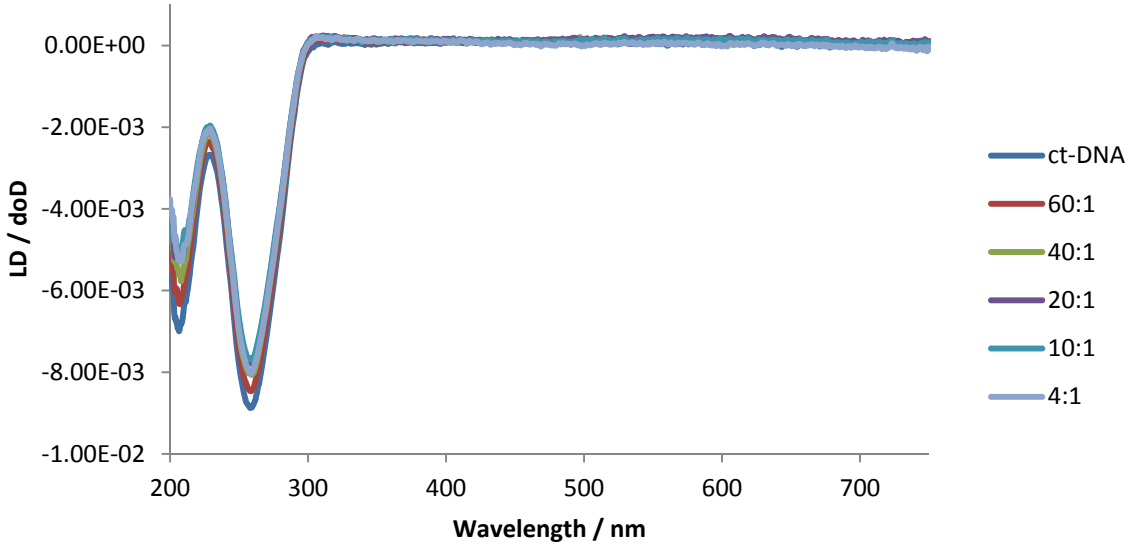

Figure 22: LD of 100 µM ct-DNA in 20 mM NaCl and 1 mM $(CH_3)_2AsO_2Na.3H_2O$ (pH 6.8) with increasing concentrations of MeCN. Legend shows ct-DNA:20 % MeCN solution ratios.

3.2.2 Ester Cylinder

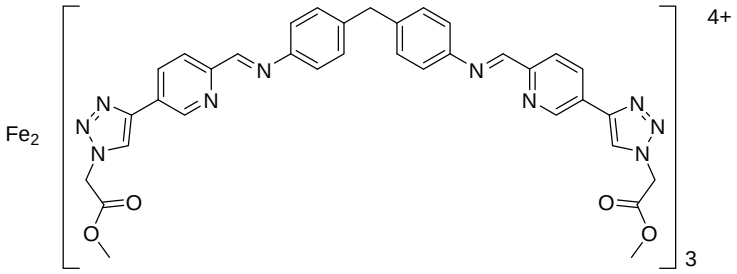

As discussed in *section 3.1.2*, the functionalised helicates are not as water soluble as the parent cylinder, so experiments were performed at a lower concentration in order to get a high ratio of DNA:complex whilst avoiding precipitation.

A solution of the ester cylinder was therefore titrated into the orientated sample of ct-DNA, keeping DNA concentration constant, producing results shown in Figure 23.

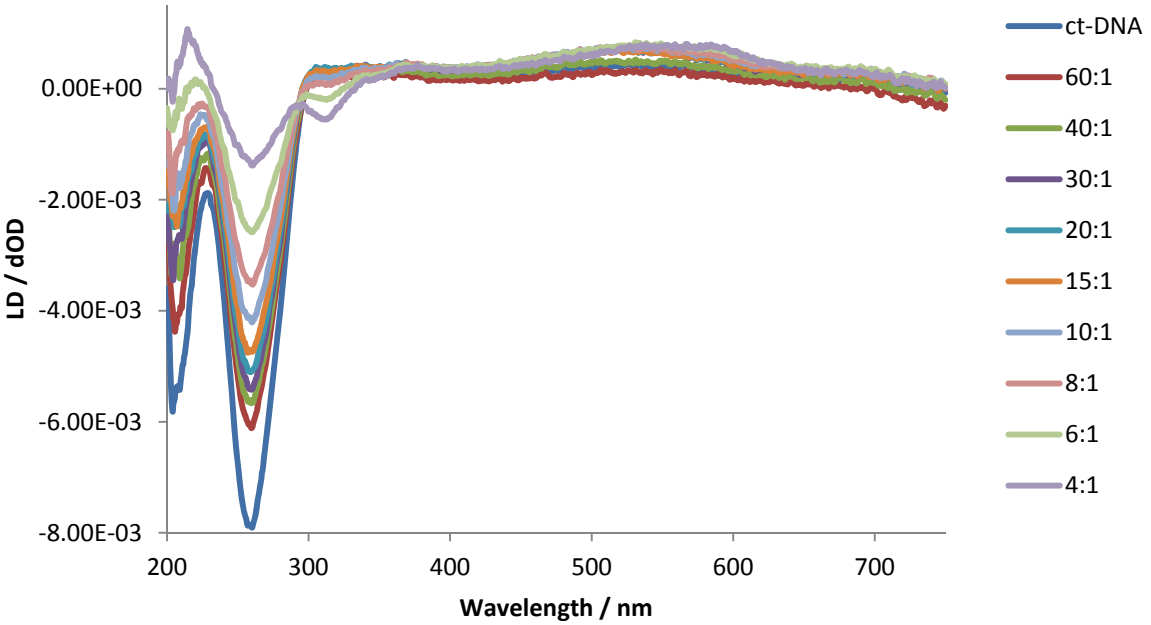

Figure 23: LD of 100 µM ct-DNA in 20 mM NaCl and 1 mM $(CH_3)_2AsO_2Na.3H_2O$ (pH 6.8) with increasing concentrations of $[Fe_2(L_{Ester})_3]Cl_4$. Legend shows ct-DNA:complex ratios. Maximum 3% MeOH in titration solution

On addition of increasing concentrations of ester cylinder, ILD peaks were produced at 312 nm and ~585 nm. These signals indicate that the cylinder becomes orientated when added to a solution of ct-DNA, impling that the helicate is binding in a specific manner to the DNA.

The characteristic negative DNA peaks at 210 nm and 260 nm reduce in magnitude on addition of complex, mirroring that observed with the parent cylinder, Figure 20, suggesting that the ct-DNA becomes less orientated in solution.

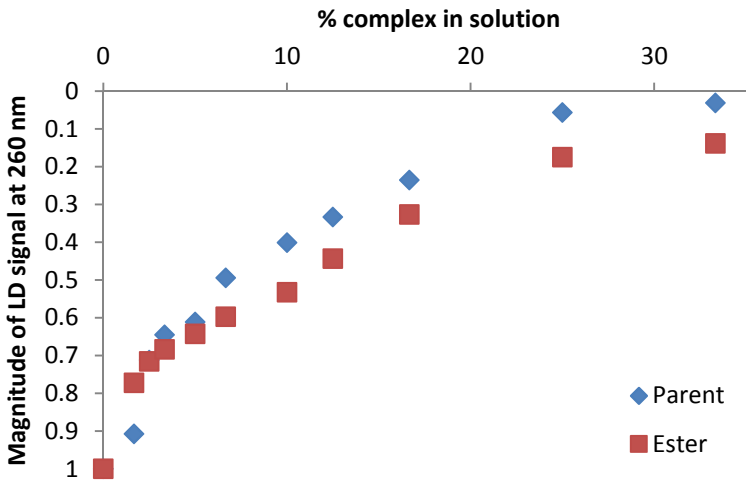

Figure 24: Normalised LD signal intensities at 260 nm for increasing ratios of parent $[Fe_2(L_P)_3]Cl_4$ and ester $[Fe_2(L_{Ester})_3]Cl_4$ cylinder complexes

By comparing the reduction of LD signal at 260 nm on addition of the parent cylinder and ester functionalised cylinders at equivalent ratios of DNA:complex, Figure 24, it is observed that the ester cylinder kinks and coils the DNA to 89 % of what the parent cylinder is capable of. This interaction suggests that the ester cylinder has a similar binding mode to the parent cylinder, and due to the structure being slightly more bulky with additional ester groups, binding is slightly hindered, but still takes place, resulting in loss of orientation for the DNA.

3.2.3 Piperidine Cylinder

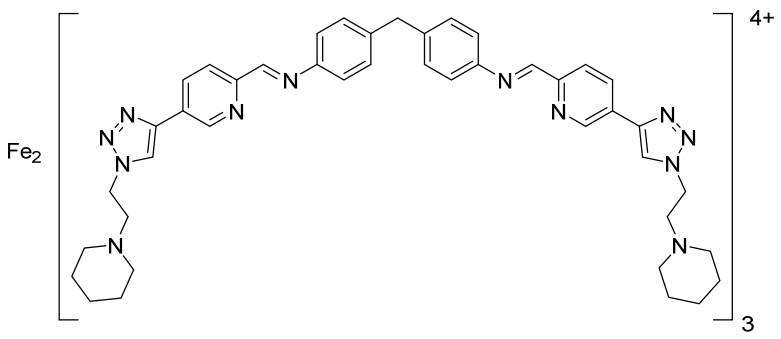

Through titrating the piperidine cylinder into an orientated solution of ct-DNA, no ILD signals are observed. The absence of ILD signals does not necessarily mean that the cylinder is not orientated on addition to the DNA, but could be the result of conflicting spectroscopy, cancelling out signals or could be the result of the cylinder binding unspecifically onto the DNA. If the cylinder has multiple binding modes, not all will be orientated in one direction to produce an ILD. This could be the case, as the piperidine functionality is also known to have the ability to bind to the backbone of DNA [10].

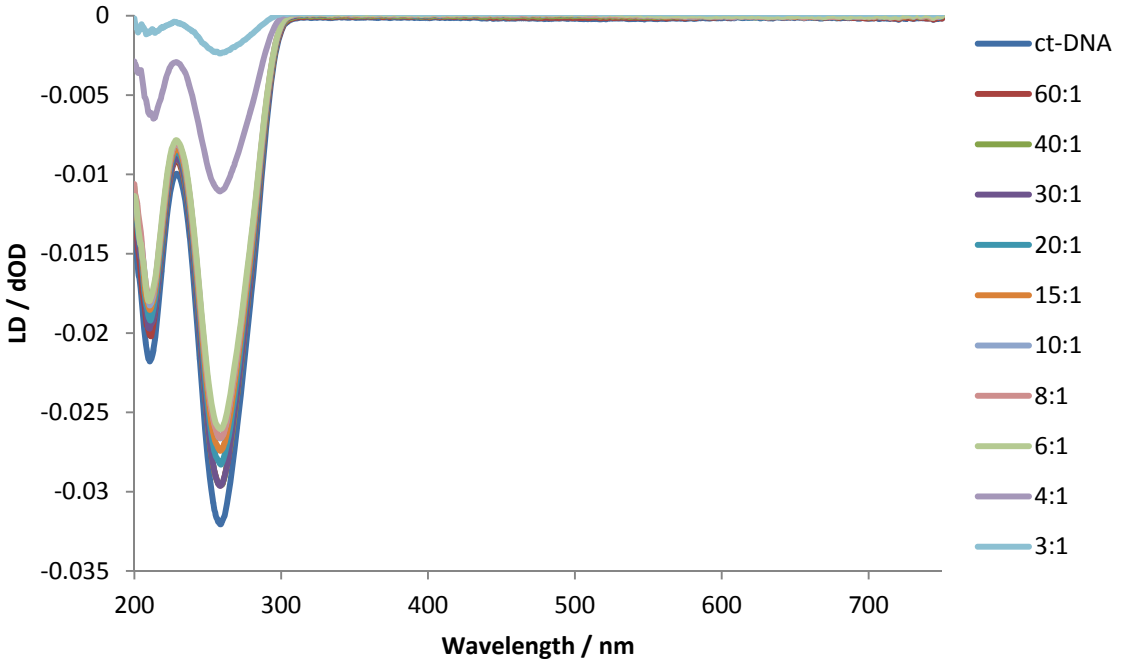

Figure 25: LD of 100 µM ct-DNA in 20 mM NaCl and 1 mM $(CH_3)_2AsO_2Na.3H_2O$ (pH 6.8) with increasing concentrations of $[Fe_2(L_{Piperidine})_3]Cl_4$. Legend shows ct-DNA:complex ratios. Maximum 4% MeOH in titration solution

It is apparent however, that through adding this complex to ct-DNA, the structure is altered with increasing DNA:complex ratios. The reduction in characteristic LD signals is observed, indicating that the DNA is becoming less orientated on addition of piperidine cylinder, Figure 26.

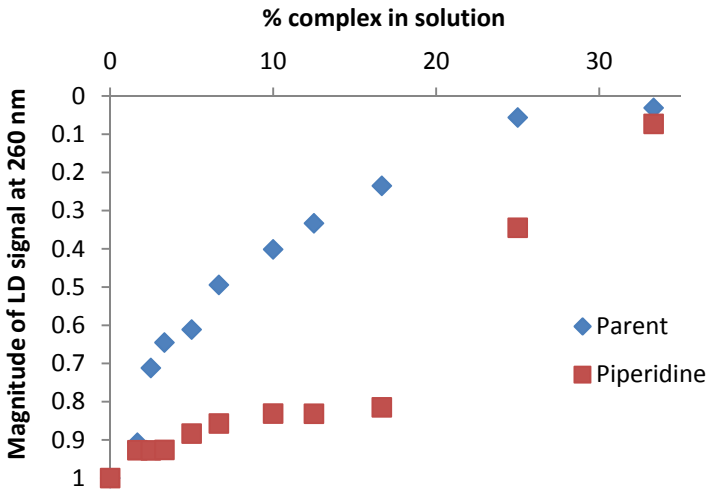

Figure 26: Normalised LD signal intensities at 260 nm for increasing ratios of parent $[Fe_2(L_P)_3]Cl_4$ and piperidine $[Fe_2(L_{Piperidine})_3]Cl_4$ complexes

By comparing the reduction in magnitude of the characteristic LD signal at 260 nm for the parent and piperidine cylinders, it is apparent that the interactions with ct-DNA are different. At a ratio of 3:1 DNA:complex, 96 % equivalent of the ct-DNA has been kinked/coiled by the piperidine cylinder compared to the parent cylinder. This coiling effect is only observed however at high loading. Below a DNA:piperidine complex ratio of 6:1, the signal at 260 nm had only decreased in magnitude by 18 %, indicating that there are two binding modes for this complex. The initial binding mode has a small effect on the ct-DNA structure, potentially just bending the DNA, to reduce its orientation slightly. The second binding mode has a strong effect on the DNA structure, dramatically reducing orientation in solution, suggesting that the DNA becomes kinked and coiled in solution on binding to the piperidine functionalised cylinder. This multiple binding mode may also reiterate why no ILD signals are observed on addition of the complex. If the piperidine helicate is binding to multiple sites on the DNA, it may not be in high enough concentration, in a specific orientation to be detected.

3.2.4 Thioacetate Cylinder

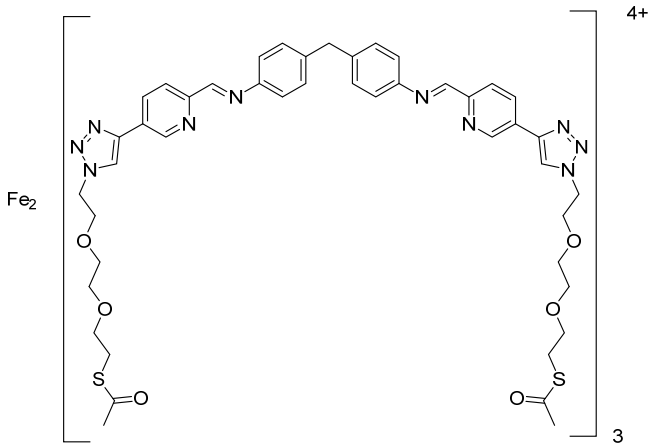

Through addition of the thioacetate cylinder to ct-DNA, numerous alterations to the characteristic DNA spectrum are observed, Figure 27. An ILD signal at 329 nm is produced, indicating that the cylinder is binding to ct-DNA in a specific manner to become orientated with the DNA. It was also found that the characteristic DNA peaks are not as greatly reduced in magnitude by addition of the thioacetate cylinder, as previously observed with the other functionalised helicates.

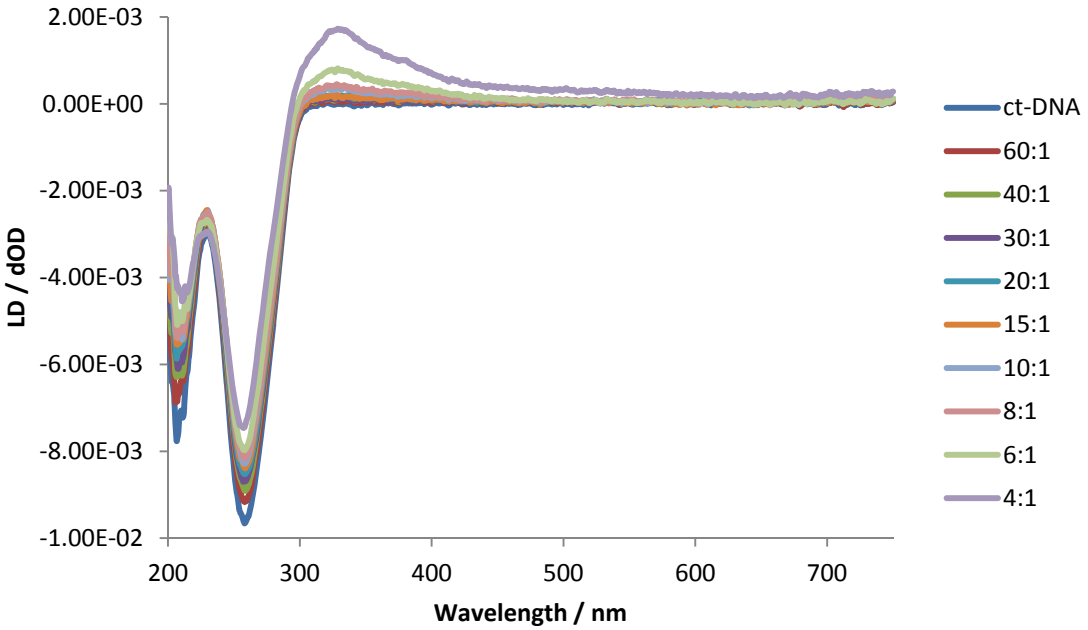

Figure 27: LD of 100 µM ct-DNA in 20 mM NaCl and 1 mM $(CH_3)_2AsO_2Na.3H_2O$ (pH 6.8) with increasing concentrations of $[Fe_2(L_{Thioacetate})_3][BF_4]_4$. Legend shows ct-DNA:complex ratios. Maximum 3% MeCN in titration solution

With increasing concentration of the thioacetate cylinder with ct-DNA, the ILD peak intensity also increases, Figure 28. The peak does not appear to be reaching a maximum intensity for the concentrations analysed. This may suggest that higher loading of the complex could be achieved onto the DNA. However, due to the insolubility of complex in aqueous buffer, a ratio of 4:1 DNA/complex was the highest ratio that could be achieved without over loading the DNA solution with MeCN. The presence of this peak does show that the cylinder is indeed binding to ct-DNA.

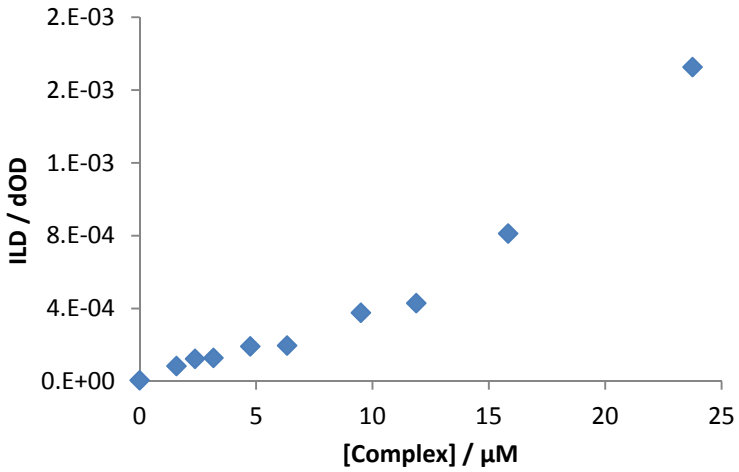

Figure 28: Intensity of ILD at 329 nm with increasing $[Fe_2(L_{Thioacetate})_3][BF_4]_4$ concentration

Unlike with the ester and piperidine cylinders, the characteristic DNA peaks at 210 nm and 260 nm are not greatly affected by addition of the thioacetate cylinder. Figure 29 shows that a gradual reduction of the peak at 260 nm is observed, but only 25 % of the orientation is lost compared to the parent cylinder. This indicates that the thioacetate cylinder may have a different binding mode on ct-DNA to the parent cylinder or that the binding constant is lower. This could be due to the large moieties added to the ligand making the cylinder too bulky to fit in the major groove of the DNA, or that the sulphur groups increase the affinity of the cylinder to an

alternative binding site on the DNA. As a result, it appears that the DNA is being bent or kinked on binding, and not dramatically coiled which would result in the DNA becoming disorientated in solution. These results indicate that the longer/more bulky the cylinder becomes, it appears to coil the DNA less effectively.

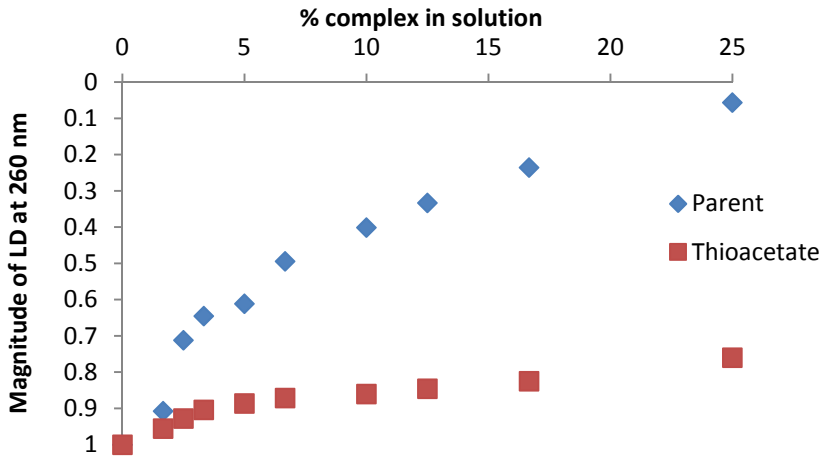

Figure 29: Normalised LD signal intensities at 260 nm for increasing ratios of complex

3.3 Stability

It has been noted that adding functionality onto the ligand of the parent cylinder dramatically alters the complex solubility and stability [14]. As stated in the previous sections, a portion of organic solvent was needed in order to get the newly functionalised clicked compounds into aqueous solution to analyse their interactions with DNA. It has also been noted, by previous Hannon group members that on addition to ct-DNA, complex stability can increase on binding [8]. This was analysed for the click functionalised cylinders.

3.3.1 Cylinder Buffer Stability

3.3.1.1 Parent Cylinder

The parent cylinder is soluble in 100 % H_2O and as shown by Figure 30, is stable in buffer solution also. A concentration of 17 µM was analysed as this is approximately the concentration of complex in a 6:1 solution ratio of ct-DNA (100 µM)/complex, which will be evaluated during this section.

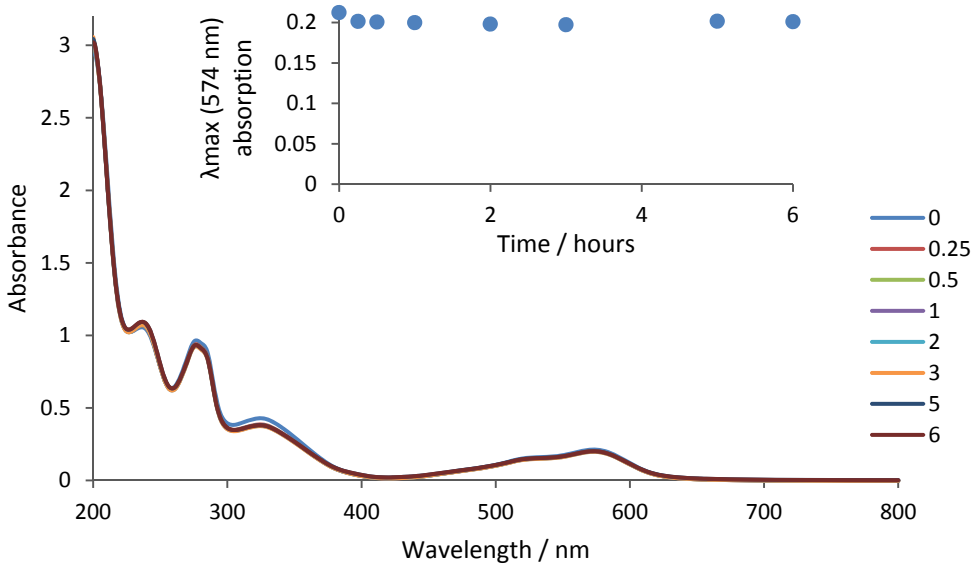

Figure 30: UV spectra of $[Fe_2(L_P)_3]Cl_4$ (17 µM) in 20 mM NaCl and 1 mM $(CH_3)_2AsO_2Na.3H_2O$ (pH 6.8) over time/hrs

3.3.1.2 Ester Cylinder

The ester cylinder is not water soluble, so was dissolved in buffer with ~3 % MeOH, equivalent to that used within DNA binding experiments. After only five hours, the complex degraded in buffered solution, indicated by loss of the MLCT band at 590 nm which results in the triple stranded helicate structures having a purple colour, Figure 31. The loss of this peak therefore corresponds to the degradation of the cylinder structure into former counter parts.

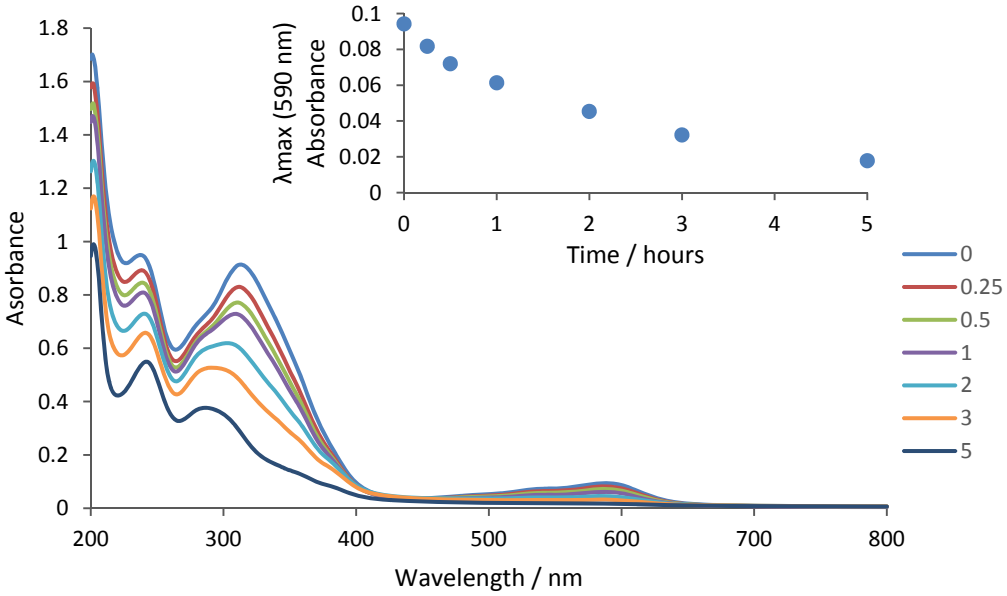

Figure 31: UV spectra of $[Fe_2(L_{Ester})_3]Cl_4$ (17 µM) in 20 mM NaCl and 1 mM $(CH_3)_2AsO_2Na.3H_2O$ (pH 6.8) over time/hrs

3.3.1.3 Piperidine Cylinder

The piperidine cylinder was dissolved in buffer with ~3 % MeOH, equivalent to that used within DNA binding experiments. After only five hours, the complex degraded in buffered solution, indicated by 70 % loss of the MLCT band at 589 nm, which gives the triple stranded helicate structures a purple colour, Figure 32. The loss of this peak therefore corresponds to the degradation of the cylinder structure into former counter parts.

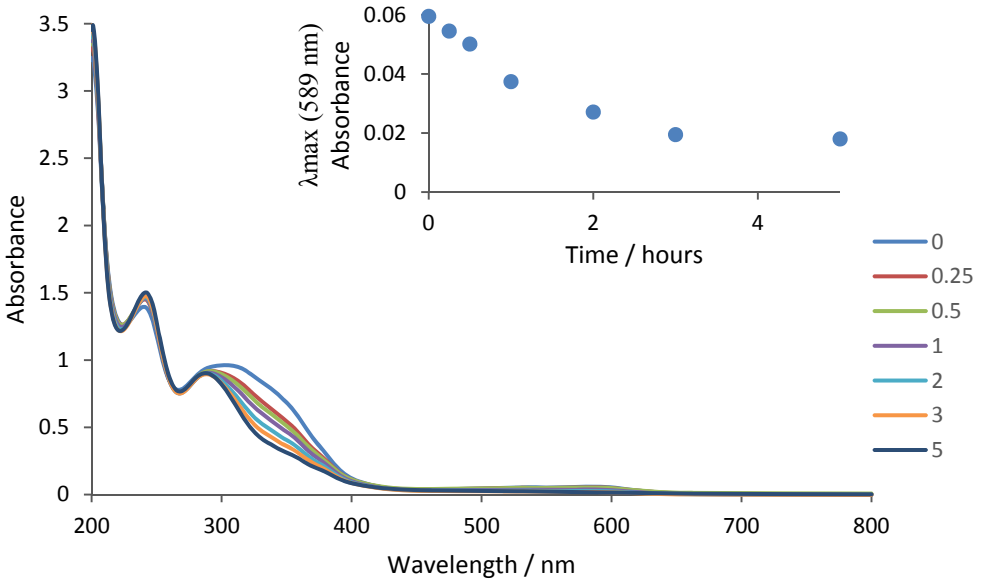

Figure 32: UV spectra of $[Fe_2(L_{Piperidine})_3]Cl_4$ (17 µM) in 20 mM NaCl and 1 mM $(CH_3)_2AsO_2Na.3H_2O$ (pH 6.8) over time/hrs

3.3.1.4 Thioacetate Cylinder

The thioacetate cylinder is not water soluble, so was dissolved in buffer with ~3 % MeCN, equivalent to that used within DNA binding experiments. After six hours, the complex degraded in buffered solution, indicated by loss of the MLCT band at 589 nm which results in the triple stranded helicate structures having a purple colour, Figure 33. The loss of this peak therefore corresponds to the degradation of the cylinder structure into former counter parts.

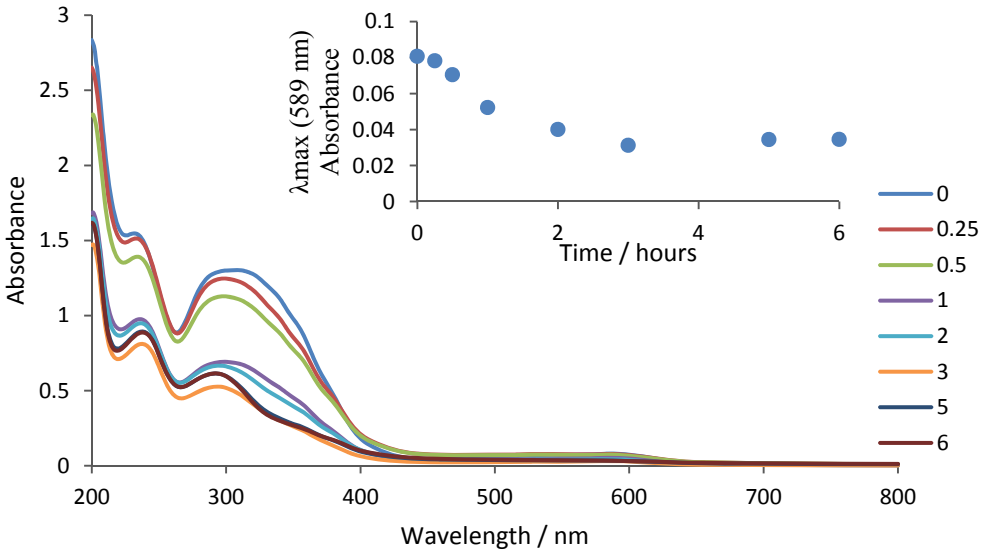

Figure 33: UV spectra of $[Fe_2(L_{Thioacetate})_3][BF_4]_4$ (17 µM) in 20 mM NaCl and 1 mM $(CH_3)_2AsO_2Na.3H_2O$ (pH 6.8) over time/hrs

3.3.2 Cylinder/DNA Stability

3.3.2.1 Parent Cylinder

The parent cylinder in the chloride salt form is water soluble and stable in aqueous solution for extended periods of time. The stability of a 6:1 ct-DNA:cylinder solution was tested for its stability by UV spectroscopy, Figure 34.

The MLCT band from the UV-Vis spectrum of the complex, shows that the cylinder is in solution. A reduction in this peak over time would indicate that the complex is breaking down to the ligand and counterparts. It was therefore this region which was of interest, as it is solely produced from the complex without interference of the DNA spectrum.

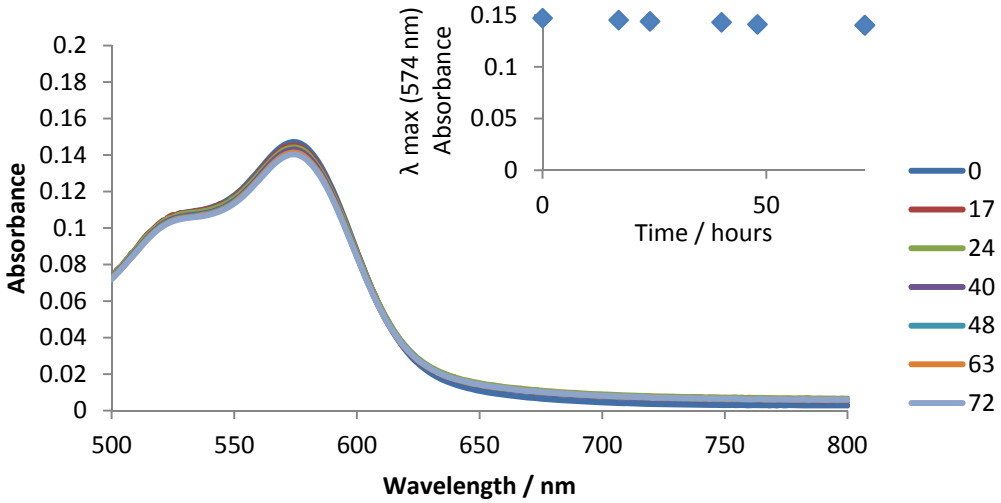

Figure 34: UV-Vis spectra of 6:1 ct-DNA (100 µM) / $[Fe_2(L_P)_3]Cl_4$ over time/hr in 20 mM NaCl and 1 mM $(CH_3)_2AsO_2Na.3H_2O$ (pH 6.8)

By analysing the λmax of the MLCT band present at 574 nm, Figure 34, it is apparent that the parent cylinder is highly stable in aqueous solution, with 95 % retention in the intensity of the absorption band over 72 hours. This was therefore used as a comparison to assess the functionalised cylinders.

It was hypothesised, that any potential degradation in the cylinders may be the result of one helicate enantiomer having a higher affinity to the DNA, which would result in degradation of the non-bound enantiomer. The enantiomers of the parent cylinder are known to have higher affinities for different binding sites [7], which could result in the compounds high stability in solution as it all interacts with DNA in some manner.

If this were the case, over time a CD signal would be produced from the one enantiomer that was binding, Figure 35. Through recording the CD spectra of the same 6:1 ct-DNA/complex solution over time, enaniomeric selectivity and stability were analysed.

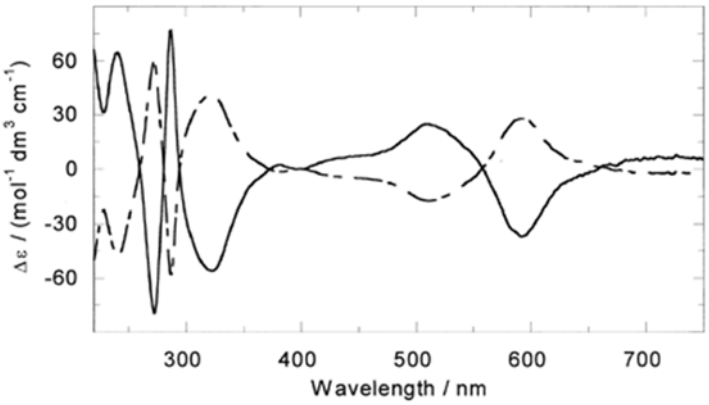

Figure 35: CD spectra of M-$[Fe_2L_3]^{4+}$ (solid line) and P-$[Fe_2L_3]^{4+}$ (dashed line) [reproduced from ref[7]]

Due to the high stability of the parent cylinder, it was expected that there would be no alteration of the CD spectra over time. This was largely true, Figure 36, however a reduction in signal at 323 nm was observed. This slight shift in the spectra could be result of the 5 % degraded species in solution, or an increased interaction between the cylinder and ct-DNA when left for an extended period of time.

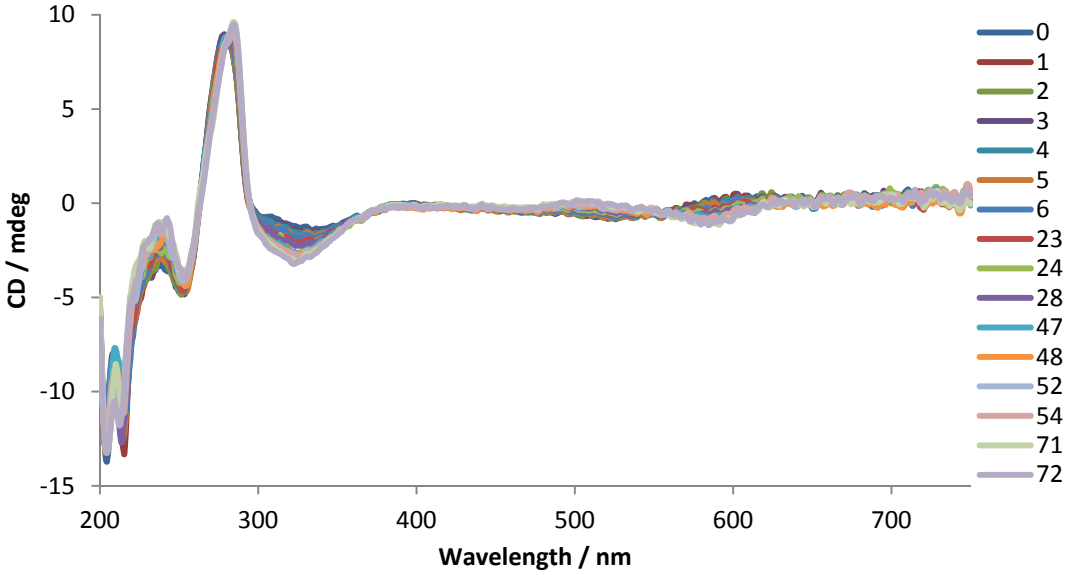

Figure 36: CD spectra of 6:1 ct-DNA (100 µM) / $[Fe_2(L_P)_3]Cl_4$ over time/hrs in 20 mM NaCl and 1 mM $(CH_3)_2AsO_2Na.3H_2O$ (pH 6.8)

3.3.2.2 Ester Cylinder

On analysing the UV absorbance of the MLCT band present in the characteristic UV spectrum of the ester cylinder, it is possible to identify the relative stability of the compound in the presence of ct-DNA. This area of the UV spectrum, 500-800 nm, is not affected by the UV spectrum of ct-DNA; hence any alteration in this peak will correspond to the cylinder only. It is apparent that the ester cylinder is not as stable as the parent in aqueous solution, through reduction of the signal in this region, Figure 34.

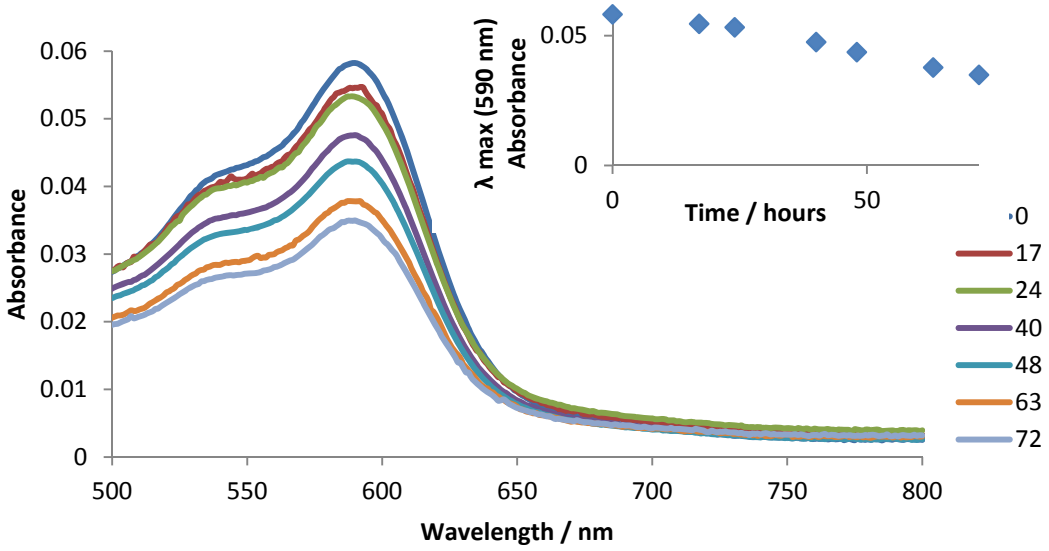

Figure 37: UV-Vis spectra of 6:1 ct-DNA (100 µM) / $[Fe_2(L_{Ester})_3]Cl_4$ over time/hrs in 20 mM NaCl and 1 mM $(CH_3)_2AsO_2Na.3H_2O$ (pH 6.8)

The intensity of λmax, at 590 nm decreases in magnitude over time, Figure 37. Compared to the 95 % of parent cylinder intact after 72 hours, only 60 % of the ester cylinder is still in its helicate formation after the same period of time. After 17 hours, 94 % of the cylinder is still intact however, showing that results from the CD and LD experiments, shown in *sections 3.1.2* and *3.2.2*, will be the effects of the intact cylinder, rather than any degraded species as the titration experiments were performed within this time. It also shows that stability of the complex

has been greatly increased on interaction with ct-DNA, compared to the complex in just buffered solution, *section 3.3.1.2*.

As a result of 40 % of the ester complex breaking down over 72 hours, it was investigated whether this was the result of instability of one enantiomer, due to lack of interaction with ct-DNA.

Figure 38 shows CD spectra of the same solution over 72 hours, showing changes of peak intensities between 280-330 nm and the evolution of peaks at 236 nm and between 500-650 nm. These slight changes in the spectra over time correspond to an M enantiomer spectrum becoming more apparent, Figure 35 [7]. This suggests that the M enantiomer of the ester cylinder has a higher affinity to ct-DNA than the P, resulting in P degrading over time as not stabilised by the DNA structure. Consequently, with time a larger proportion of M enantiomer becomes present in the solution mixture and a CD signal for the cylinder is observed. It was not possible to isolate the M and P enantiomers of the ester cylinder, and so CD spectra could not be obtained of the pure samples. Consequently it was not possible to quantify the amount of enantiomer created during this experiment.

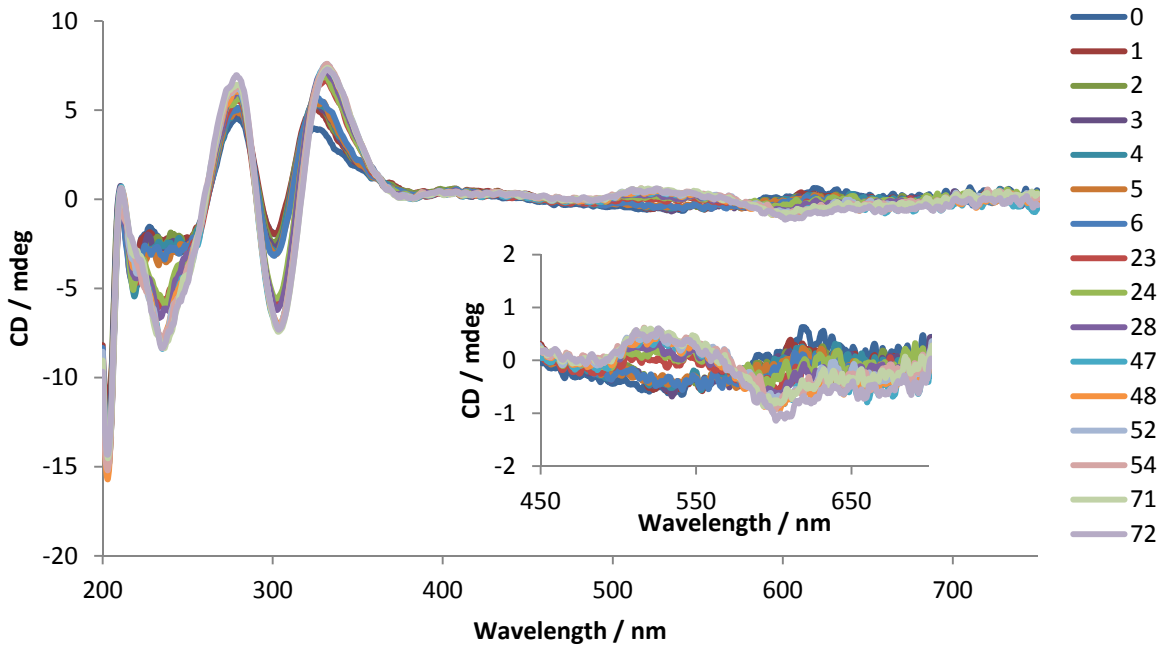

Figure 38: CD spectra of 6:1 ct-DNA (100 µM) / $[Fe_2(L_{Ester})_3]Cl_4$ over time/hrs in 20 mM NaCl and 1 mM $(CH_3)_2AsO_2Na.3H_2O$ (pH 6.8)

3.3.2.3 Piperidine Cylinder

Analysis of piperidine cylinder stability on binding to ct-DNA was also analysed through the measurement of the UV absorbance between 500-800 nm, over a 72 hour period. It is apparent that the piperidine cylinder is not as stable as the parent in aqueous solution, indicated by the decreased magnitude of λmax, at 589 nm over time, Figure 39.

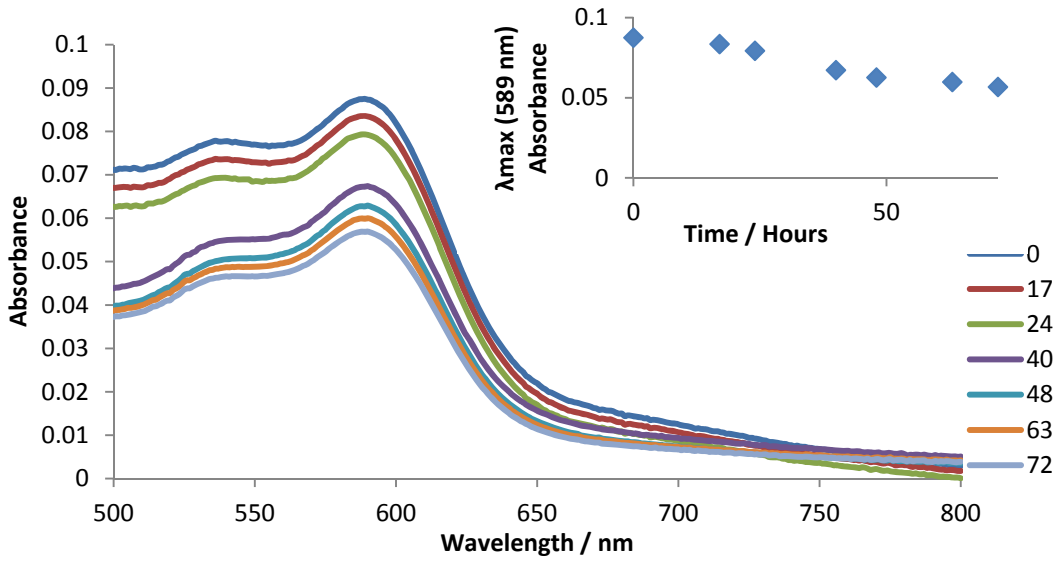

Figure 39: UV-Vis spectra of 6:1 ct-DNA (100 µM) / $[Fe_2(L_{Piperidine})_3]Cl_4$ over time/hrs in 20 mM NaCl and 1 mM $(CH_3)_2AsO_2Na.3H_2O$ (pH 6.8)

Compared to the 95 % of parent cylinder being intact after 72 hours, only 64 % of the piperidine cylinder remains in solution after the same period of time. This degradation occurs gradually over the three days, apparent by the shallow gradient of the curve. After 17 hours, 96 % of the cylinder was still intact, showing that results from the CD and LD experiments, shown in *sections 3.1.3* and *3.2.3*, will be the effects of the intact piperidine complex, rather than any degraded species, as the titration experiments are performed within this time. It also shows that on interaction ct-DNA, the stability of the complex is greatly increased compared to that observed in *section 3.3.1.3*.

As 35 % of the piperidine complex degraded over 72 hours, it was investigated whether this was the result of one enantiomer being unstable, due to lack of interaction with the ct-DNA. Figure 40 shows little alteration in the CD spectrum over time, with no detectable ICD signals being produced, suggesting that degradation is equal for both enantiomers, and neither has a higher affinity to ct-DNA.

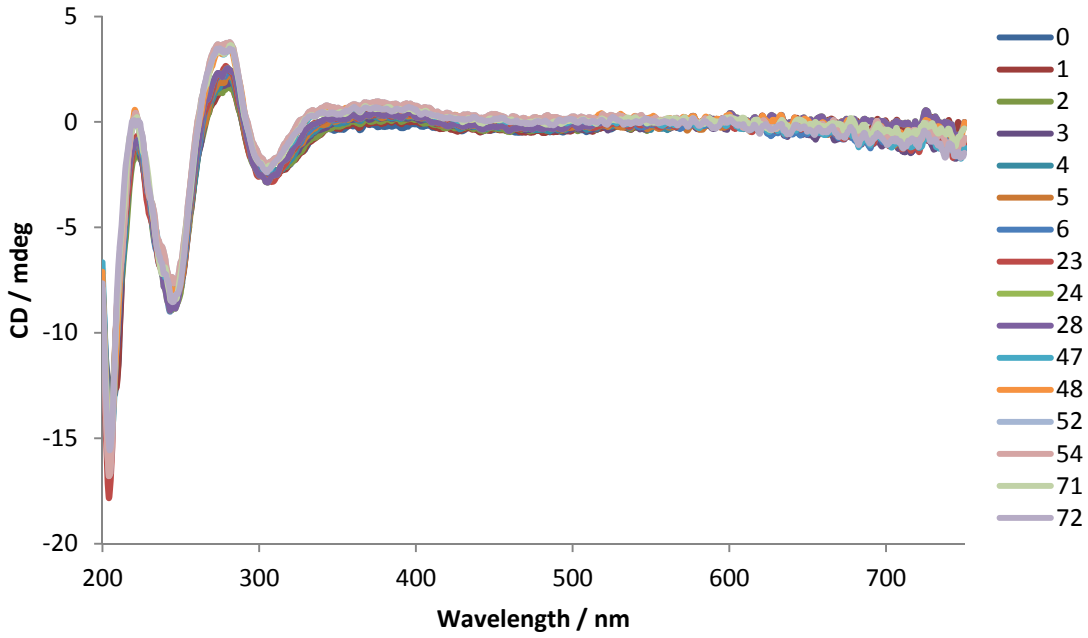

Figure 40: CD spectra of 6:1 ct-DNA (100 µM) / $[Fe_2(L_{Piperidine})_3]Cl_4$ over time/hrs in 20 mM NaCl and 1 mM $(CH_3)_2AsO_2Na.3H_2O$ (pH 6.8)

3.3.2.4 Thioacetate Cylinder

When the stability of the thioacetate functionalised cylinder was monitored by UV-Vis spectroscopy, Figure 41, it appeared that a large portion of the cylinder quickly degraded with time. By evaluating the λmax intensity at 589 nm of the MLCT signal, a large decrease in absorbance was observed within 24 hours and then the degradation of the complex declined slowly to an almost steady state. After 24 hours almost 50 % of the MLCT signal had been lost. After a further two days, 37 % remained in solution, indicating that those cylinders coordinated to the DNA structure are stabilised.

Due to the increased size of the thioacetate cylinder compared to the parent, the complex may not be able to bind as strongly to DNA due to steric hindrance. Consequently less complex (~40 %) may only be able to bind to the DNA, resulting in the dramatic loss in complex stability after a short period of time and then the steady levels of stability thereafter.

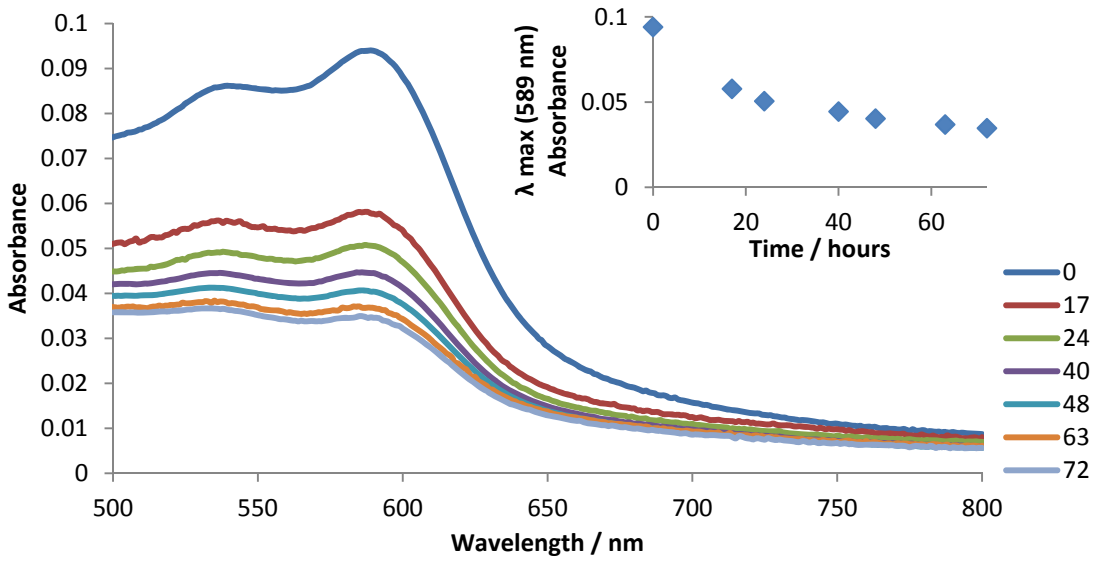

Figure 41: UV-Vis spectra of 6:1 ct-DNA (100 µM) / $[Fe_2(L_{Thioacetate})_3][BF_4]_4$ over time/hrs in 20 mM NaCl and 1 mM $(CH_3)_2AsO_2Na.3H_2O$ (pH 6.8)

CD spectra were then taken on an equivalent solution of ct-DNA and thioacetate cylinder over a period of 72 hours, Figure 42. The CD spectra does not greatly alter with time, however there are slight increases in peak intensities at 243 nm and 282 nm. This may be the result of increased interactions between ct-DNA and ligand which occur in solution as a result of the degraded cylinder. Small additional peaks between 500-650 nm were detected, which would suggest the evolution of one enantiomer with time. This change in spectra comparable to the ester cylinder, indicating that the M enantiomer has a slightly higher binding affinity to the DNA, making it more stable over time compared with the degrading P enantiomer.

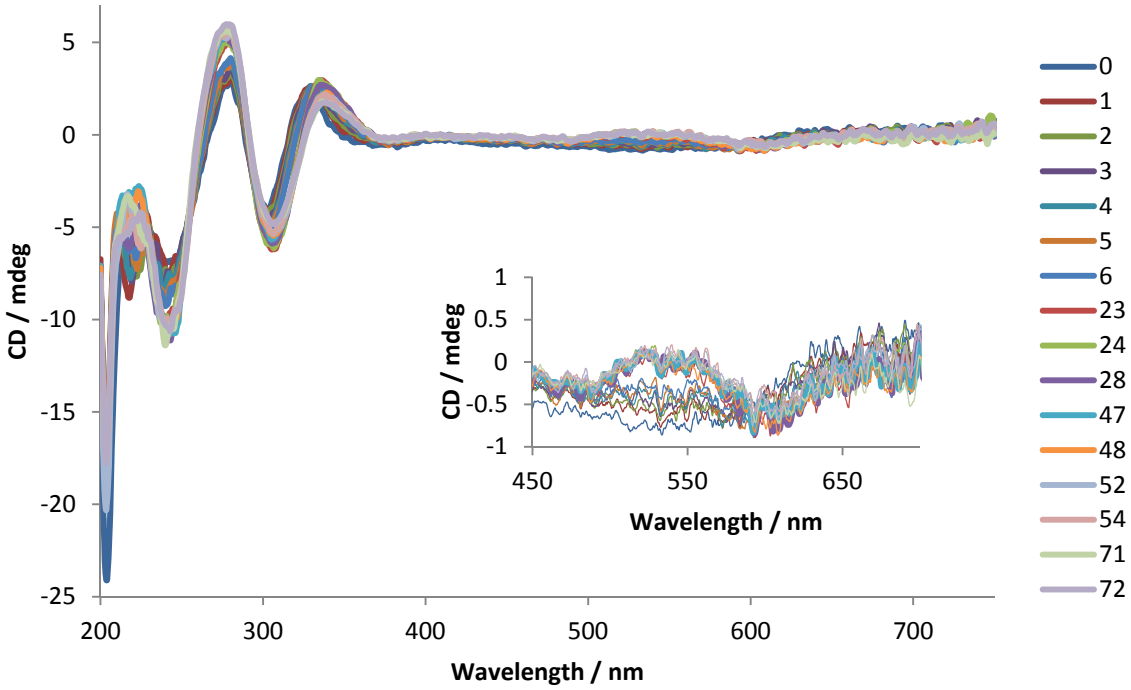

Figure 42: CD spectra of 6:1 ct-DNA (100 µM) / $[Fe_2(L_{Thioacetate})_3][BF_4]_4$ over time/hrs in 20 mM NaCl and 1 mM $(CH_3)_2AsO_2Na.3H_2O$ (pH 6.8)

3.4 DNA Melting Experiment

On binding to DNA, it is known that compounds are able to stabilise the overall DNA structure resulting in more energy needed to disrupt and unwind the double stranded helix [15]. This change in the energy it takes to 'melt' DNA gives another indication that the compound is indeed binding to DNA. Solutions of ct-DNA (100 µM) containing each complex were tested to see whether they stabilised the structure of DNA on binding, Figure 43. 6:1 DNA/complex solutions were heated from 25-100 °C.

On heating each solution, the intensity of absorbance for the characteristic DNA peak at 260 nm was measured. This peak corresponds to the bases present in the DNA structure [16]. On melting the ct-DNA, the double helix becomes unwound, resulting in unpaired bases and an

increase in the peak intensity at 260 nm. As such, if the temperature for unwinding increases, the DNA is held in the helical structure due to increased stability.

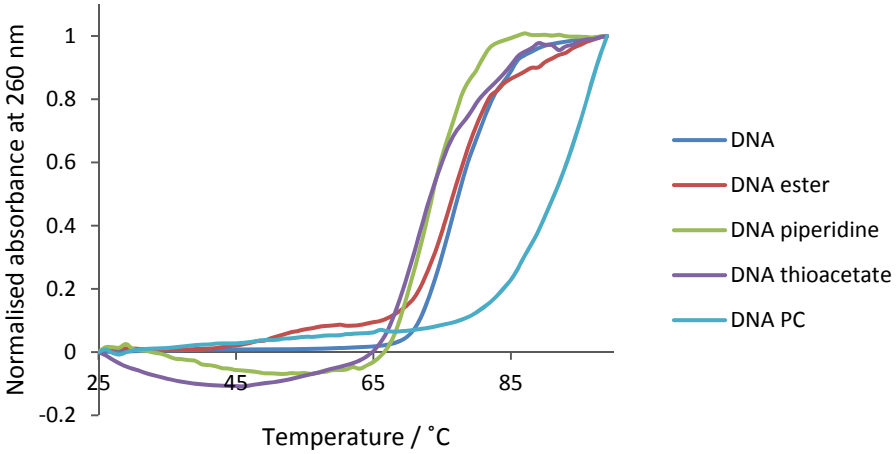

Figure 43: Normalised DNA melting curves for 6:1 ct-DNA (100 µM) /complex solutions at 260 nm

The melting temperature (T_m) of DNA can be calculated from the point where half of the helical structure has unravelled, hence the mid-point of the gradient to each curve. These values were calculated for DNA in the presence of each complex, Figure 44. From these values it can be concluded that the parent cylinder stabilises the DNA structure, whereas the functionalised helicates reduce stability of the DNA to varying degrees.

Cylinder	***T_m***
ct-DNA	80
Parent	91
Ester	79
Piperidine	76
Thioacetate	76

Figure 44: T_m values calculated for each 6:1, ct-DNA (100 µM) / cylinder solution

As stated, these values are gained from measuring the UV-Vis signal at 260 nm, which is a characteristic λmax for ct-DNA. However, this region in the UV spectra is also where peaks from the ligands are found in the spectra on the cylinders alone. This is the reason for differing absorbance's present at the start of the experiments, despite using the same concentrations of DNA in each sample. It was thought that the results shown in Figures 43 and 44 may not show just the stability of DNA, but also that of the complexes. As the solutions are heated, it is likely that the functionalised helicates become unstable and so degrade into the ligand and iron species in solution. As a result, if free ligand were in solution, the UV-Vis absorbance at 260 nm would increase, and so may not be just the result of ss-DNA as assumed above.

The stability of the DNA/complex solutions were further investigated at elevated temperatures, by observing the UV region around the MLCT band, analysing if the iron complex remains intact on heating, Figure 45.

As temperature increased, the intensity of the MLCT bands decreased for each of the iron helicates, with no complex being present over 75 ºC, apart from the parent complex. These results strongly correlate to the apparent T_m of each of the cylinders, with the least stable cylinder, according to the rate at which the λmax at 589 nm decreases, having the lowest T_m. It can therefore be concluded that the stability of the DNA/helicate complexes cannot solely be evaluated using UV melting techniques as results are ambiguous due to cylinder degradation and ligand absorbance overlapping DNA UV signals.

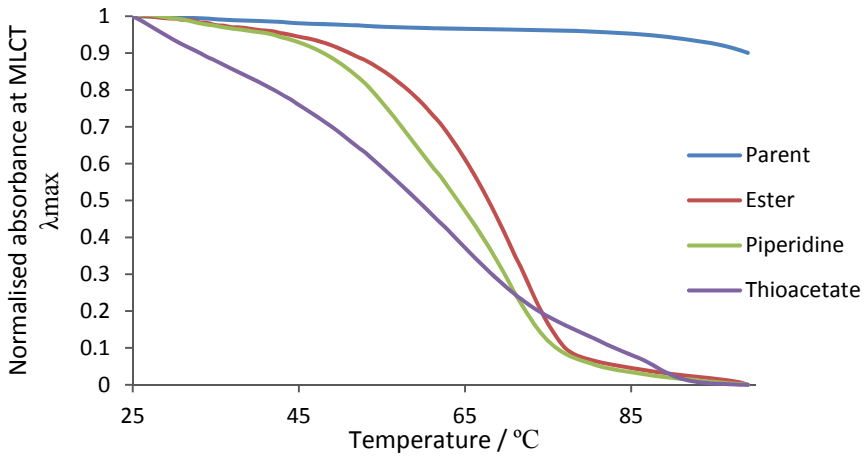

Figure 45: λmax of MLCT band at 589/590 nm with increased temperature

3.5 Ethidium Bromide Displacement

Ethidium bromide, Figure 46, is a cationic dye which intercalates with DNA resulting in a DNA:EB complex which is fluorescent [17]. Displacement of this fluorescent tag by another complex can be used to investigate the intercalating nature of compounds. When ethidium bromide becomes displaced from DNA, it no longer fluoresces; hence the quenching of this system by addition of the click functionalised cylinders was investigated. It is known that the parent cylinder is able to displace this intercalator [18]; hence all results will be compared to the original helicate.

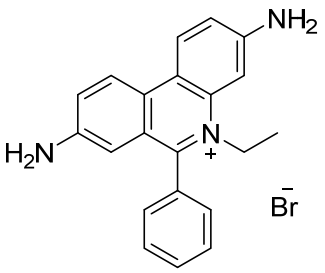

Figure 46: Structure of Ethidium Bromide

a) Parent Cylinder $[Fe_2(L_P)_3]Cl_4$

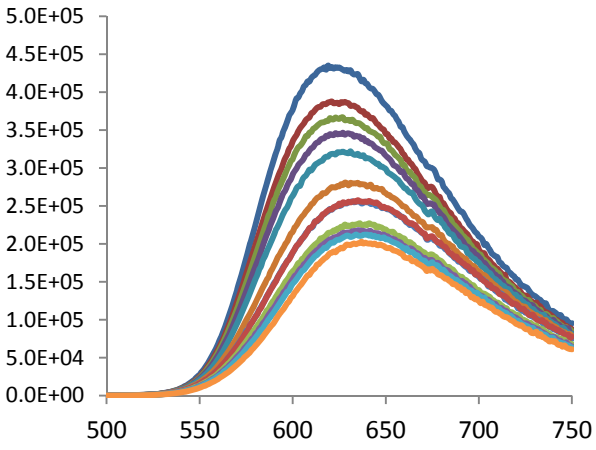

b) Ester Cylinder $[Fe_2(L_{Ester})_3]Cl_4$

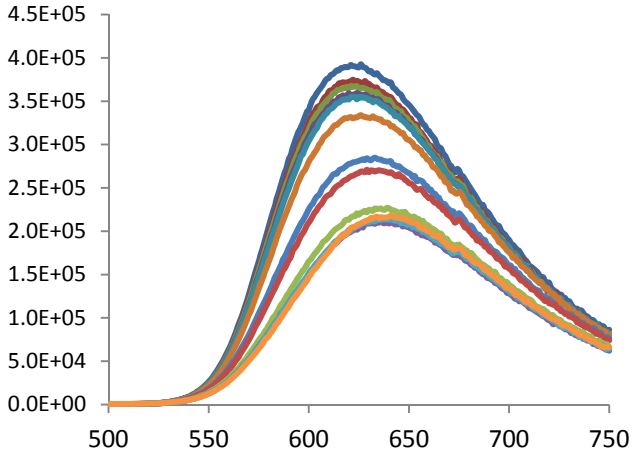

c) Piperidine Cylinder $[Fe_2(L_{Piperidine})_3]Cl_4$

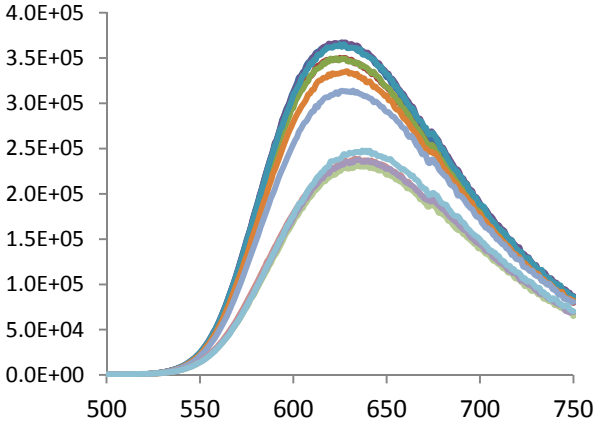

d) Thioacetate Cylinder $[Fe_2(L_{Thioacetate})_3][BF_4]_4$

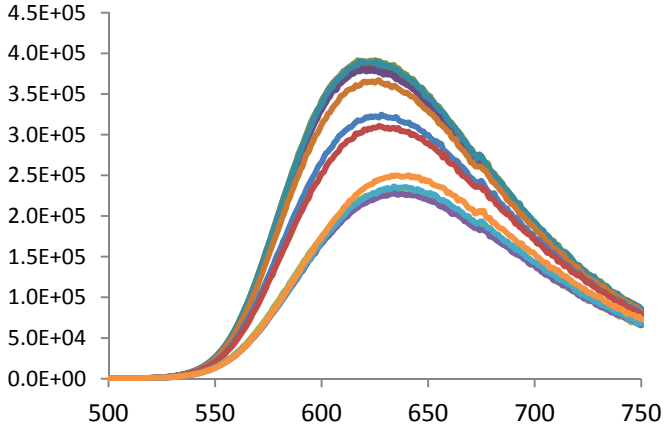

e) Buffer control

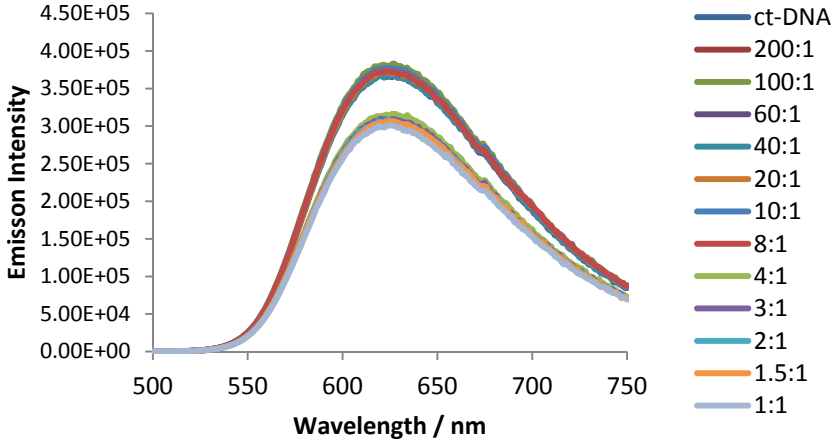

Figure 47: Ethidium Bromide displacement curves, displaying emission signal between 500-750 nm with increasing ethidium bromide (15 µM) : complex ratios of 200:1 to 1:1

On addition of each complex to a solution containing DNA:EB, the fluorescent signal decreased. Whilst titrating in the cylinder solutions, aliquots of DNA:EB were also added to the solution in order to maintain the concentration of ethidium bromide, so any effects on the emission signal would be the result of adding the complex solution. A solution of buffer was also added to the ethidium bromide solution, to determine whether the effects observing were due to the photo-bleaching of the fluorescent tag on repeated exposure to light during the scans. The intensities of λmax over increasing concentrations of ethidium bromide:complex were therefore compared to determine the intercalating ability of the new iron helicates, Figure 48.

As stated, the parent cylinder is known to displace ethidium bromide from ct-DNA and intercalate into the structure. This is observed from the reduction in emission signal from the solution on addition of the parent compound. A gradual decrease is observed, with 43 % of the original emission signal being retained at a 1:1 ratio of EB:parent cylinder.

When only buffer was added to the same solution, the emission signal decreased during the experiment. This indicates that there was some photobleaching of the fluorescent solution as a result of exposure to light on addition of the titration solutions.

On addition of the ester cylinder, $[Fe_2(L_{Ester})_3]Cl_4$, 50 % of the emission signal was lost at 1:1 ratio of EB:complex. This complex exhibits similar activity to the parent cylinder, indicating that on addition of the small ester groups, the chemical properties of this class of compound were not dramatically altered, allowing for intercalation into the DNA structure to still occur.

The cylinders functionalised with piperidine and thioacetate moieties showed little reduction of emission at ratios under 40:1 EB:complex. At higher ratios, a decrease in emission was observed to ~60 % of the original emission signal. This decrease in intercalating ability may be the result of the additional functionality on the cylinders, making the structures too bulky to be

able to intercalate into DNA. It can be concluded however, that these new complexes are less proficient intercalators than ethidium bromide.

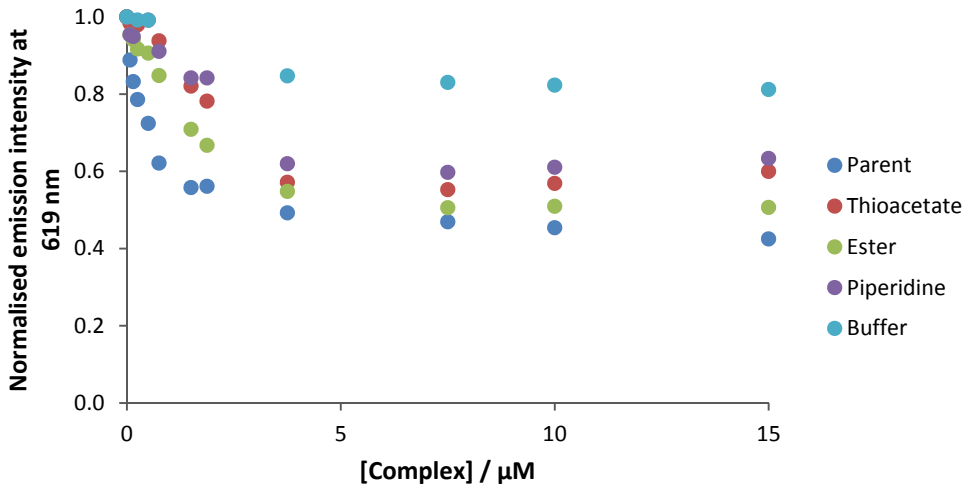

Figure 48: Normalised λmax intensities at 619 nm for DNA:EtBr/complex solutions with increasing concentration of complex

3.6 Hoechst Displacement

Hoechst compounds are blue fluorescent dyes which bind to the minor groove of DNA [19]. They are commonly used in microscopy as nucleus dyes, and can be used to investigate whether compounds are minor groove binders. As a result, it was investigated whether the iron helicate complexes are able to bind to DNA via the minor groove, through measuring displacement of hoechst from a solution of DNA. When Hoechst 33258, Figure 49, is bound to DNA, it has a fluorescent signal [20]. When the hoechst is displaced from the minor groove, the compound is no longer fluorescent. Hence, by titrating compounds into a solution of hoechst and DNA, it can be investigated whether these new iron complex are able to bind in this manner, Figure 50.

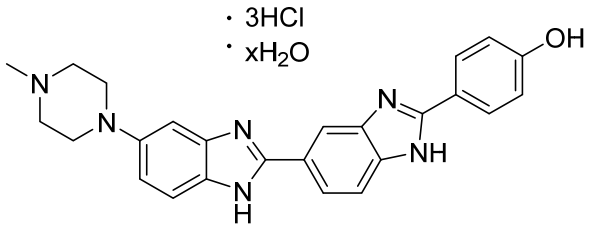

Figure 49: Structure of Hoechst 33258

It has previously been shown that the parent cylinder is able to displace hoechst 33258 from ct-DNA, resulting in loss of fluorescence from the dye. This shows that the cylinder is capable of using the minor groove as a binding site, despite the major groove being the preferred site of binding [7]. This may enlighten to why the parent cylinder is able to bind to, and affect the structure of ct-DNA to such a high degree, consequence of the ability to bind to multiple binding sites.

The displacement of hoechst 33258 was therefore investigated with the three iron helicate complexes previously discussed. They were each titrated into a solution of hoechst/ct-DNA, and the emission signal measure, with increasing ratios of complex:hoechst, Figure 50.

a) Parent Cylinder $[Fe_2(L_P)_3]Cl_4$

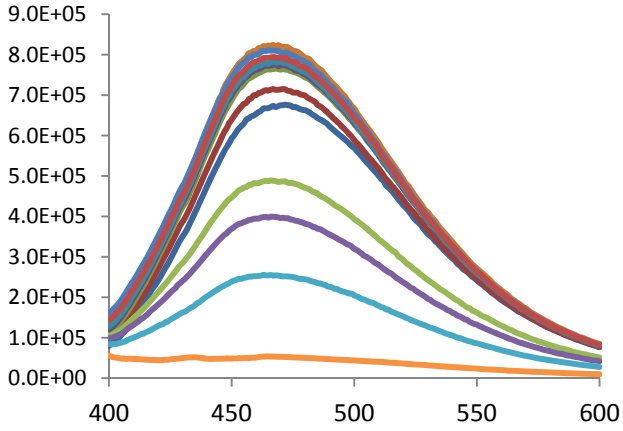

b) Ester Cylinder $[Fe_2(L_{Ester})_3]Cl_4$

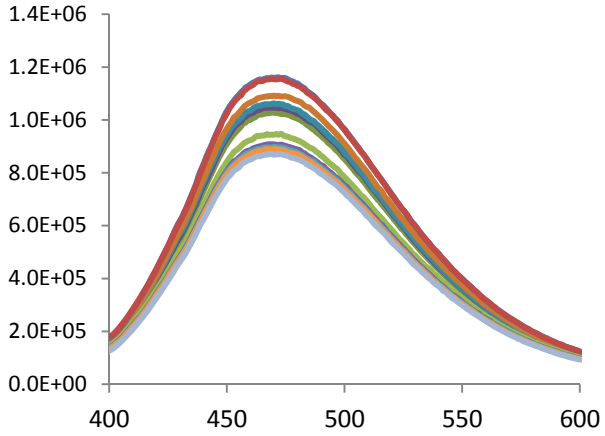

c) Piperidine Cylinder $[Fe_2(L_{Piperidine})_3]Cl_4$

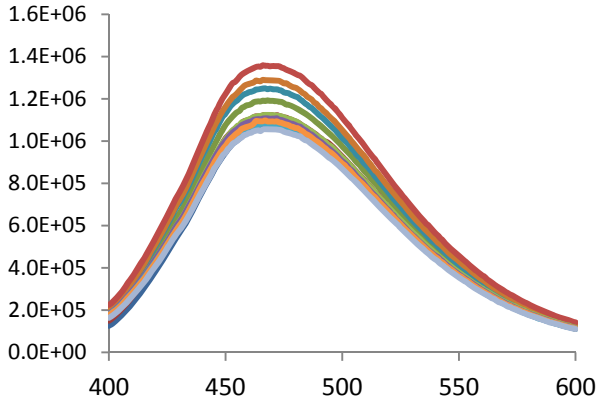

d) Thioacetate Cylinder $[Fe_2(L_{Thioacetate})_3][BF_4]_4$

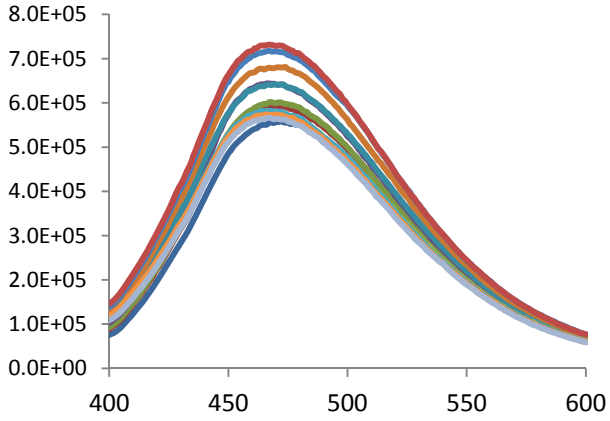

e) Buffer Control

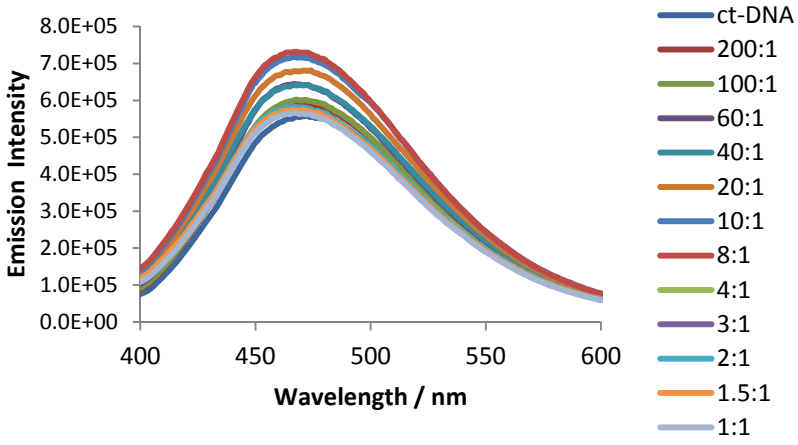

Figure 50: Hoechst displacement curves, legend shows hoechst (1.5 μM):complex ratios

On addition of each complex to the solution of hoechst coordinated ct-DNA, a reduction in emission signal was witnessed. This was compared to just the addition of buffer to the solution, as it is known that hoechst dyes quench easily when exposed to light [20]. On comparison of the λmax intensities, with increasing hoechst:complex ratios, Figure 51, it is apparent that none of the compounds have a large effect on the fluorescence at low concentrations. Only when the ratio reaches >10:1 does displacement occur. This indicates that below these concentrations, the cylinders are not a strong enough minor groove binder in comparison of hoechst for it to be displaced. This reiterates the fact that the parent cylinders preferred binding site is the major groove and not the minor.

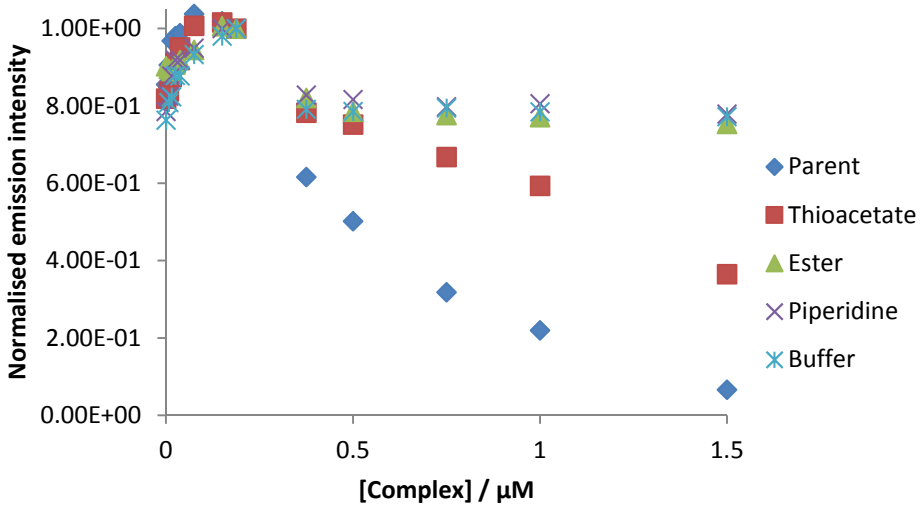

Figure 51: Normalised λmax intensities for DNA:hoechst/complex solutions with increasing concentration of complex

On closer examination of these results, Figure 49, the parent cylinder displaces the most hoechst when a 1:1 concentration is reached. This resulted in virtually no emission signal being recorded, indicating that all hoechst had been displaced under these conditions. It appears that the ester and piperidine functionalised cylinders had no effect on the hoechst fluorescence and the pattern of the curves match that of the buffer experiment. This result may reflect those seen

during CD experiment, *sections 3.1.1* and *3.1.2*. It was concluded that the ester cylinder interacted similarly to the parent cylinder and so is likely to bind to the major groove. And the piperidine cylinder was expected to also bind in the major groove at high concentrations, so any binding of this cylinder at low ratios, may not have been detectable due to other factors, such as fluorescence quenching.

The thioacetate cylinder does show some displacement of hoechst. The reduction in signal equates to 64 % displacement in comparison to the parent cylinder, Figure 52. This may support the results produced from LD, *section 3.2.3*, where the thioacetate cylinder did not show to have a large structural effect on binding to DNA. As previously found [1], it is thought that the dramatic kinking and coiling of ct-DNA that the parent cylinder exhibits is as a result of major groove binding. The slight bending of the DNA exhibited by the thioacetate cylinder may therefore be the result of binding primarily to the minor groove. It can be concluded however, that due to the large functional groups added to the cylinder structure, it is not as good of a minor groove binder as the parent cylinder.

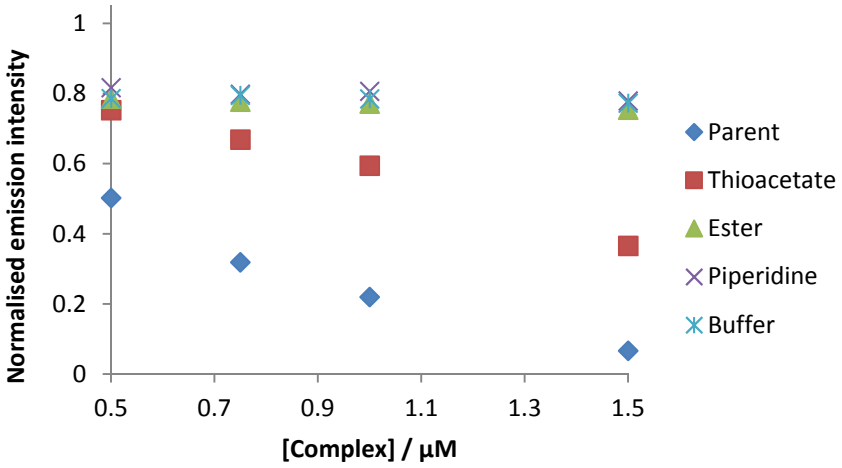

Figure 52: λmax intensities of each complex with increasing ratios of hoechst (1.5 µM):complex from 10:1 to 1:1

3.7 Three Way Junction (3WJ) Studies

As well as double stranded DNA, the parent cylinder has also been shown to interact with other DNA structures. Specifically, it is able to interact and stabilise fork and three way junction (3WJ) structures [2]. Due to the size, shape and charge of the helical structure, it is the perfect fit to stabilise the heart of a 3WJ, Figure 53.

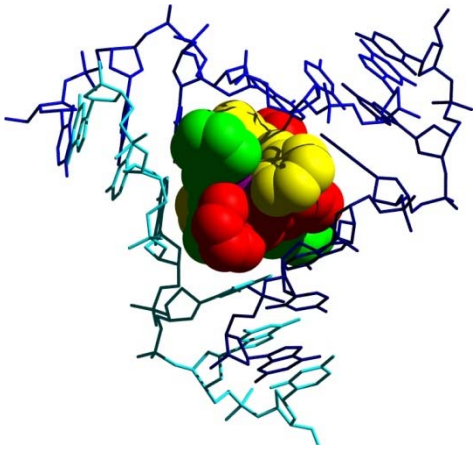

Figure 53: Parent cylinder binding in a 3WJ [reproduced from ref[2]]

The cationic nature of the triple stranded helicate attracts the negatively charged DNA strands, resulting in the stable 3WJ structure forming around the cylinder. The construction of this 3D DNA structure does not occur at room temperature when the cylinder is not present. It was therefore investigated whether the click functionalised cylinders were able to interact with this 3WJ, and whether there was a greater or lesser interaction compared with the parent cylinder as a result of the additional functionality attached to the helicates.

In order to investigate this, polyacrylamide gel electrophoresis was utilised. By radio labelling a strand of DNA with ^{32}P, it is possible to track the formation of varying DNA structures by analysing how they travel through the gel. It was possible to monitor and quantify the degree of 3WJ formation on the addition of each cylinder, through monitoring the location of the radiolabelled DNA stand, Figure 54.

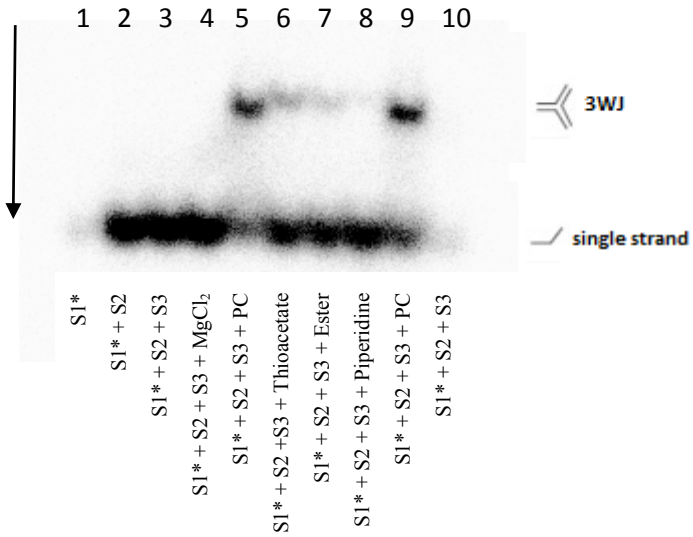

Figure 54: Autoradiogram of PAGE gel demonstrating 3WJ formation in the presence of iron triple stranded helicates at 3:1 DNA strands:complex concentration

In order to form a DNA 3WJ, three complementary strands were incubated with the respective cylinders, before being passed through polyacrylamide gel, which separated the 3WJ structures from the unbound, single stranded (ss) DNA. These single stranded species have a lower molecular weight to the 3WJ/complex conjugates, so travel further through the gel, as demonstrated in Figure 55. By identifying these two structural differences in the gel, the proportion of radiolabelled DNA in each state can be evaluated, and a comparison of the percentage of 3WJ formed can be determined. Each lane corresponds to a different set of experimental conditions, as outlined in Figure 56.

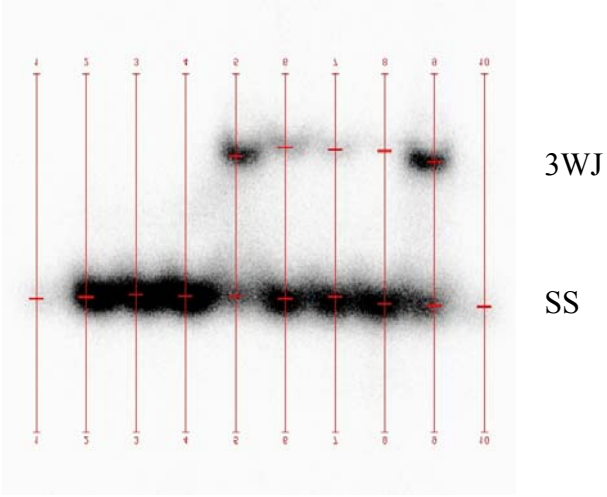

Figure 55: Highlighted view of gel shown in Figure 54, with lane assignment

In lanes 1-4 and 10, no cylinders were present during incubation of the DNA strands. As a result, no 3WJ was formed, or could be detected within the PAGE gel. This corresponds to results previously found using this method [21]. It was found however, that in the presence of each of the cylinders evaluating, some 3WJ species were formed, as determined through the presence of a band in equivalent location to that found when the parent cylinder is present. Through calculating the percentage of radiolabelled DNA present in each band present in the gel, it can be concluded that the functionalised cylinders are unable to stabilise the 3WJ structure to the same degree as the parent cylinder, with the order of cooperation between the DNA strands and the cylinders follow that the parent > thioacetate > ester > piperidine, Figure 56.

Each of the cylinders carries a 4+ charge, so it is likely due to electrostatic interactions that this class of compound is able to encourage formation of the 3WJ. Despite the ester cylinder having the smallest alteration to the original parent cylinder structure, it does not form the greatest amount of 3WJ/complex conjugate. This may indicate that the chemical properties of the cylinder have been altered to hinder the promotion of 3WJ formation. Despite the thioacetate

cylinder being functionalised with a larger group clicked onto the structure, it is able to promote 3WJ formation. This indicates that the shape of the cylinder has only increased on one plane, resulting in the complex being able to still fit within the heart of the junction. These results indicate that as a result of the additional functionalities clicked onto the helicates, the structures are not such a 'perfect fit' as the parent cylinder for this type of DNA interaction [22].

LANE	LANE CONTENT	3WJ	SS-DNA	**% 3WJ**
1	S1*	-	87	-
2	S1* + S2	-	1137	-
3	S1* + S2 + S3	-	1261	-
4	S1* + S2 + S3 + MgCl	-	1408	-
5	S1* + S2 + S3 + $[Fe_2(L_P)_3]Cl_4$	657	558	**54**
6	S1* + S2 + S3 + $[Fe_2(L_{Thioacetate})_3][BF_4]_4$	264	914	**22**
7	S1* + S2 + S3 + $[Fe_2(L_{Ester})_3]Cl_4$	141	750	**16**
8	S1* + S2 + S3 + $[Fe_2(L_{Piperidine})_3]Cl_4$	52	946	**5**
9	S1* + S2 + S3 + $[Fe_2(L_P)_3]Cl_4$	711	525	**58**
10	S1* + S2 + S3	-	82	-

Figure 56: Table showing contents of each gel lane and the quantification of 3WJ formed on cylinder binding

3.8 Cell Studies

Knowing that these click functionalised cylinders are able to interact and cause a structural change to DNA on binding, it was investigated whether they were cytotoxic to various cancer cell lines. By disrupting the structure of DNA, it was hoped that these complexes would be able to cause cell death as a result. The parent cylinder has been shown to enter cells and cause cell death via this manner [4]. In order to analyse cell toxicity, MTT assays were performed using a variety of cancer cells lines, to obtain the relative IC_{50} values for each complex. This technique is a tetrazolium based colorimetric assay, which analyses cell growth through conversion of thiazolyl blue tetrazolium bromide (MTT) to MTT-formazan by mitochondrial dehydrogenase which is present in living cells [23].

Figure 57: Conversion off MTT to formazan via mitochondrial reductase

3.8.1 MTT Assays

MTT assays were performed on two cancer cell lines: **A549**: Human alveolar adenocarcinoma cell line and **MDA-MB-231**: breast cancer cell line.

Through testing the toxicity of each of the iron helicates on different cancer cell lines, it was hoped to identify some selectivity between the different complexes.

24 hr Treatment:

The toxicity of these iron helicates was first analysed after treatment for 24 hours. After this period, a solution of MTT was added to the cells. This, however, showed that the compounds were not toxic to cells as the IC_{50} values were all >100μM. As a result, all future cell studies were performed with 72 hour treatments.

72 hr Treatment:

After treatment for 72 hours, the click functionalised iron helicates were all toxic to cells to varying degrees, Figure 58. All experiments were repeated in triplicate and in both cell lines tested the toxicity of the helicates followed the pattern of thioacetate > piperidine > ester.

For the lung cancer cell line, A549, the parent cylinder appeared most toxic, with it being even more toxic than cisplatin. By functionalising the cylinder, it required at least three times the

concentration to result in cell death. This may indicate that the parent cylinder could be used as a drug candidate for this type of cancer as it is highly active at low concentrations.

For the breast cancer cell line, MDA-MB-231, toxicity of the thioacetate functionalised cylinder was comparable to that of the parent cylinder and cisplatin. This may indicate that the thioacetate cylinder is able to interact with this cancer cell type similarly to the parent complex. The ester functionalised cylinder was half as toxic as these compounds, indicating that this helicate would not be an appropriate drug treatment for these cancer cell lines. The piperidine functionalised cylinder showed it was toxic to this cell line, however, not comparable to the known drug molecule, cisplatin.

Compound	**Cell Type**	
	A549	**MDA**
Parent	**11 ± 4**	**27 ± 3**
Ester	**47 ± 2**	**51 ± 2**
Piperidine	**36 ± 6**	**32 ± 5**
Thioacetate	**31 ± 6**	**23 ± 4**
Cisplatin	**17 ± 4**	**24 ± 1**

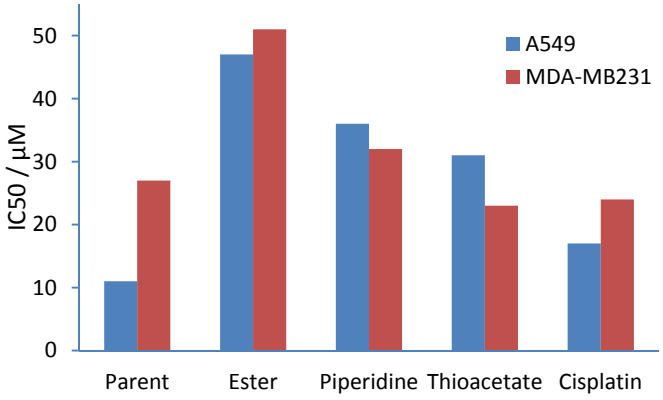

Figure 58: Average IC_{50} values (µM) of iron helicate complexes with respective cell lines

It can be concluded from these toxicity results, that the addition of functional groups to the parent cylinder alters cell toxicity, with varying outcomes depending on how the helicate was functionalised. The ester cylinder appeared to be least active against these cancer cell lines and the thioacetate cylinder being comparably most active, with similar activity to cisplatin when treating a breast cancer cell line.

3.9 Summary

Overall it was found that by functionalising the triple stranded iron helicates described using click chemistry, a range of functional groups could be incorporated into the structure easily, including ester ($[Fe_2(L_{Ester})_3]Cl_4$), piperidine ($[Fe_2(L_{Piperidine})_3]Cl_4$) and thioacetate $[Fe_2(L_{Thioacetate})_3][BF_4]_4$ moieties. In doing so, the fundamental DNA binding properties of such triple stranded iron helicates was retained, with each new complex showing some binding interaction with DNA. On addition of these different moieties the physical and chemical properties of the compounds were manipulated, with a decrease in stability and solubility in aqueous solution being observed compared to the parent compound. Despite this, each novel complex interacted with ct-DNA and were able to stabilise DNA 3WJ formation. It was also shown that the functionalised supramolecular helicates were toxic towards cancerous cell lines, to varying degrees, and as such show promising results towards the aims of this research.

3.9.1 Ester Cylinder, $[Fe_2(L_{Ester})_3]Cl_4$

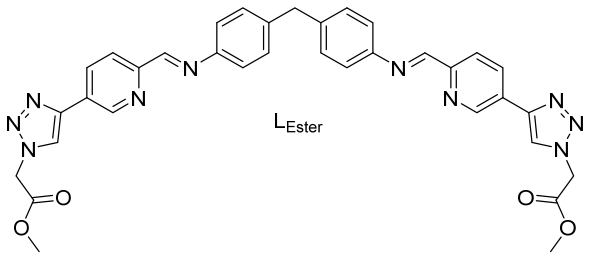

L_{Ester}

The ester functionalised cylinder, $[Fe_2(L_{Ester})_3]Cl_4$, was soluble in methanol and partially soluble in acetonitrile, which allowed for the complex to be dissolved in aqueous solution, meaning that the interactions between this complex in different biological systems could be investigated.

It was found that this cylinder complex interacted with ct-DNA to induce a CD signal as a result of DNA/cylinder interactions. On addition of $[Fe_2(L_{Ester})_3]Cl_4$ to a solution of ct-DNA, orientation of the genomic DNA was reduced as a result of the kinking and coiling of ct-DNA

occurring on complex binding. The presence of an induced LD signal indicated that the cylinder incurs a specific binding mode when interacting with ct-DNA, likely to be major groove binding which is backed up through the lack of ethidium bromide and hoechst displacement observed. On binding to ct-DNA, stability of the cylinder was increased, however it was found that the P enantiomer had a lower affinity to ct-DNA compared with the M, resulting in an enantiomeric excess of the M conformer over time.

As well as interacting with ct-DNA, this complex was also able to stabilise a DNA 3WJ. Through addition of the ester groups, however, it was found that the complex became least toxic towards certain cancer cell lines, compared to the parent and other newly functionalised cylinders.

3.9.2 Piperidine Cylinder $[Fe_2(L_{Piperidine})_3]Cl_4$

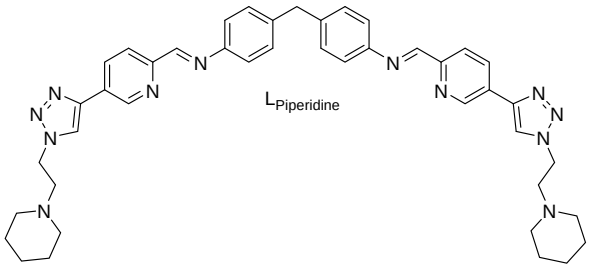

The piperidine cylinder, $[Fe_2(L_{Piperidine})_3]Cl_4$, was soluble in methanol, however addition of the piperidine groups made it the least soluble of those new cylinders analysed, as such slightly higher ratios of solvent were required to dissolve the complex in aqueous solution. On addition of this compound to ct-DNA an induced CD signal was produced, indicating a binding interaction was occurring between the two species. No induced LD signal was observed on titrating $[Fe_2(L_{Piperidine})_3]Cl_4$ with ct-DNA, showing that the complex did not become orientated in solution, indicating that the binding interaction with DNA was not specific. Despite this, orientation of the ct-DNA was greatly reduced on addition of this cylinder, comparable to that of the parent cylinder, indicating that a structural change was occurring.

Through lack of ethidium bromide and hoechst displacement, it was theorised that the complex bound to ct-DNA via major groove binding, with the side chains being able to interact with the sugar backbone of DNA.

Very little 3WJ structure was stabilised by this cylinder, likely due to the bulky side chains added when functionalised. Cell toxicity was reduced slightly compared to that observed for the parent cylinder, however, the complex was still able to enter the cancerous cells to induce cell death.

3.9.3 Thioacetate Cylinder $[Fe_2(L_{Thioacetate})_3][BF_4]_4$

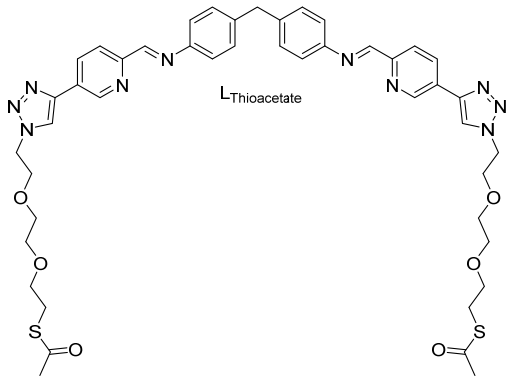

The thioacetate cylinder, $[Fe_2(L_{Thioacetate})_3][BF_4]_4$, was highly soluble in acetonitrile, allowing for dilution into aqueous solution for biological studies. On addition of this complex to ct-DNA, induced peaks were observed within the CD and LD spectra. This indicated that the cylinder was binding to ct-DNA via a specific binding mode and causing a structural change.

It was theorised that this iron helicate binds to ct-DNA via the minor groove. This was indicated by the compounds ability to displace hoechst from ct-DNA and through the lack of kinking/coiling of DNA observed in the LD spectrum. Both results are indicators that the complex is able to bind into the minor groove of DNA, which would suggest that the long chains added to the cylinder structure have resulted in this altered binding mode.

The complex was able to stabilise DNA 3WJ structures, showing that the long side chains did not dramatically alter the height of the complex which is known to be crucial in its ability to

enter the central cavity and stabilise such structures. It was also found that this compound had similar toxicity results to those observed with the parent cylinder towards cancer cell lines. As such, addition of the thioacetate group via click chemistry to the helicate structure has altered the binding affinity/mode to DNA, compared to the parent cylinder, yet has maintained the toxic nature desired from this class of compounds. By incorporating this moiety into the structure, a sulphur atom has been introduced which can consequently be used to explore the limitations of this complex further, through AuNPs interaction (*Chapter 4*).

3.10 References

1. M. J. Hannon, V. Moreno, M. J. Prieto, E. Moldrheim, E. Sletten, I. Meistermann, C. J. Isaac, K. J. Sanders and A. Rodger, *Angew. Chem. Int. Ed*., 2001, **40**, 879- 884
2. A. Oleksi, A. G. Blanco, R. Boer, I. Usón, J. Aymamí, A. Rodger, M. J. Hannon and M. Coll, *Angew. Chem. Int. Ed*., 2006, **45**, 1227- 1231
3. H. Yu, X. Wang, M. Fu, J. Ren and X. Qu, *Nucleic Acids Res.*, 2008, **36**, 5695–5703
4. A. C. G. Hotze, N. J. Hodges, R. E. Hayden, C. Sanchez-Cano, C. Paines, N. Male, M-T. Tse, C. M. Bunce, J. K. Chipman and M. J. Hannon, *Chem. Biol.*, 2008, **15**, 1258-1267
5. A. Rodger and B. Nordén, Circular Dichroism & Linear Dichroism, Oxford University Press Inc., New York, 1997
6. V. I. Dodero, Z. B. Quirolo and M. A. Sequeira, *Front. Biosci.*, 2011, **16**, 61-73
7. I. Meistrmann, V. Moreno, M. J. Prieto, E. Moldrheim, E. Sletten, S. Khalid, P. M. Rodger, J. C. Peberdy, C. J. Issac, A. Rodger and M. J. Hannon, *Proc. Natl. Acad. Sci. USA*, 2002, **99**, 5069-5074
8. J. Norman, *PhD Thesis*, U. Birmingham, 2012
9. J. M. Berg, J. L. Tymoczko, L. Stryer, Biochemistry. 5th Ed., W. H. Freeman, New York, 2002, Section 27.1

10. J. E. Reed, A. A. Arnal, S. Neidle and R. Vilar, *J. Am. Chem. Soc.*, 2006, **128**, 5992-5993
11. R. Marington, T. R. Dafforn, D. J. Halsall, J. I. MacDonald, M. Hicks and A. Rodger, *Analyst*, 2005, **130**, 1608–1616
12. A. Rodger, K. J. Sanders, M. J. Hannon, I. Meistermann, A. Parkinson, D. S. Vidler, I. S. Haworth, *Chirality*, 2000, **12**, 221-236
13. A. Rodger, R. Marrington, M. A. Geeves, M. Hicks, L. de Alwis, D. J. Halsalld and Timothy R. Dafforn, *Phys. Chem. Chem. Phys*., 2006, **8**, 3161–3171
14. L. Cardo, V. Sadovnikova, S. Phongtongpasuk, N. J. Hodges and M. J. Hannon, *Chem. Commun.*, 2011, **47**, 6575-6577
15. J. M. Kelly, A. B. Tossi, D. J. McConnell and C. OhUigin, *Nucleic Acids Res.*, 1985, **13**, 6017- 6034
16. M. F. Ottaviani, F. Furini, A. Casini, N. J. Turro, S. Jockusch, D. A. Tomalia and L. Messori, *Macromolecules*, 2000, **33**, 7842-7851
17. V. A. Izumrudov, M. V. Zhiryakova and A. A. Goulko, *Langmuir*, 2002, **18**, 10348-10356
18. J. Malina, M. J. Hannon and V. Brabec, *Nuc. Acids Res.*, 2008, **36**, 3630-3638
19. P. E. Pjura, K. Grzeskowiak and R. E. Dickerson, *J. Mol. Biol.*, 1987, **197**, 257-271
20. F. G. Loontiens, P. Regenfuss, A. Zechel, L. Dumortier and R. M. Clegg, *Biochemistry*, 1990, **29**, 9029-9039
21. J. Malina, M. J. Hannon and V. Brabec, *Chem. Eur. J.*, 2007, **13**, 3871-3877
22. L. Cerasino, M. J. Hannon and E. Sletten, *Inorg. Chem.*, 2007, **46**, 6245-6251
23. G. Ciapetti, E. Cenni, L. Pratelli and A. Pizzoferrato, *Biomaterials*, 1993, **14**, 359-364

Chapter 4

Gold Nanoparticle/Helicate Interactions

The research area of nanomedicine is being applied to a range of fields including drug delivery, biodiagnostics, therapeutics and biomedical imaging [1, 2]. Nanoparticles in particular, have unique properties which are anticipated could have the potential to eradicate limitations of conventional treatments such as bioavailability and toxicity [3, 4], through targeted delivery and proficient bioaccumulation. Of these, gold nanoparticles (AuNPs), are the most stable metallic nanoparticle [5, 6].

For this research spherical AuNPs were utilised, as they are easily synthesised [7] and extensive research has previously been performed on such particles [8]. Research has shown that AuNPs can be easily up taken in mammalian cells [9, 10] and are able to accumulate in cancer cells [11] and depending on their size and charge, can amass in different organs [12]. As such the use of such particles may allow for targeted drug delivery to specific cancer cell lines.

4.1 Research Objective

The aim of this project was to attach the know iron(II) helicate structure, discussed in previous chapters, to the surface of AuNPs. By attaching many cylinders to the gold surface, it is hoped that high concentrations of complex can be achieved in aqueous solution, resulting in numerous interactions occurring with DNA simultaneously, as with multiple zinc fingers on a protein surface [13]. Consequently, it was anticipated that the intramolecular coiling and kinking affect seen with this class of compound [14] may be enhanced and as such, DNA replication could be inhibited; resulting in a potential anticancer treatment. On addition of this complex to AuNPs, it is also anticipated that the nanoparticles can be used as a targeting delivery devise towards

cancerous cell lines [9-11]. As nanoparticles are shown to accumulate in cancerous cells, this may result in an increased potency of the complex as an anticancer agent, as well as reducing the possible toxicity effects towards healthy cell lines.

It will be attempted to attach the parent cylinder $[Fe_2(L_P)_3]Cl_4$ ($L_P = C_{25}H_{20}N_4$), to the surface of AuNPs via two methods. Firstly, it will be attempted to attach the complex using electrostatic interactions, between the tetracationic charge of the cylinder and the negatively charged nanoparticle surface. Addition of a positively charged compound onto the stabilised gold surface will reduce the overall stabilising charge on the nanoparticle, which could lead to aggregation of the nanoparticles, so it is possible this may not be a viable method.

Secondly, the iron cylinder will be attached to AuNPs via sulphur linkers. The thioacetate cylinder $[Fe_2(L_{Thioacetate})_3][BF_4]_4$ ($L_{Thioacetate} = C_{45}H_{50}N_{10}O_6S_2$) synthesised and discussed in *chapters 2 and 3*, has an additional side arm linked onto the ligand which contains a sulphur group. It will therefore be attempted to attach this cylinder onto the nanoparticle surface by adsorption [15], Figure 1. The resulting functionalised nanoparticles will then be tested for their effects on DNA with a hope that the cylinder is still be able to interact with DNA structures to cause a structural change. As many cylinders will be attached to the gold surface, it is anticipated that the effects currently observed between such structures and DNA, *chapter 3*, will be enhanced as a result of incorporating with nanotechnology.

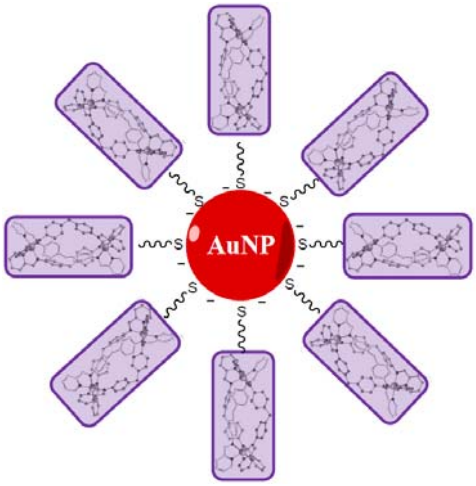

Figure 1: Schematic drawing of the Fe(II) cylinder interacting with the surface of a AuNP

4.2 Gold Nanoparticles

4.2.1 Gold Nanoparticle Synthesis

The synthesis of citrate coated gold nanoparticles, cAuNPs, by the Turkevich method is a well-known process [7] whereby spherical, monodispersed particles can be synthesised in aqueous solution using a simple technique. The citrate ions act as both a reducing and capping agent, hence the concentration of reagents and reaction time given, govern the particle size synthesised, with a higher concentration of reducing agent giving a smaller particle size [16, 17].

For this research nanoparticles of approximately 16 nm in diameter were synthesised, as research into functionalising such particles for use in anticancer research has previously been performed [8-11]. Citrate coated AuNPs are very stable as the negative charge of the citrate coating causes repulsion between the particles, ensuring they do not aggregate in solution and remain a colloidal suspension.

For that reason, a solution of gold(III) chloride, $HAuCl_4.3H_2O$, (1 mM, 100 mL) was reacted with sodium citrate, $Na_3(C_6H_5O_7).2H_2O$, (38.8 mM, 10 mL) to reduce the Au^{3+} to colloidal Au^0. To the vigorously stirred, boiling solution of $HAuCl_4$, the reducing agent was added. This

mixture was heated for 10 mins and then stirred without heat for a further 15 mins. Adding the citrate solution into the centre of the vortex of the stirring Au^{3+} solution aided formation of uniform AuNPs. This resulted in a deep red solution with a UV λmax absorption of 524 nm, which is the characteristic surface plasmon resonance (SPR) of such cAuNP, Figure 2. The cAuNPs were further tested for their size, stability and appearance using dynamic light scattering (DLS), zeta potential and transmission electron microscopy (TEM) respectively.

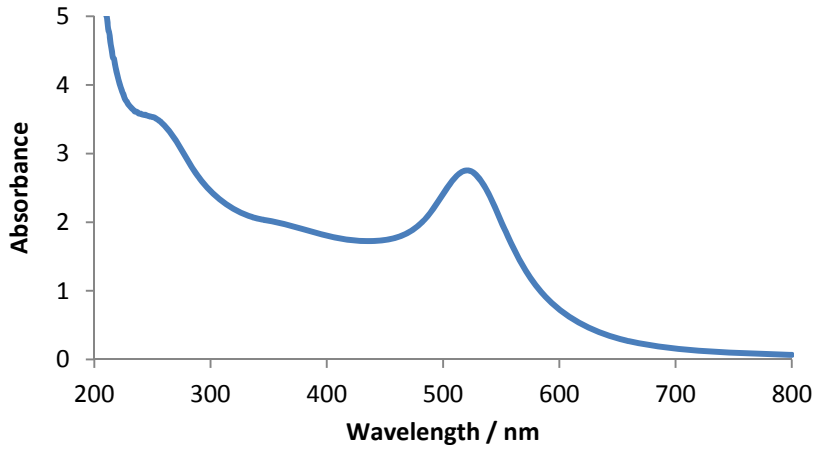

Figure 2: UV spectrum of citrate coated AuNPs (2.5 nM)

4.2.2 Gold Nanoparticle Analysis

4.2.2.1 Dynamic Light Scattering (DLS)

DLS measures the light scattered from particles moving in Brownian motion and relates this to particle size; with smaller particles having a larger Brownian motion causing laser light to be scattered at different intensities. This is then corresponded to the size of particle using the Stokes-Einstein relationship, resulting in a size distribution profile of the nanoparticles in suspension [18, 19].

This technique uses a number of assumptions to produce this derivative. Firstly that the particles are in Brownian motion, so a probability density function can be used, Eq.1. Secondly that the

particles are spherical, so the Stoke-Einstein equation can be used; Eq. 2, to gain the diffusion constant and subsequently information on the particle radius.

$$P(r) = (4\pi Dt)^{-3/2} \exp(-\frac{r^2}{4Dt}) \qquad \text{(Eq. 1)}$$

$$D = \frac{kT}{6\pi\eta R} \qquad \text{(Eq. 2)}$$

Equations used within DLS measurements, where: D: diffusion coefficient, k: boltzmann constant, T: temperature, η: viscosity, R_H: hydrodynamic radius

When assuming the sample measured relates only to spherical material, it may result in bias or inaccurate results being given. Figure 3 demonstrates how the data could be misinterpreted, given different sample situations. For this project, it is expected that the nanoparticles made were spherical, and it is desired to analyse the change in size of these particles when the surface is functionalised, Figure 3 (a), so any anomalous data would likely be the result of aggregated species, Figure 3 (c), or foreign particles such as dust.

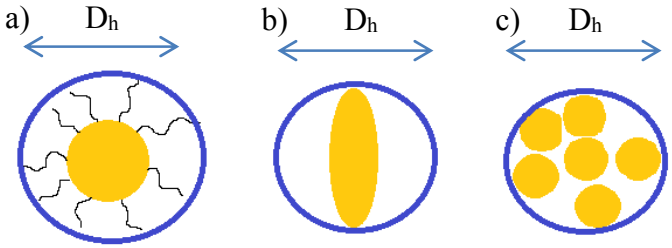

Figure 3: Hydrodynamic radius presumptions a) functionalised nanoparticles, b) non-spherical particles, c) aggregates

The technique is easily performed, simply by measuring the light scattered by particles present in solution. The instrumentation then manipulates the data, as described above, to fit data to corresponding diameter values, Figure 4. This is a very fast and reproducible technique which requires simple sample preparation and hence is a standard technique used to analyse

nanoparticles [20]. DLS is an ideal technique to analyse how functionalising nanoparticles can affect their physical properties [21]. By comparing results from different samples, a size change in the particles in colloidal suspension can indicate if functionalization of particles has been achieved, and so was used throughout this research to investigate how gold nanoparticles were altered in appearance and behaviour when exposed to different functionalities.

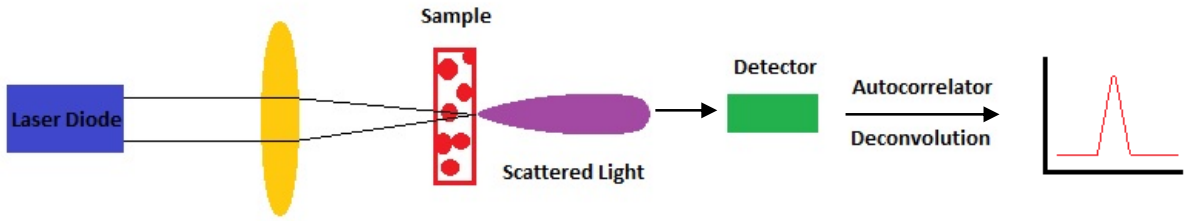

Figure 4: Schematic showing basic experimental procedure of DLS [reproduced from ref[22]]

DLS results for cAuNPs:

Distribution: Intensity: 25.70 ± 10.01 nm Cumulant Diameter: 26.20 nm

Volume: 17.44 ± 6.199 nm Polydispersity Index: 0.545

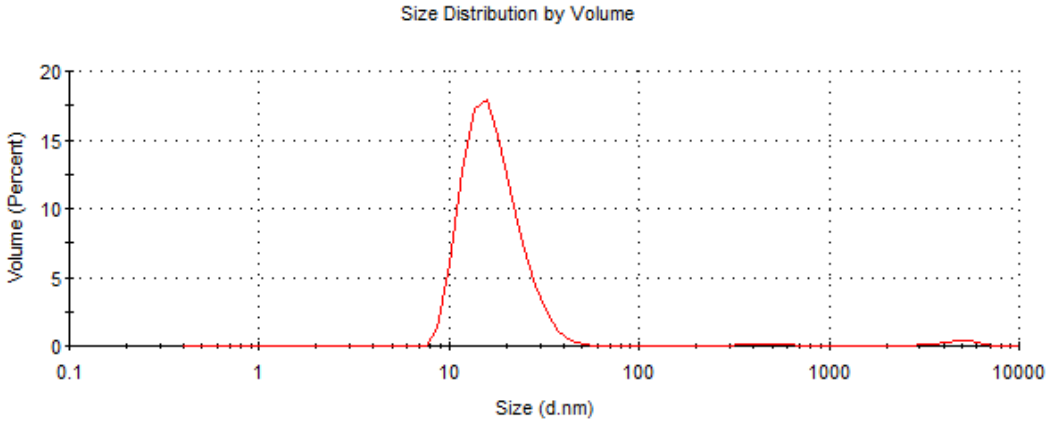

Figure 5: Spectral data showing the size distribution of citrate nanoparticles, cAuNPs

DLS results, Figure 5, indicate that the majority of the particles synthesised were ~17 nm in diameter, with some larger impurities present. These may have resulted from the synthesis,

despite the sample being filtered twice before taking the measurements, or could potentially have been a result of the test solution being too concentrated.

4.2.2.2 Zeta (ζ) Potential

Zeta potential is the measure of electrokinetic potential within a colloidal system. The potential difference measured is that between the polar solvent, typically water, and the charged area surrounding the surface of the nanoparticles is measured [23], Figure 6 [24].

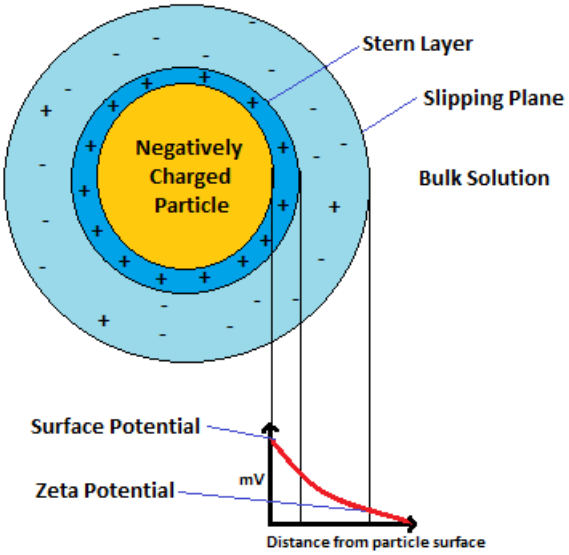

Figure 6: Potential difference as a function of distance from a charged particle surface, suspended in solution [reproduced from ref[24]]

This technique is used to determine the charge state of nanoparticle surfaces and the stability of particles in solution. These are indicated by the sign and magnitude of the measurement, with the sign indicating whether the surface is positively (+) or negatively (-) coated. The greater the magnitude of ζ potential, the higher the stability, as a larger potential difference is present between the particle surface and surrounding solution, creating a bigger repulsive force between particles, making them more stable [25].

It is considered that particles with a ζ potential magnitude of 30 mV are moderately stable. The closer to zero the ζ potential gets, the less stable the particles become and more likely they will flocculate and aggregate over time, Figure 7. This is due to there being less potential difference between particle surfaces within solution, allowing for the interactions with neighbouring particles.

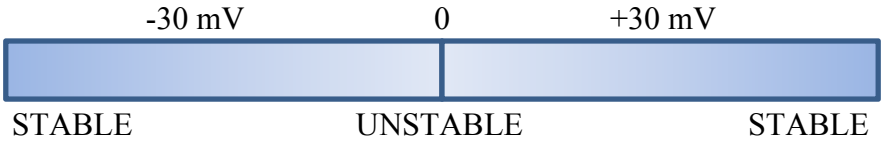

Figure 7: Zeta potential values related to stability

It is important that colloidal systems are stable over time, as instability can lead to aggregation of particles, which may result in sedimentation and the ultimate phase separation of the particles and solution, Figure 8 [26]. As such, the colloidal suspension would no longer have the desired characteristics, becoming irreversibly coagulated deeming them useless. Consequently, stability of the AuNPs was closely monitored on surface modification, ensuring that despite altering the surface functionality of the particles, the desired characteristics and reason for utilising these colloids, will be maintained.

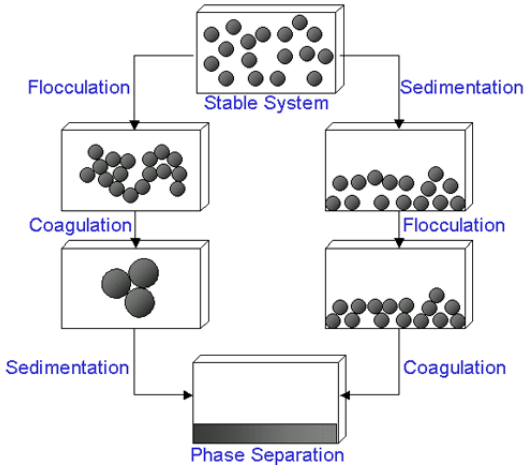

Figure 8: Schematic diagram demonstrating variation in colloidal stability [reproduced from ref[26]]

Zeta Potential results for cAuNPs:

ζ Potential (mV): -43.2 ± 17.9

Conductivity (mS/cm): 0.761

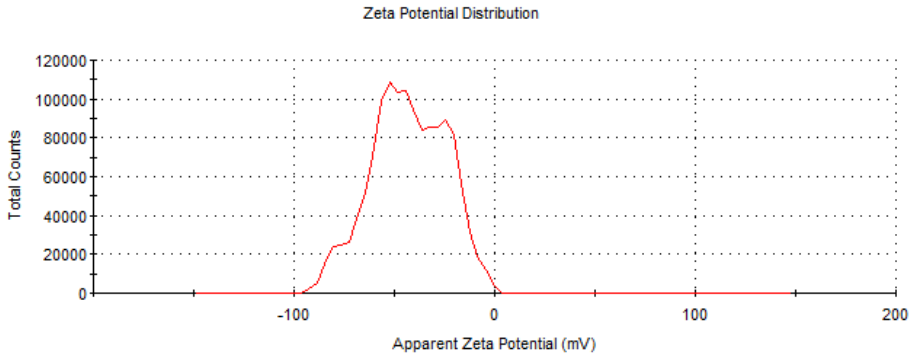

Figure 9: Spectral data showing the zeta potential distribution of cAuNPs

Zeta potential experiments were repeated three times to ensure reliable results. Figure 9, shows typical results for cAuNPs, with a value of -43 mV, indicating very stable nanoparticles in solution. The negative value is due to the citrates on the surface of the gold being in a deprotonated state, with three COO^- groups capping and stabilising the nanoparticles.

4.2.2.3 Transmission Electron Microscopy (TEM)

Transmission electron microscopy (TEM) is a technique where an electron beam is transmitted through an ultra-thin specimen, generating a high resolution image which is highly magnified. This technique can therefore be used to image nanoscale material, and is ideal to analyse cells and nanoparticles [27].

TEM has a range of applications including in cancer research [28], nanotechnology [29] and materials science [30]. However, there are some limitations to this technique. There is a low throughput of samples, with time consuming sample preparation and sample scanning. The field of view observed is relatively small, so the region being analysed may not represent the entire

sample. In the case of biological samples the electron beam may also damage or alter samples, giving unreliable data. Despite this, it is a technique routinely used to analyse the morphology of nanoparticles.

For this work, TEM was used to gain additional knowledge on the size, shape and overall morphology of nanoparticles synthesised. Particle size and shape have been found to have a key role in bio-distribution [31], so uniform, un-aggregated particles are desired.

TEM results for cAuNPs:

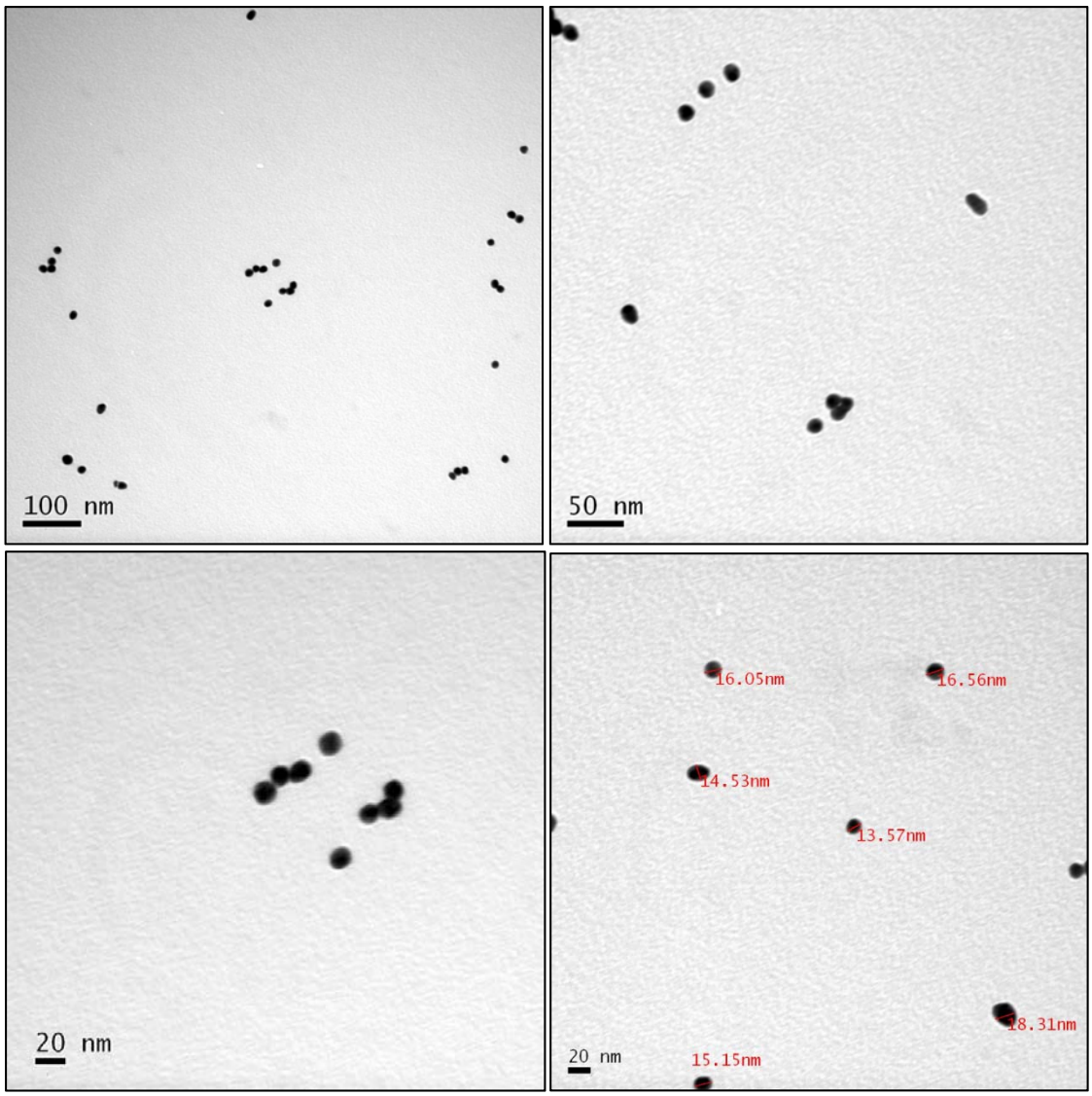

Figure 10: TEM images of citrate coated gold nanoparticles, showing representative particles from two samples at a variety of magnifications

From TEM images of cAuNPs, Figure 10, it was observed that uniform nanoparticles of circular morphology were formed during synthesis using the Turkevich method. The size range appeared to be ~16 nm which corresponds to those results found using DLS and UV-Vis. As a result of these findings, these AuNPs were used for further research, to investigate if they could successfully be functionalised with triple stranded iron helicates.

4.3 Combining Gold Nanoparticles with Supramolecular Helicates

4.3.1 Parent Cylinder

The cAuNPs discussed are capped with citrate molecules which surround the particles with a negative charge; stabilising them in solution. It was therefore investigated whether complexes could be attached to the surface simply through electrostatic interactions [32, 33].

Within the Hannon group, the triple stranded iron helicate $[Fe_2(C_{25}H_{20}N_4)_3]^{4+}$ was developed, Figure 11 [34]. This is a tetracationic species which demonstrates unique interactions with negatively charged DNA structures, and so has the potential to interact with the negatively charged surface of nanoparticles.

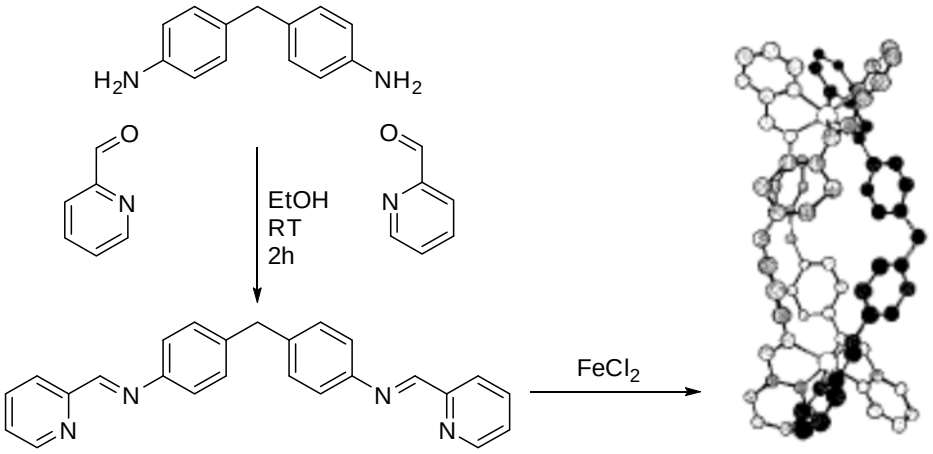

Figure 11: Formation of the ligand and model structure of the tetracationic triple stranded supramolecular cylinder $[Fe_2(L_P)_3]Cl_4$ [reproduced from ref[34]]

By adding this cationic complex to a solution of cAuNPs, it was predicted that coagulation may occur as a result of adding a positively charged molecule to the negative nanoparticles. This will decrease the overall charge on the particle surface, resulting in the zeta potential becoming closer to 0 mV. As this occurs, the colloidal system becomes less stable, leading to aggregation and causing particles to sediment out of solution. This effect will be directly affected by the concentration of both species.

This concept was therefore tested by adding small quantities of parent cylinder to cAuNPs, Figure 12. By observing the addition of a peaks at wavelengths >520 nm, aggregation of the nanoparticles can be analysed, signals appearing in this region will imply that large aggregate species have been formed.

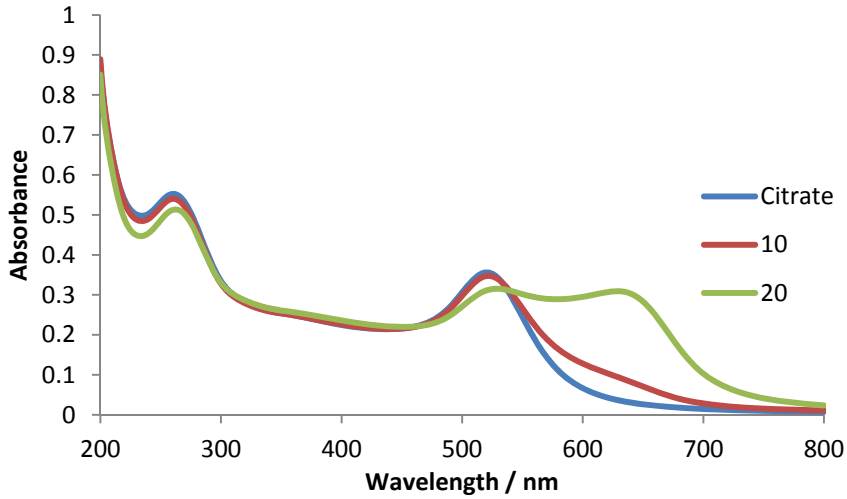

Figure 12: UV-Vis spectra of cAuNPs (0.5 nM) with the addition of $Fe_2(L_P)_3]Cl_4$ (10 μM). Legend indicates volume of $Fe_2(L_P)_3]Cl_4$ added to cAuNPs (μL)

To cAuNPs (0.5 nM, 1 mL) [35], 10 μL aliquots of $[Fe_2(L_P)_3]Cl_4$ (10 μM) in water were added. After only two additions of complex to nanoparticles, the solution turned from red in colour to black with precipitate formation. The characteristic SPR peak at 524 nm of the citrate nanoparticles shifted to 645 nm. This broadening and shifting of the UV peak is characteristic

of aggregated nanoparticles, showing that adding a tetracationic complex to citrate coated AuNPs is not a viable technique to functionalise the nanoparticle surface.

4.3.2 Surfactant Coated Gold Nanoparticles, ZAuNPs

As the aim of this research is to functionalise AuNPs with the tetracationic cylinders developed within the Hannon group, a method of stabilising nanoparticles to circumvent aggregation was investigated.

Zonyl FSA is a fluorosurfactant which has been used to stabilise AuNPs by other research groups [36], to allow for them to be functionalised with positive substituents. This surfactant is able to coat cAuNPs, increasing the repulsion between nanoparticles, making them more stable.

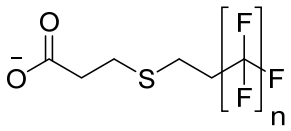

Figure 13: Zonyl FSA fluorosurfactant

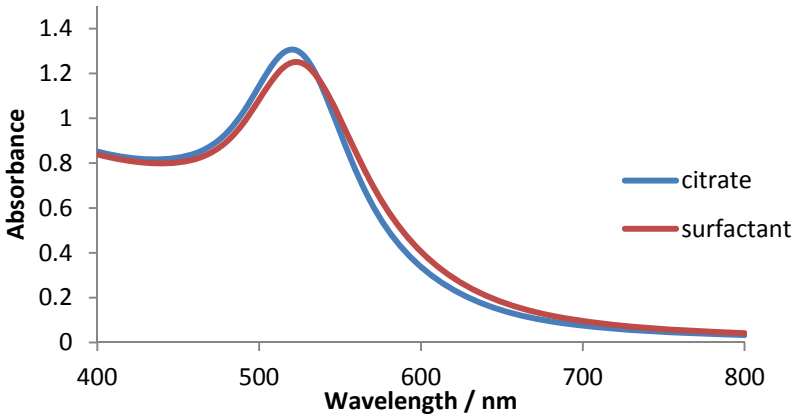

Figure 14: UV spectra of citrate (cAuNPs) and surfactant coated AuNPs (1 nM)

It was found that when only 2 µL of the surfactant solution had been added to the cAuNPs (1 mL), the nanoparticles appear fully coated as no further shift to the SPR was observed. With this addition, the λmax of the nanoparticles shifted from 524 nm to 527 nm. This corresponds

to the functionalisation of the nanoparticle surface, hence this ratio of solutions was used for all future experiments performed with 'zonyl' coated nanoparticles (ZAuNPs).

As discussed, it is known that the use of this surfactant stabilises nanoparticles, which can be observed through further zeta potential analysis, Figure 15.

ζ Potential (mV): -52.9 ± 12.7

Conductivity (mS/cm): 0.0384

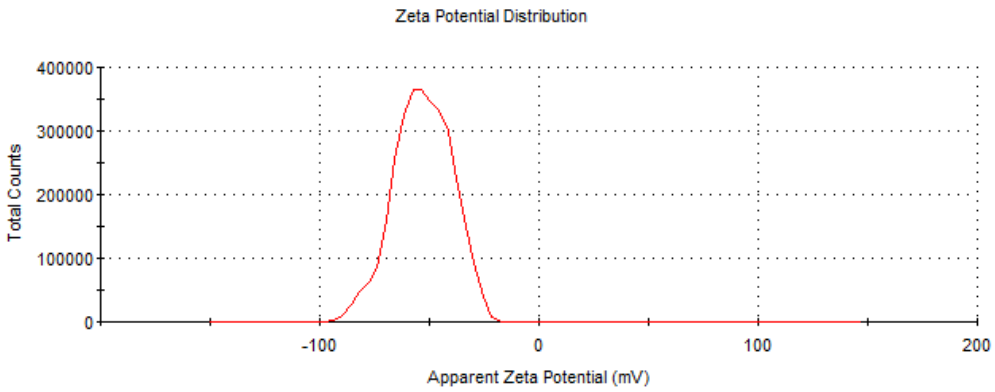

Figure 15: Zeta potential distribution of ZAuNPs

On addition of the surfactant, where a solution of cAuNPs containing the surfactant was stirred overnight, followed by purification by centrifugation, the ζ potential decreased by a ~10 mV. This implies that the nanoparticles will be more stable than the citrate coated, and hence should be able to withstand a higher concentration of cationic species on the surface before aggregation occurs.

The size of the nanoparticles was not greatly increased on the addition of the surfactant, as indicated by the DLS results, Figure 16.

Size Distribution: Intensity: 34.32 ± 13.67 nm Cumulant Diameter: 47.73 nm

Volume: 23.86 ± 7.78 nm Polydispersity Index: 0.770

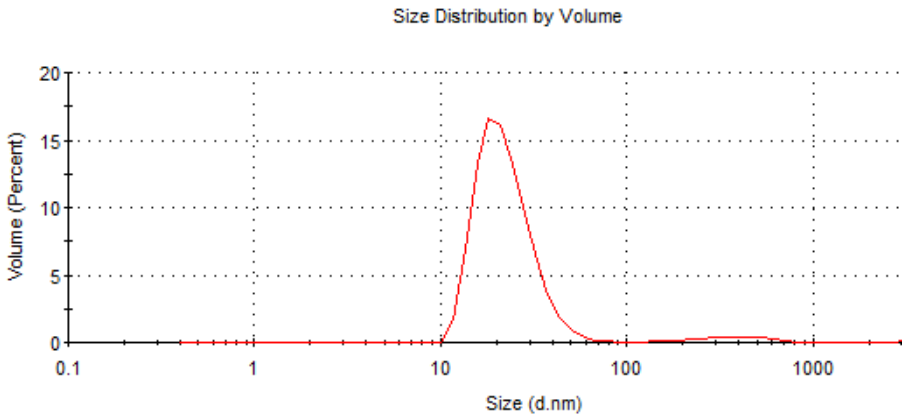

Figure 16: DLS results for ZAuNPs

DLS results show slightly higher diameter readings for ZAuNPs, with an increased reading compared to results found with the cAuNPs. This increase indicated that all nanoparticles had been additionally coating with surfactant [36]. The cumulate diameter was higher than expected, which could have been as a result of foreign material being present in the cuvette the sample was run in, or there may be aggregated species in the solution from purification through centrifugation. The samples were however filtered before being analysed, and the vast majority of particles appeared to be in error range of the expected diameter. Repeating this experiment after further purification by centrifugation and resuspension in water gave the same results, indicating that any excess surfactant had been purified out of solution, yet that some aggregation may have resulted from this purification process.

TEM of ZAuNPs

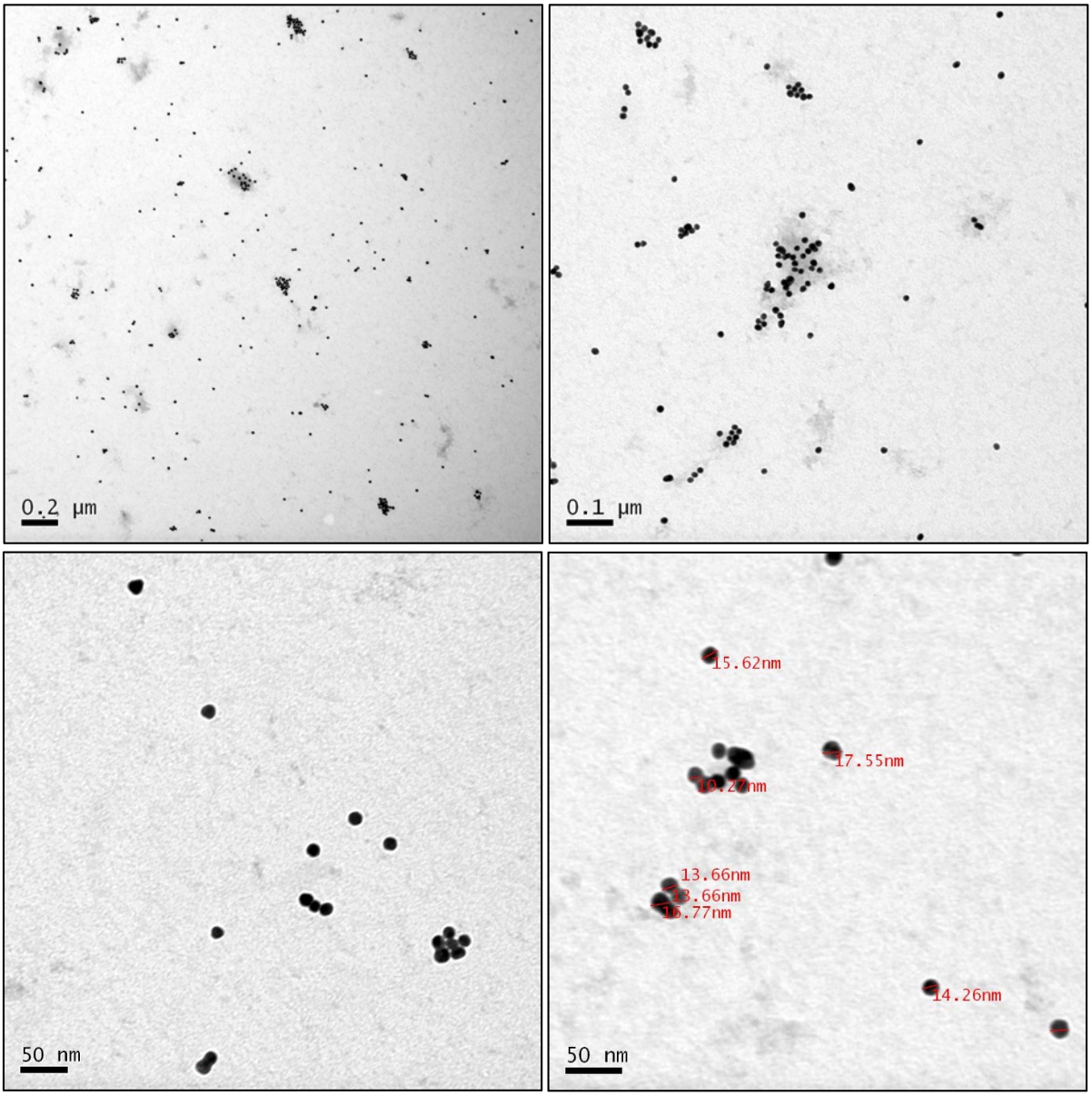

Figure 17: TEM images of ZAuNPs showing representative particles from two samples at a variety of magnifications

The diameter of particles observed via TEM was ~16 nm in size, Figure 17. This is consistent with results expected, as coating the AuNPs with a surfactant was not likely to increase the overall size very dramatically [36], and was only used to enhance the stability. Individual nanoparticles are observed, however clumps of nanoparticles were also present. These clusters

may be the cause of the larger species observed within DLS experiments, but it can clearly be shown that all nanoparticles are spherical and similar in size.

As well as analysing these particles suspended in water, the stability of these particles was analysed in cell media (DMEM) over a period of 72 hrs, Figure 18.

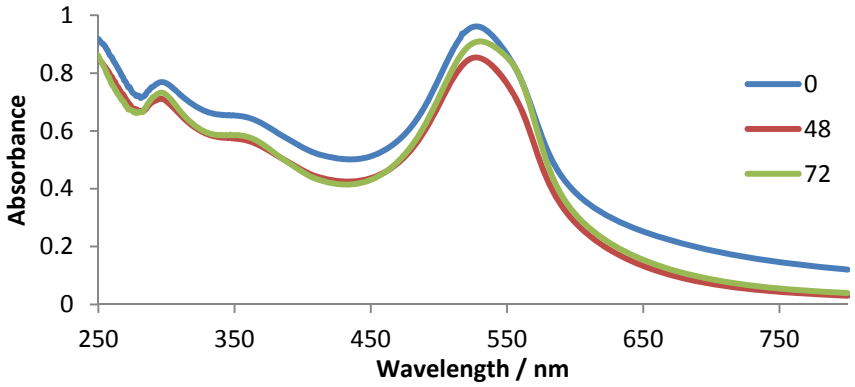

Figure 18: Stability of ZAuNPs (1 nM) suspended in media over 72 hrs. Legend indicates time / hours

As shown from the UV spectra, the particles are relatively stable under these conditions, with only slight broadening of the peak over time. No new peaks above 575 nm were observed, indicating that no large aggregates were formed during this period of time. This indicates that these particles are stable enough to perform cell studies with, to analyse if and how they interact with cells without aggregation affecting results.

4.4 Addition of Cylinders to ZAuNPs

4.4.1 Parent Cylinder

As discussed, it was hypothesised that tetracationic iron helicates have the potential to attach to the surface of cAuNPs via electrostatic interactions. Through stabilising these particles with fluorosurfactant ‘zonyl FSA’ it was hoped that on addition of the helicate, aggregation would not occur. This was first investigated using UV-Vis spectroscopy.

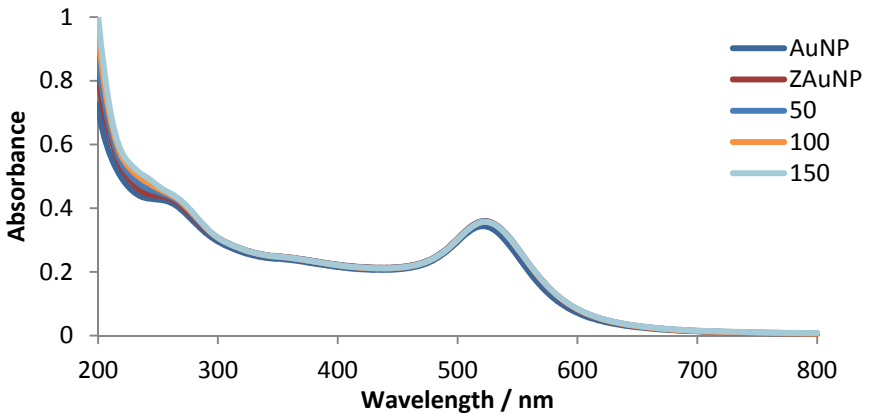

Figure 19: UV-Vis of ZAuNP (0.5 nM) with the addition of $Fe_2(L_P)_3]Cl_4$ (10 µM) in 50 µL aliquots. Legend indicates the volume of cylinder added in µL

The AuNP signal and complex signal peaks overlap, resulting in the UV profile of the supramolecular cylinder being masked. On addition of $[Fe_2(L_P)_3]Cl_4$ to ZAuNPs, no aggregation was now observed. There is a slight shift in the SPR band to 527 nm but the peak does not appear to have broadened and no additional peak for aggregated species was detected, as previously observed with cAuNPs.

Consequently, higher concentrations of parent cylinder were added to the nanoparticles in a ratio of 1:750 and 1:1000 ZAuNPs/cylinders, Figure 20.

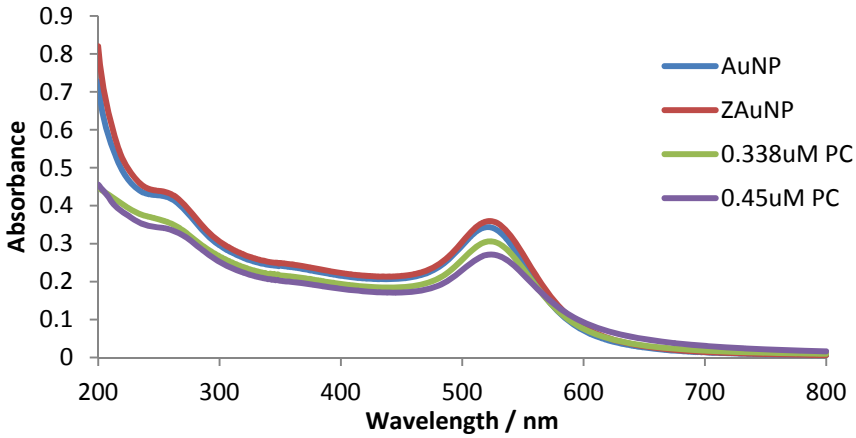

Figure 20: UV-Vis of ZAuNPs (0.45 nM) with varying complex solution added

No aggregation was observed on addition of these higher complex ratios. There was a shift in the SPR peak however, to 528 nm, indicating that some complex was interacting with the nanoparticle surface. This peak shift was not as great as those observed in literature cases, when functionalising nanoparticles [37, 38]. However, this was rationalised to be the result of it only being an electrostatic interaction and not the complex adsorbtion onto the gold surface.

A ratio of nanoparticle (1 nM) : complex (1 μM) was used in subsequent experiments, as this appeared to give a thousand times coverage of cylinder per nanoparticle, whilst maintaining the stability of the colloidal suspension.

The particles were synthesised by combining the stock solution of cAuNPs (~5 nM) containing a 0.2 % proportion of zonyl FSA with an equal volume of 5 μM cylinder solution in water. This mixture was stirred at room temperature, in the dark overninght. To purify, 1 mL alliquots of the mixture were centrifuged at × 12000 min^{-1} for 30 mins or until a pellet was formed. The supernatant was then carefully removed and the pellet re-suspended, to repeat the purification step one further time. During this purificarion process, it was observed that the nanoparticles did not aggregate, and maintained their deep-red colour.

As the characteristic UV spectrum of the parent cylinder is masked by that of the nanoparticles, it was necessary to fully characterise the functionalised nanoparticles and establish that the intact cylinder was electrostatically bound to the surface of the nanoparticles.

Firstly the ζ potential of the nanoparticles was analysed. By adding the tetracationic species to the negative nanoparticle surface, it was predicted that the surface charge on the nanoparticle would decrease in magnitude and that the value would reach closer to 0 mV.

ζ Potential (mV): -34.8 ± 13.3

Conductivity (mS/cm): 0.00976

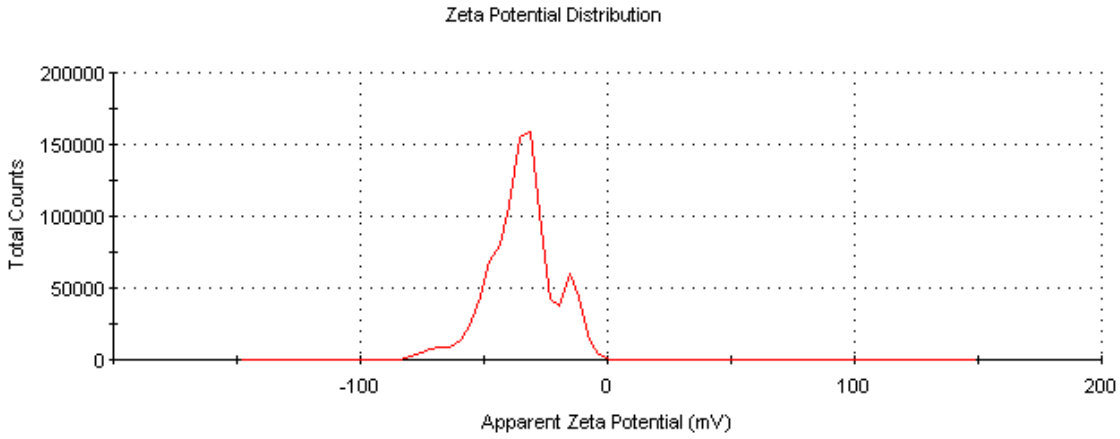

Figure 21: ZAuNP / $[Fe_2(L_P)_3]Cl_4$ at 5 nM: 5 µM ratio

As expected, the zeta potential decreased in magnitude through the addition of the tetracationic supramolecular helicate from -52.9 mV for ZAuNP to -34.8 mV for the nanoparticles coated with parent cylinder (PC-ZAuNP). This loss of 18 mV indicated that a large number of cationic species were attached to the nanoparticles, showing that despite purification by centrifugation, some cationic species remain attached through electrostatic interaction.

By assuming this complex had been attached to the nanoparticle surface, it was investigated whether any characteristic DNA binding activity of the cylinder was retained. By comparing the PC-ZAuNP interaction with ct-DNA with the free parent cylinder, it may give an indication if the cylinder remains intact when interacting with the nanoparticles.

The parent cylinder kinks and coils ct-DNA, apparent by the stiffening of DNA and reduction of the peak at 260 nm, *Chapter 3 Figure 20*. An ILD observed at 573 nm is characteristic of the parent cylinder as a result of the MLCT. These will be key alterations to the ct-DNA structure which will be analysed on addition of PC-ZAuNPs.

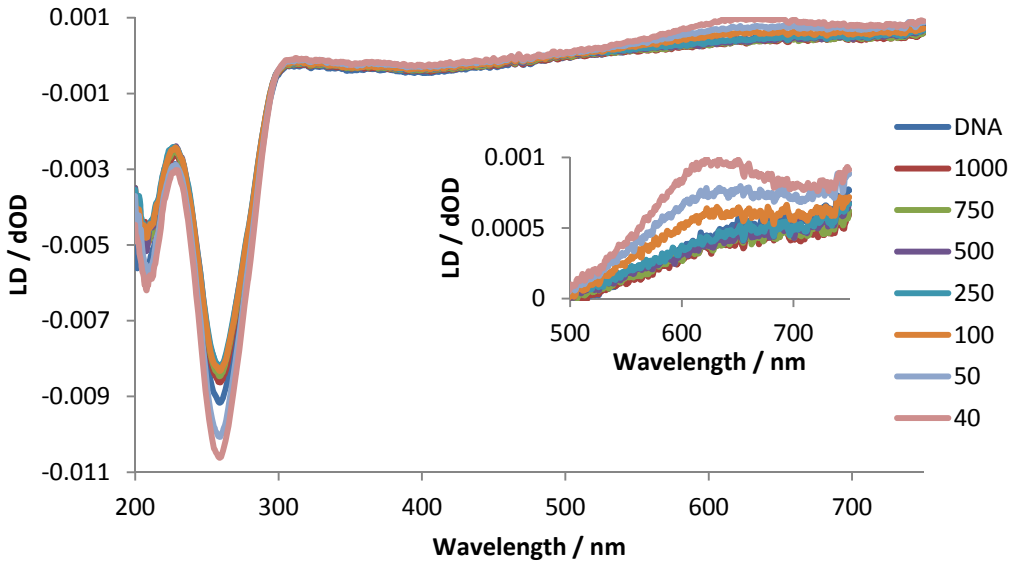

Figure 22: LD titration of 100 µM ct-DNA in 20 mM NaCl and 1 mM Tris-HCl (pH 7.2) with increasing concentrations of PC-ZAuNP. Legend shows ct-DNA:complex ratios (n:1)

On addition of PC-ZAuNPs to ct-DNA, an ILD signal was generated at ~ 625 nm, Figure 22. This wavelength does not correspond to λmax in the characteristic UV-Vis spectrum of these nanoparticles or the free parent cylinder, so it is suitable to presume that this peak is generated as a result of a DNA/AuNP interactions. This induced peak indicates that the nanoparticles are interacting with ct-DNA in a specific manner, to become orientated in solution on binding.

When working with nanoparticles, less concentrated solutions of the complex were used, compared with the free cylinder, to avoid aggregation. Despite this, spectral differences to the ct-DNA peak at 260 nm were observed, Figure 23, demonstrating how interacting with PC-ZAuNPs may result in structural change on binding.

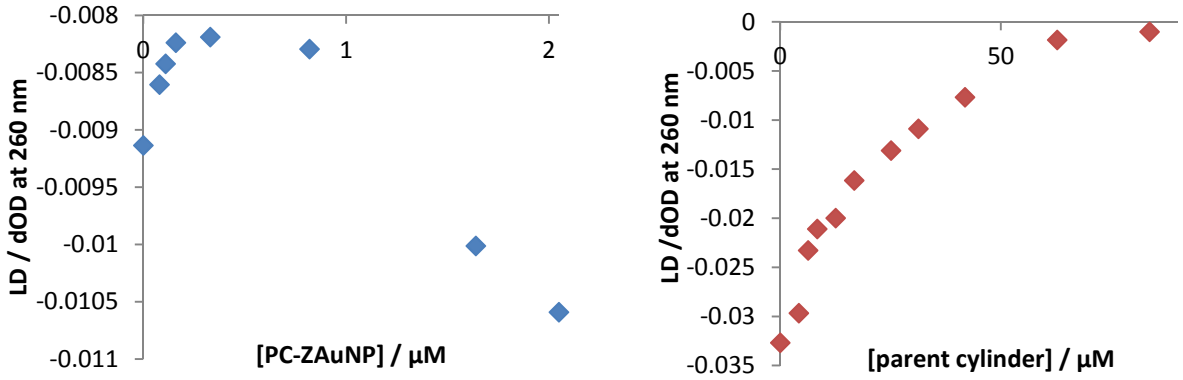

Figure 23: Intensity of LD signal at 260 nm for PC-ZAuNP (blue) and free $[Fe_2(L_P)_3]Cl_4$ (red)

Initially, the signal at 260 nm decreases on addition of PC-ZAuNPs, yet once the concentration ratio meets 100:1 ct-DNA:PC-ZAuNPs the peak intensity increases. This is the opposite effect observed for the free parent cylinder, which shows continual DNA stiffening and loss of signal with increasing ratios of complex. These conflicting effects may indicate how by having the complex attached to a surface may alter the binding mode and affinity to ct-DNA.

It was therefore investigated what effect un-functionalised, surfactant coated nanoparticles, ZAuNPs had on ct-DNA, Figure 24.

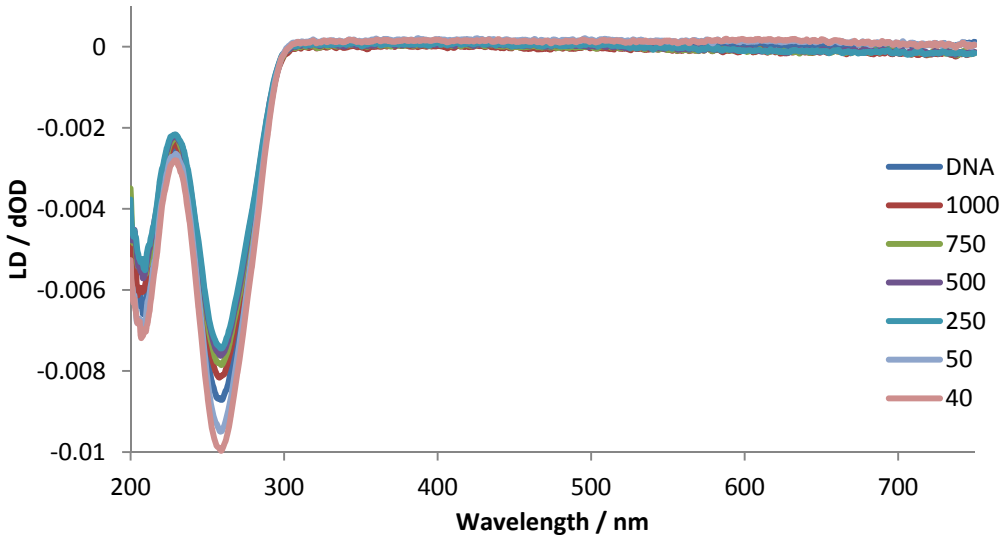

Figure 24: LD titration of 100 µM ct-DNA in 20 mM NaCl and 1 mM Tris-HCl (pH 7.2) with increasing concentrations of ZAuNPs. Legend shows ct-DNA:complex ratios (n:1)

Equivalent ratios of ZAuNPs to ct-DNA were used, as with PC-ZAuNPs, in order to directly compare the effects when functionalised. No induced signal was produced when ZAuNPs were added to ct-DNA, as previously observed with PC-ZAuNPs. This indicates the ILD was as a result of the iron species being present in solution. Absence of an ILD, also indicates that ZAuNPs interact unselectively in a non-specific orientation with ct-DNA.

Despite no ILD on addition of ZAuNPs, changes to the intensity of the characteristic LD peak at 260 nm was observed, Figure 25. Presence of ZAuNPs in solution, affected the orientation and perhaps structure of ct-DNA, very similar to that observed when PC-ZAuNPs were added. This implies that the spectroscopy observed below 300 nm is largely due to the effects of the nanoparticles and > 300 nm represents effects of the nanoparticle functionality.

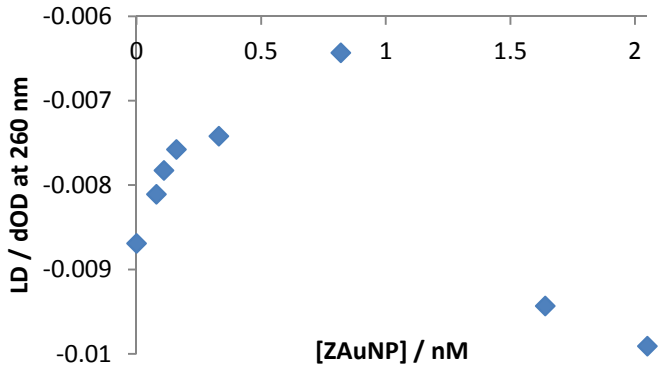

Figure 25: Intensity of LD at 260 nm, with increasing concentration of ZAuNPs

To further investigate if the parent cylinder was attached to the nanoparticle surface, CD analysis was performed. The parent cylinder is a triple stranded helicate, formed in a racemic mixture containing an M and P enantiomer. As a racemic mixture the cylinder does not have a CD spectrum, yet when the enantiomers are separated, each enantiomer has a CD spectra, due to the chiral nature of the complex [39].

By attaching one of these enantiomers to the nanoparticles surface, it was hoped to confirm the presence of the intact cylinder, through viewing the same CD spectrum as that of the 'free' enantiomer.

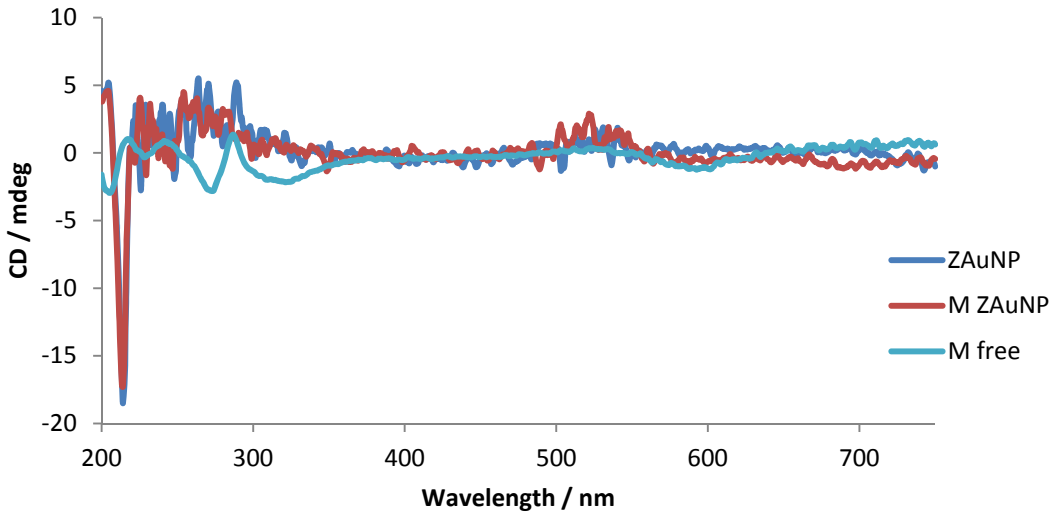

Figure 26: CD spectra of 'free' M enantiomer of the parent cylinder (5 μM), compared to ZAuNPs (5 nM) and those functionalised with M enantiomer M-ZAuNPs (5 nM : 5 μM)

The same concentration of free M enantiomer was analysed as that mixed with ZAuNPs to functionalise the M-ZAuNPs. The ZAuNP and those which had been exposed to the complex enantiomer, show very similar CD profiles, with no apparent complex peaks. This indicates that the species attaching to the nanoparticle surface is likely not to be the intact iron cylinder.

It was suspected that the parent cylinder may be unstable in these given conditions, so stability of the iron complex was monitored in the presence of zonyl-FSA over a period of 49 hours. A ten times more concentrated solution of complex was used during this experiment in order to clearly observe the stability of the complex by UV-Vis, analysing the characteristic MLCT band at 572 nm of the purple coloured cylinder, to access if the complex remained stable in solution.

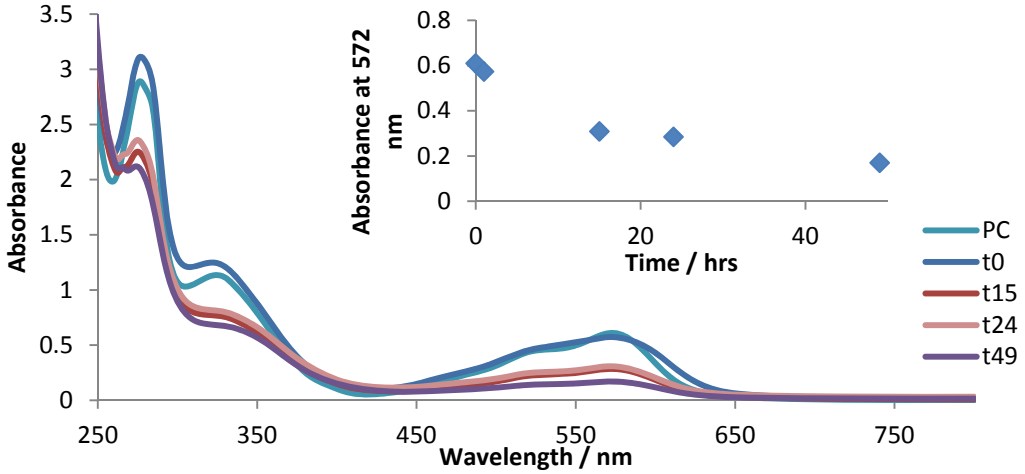

Figure 27: Stability of $[Fe_2(L_P)_3]Cl_4$ (50 µM) in a 2 % solution of zonyl FSA in water over 49 hrs. Legend indicates time / hours

It was observed that after 15 hours, the time in which the solution was left to stir in the presence of the nanoparticles, the cylinder concentration had decreased by 50 %, resulting in iron ions and ligand components being in solution.

It was hoped that altering the pH of the solution would increase the observed stability of the complex in the presence of zonyl FSA, so slightly more acidic and basic pH solutions were analysed over time, Figure 28. Altering the pH however appeared to have no observable effect on complex stability with time.

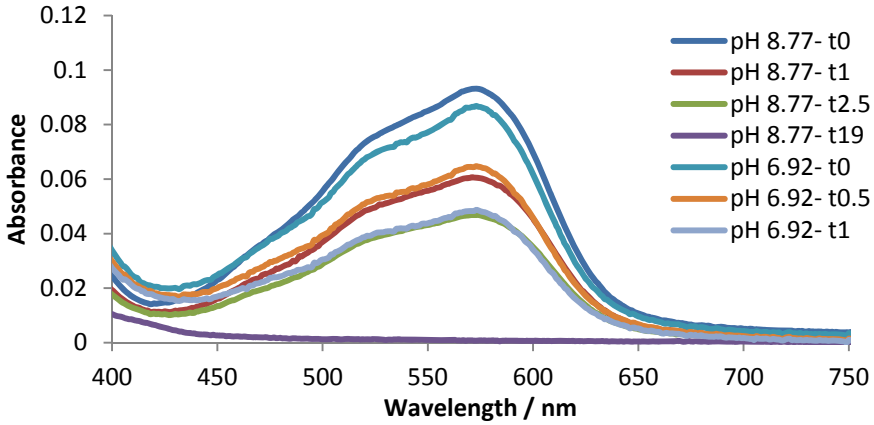

Figure 28: Stability of $[Fe_2(L_P)_3]Cl_4$ in a 0.2 % solution of zonyl FSA at different pHs. Legend indicates pH solution a time it was measured / hours

After collating all information on PC-ZAuNPs, it was concluded that the parent cylinder, $[Fe_2(L_P)_3]Cl_4$ was not attached to ZAuNPs via electrostatic interaction, but that it most likely degrades under reaction conditions, resulting in free Fe^{2+} ions and ligand in solution. The iron ions would be free to interact with the negatively charged nanoparticle surface, forming strong electrostatic interactions able to withstand purification via centrifugation. This would explain the change in ζ potential observed, and the difference in ct-DNA interaction observed by LD. It can therefore be concluded that this is not a viable technique to combine the known supramolecular helicate, $[Fe_2(L_P)_3]Cl_4$, with nanoparticles.

4.4.2 Ruthenium Cylinder

Stability of the parent cylinder, $[Fe_2(C_{25}H_{20}N_4)_3]^{4+}$ is not substantial enough to withstand conditions needed to functionalise AuNPs, through electrostatic interactions. Consequently, the ruthenium analogue of this complex was analysed, to assess whether addition of these tetracationic helicate structures could be attached to nanoparticles through electrostatic interactions.

The ruthenium analogue has previously been synthesised within the Hannon group [40], showing different properties in terms of stability, solubility and synthetic technique required, compared with the iron complex, indicating that this may withstand exposure to nanoparticles.

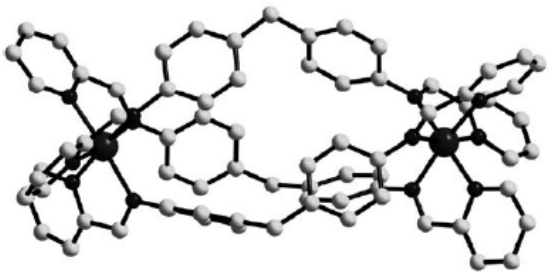

Figure 29: Structure of $[Ru_2(L_P)_3]^{4+}$ cation. Ru large black spheres, N small clack spheres, C small gray spheres. Hydrogen atoms, anions and cocrystallized solvent molecules are omitted for clarity [reproduced from ref[40]]

The ruthenium helicate, $[Ru_2(C_{25}H_{20}N_4)_3]^{4+}$ is more stable than the iron analogue, due to more inert metal-ligand bonds. Consequently, it is difficult to synthesise, requiring high temperatures, increased reaction time or microwave reactor synthesis to form the triple stranded complex. The major products when reacting a ruthenium source with the bis-pyridyl-imine ligand are the double stranded complex and polymer species. The desired triple stranded helicate is formed in low yield, so the iron analogue is conventionally used, and has had more research performed on it.

The ruthenium helicate will be beneficial to use for many reasons, as well as increased stability in solution, it also exhibits fluorescent qualities, Figure 30 [40]. This fluorescence could be used to analyse if the cylinder was attached to the gold nanoparticle surface, or if the electrostatic interactions are not strong enough to functionalise the AuNPs.

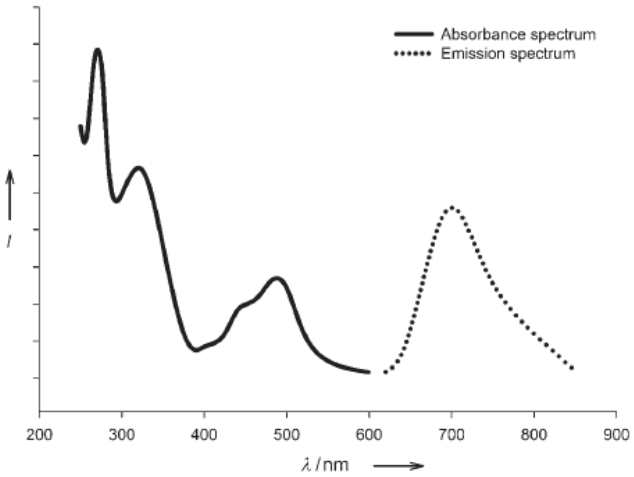

Figure 30: Absorption (solid line) and emission (dotted line) spectra (λ_{ex} = 480 nm) for $[Ru_2L_3](PF_6)_4$ in MeCN (298 K) [reproduced from ref[40]]

In order to attach the ruthenium helicate to the surface of AuNPs, the surface was coated with zonyl FSA for the reasons previously discussed, *section 4.3.2*. This would allow for a larger

concentration of tetracationic species to be combined with the negatively charged nanoparticles before aggregation occurs.

4.4.2.1 Ru-ZAuNP UV-Vis

To observe if the ruthenium cylinder was interacting with the surface of ZAuNPs, UV spectra of nanoparticle solutions, before and after purification were performed.

Solutions of cAuNPs (5 nM) containing 0.2 % w/v zonyl FSA, with an equal volume of ruthenium cylinder (5 μM, in MeCN) were stirred overnight in darkness. 1 mL aliquots were purified twice by centrifugation and re-suspended in 1 mL H_2O. Spectra were then run before and after this purification, Figure 31.

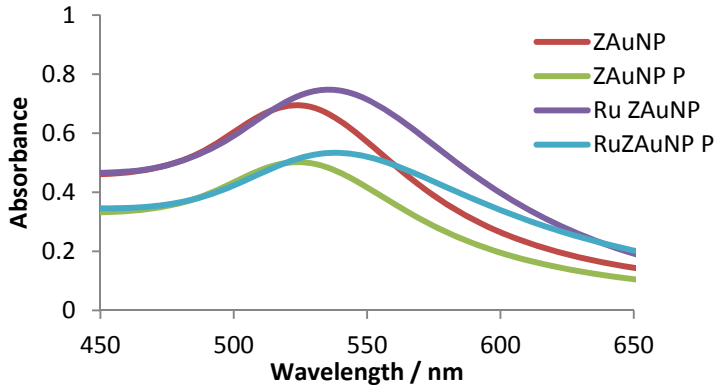

Figure 31: UV spectra of AuNPs functionalised with surfactant (ZAuNP, ZAuNP P) and $[Ru_2(L_P)_3][PF_6]_4$ (Ru ZAuNP, Ru AuNP P), before and after purification

As demonstrated in *section 4.3.2* the SPR shift of ZAuNPs was to 527 nm, this was not affected by purifying through centrifugation, showing that the zonyl FSA was retained on the surface. The absorbance intensity did decrease after purification however, due to nanoparticles being lost in the supernatant between purification steps. This was unavoidable, and despite changing the speed of centrifugation, it was found that some nanoparticles remained in suspension, so a speed which caused most to sediment without aggregation was used.

On addition of the ruthenium cylinder (1:1 volume ratio of 5μM $[Ru_2(L_P)_3][PF_6]_4$ / 5 nM ZAuNP), a large shift in the SPR was observed to 538 nm. This indicated that the cylinder was interacting with the gold surface, even after purifying twice by centrifugation. The functionalised nanoparticles were less stable than the initial ZAuNP, expected due to the decreased repulsive forces between the nanoparticles on addition of the tetracationic cylinder. On purification of the Ru-ZAuNPs, some flocculation was observed, and can be seen by the slight broadening in the UV spectrum. It was however concluded that this purification technique was satisfactory for these nanoparticles, as few particles were lost during washing, and the majority could be re-suspended in solution, un-aggregated. Figure 32. Ru-ZAuNPs were always prepared just before use, to minimise any further aggregation or change in functionality of the particles over time.

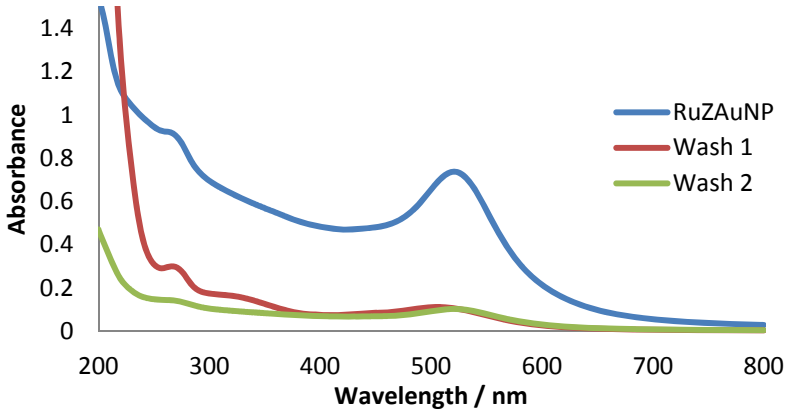

Figure 32: UV-Vis of Ru-ZAuNP (5 nM) and the supernatant from subsequent purification washes

4.4.2.2 Ru-ZAuNP Characterisation

- **Ru-ZAuNP zeta potential** **ζ Potential (mV):** -43.3 ± 6.85

  Conductivity (mS/cm): 0.0113

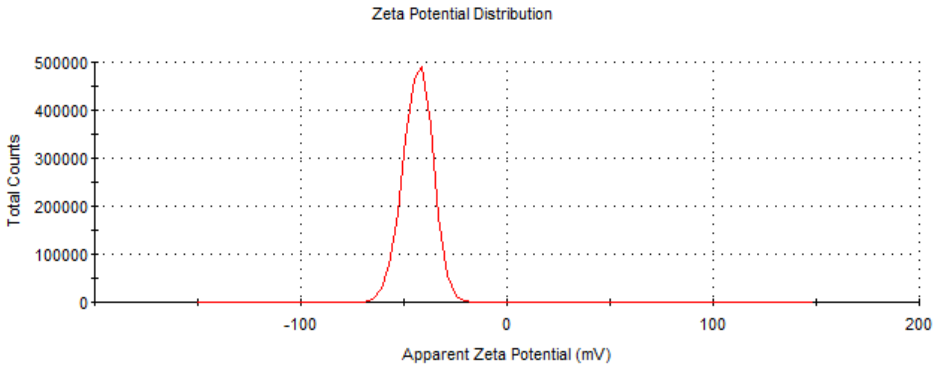

Figure 33: Zeta potential of Ru-ZAuNP (2.5 nM)

On addition of the ruthenium cylinder to ZAuNPs, the zeta potential increased from around -53 mV to -43 mV. This implies that a positively charged species had been added to the nanoparticle surface, reducing the overall negative charge, making the particles slightly less stable in solution. This would be consistent with the ruthenium cylinder being incorporated on the surface of the nanoparticles via an electrostatic interaction.

- **Ru-ZAuNP DLS**

Distribution: Intensity: 26.10 ± 10.01 nm Cumulant Diameter: 25.30 nm

Volume: 23.18 ± 5.372 nm Polydispersity Index: 0.252

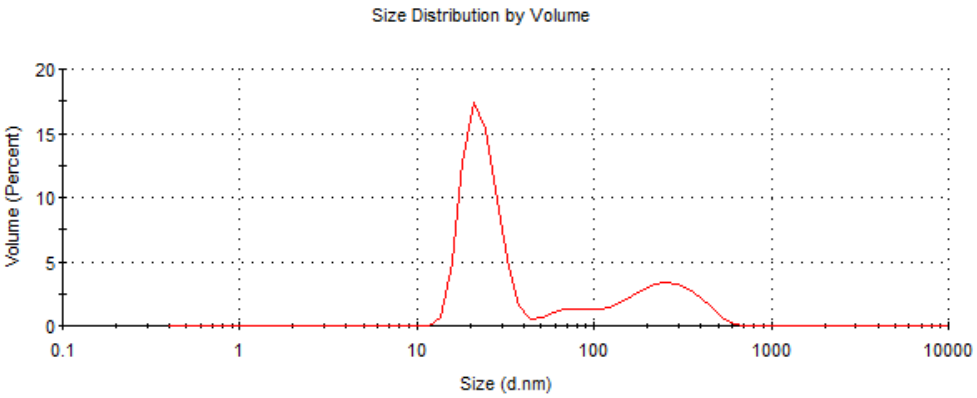

Figure 34: DLS results for Ru-ZAuNP (2.5 nM)

DLS data indicates that on functionalising ZAuNPs with ruthenium cylinder, the size of the nanoparticles slightly increased. This would be consistent with addition of a 2 nm by 1 nm complex, suggesting the metal complex may be intact as, on addition to the nanoparticles. Larger species are also present in solution, likely to be aggregates that have formed during the purification, resulting from the positively charged complex interacting with the negatively charged nanoparticles.

- **Ru-ZAuNP fluorescence**

The ruthenium cylinder has a key characteristic that the iron cylinder lacks, as well as being more stable, it is also fluorescent. This therefore gives another method of detecting the ruthenium cylinder on the nanoparticle surface, or whether the complex is removed during purification stages.

Solutions of free ruthenium cylinder which was used during the synthetic stages of Ru-ZAuNPs and the subsequent nanoparticles were tested for their luminescent properties, Figure 35.

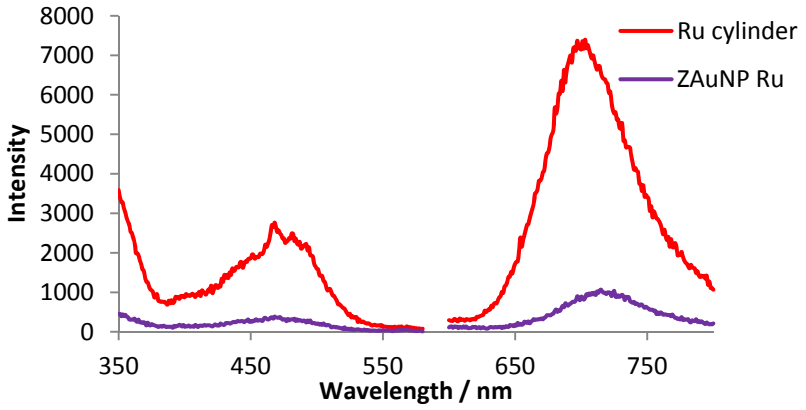

Figure 35: Absorption (350-573 nm) and emission (600-800 nm) spectra (λ_{ex} = 480 nm) for $[Ru_2(L_P)_3][PF_6]_4$ in MeCN/H_2O (5μM) 'free' and 'bound' to ZAuNP (5 nM) (298 K)

From absorption and emission profiles of the free ruthenium cylinder and Ru-ZAuNPs, it was apparent that some ruthenium complex was bound to the nanoparticles. Approximately 15 %

of the original emission profile was retained on the nanoparticles, showing that even after purification twice by centrifugation and washing, the cylinder is retained on the nanoparticle surface through electrostatics. AuNPs are known to quench fluorescence of metal complexes, so it is not possible to quantify the amount of ruthenium cylinder attached to the nanoparticles by this experiment [36]. These results show that AuNPs have successfully been functionalised with a supramolecular helicate.

- **TEM of Ru-ZAuNP**

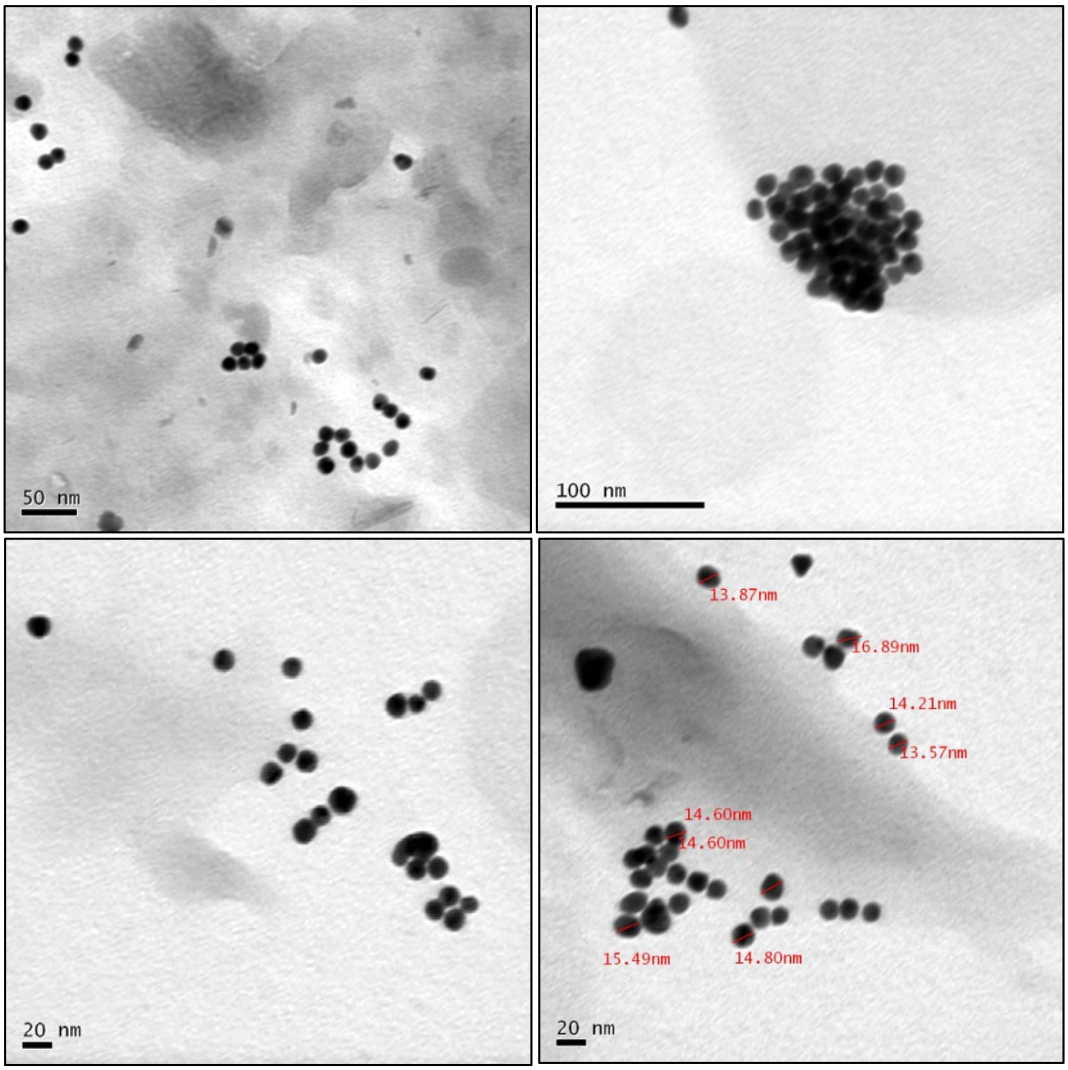

Figure 37: TEM images of Ru-ZAuNP showing representative particles from two samples at a variety of magnifications

TEM images show that the AuNPs retained their spherical shape on addition of the ruthenium cylinder. The size of the particles was not greatly increased compared to the bare ZAuNP nanoparticles. On average, the particles are still ~16 nm in diameter. The ruthenium cylinder has dimensions of 2 nm by 1 nm, so it was expected that the overall size of the particles would have increased. This may give an indication that the ruthenium complexes are lying on the surface of the nanoparticles so only an additional nanometre would be added around the surface. The ruthenium complex may also not be contrasted and therefore would be undetectable via this technique as only two heavy atoms lie in the core of the cylinder ~0.5 nm from the surface. Some larger aggregates were also detected at ~100 nm in diameter, reiterating the fact that the nanoparticles are less stable due to tetracationic species binding to the gold surface.

4.4.2.3 Ru-ZAuNP Stability in Media

Stability of ruthenium cylinder functionalised nanoparticles, Ru-ZAuNPs, was analysed in media solution, to determine whether cell toxicity studies of the particles towards cancer cell lines could be carried out. If it appeared the nanoparticles aggregated in media, defective toxicity results would be achieved, deeming such experiments useless. Stability was investigated by measuring the UV-Vis spectrum of the Ru-ZAuNPs suspended in media over a period of 24 hours, Figure 38.

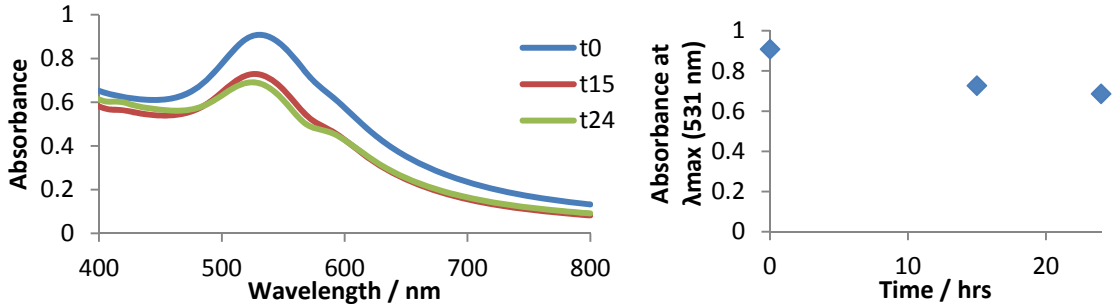

Figure 38: UV-Vis spectra of Ru-ZAuNP (5 nM) over a period of 24 hrs, legend indicates time solution was scanned / hours

Evaluating intensities of the characteristic UV peaks over time, can give an indication of the nanoparticle stability. After 24 hrs in media solution, 75 % of the peak intensity at 531 nm was retained. This indicated that some nanoparticles were lost to aggregation/degradation over time, but that the majority remained suspended in solution.

4.4.2.4 Ru-ZAuNP / DNA Interactions

4.4.2.4.1 Ru-ZAuNP CD

On addition of the ruthenium functionalised nanoparticles to ct-DNA, very little observable effect was detected to the characteristic CD signal of ct-DNA. The ct-DNA signals increased in intensity slightly, however no ICD peaks were observed, indicating little binding interactions occurring between ct-DNA and Ru-ZAuNPs. This may be due to the compound being bound to the nanoparticle surface, and so not free to access grooves in the DNA structure. It does however indicate that the ruthenium complex is not dissociating from the nanoparticle surface in order to bind to the DNA.

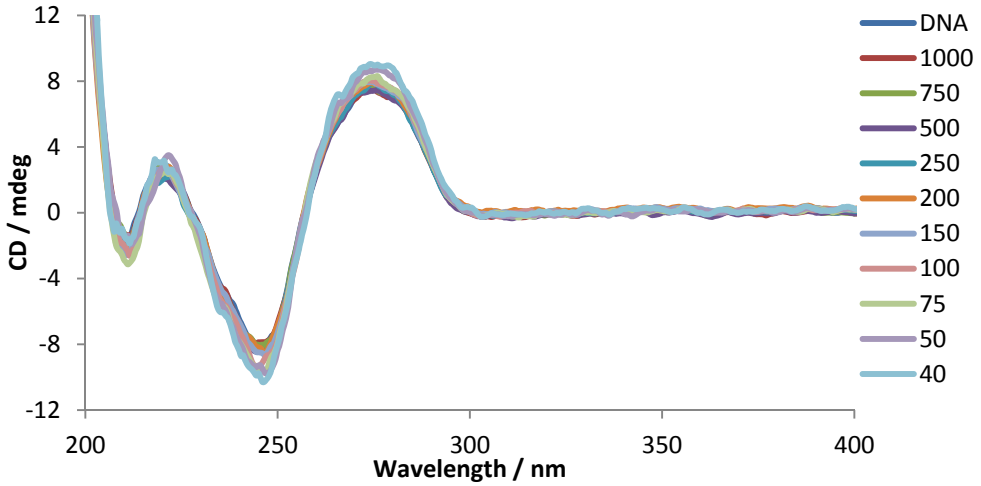

Figure 39: CD titration of 100 µM ct-DNA in 20 mM NaCl and 1 mM Tris-HCl (pH 7.2) with increasing concentrations of Ru-ZAuNP. Legend shows ct-DNA:complex on nanoparticle ratios (n:1)

4.4.2.4.2 Ru-ZAuNP LD

On addition of Ru-ZAuNP to ct-DNA, an ILD signal was observed around 633 nm, Figure 40. This indicated that the nanoparticles became orientated in solution, by binding to the duplex DNA in a specific manner. This wavelength does not correspond to λmax in the characteristic UV-Vis spectrum of these nanoparticles or the free ruthenium cylinder, so it is suitable to presume that this peak is generated as a result of a DNA/NP interactions.

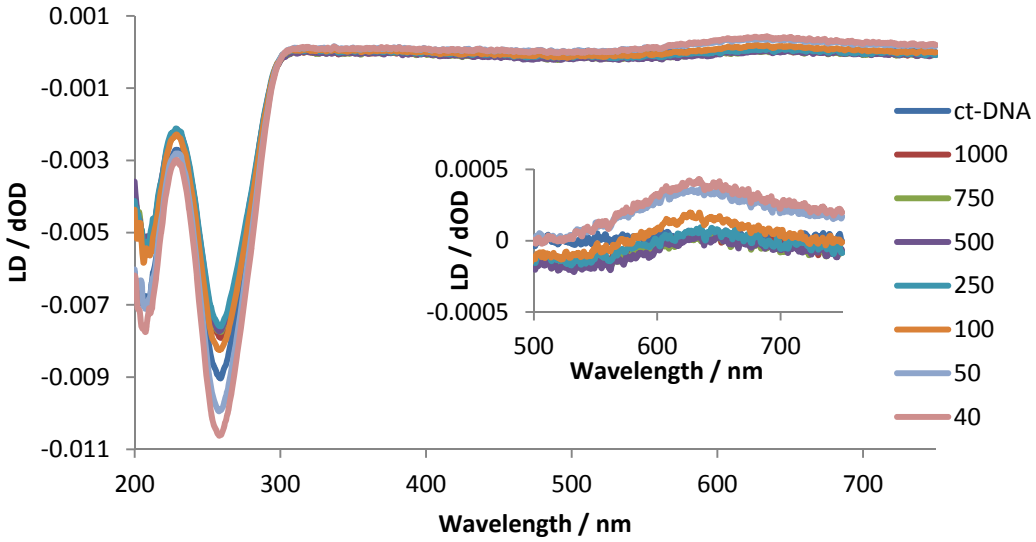

Figure 40: LD titration of 100 µM ct-DNA in 20 mM NaCl and 1 mM Tris-HCl (pH 7.2) with increasing concentrations of Ru-ZAuNP. Legend shows ct-DNA:complex on nanoparticle ratios (n:1)

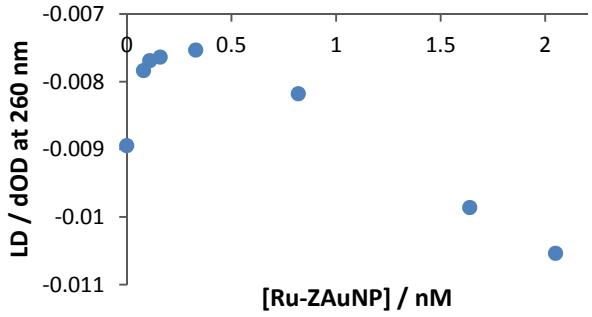

Figure 41: Intensity of LD signal at 260 nm for Ru-ZAuNP

The intensity of the characteristic ct-DNA peaks are also altered on addition of Ru-ZAuNPs to the solution, Figure 41. The trend on addition of these nanoparticles is the same as that observed with the PC-ZAuNP and ZAuNP, indicating that this structural change to ct-DNA is as a result of the nanoparticles being in solution, rather than the functionality attached to them.

It was concluded that by adding this ruthenium supramolecular helicate to the surface of AuNPs via electrostatic interactions, the DNA binding affinity of the complex may be hindered. Being bound to the nanoparticle surface likely inhibits the ability of the cylindrical structure to fit into the grooves of DNA, to subsequently kink and coil the DNA and inhibit DNA replication. As a result it appeared that binding cylinders to the nanoparticles via electrostatics was not greatly advantageous.

4.4.3 Thioacetate Cylinder

As demonstrated in *section 3.1.4* the parent cylinder was modified by click chemistry to incorporate additional thioacetate functionality, $[Fe_2(L_{Thioacetate})_3][BF_4]_4$ where $L_{Thioacetate}$ = $C_{49}H_{62}N_{10}O_6S_2$. This complex is able to interact and bind to ct-DNA to induce structural change.

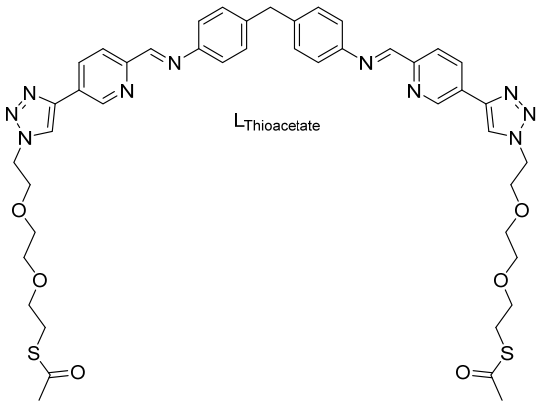

Due to the sulphur containing moieties attached, the interaction between this iron helicate and AuNPs was investigated.

4.3.3.1 Thioacetate-ZAuNP UV-Vis

As demonstrated in *section 4.3.2* the SPR shift of ZAuNPs is 527 nm, this was not affected by purifying through centrifugation, showing that the zonyl is retained on the surface. On addition

of $[Fe_2(L_{Thioacetate})_3][BF_4]_4$ to the ZAuNPs (Thio-ZAuNP), a shift in the SPR to 537 nm was observed. This indicates that the cylinder is interacting with the gold surface, even after purifying by centrifugation.

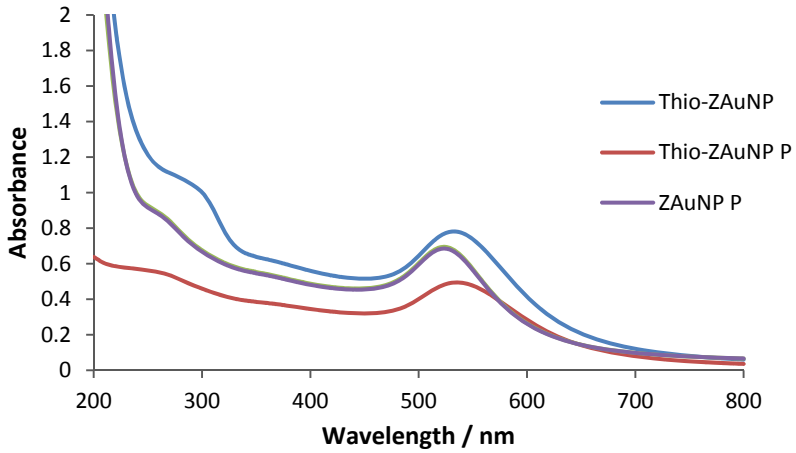

Figure 42: UV-Vis of ZAuNP (5 nM) and Thio-ZAuNP before and after purification (P)

The absorbance intensity decreased after purification, as some nanoparticles were lost in the supernatant between purification steps. This unfortunately appeared unavoidable, and despite changing the speed of centrifugation and volume purified, it was found that some nanoparticles remained in suspension, so a speed which caused most to sediment without aggregation was used.

The nanoparticles appeared to be less stable than the initial ZAuNP, which was expected due to adding a tetracationic complex to the negatively charged nanoparticle surface. On purification, some flocculation was observed, resulting in a slight broadening of the UV spectrum. Thio-ZAuNPs could however be re-suspended in H_2O and were always prepared just before use, to minimise further aggregation or change in functionality of the nanoparticles.

4.4.3.2 Thioacetate-ZAuNP Characterisiation

- **Thioacetate-ZAuNP DLS**

Distribution: Intensity: 148.4 ± 75.23 nm Cumulant Diameter: 116.9 nm

Volume: 69.16 ± 23.62 nm Polydispersity Index: 0.205

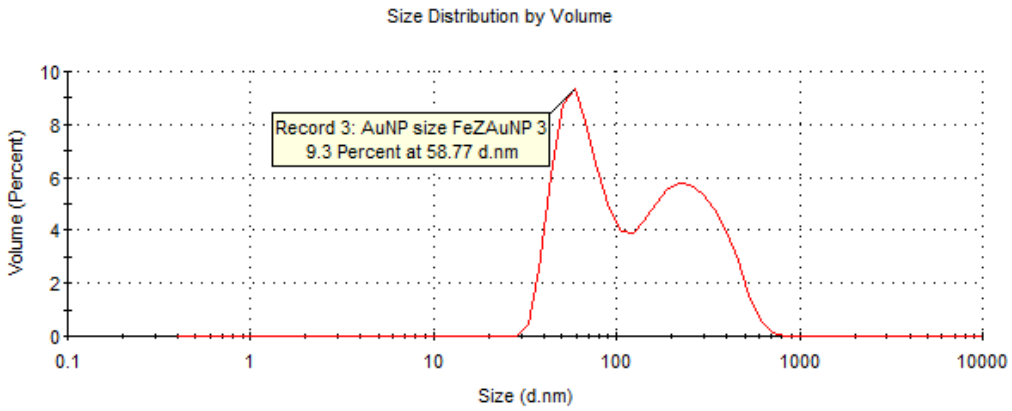

Figure 43: DLS results of Thio-ZAuNPs (2.5 nM)

On analysing the thioacetate nanoparticles by DLS, Figure 43, it appeared that the size of nanoparticles had greatly increased on addition of the iron complex. This large increase potentially indicates that by adding the positively charged complex to the nanoparticle surface, the repulsive forces keeping the nanoparticles stable in solution were reduced, meaning that aggregation may be more likely. Other factors such as the sample being at too high a concentration and ineffective filtering of the sample may also have resulted in similar results.

- **Thioacetate-ZAuNP Zeta Potential**

ζ Potential (mV): -49.9 ± 9.05

Conductivity (mS/cm): 0.0177

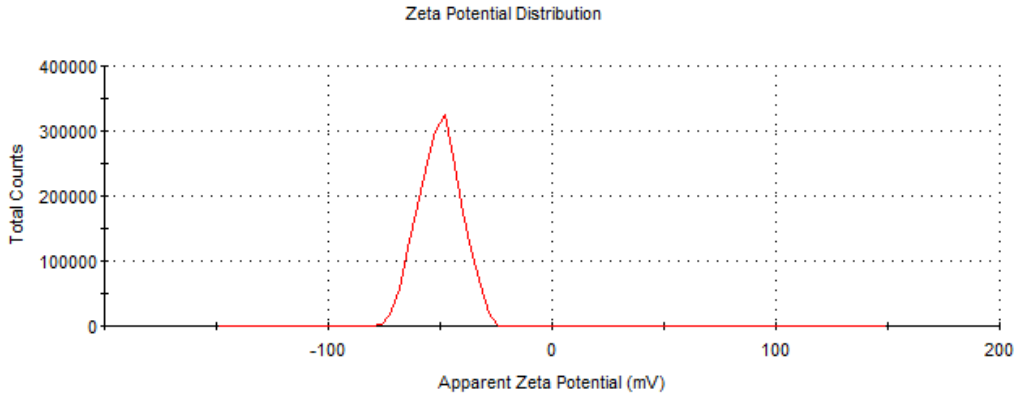

Figure 44: Zeta Potential analysis of Thio-ZAuNPs

On addition of the thioacetate cylinder, $[Fe_2(L_{Thioacetate})_3][BF_4]_4$, to ZAuNPs, the zeta potential increases slightly. This result indicated that a positively charged species was interacting with the negatively charged particles. Despite the addition of a positively charged compound in solution, this ζ potential indicates that the nanoparticles still have an overall negative charge and are stable in solution.

- **Thioacetate-ZAuNP TEM**

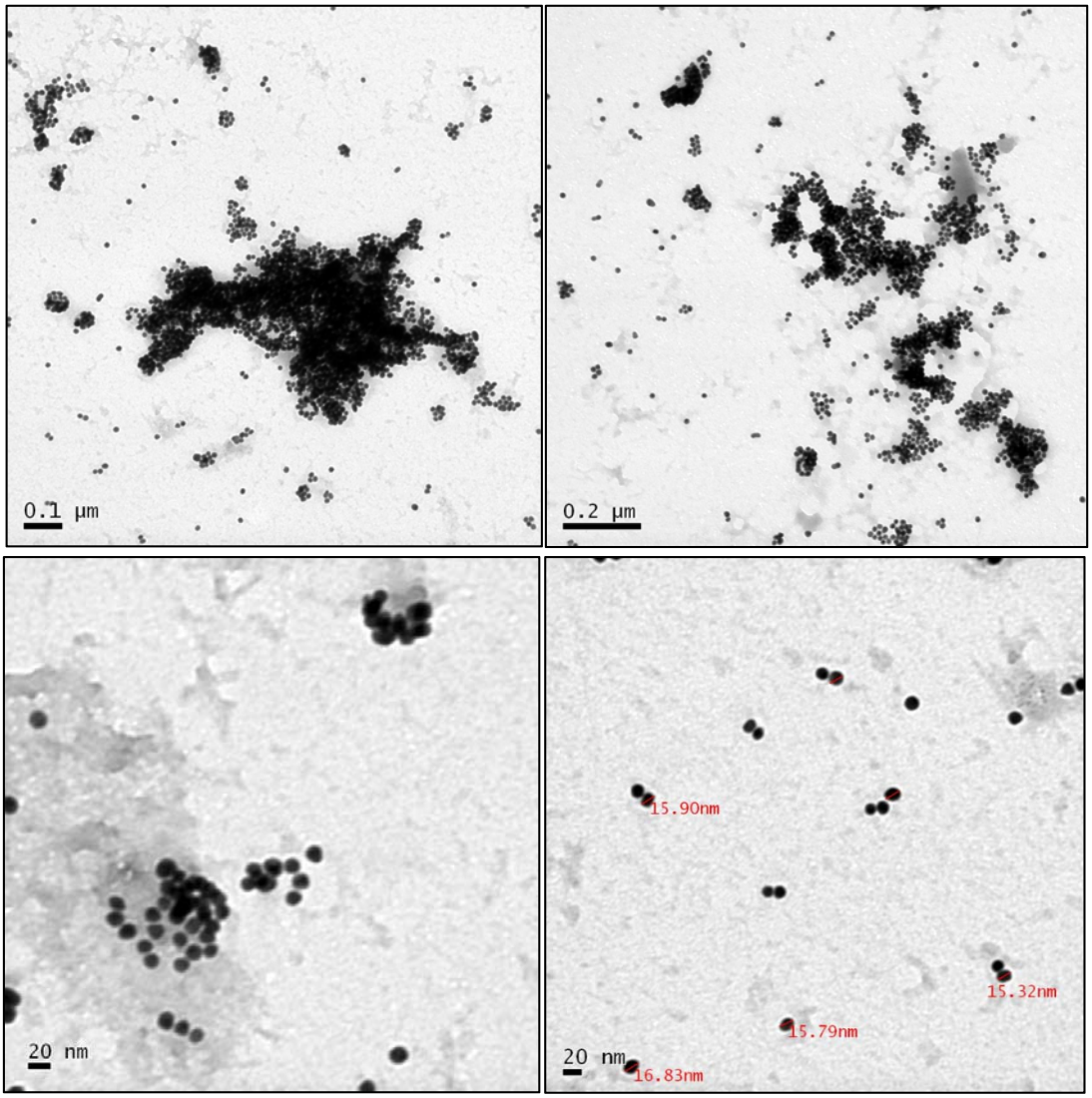

Figure 45: TEM images of Thio-ZAuNP showing representative particles from two samples at a variety of magnifications

As expected from DLS data, when viewing the thioacetate functionalised nanoparticles via TEM, large aggregate species were present. Despite being re-suspended in solution after purification and only a slight SPR band shift, it appeared that addition of the tetracationic complex caused aggregate species to be prominent in the nanoparticle solution. Individual nanoparticles retained their spherical shape with a diameter of ~16 nm. Despite this, the particles are more drawn together, despite being relatively stable in aqueous solution. This may

indicate that there is cross-coupling occurring between nanoparticles as a result of the cylinder having six thioacetate groups per complex, three on each side of the iron centres. These multiple linkers may be the cause of aggregate species despite the apparent high stability of the particles, based on UV-Vis, ζ potential and appearance.

4.4.3.3 Thioacetate-ZAuNP /DNA Interaction

4.4.3.3.1 Thioacetate-ZAuNP CD

On addition of Thio-ZAuNP to ct-DNA, few observable changes were made to the characteristic B-DNA signals of ct-DNA, Figure 46. A slight ICD signal was observed at 313 nm, indicating that there is an interaction occurring between the nanoparticles and ct-DNA, and that the cylinder may still be able to interact with the grooves of DNA, despite being bound to the nanoparticle surface.

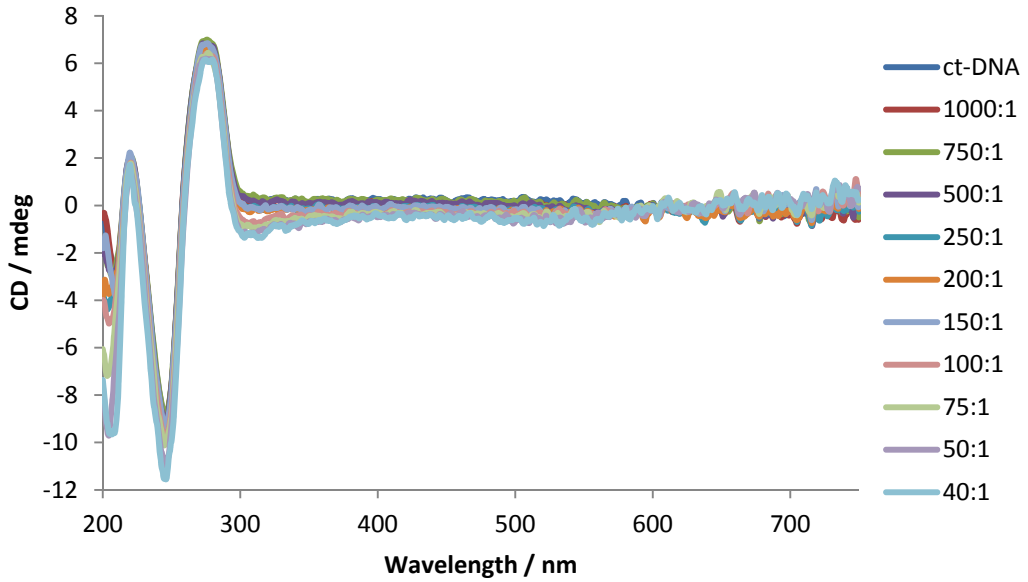

Figure 46: CD titration of 100 µM ct-DNA in 20 mM NaCl and 1 mM Tris-HCl (pH 7.2) with increasing concentrations of Thio-ZAuNP. Legend shows ct-DNA:complex ratios

4.4.3.3.2 Thioacetate-ZAuNP LD

On addition of Thio-ZAuNP to ct-DNA the characteristic negative B-DNA signals changed with increasing concentration of Thio-ZAuNPs. This signal follows the same pattern as when other nanoparticle solutions, ZAuNP and RuZAuNP interact with ct-DNA. An induced signal at 304 nm indicates that the Thio-ZAuNPs are binding to DNA and becoming orientated in solution, Figures 47 and 48, a pattern not observed with the bare ZAuNPs.

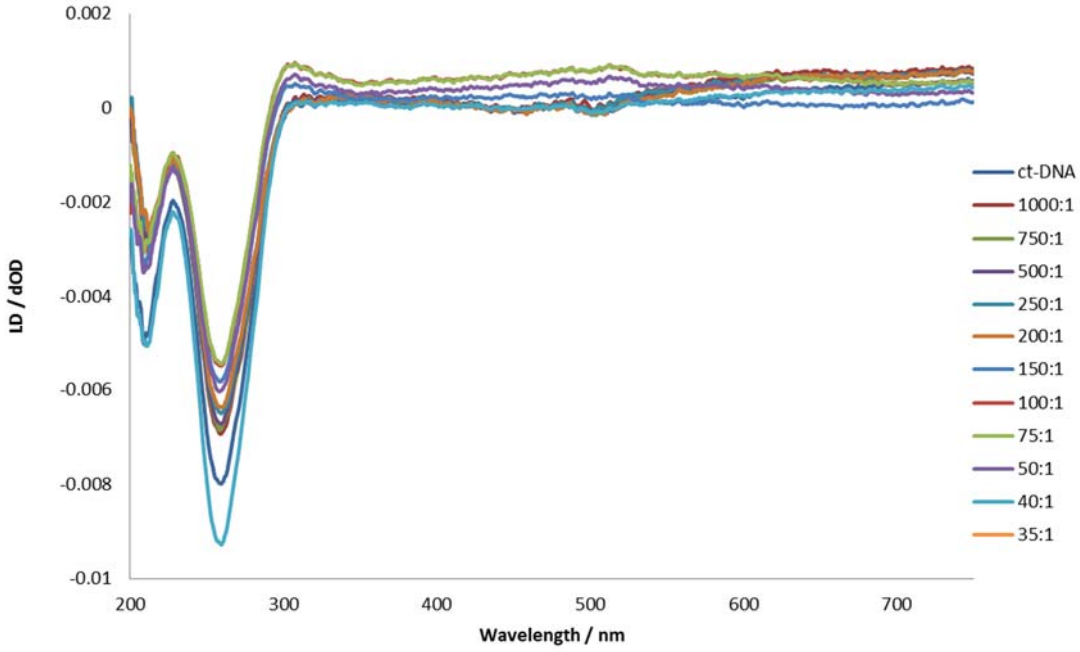

Figure 47: LD titration of 100 µM ct-DNA in 20 mM NaCl and 1 mM Tris-HCl (pH 7.2) with increasing concentrations of Thio-ZAuNP. Legend shows ct-DNA:complex ratios

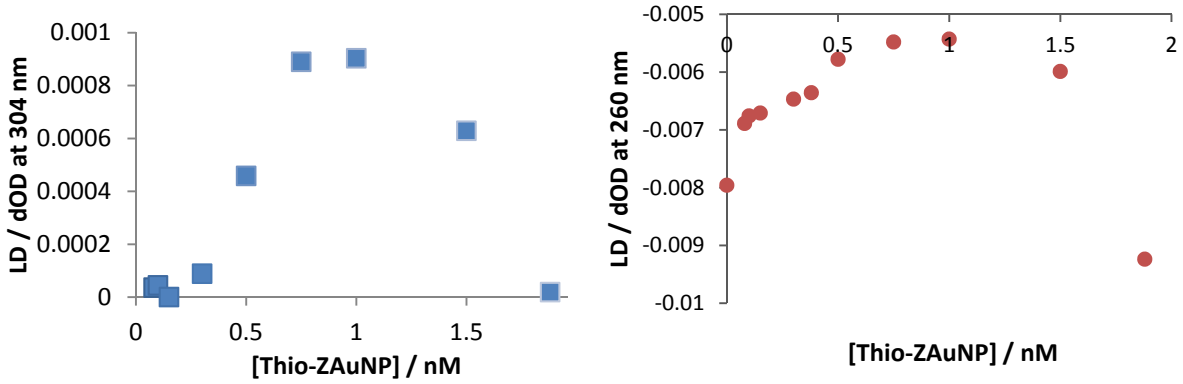

Figure 48: Intensity of ILD at 304 nm (blue) and 260 nm (red) with increasing concentration of Thio-ZAuNP

These results are different to those observed when the free thioacetate complex, $[Fe_2(L_{Thioacetate})_3][BF_4]_4$, is added to ct-DNA, *section 3.2.4*. In the case of the free cylinder, ct-DNA signals continually decreased with increased complex concentration due to stiffening and coiling of the DNA on binding and the ILD signal is at 329 nm. These spectral differences may be due to conflicting spectroscopy from the DNA, nanoparticle and iron complex.

4.5 AuNP/3WJ Polyacrylamide Gel Studies

Polyacrylamide gel electrophoresis, PAGE, is a technique used to separate charged macromolecules, based on molecular size and overall charge [41]. The technique can be used to investigate interactions of compounds with a variety of biological macromolecules including proteins, RNA and oligonucleotides [42].

Within the Hannon group, PAGE has previously been used to show supramolecular helicates interacting with alternative DNA and RNA structures, specifically folk structures and three-way junctions, 3WJ [42, 43]. Interactions between nanoparticles and DNA have previously been investigated using gel techniques to investigate such interactions with silver nanoparticles [44] and in order to fluorescently label DNA strands [45].

Through using this technique, it was hoped to investigate whether DNA 3WJs can be formed in the present of helicate functionalised nanoparticles. The free tetra-cationic cylinders are able to stabilise 3WJs, and promote three complementary DNA strands interacting with each other to form junction structures [42]. It was therefore investigated what effect anchoring the helicate structures to AuNPs had on the ability of such compounds to stabilise the DNA, compared to the free cylinders, Figure 49.

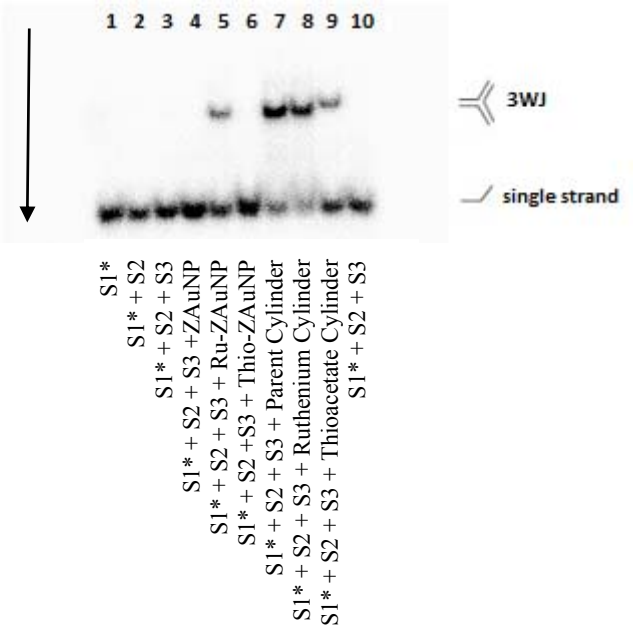

Figure 49: Autoradiogram of gel demonstrating 3WJ formation in the presence of triple stranded helicates

Under the conditions used, no 3WJ species are formed when only the three DNA strands were incubated prior to running the experiment. Only in the presence of the helicate species are 3WJ structures observed in the gel.

In lanes 7-9, free cylinders were incubated with the three complementary DNA strands, prior to running the gel. In each of these lanes 3WJ was formed, indicated by the higher, slower running spots on the gel. Ratios of single stranded DNA: 3WJ were calculated by the relative spot intensities on the autoradiogram, Figure 50.

Results show that the parent and ruthenium cylinders, which are of similar size and shape, promote equal quantities of 3WJ formation. The thioacetate cylinder, which has six additional groups attached to the parent structure, also promotes 3WJ formation, yet only half of much as for the original structures. This may be due to the bulky structure of the functionalised cylinder, hindering the ability of the DNA strands to come together, making for a poor fit into the central cavity of the junction. The spot which represents the thioacetate/3WJ species in the gel, is

slightly higher than the other corresponding 3WJ species, consistent with results observed in *section 3.7*, which is likely due to the higher molecular mass of the thioacetate cylinder causing the conjugate species to run slower in the gel.

Lane	*Contents of lane*	*3WJ*	*SS DNA*	*% 3WJ*
1	**S1***	**-**	1123	**-**
2	**S1* + S2**	**-**	943	**-**
3	**S1* + S2 + S3**	**-**	1046	**-**
4	**S1* + S2 + S3 +ZAuNP**	**-**	1303	**-**
5	**S1* + S2 + S3 + Ru-ZAuNP**	524	913	**36.5**
6	**S1* + S2 +S3 + Thio-ZAuNP**	**-**	1117	**-**
7	**S1* + S2 + S3 + Parent Cylinder**	1223	585	**67.6**
8	**S1* + S2 + S3 + Ruthenium Cylinder**	881	413	**68.1**
9	**S1* + S2 + S3 + Thioacetate Cylinder**	506	869	**36.8**
10	**S1* + S2 + S3**	**-**	879	**-**

Figure 50: Table representing the contents of the gel in *Figure 49*, with quantitative values of single stranded (ss) and 3WJ ratios for each lane of PAGE gel

On combining the three complimentary strands with functionalised nanoparticles, lanes 4-6, no induced formation of 3WJ was witnessed for ZAuNPs and Thio-ZAuNPs. It was expected for ZAuNPs, that no junction structures would be formed as no helicate was present and the overall negative charge of the nanoparticles would not encourage the negative DNA strands to come together.

On incubation with Thio-ZAuNPs, no 3WJ was formed, likely resulting from the thioacetate cylinder being anchored onto the nanoparticle surface, making it unavailable to promote 3WJ formation. Lack of 3WJ may also be because of a change of the electrostatics within the system. The tetracationic cylinder is now incorporated into an overall negatively charged surface of the nanoparticles. This overall negative charge may result in the DNA strands becoming unreceptive to the structural advantages of the cylinder itself, and only 'see' the nanoparticle as a whole.

RuZAuNPs do promote some 3WJ formation, indicating that the structure is stabilised within the central cavity of the junction, as has previously been seen [42]. The ruthenium cylinder is only attached to the negatively charged particles by electrostatics, so may be labile on the surface, meaning it is still able to interact with the DNA strands. This may give an early indication, that nanoparticles could be used as a delivery mechanism for the cylinders, allowing them to interact solely with highly desirable DNA target.

4.6 AuNP Cell studies

4.6.1 Cell Toxicity

As described in *section 3.8.1,* MTT assays can be performed to calculate the IC_{50} of a given compound for a specific cell line. This assay was performed using nanoparticles functionalised with the surfactant (ZAuNP), $[Fe_2(L_{Thioacetate})_3][BF_4]_4$ (Thio-ZAuNP) and $[Ru_2(L_P)_3]Cl_4$ (Ru-ZAuNP). Toxicity was tested in two different cancer cell lines, A2780: human ovarian carcinoma and A549: adenocarcinomic human alveolar basal epithelial cells, and the relative toxicities were compared with the known anticancer metallo-drug, cisplatin, Figure 51.

Cell Type

	A2780	**A549**
Cisplatin	**8.72** ± 0.85	**14.83** ± 3.08
ZAuNP	**6.10** ± 2.43	**5.63** ± 3.13
ThioZAuNP	**10.57** ± 6.52	**16.81** ± 1.63
Ru-ZAuNP	**5.42** (Preliminary)	**7.41** (Preliminary)

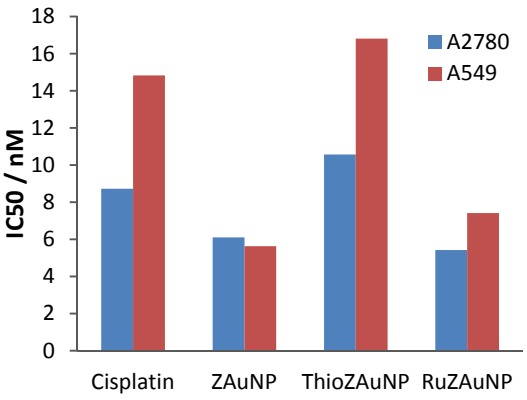

Figure 51: Average toxicity results of functionalised nanoparticles after 72 hrs, IC_{50} / nM

The toxicity of these nanoparticles were analysed after 72 hours. It appeared that each of nanoparticles tested were highly toxic towards both cancer cell lines. This may be as a result of the highly anionic nature of the nanoparticle surfaces, as it has been shown this can result in toxic side effects, resulting from how the particles force entry into the cells through the negatively charged bilayer [46].

The nanoparticles analysed appeared to have a similar toxicity to that of cisplatin. These results show that by functionalising nanoparticles with triple stranded helicates, they are able to exhibit cytotoxic characteristics, which was the desirable effect.

By attaching $[Fe_2(L_{Thioacetate})_3][BF_4]_4$ to AuNPs, the IC_{50} decreases by almost half compared to the free cylinder for the A549 cell line, assuming the nanoparticles are functionalised 1 nM: 1 μM, NP/complex (*section 3.8*). This indicates that despite hindering DNA interactions by being attaching to nanoparticles, the complex is able to enter cells and induce cell death more readily.

Due to lack of compound, preliminary results were obtained for the cytotoxic effects of RuZAuNPs. Initial results show that through combining the ruthenium helicate with gold nanoparticles, a highly cytotoxic agent is formed.

4.6.2 Cell Interaction

As well as investigating how toxic the nanoparticles were to the cancer cell lines, how they interacted with the cells was also examined via TEM. By incubating each nanoparticle (2.5 nM) with cells for 24 hours, it was hoped to gain more knowledge as to how the nanoparticles enter cells and induce cell death.

4.6.2.1 A2780: human ovarian carcinoma

Images were first taken of the cells without nanoparticles present, to view the organelles and general cell appearance unaltered from any outside influence. By comparing these images to those found when nanoparticles are present, effects to the cell were investigated.

A2780 Control

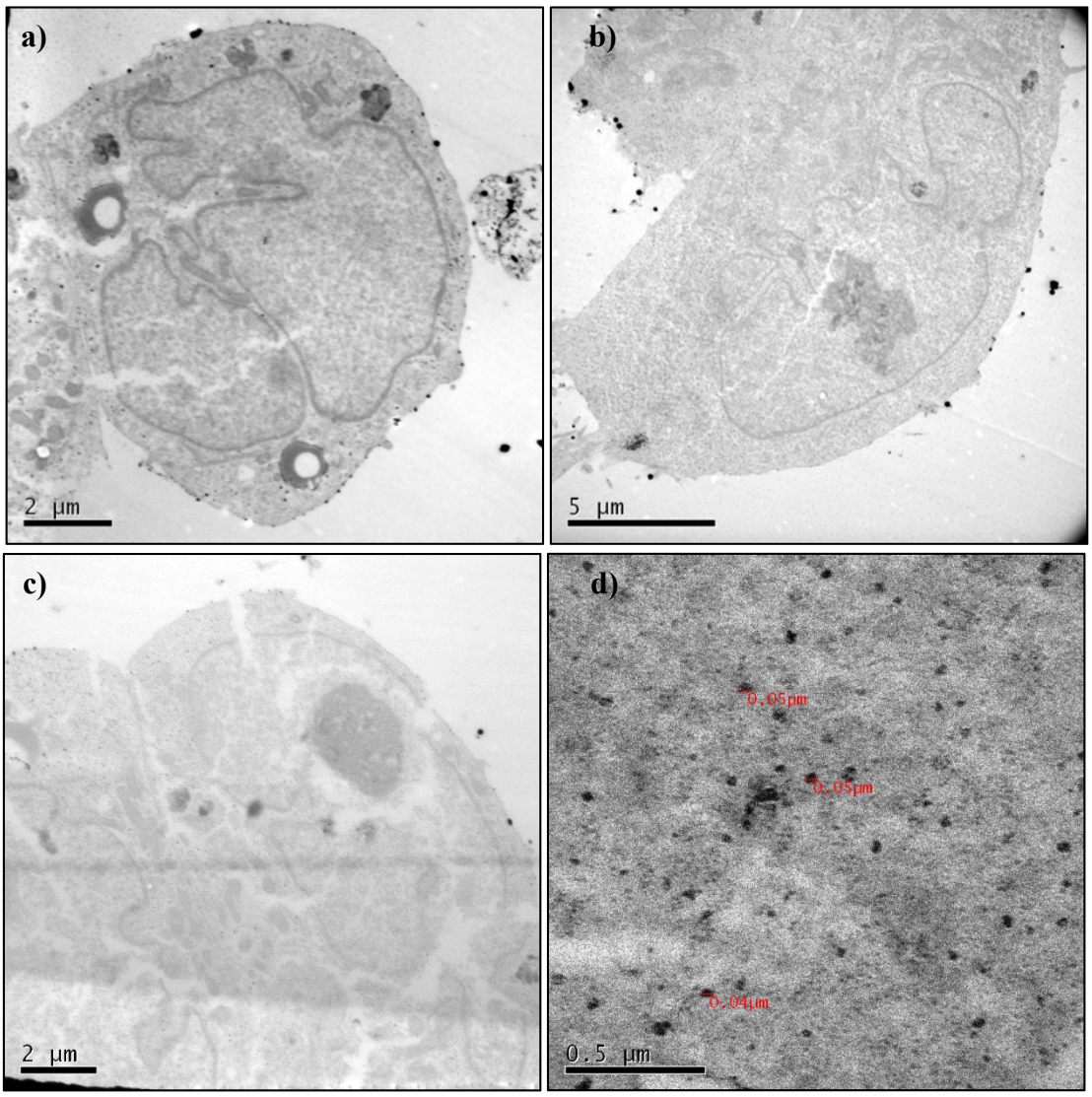

Figure 52: TEM images of control A2780 cells, showing a representative selection of cells at different magnifications

Control images, Figure 52, show cells 10-15 μm in size. Despite the cells not being stained, the internal structure of the cells and organelles can clearly be seen. Dark matter is present in the control samples around the edge of the cells, resulting from the sample preparation. These dark marks are >50 nm in diameter and do not have a large contrast to the rest of the cell body. As a result any matter of this appearance apparent in experimental cell samples will not be analysed as an occurrence resulting from the nanoparticles.

A2780 ZAuNP

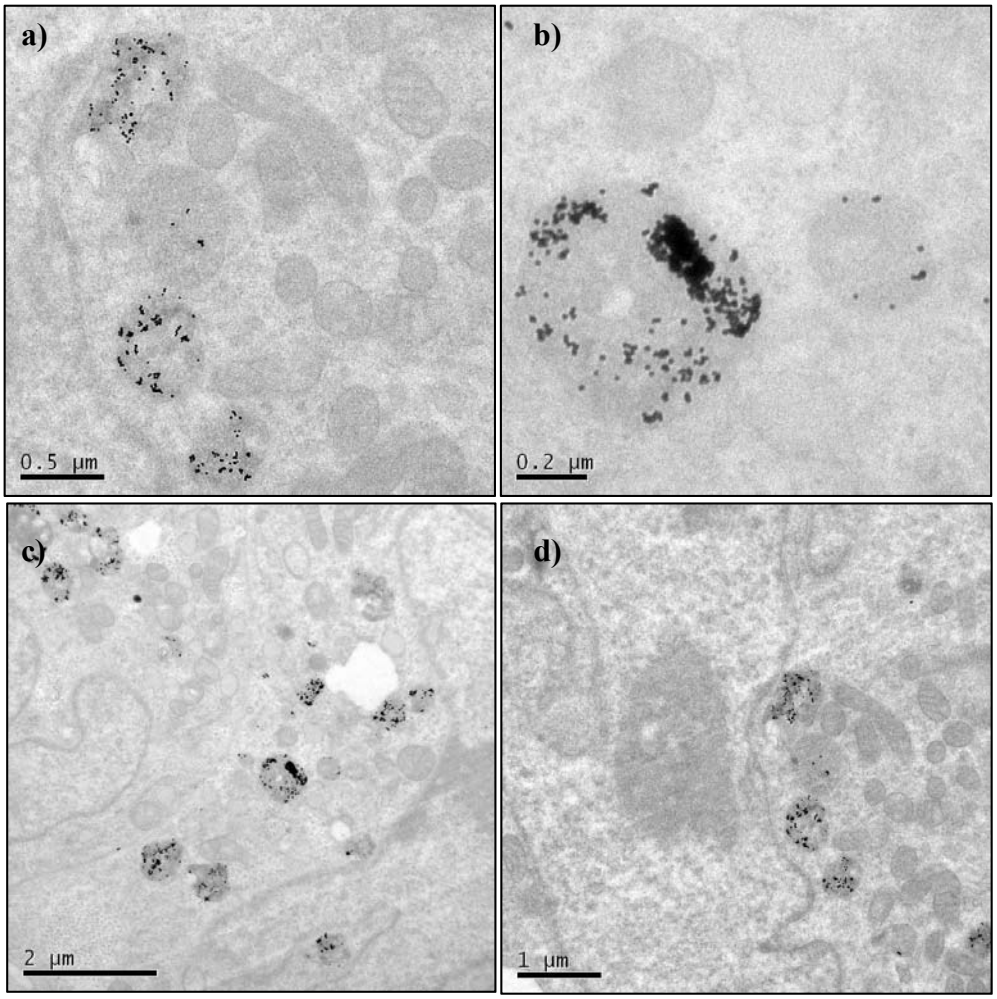

Figure 53: TEM images of A2780 cells incubated with ZAuNPs, showing a representative selection of cells at different magnifications

After incubation of the ovarian cancer cell line with ZAuNPs for 24 hours, it was witnessed that nanoparticles had entered the cells. On closer inspection, it appeared the nanoparticles were contained within vesicles, with multiple ZAuNPs being engulfed into the cells together. Definition between each nanoparticle can be seen, indicating that the highly negative surface charge on the nanoparticles, allows them to maintain stability in the media and cell environment without forming large aggregates.

These results suggest that the nanoparticles entered the cells via endocytosis [47], where they are engulfed into the cells by being encapsulated within a portion of cell membrane. It has previously been found that larger nanoparticles, ~50 nm, may be up taken by cells my readily by this method, which may also be the cause of multiple nanoparticles being taken up by the cells [48].

A2780 RuZAuNP

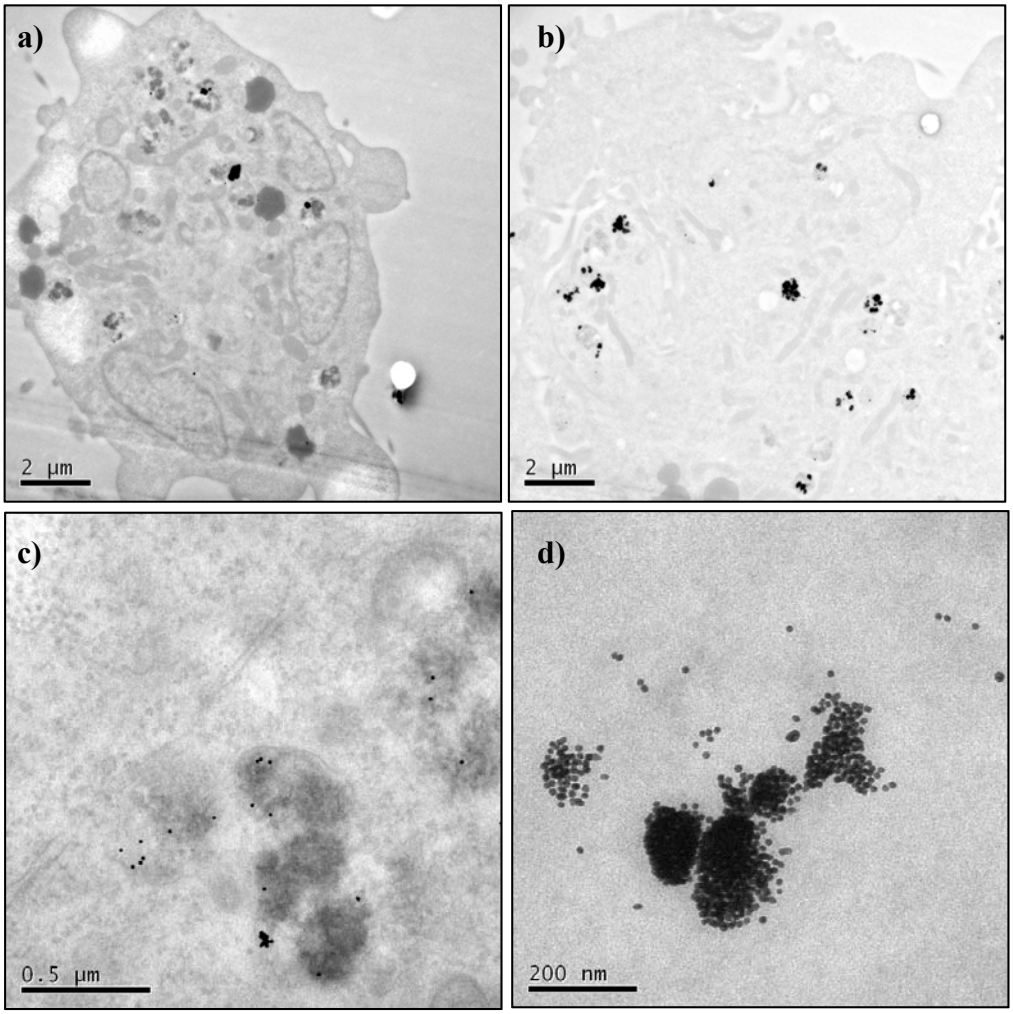

Figure 54: TEM images of A2780 cells incubated with RuZAuNPs, showing a representative selection of cells at different magnifications

On addition of RuZAuNPs to A2780 cells, it was observed that the functionalised nanoparticles had entered cells after 24 hours. In this instance, it appeared that as well as single nanoparticles, aggregate species of ~100-200 nm had entered the cells. Unlike with ZAuNPs, no vesicle boundary was detected surrounding the nanoparticles, Figure 54 (d). Absence of this indicates another route was taken for the nanoparticles to enter the cell. RuAuNPs appeared to be sporadically located throughout the cells, indicating that uptake is not directed to a specific organelle, Figure 54 (a) and (b).

A2780 Thio-ZAuNP

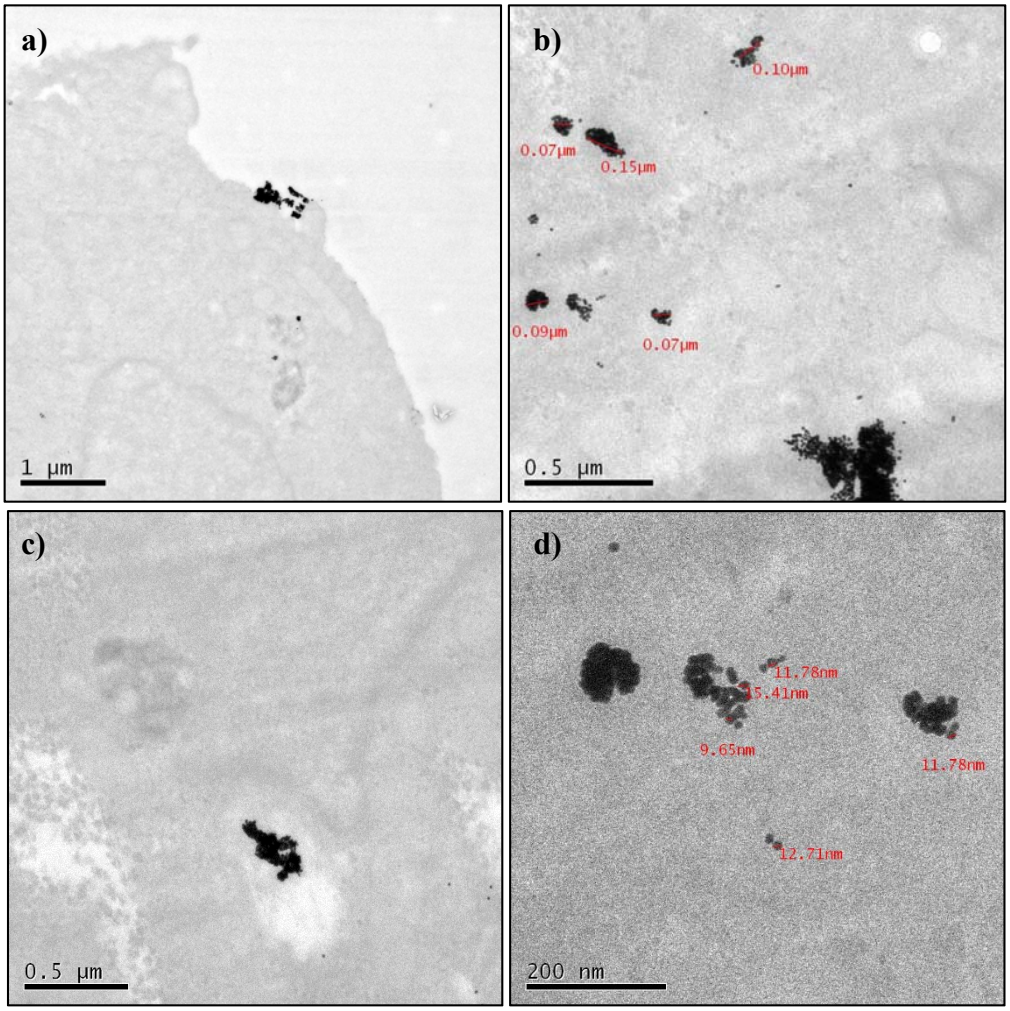

Figure 55: TEM images of A2780 cells incubated with Thio-ZAuNPs showing a representative selection of cells at different magnifications

As with Ru-ZAuNPs, on addition of the thioacetate functionalised particles, Thio-ZAuNPs, they appeared to have entered cells as aggregates, Figure 55 (b). These larger aggregate species are made up of smaller ~15 nm particles, indicating that it was Thio-ZAuNPs being observed in the cells. The particles appear to be entering a cell in Figure 55 (a), and once inside the cells, are not surrounded by vesicles, Figure 55 (d).

Consequently it can be hypothesised that when a cylinder complex is attached to surfactant coated nanoparticles, ZAuNPs, the mode of action to enter the ovarian cancer cells is altered.

This may be the cause of the higher toxicity results detected for ZAuNPs within MTT assays (*section 4.6.1*).

4.6.2.2 A549: adenocarcinomic human alveolar basal epithelial cells

Equivalent experiments to those described in *section 4.6.2.1* were performed with the epithelial cancer cell line, A549. By comparing two different cell lines, it was examined whether the mode of uptake and effects caused to cells were altered on changing cell type.

A549 Control

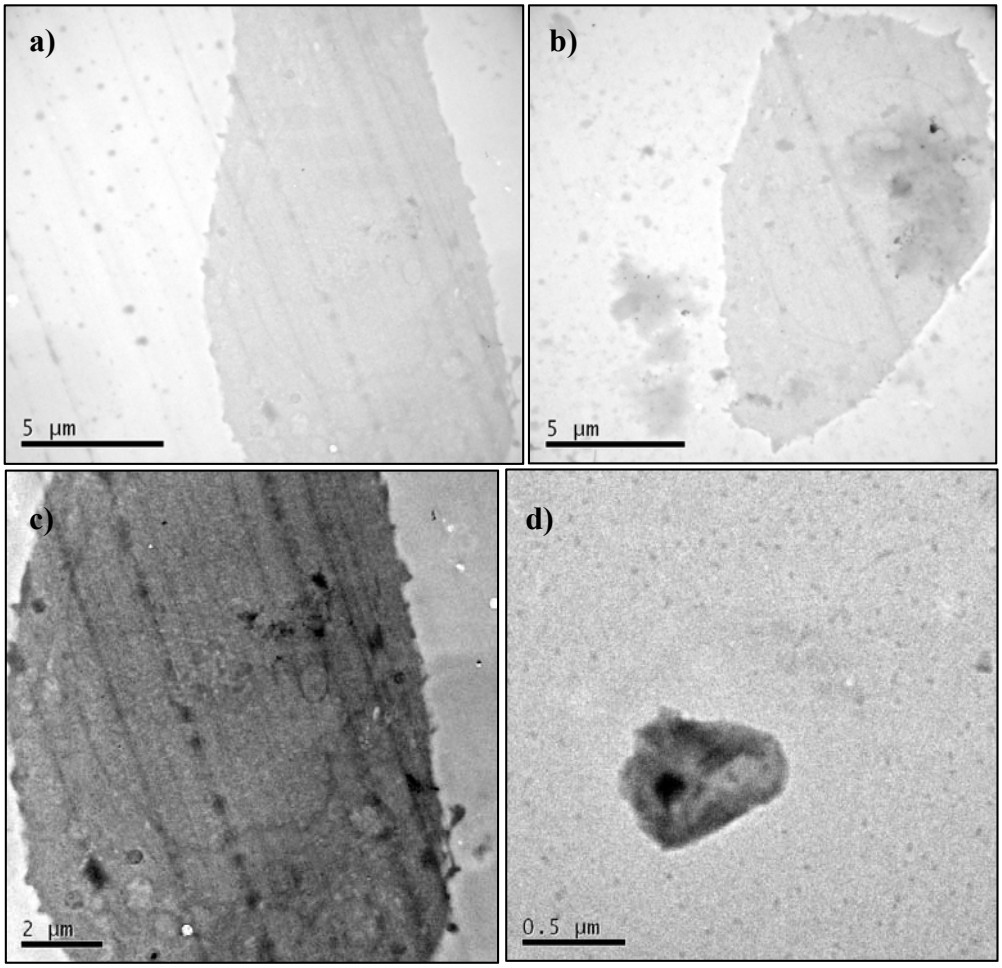

Figure 56: TEM images of control A549 cells showing a representative selection of cells at varying magnifications

Control images, Figure 56, show cells approximately 10 by 15 µm in size. Some internal structure of the cells can clearly be seen, however there is less contrast in the cells making specific organelles less visible. From these images, it can be seen that the cell membranes are not smooth and that there is no nanosized matter visible within the cells prior to treatment.

A459 ZAuNP

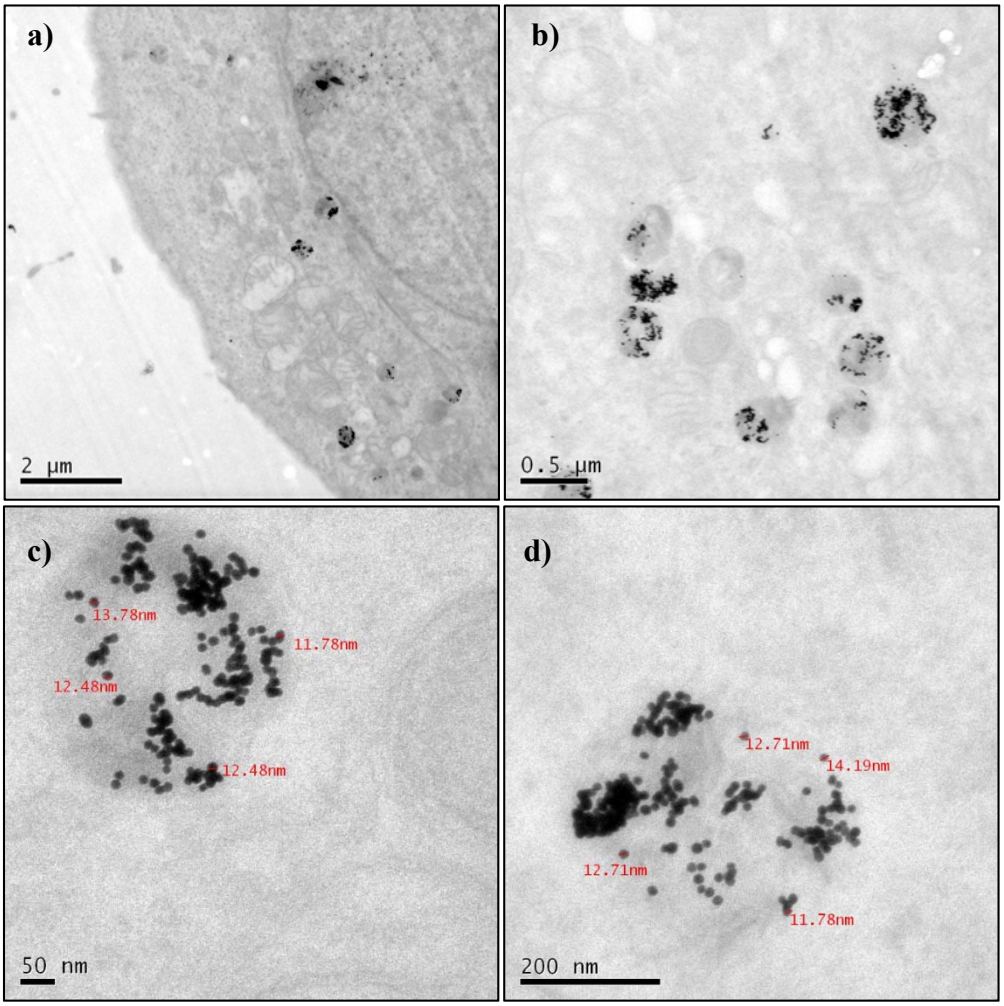

Figure 57: TEM images of A549 cells incubated with ZAuNPs showing a representative selection of cells at varying magnifications

On addition of ZAuNPs to this cell line, the highly contrasting AuNPs can clearly be visualised within cells. As seen with the A2780s, engulfed nanoparticles appear to be within vesicle

structures, and despite there being multiple nanoparticles within each vesicle, nanoparticles were mostly un-aggregated. It appears that ZAuNPs interact with the two cell lines in a similar way, which may result in the highly toxic nature of the nanoparticles towards both cell lines.

A459 RuZAuNP

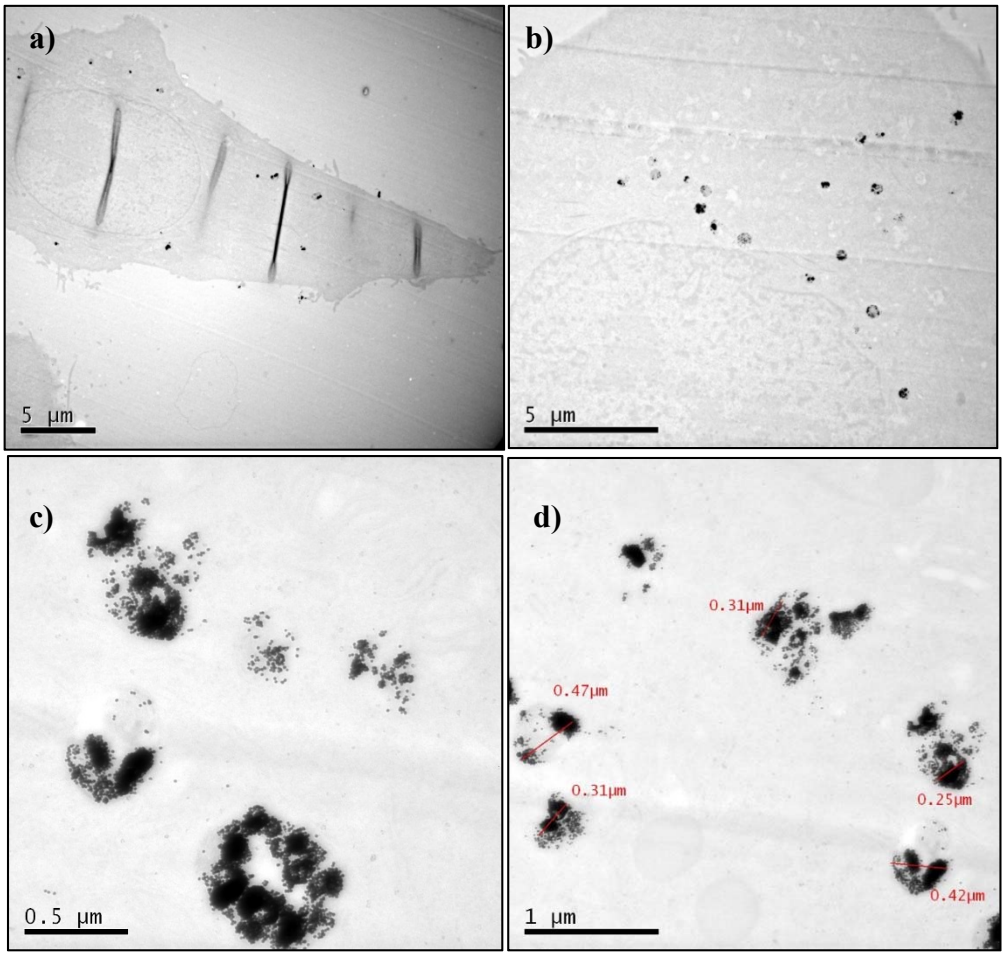

Figure 58: TEM images of A549 cells incubated with RuZAuNPs showing a representative selection of cells at varying magnifications. (a) Image of entire cell, black lines indicate folds from the sample preparation

On addition of RuZAuNPs to the A549s, it appeared nanoparticles had entered cells after 24 hours. In this instance, it appeared that aggregates had entered the cells via vesicles of ~0.4 µm in size, Figures 58 (c) and (d). This is different to that observed for the A2780 cell line, where

no membrane boundary was detected around the nanoparticles. There was no evidence of the nanoparticles having entered the nucleus after the 24 hr incubation period, Figures 58 (a) and (b), indicating that they were being retained in the vesicle structures or that they were not able to enter the nucleus as a result of them being aggregated after incubation with the cells.

A549 Thio-ZAuNP

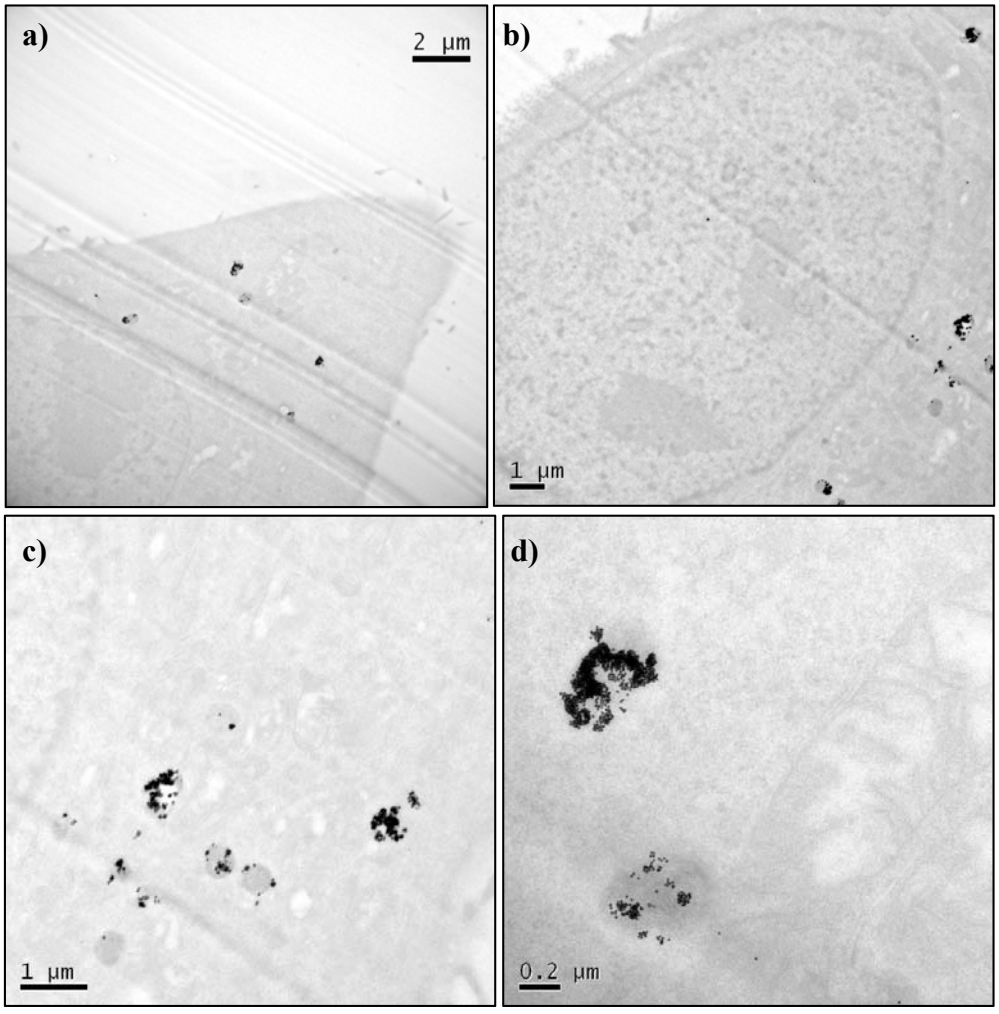

Figure 59: TEM images of A549 cells incubated with Thio-ZAuNPs showing a representative selection of cells at varying magnifications

On addition of Thio-ZAuNPs to A549 cells, the nanoparticles appear to enter cells in groups, rather than single particles. As detected with ZAuNPs and RuZAuNPs, the nanoparticles appear

to be surrounded by an intercellular membrane, indicating that these nanoparticles entered cells via endocytosis. Unlike when incubated with A2780s, Figure 55, the nanoparticles appeared to be less aggregated overall, with smaller clusters of nanoparticles being detected. After 24 hours of incubation, it appears individual nanoparticles are no longer bound within vesicle structures, Figure 59 (c), indicating that on further incubation, Thio-ZAuNPs may distribute throughout the cells.

4.7 Thioacetate-Gold Surface Interaction

Note: Experimental results were performed in collaboration with Sam Adams. Results are included for completeness.

The thioacetate functionalised cylinder described in *section 3.1.4* allows for a covalent linkage to be formed between the helicate complex and the gold surface of a nanoparticle. The effect of binding the cylinder to the nanoparticle surface has been investigated regarding DNA binding and cell cytotoxicity, the morphology of the cylinder, and how it interacts with the gold surface was also investigated with the use of ellipsometry and surface plasmon resonance, SPR.

4.7.1 Ellipsometry

Ellipsometry is an optical technique which can be used to analyse the surface of materials, analysing changes in polarised light over the surface. Specifically it can be used to get information on monolayer formation on a gold surface [49, 50]. As such, it was investigated what effect addition of the thioacetate cylinder in acetonitrile had to a gold surface.

Each thioacetate cylinder has six positions where an interaction can occur with gold, two thioacetate moieties per ligand. It was therefore investigated how these sulphur linkers and so the cylinder, interacted with a gold surface.

Firstly a gold surface was analysed by incident radiation, to gain information of the bare gold surface. Additional gold surface samples were then incubated with the thioactate cylinder (1 mg/mL in MeCN), for increasing increments of time. The samples were then washed with MeCN and the solvent residue remove. The incubated samples were then also analysed using incident radiation, to measure an optical response from the functionalised gold surfaces. By analysing the change in polarization from the incident radiation, on how it interacts with the material on the surface, changes to the surface height can be established.

From initial ellipsometry results, it appeared that the cylinder complex was lying on the gold surface. Dimensions of the parent cylinder are known to be 2 nm by 1nm [34], and as such the overall length of the thioacetate functionalised cylinder would be much greater at approximately 6.5 nm. On attaching this helicate to the gold surface, a maximum coating of 1.7 nm was observed. This increase to the gold surface indicates that the cylinder is binding as a result of the sulphur containing moieties and strongly suggests that it is lying on the surface, in a horizontal orientation, Figure 60.

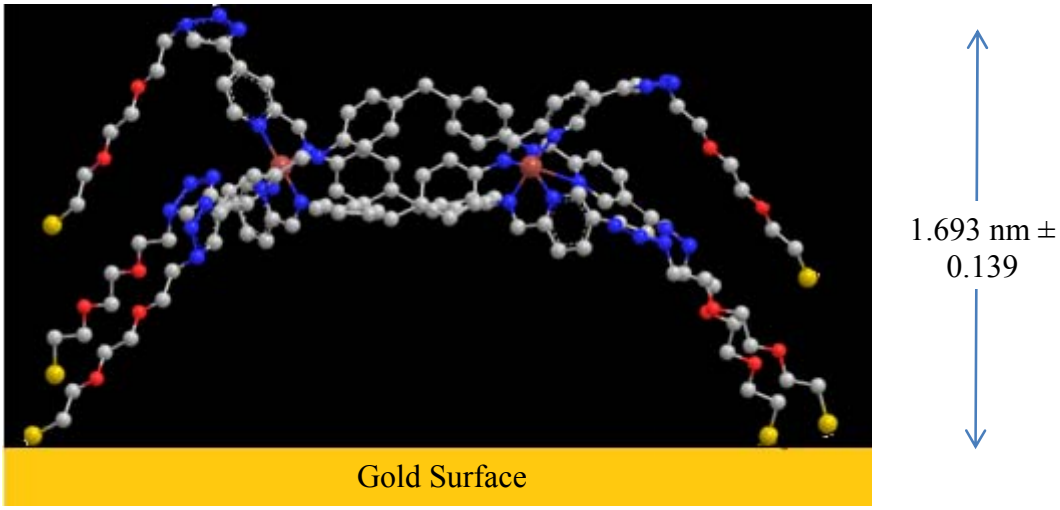

Figure 60: Cylinder model demonstrating how $[Fe_2(L_{Thioacetate})_3][BF_4]_4$ may interact with a gold surface

From modelling the structure of the cylinder, based on models previously produced in the Hannon group for the parent cylinder, it appeared that only four of the six sulphur groups would be able to orientate to the gold surface at one time. The model indicates that both sides of the cylinder would be able to interact with the gold surface, giving an indication as to why the complex is lying on the metal surface as opposed to attaching end on. These four interactions would be more desirable than three from one end of the cylinder.

The thioacetate complex lying along the surface of the gold may be the cause of little/different activity observed with ct-DNA in *section 4.4.3.3* and 3WJ structures in *section 4.5*. As the helicate is lying on the surface it would be unable to bind to the DNA major groove or enter the heart of a DNA 3WJs as previously observed with the free cylinder, *sections 3.1.4 and 3.7*. In order to prevent this from occurring, a reproducible method to functionalise the cylinder on one side is required.

4.7.2 Surface Plasmon Resonance: SPR

Another technique used to investigate the thioacetate cylinder interacting with a gold surface was surface plasmon resonance, SPR. This technique can be used to measure adsorption of a material onto a metal surface and as such is used as an optical chemical or biosensor [51-53]. Within this research, SPR was used to investigate what affinity the thioacetate cylinder had to various DNA structures when attached to a gold surface. By flowing various DNA solutions over the gold surface, it was hoped that an affinity would be observed when the cylinder was present.

Within these experiments three different DNA structures were analysed: ct-DNA, ds-26 (double stranded DNA of 26 bases) and h-Telo quadruplex DNA. These DNA structures were tested as most of the DNA binding studies were performed with ct-DNA, and it was hoped that binding affinities to shorter duplex DNA may be easily detected. A folded G-quadruplex structure was analysed to identify if the helicate, which was suspected to be lying on the gold surface, would be able to interact with the planar surface of a quadruplex, an interaction which has previously been identified [54]. 3WJ DNA was not tested as it was already shown in *section 4.5*, that on binding the thioacetate helicate to AuNPs, the binding affinity to such structures was lost.

It was first investigated whether the bare gold surface showed any affinity to the DNA solutions, without the iron helicate present. After 10 minutes of the system equilibrating, the various DNA solutions (15 μM) were injected over the bare gold surface. These solutions were washed over the surface for 30 minutes before being washed away with tris-HCl buffer (pH 8.0). After this period, the gold surface showed no affinity to the duplex DNA solutions. There was a slight affinity of the gold surface to quadruplex DNA, but this was a weak interaction, Figure 61.

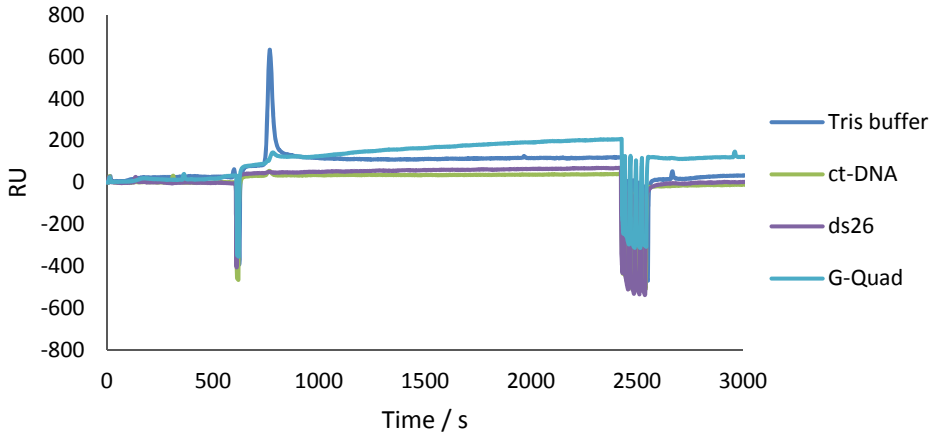

Figure 61: SPR date for DNA binding affinity onto bare gold surface

When the thioacetate cylinder (1 mM) was added in acetonitrile to the gold surface, as with the ellipsometry data, a binding affinity was observed, Figure 62. Even after washing the surface with excess acetonitrile (at 2400 s), the cylinder was still bound to the surface, another indication that the cylinder does indeed bind to gold and therefore to AuNPs.

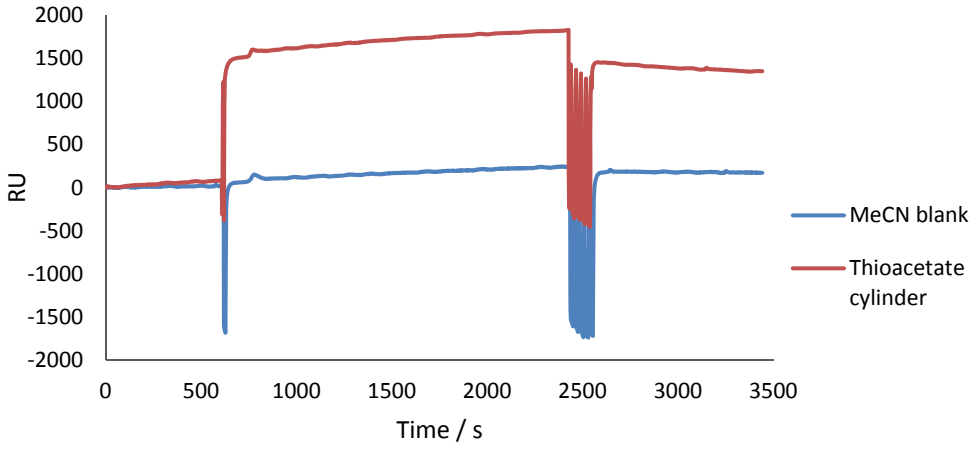

Figure 62: SPR data showing $[Fe_2(L_{Thioacetate})_3][BF_4]_4$ on the Au surface with MeCN blank

Once the cylinder was attached to the gold surface, the DNA solutions were washed over the surface to explore the binding affinity of the bound cylinder. This experiment showed no binding affinity towards ct-DNA and only a slight interaction with the quadruplex and ds-26

DNA strands, Figure 63. These results were higher than for the bare gold surface, but were not comparable to literature results [51-53].

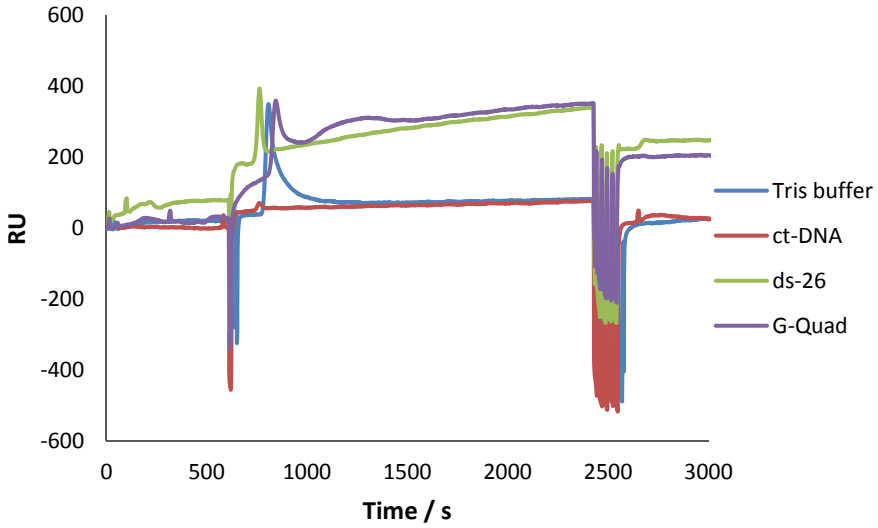

Figure 63: SPR data for DNA interactions over a gold surface with $[Fe_2(L_{Thioacetate})_3][BF_4]_4$ bound

4.8 Conclusions

Through addition of metal helicate species to the surface of gold nanoparticles, it can be concluded that stable, functionalised nanoparticles were formed which were able to interact with DNA structures and enter cancer cells.

Through electrostatic interactions, a ruthenium helicate was incorporated onto the surface of AuNPs. These fluorescent particles were able to interact with ct-DNA to induce a structural change and promoted formation of other DNA structures such as 3WJs. Initial studies suggested that these particles were highly toxic towards certain cancer cell lines. It would therefore be advantageous to explore the toxicity and selective drug delivery capabilities of these nanoparticles further, in the future.

Through adding additional functionality to the parent cylinder developed within the Hannon group, it was possible to alter the helicate properties, and through addition of new sulphur

moieties, a triple stranded iron helicate, $[Fe_2(L_{Thioacetate})_3][BF_4]_4$, was attached to AuNPs and gold surfaces through covalent bonding. Whilst attached to the nanoparticle surface these structures were able to interact with ct-DNA and induce a structural change.

The activity of this 'thioacetate complex' was however hindered by binding to the gold surface, shown by CD, LD, PAGE and SPR studies. The free complex is able to kink and coil ct-DNA on binding and can induce 3WJ formation. The Thio-ZAuNPs however, showed weaker interactions with ct-DNA and only minor binding affinities to ds-26 and quadruplex DNA. These results indicate that it is important for future work in this area, to synthesise helicate structures which are only functionalised on one side of the cylindrical structure. This would allow the cylinders to be more mobile on the gold surface and so able to interact with the grooves of ct-DNA and other DNA structures, such as the heart of a 3WJ.

The main intention of this project however was achieved, providing useful insight into how this area of research can be progressed in the future, to hopefully produce a successful anticancer therapy, using supramolecular chemistry with nanotechnology.

4.9 References

1. W. E. Bawarski, E. Chidlowsky, D. J. Bharali and S. A. Mousa, *Nanomed. Nanotechnol.*, 2008, **4**, 273–282
2. N. L. Rosi and C. A. Mirkin, *Chem. Rev.,* 2005, **105**, 1547-1562
3. P. C. Chen, S. C. Mwakwari and A. K. Oyelere, *Nanotechnol Science Appl.,* 2008, **1**, 45-66
4. N. Sanvicens and M. P. Marco, *Trends Biotechnol.*, 2008, **26**, 425-433
5. R. Bhattacharya, C. R. Patra, A. Earl, S. Wang, A. Katarya, L. Lu, J. N. Kizhakkedathu, M. J. Yaszemski, P. R. Greipp, D. Mukhopadhyay and P. Mukherjee, *Nanomed. Nanotechnol.,* 2007, **3**, 224–238
6. M.-C. Daniel and D. Astruc, *Chem. Rev.*, 2004, **104**, 293-346
7. J. Turkevich, P. C. Stevenson and J. Hillier, *Discuss. Faraday Soc.*, 1951, **11**, 55-75
8. S. D. Brown, P. Nativo, J-A. Smith, D. Stirling, P. R. Edwards, B. Venugopal, D. J. Flint, J. A. Plumb, D. Graham and N. J. Wheate, *J. Am. Chem. Soc*., 2010, **132**, 4678–4684
9. B. Devika Chithrani, A. A. Ghazani and W. C. W. Chan, *Nano Lett.*, 2006, **6**, 662-668
10. E. E. Connor, J. Mwamuka, An. Gole, C. J. Murphy and M. D. Wyatt, *Small*, 2005, **3**, 325-327
11. H. K. Patra, S. Banerjee, U. Chaudhuri, P. Lahiri and A. K. Dasgupta, *Nanomedicine*, 2007, **3**, 111-119
12. S. Hirn, M. Semmler-Behnke, C. Schleh, A. Wenk, J. Lipka, M. Schäffler, S. Takenaka, W. Schmid, U. Simon and W. G. Kreyling, *Eur. J. Pharm. Biopharm.*, 2011, **77**, 407-416
13. N. P. Pavletich and C. O. Pabo, *Science*, 1993, **261**, 1701-1707
14. I. Meistrmann, V. Moreno, M. J. Prieto, E. Moldrheim, E. Sletten, S. Khalid, P. M. Rodger, J. C. Peberdy, C. J. Issac, A. Rodger and M. J. Hannon, *Proc. Natl. Acad. Sci. USA*, 2002, **99**, 5069-5074
15. P. Ghosh, G. Han, M. De, C. K. Kim and V. M. Rotello, *Adv. Drug Deliv. Rev.*, 2008, **60**, 1307-1315
16. F. Westerlund and T. Bjørnholm, *Curr. Opin. Colloid Interface Sci.*, 2009, **14**, 126–134
17. J-W. Park and J. S. Schumaker-Parry, *J. Am. Chem. Soc.*, 2014, **136**, 1907-1921
18. W. I. Goldburg, *Am. J. Phys.*, 1999, **67**, 1152-1160

19. H. Soo Choi, W. Liu, P. Misra, E. Tanaka, J. P. Zimmer and B. Itty Ipe, *Nat Biotechnol*, 2007, **25**, 1165-1170
20. B. J. Berne and R. Pecora, Dynamic Light Scattering: with applications to chemistry, biology and physics, Courier Corporation, New York, 2000, 6-91
21. J. B. Falabella, T. J. Cho, D. C. Ripple, V. A. Hackley and M. J. Tarlov, *Langmuir*, 2010, **26**, 12740-12747
22. Particle Sizing Systems: Building solutions one particle at a time, Definitions, Dynamic light scattering, Figure B
23. R. J. Hunter, Zeta Potential in Colloid Science: Principles and Applications, Vol. 2, Academic Press, London, 2013
24. A. Liese and L. Hilterhaus, *Chem. Soc. Rev.*, 2013, **42**, 6236-6249
25. G. Sonavanea, K. Tomoda and K. Makinoa, *Colloids Surf., B*, 2008, **66**, 274-280
26. Malvern Instruments Ltd, Support, Research Centre, Technical notes, Zeta potential-An introduction in 30 minutes, Version 3, 2015
27. D. B. Williams and C. B. Carter, The Transmission Electron Microscope, Second Ed., Springer, New York, 2009, 3-22
28. P. Wu, X. Zhu, W. Jin, S. Hao, Q. Liu and L. Zhang, *Biochem. Biophys. Res. Commun.*, 2015, **460**, 183-190
29. S. Gutsch, D. Hiller, J. Laube, M. Zacharias and C. Kübel, *Beilstein J. Nanotechnol.*, 2015, **6**, 964-970
30. Y. Dong, H-L. Xu, M-L. He, F-Y. Fu and C-J. Zhu, *J. Appl. Polym. Sci.*, 2015, **132**, 42251-42260
31. P. V. Devarajan, A. B. Jindal, R. R. Patil, F. Mulla, R. Gaikwad and A. Samad, *J. Pharm. Sci*, 2010, **99**, 2576-2581
32. Y. Maeda, T. Toyoda, T. Mogi, T. Taguchi, T. Tanaami, T. Matsunaga and T. Tanaka, *Electochim. Acta*, 2015, **168**, 308-312
33. A. I. Bulavchenko, A. A. Sap'yanik, M. G. Demidova, M. I. Rakhmanova, and P. S. Popovetskii, *Russ. J. Phys. Chem. A.*, 2015, **89**, 828-834
34. M. J. Hannon, V. Moreno, M. J. Prieto, E. Moldrheim, E. Sletten, I. Meistermann, C. J. Isaac, K. J. Sanders and A. Rodger, *Angew. Chem. Int. Ed.*, 2001, **40**, 879- 884
35. D. J. Lewis, T. M. Day, J. V. MacPherson and Z. Pikramenou, *Chem. Commun.*, 2006, **13**, 1433-1435

36. N. J. Roberts, S. Claire, R. M. Harris, S. Farabi, G. Zikeli, I. B. Styles, N. J. Hodges and Z. Pikramenou, *Chem. Commun.*, 2014, **50**, 617
37. Y. Liu, L. Zhang, W. Wei, H. Zhao, Z. Zhou, Y. Zhanga and S. Liua, *Analyst*, 2015, **140**, 3989-3995
38. R. Rajesh, E. Sujanthi, S. Senthil Kumar and R. Venkatesan, *Phys. Chem.*, 2015, **17**, 11329-11340
39. I. Meistermann, V. Moreno, M. J. Prieto, E. Moldrheim, E. Sletten, S. Khalid, P. M. Rodger, J. C. Peberdy, C. J. Issac, A. Rodger and M. J. Hannon, *Proc. Natl. Acad. Sci. USA*, 2002, **99**, 5069-5074
40. G. I. Pascu, A. C. G. Hotze, C. Sanchez-Cano, B. M. Kariuki and M. J. Hannon, *Angew. Chem. Int. Ed.*, 2007, **46**, 4374-4378
41. A. Chrambach and D. Rodbard, *Science*, 1971, **171**, 440-451
42. J. Malina, M. Hannon and V. Brabec, *Chem. Eur. J.*, 2007, **13**, 3871-3877
43. S. Phongtongpasuk, S. Paulus, J. Schnabl, R. K. O. Sigel, B. Spingler, M. J. Hannon and E. Freisinger, *Angew. Chem. Int. Edit.*, 2013, **52**, 11513-11516
44. V. Ahmed, J. Kumar, M. Kumar, M. B. Chauhan and N. S. Chauhan, *Int. J. Polym. Mater.*, 2014, **63**, 476-485
45. W-T. Cong, Z-X. Zhu, H-Z. He, Y. Jin, C-X. Jiang, J-K. Choi, L-T. Jin and X-K, Li, *Anal. Biochem.*, 2010, **402**, 99-101
46. N. M. Schaeublin, L. K. Braydich-Stolle, A. M. Schrand, J. M. Miller, J. Hutchison, J. J. Schlager and S. M. Hussain, *Nanoscale*, 2011, **3**, 410-420
47. B. D. Chithrani and W. C. W. Chan, *Nano Lett.*, 2007, **7**, 1542-1550
48. B. D. Chithrani, A. A. Ghazani and W. C. W. Chan, *Nano Lett.*, 2006, **6**, 662-668
49. M. D. Porter, T. B. Bright, D. L. Allara and C. E. D. Chidsey, *J. Am. Chem. Soc.*, 1987, **109**, 3559-3568
50. Z. Balevivius, I. Baleviciute, S. Tumenas, L. Tamosaitis, A. Stirke, A. Makaraviciute, A. Ramanaviciene and A. Ramanavicius, *Thin Solid Films*, 2014, **571**, 744-748
51. B. Liedberg, I. Lundstriim and E. Stenberg, *Sensors Actuat. B-Chem.*, 1993, **11**, 63-72
52. J. Homola, S. S. Yee and G. Gauglitz, *Sensors Actuat. B-Chem.*, 1999, **54**, 3-15
53. J. Homola, *Chem. Rev.*, 2008, **108**, 462-493
54. H. Yu, X. Wang, M. Fu, J. Ren and X. Qu, *Nucleic Acids Res.*, 2008, **36**, 5695–5703

Chapter 5

Conclusions and Future work

5.1 Conclusions

As a result of past success within the Hannon group, developing supramolecular helicates based on the cylinder structure $[Fe_2(C_{25}H_{20}N_4)_3]Cl_4$, it was hoped to add new functionality to this triple stranded complex in order to enhance the DNA binding and cell recognition of the metallo-cylinders. This was hoped to be achieved by conjugating new functionality onto the ligand termini via a novel synthetic route (*Chapter 2*) and then functionalising gold nanoparticles, AuNPs, with the cylinder compounds (*Chapter 4*).

The novel used of click chemistry was used to successfully add different functional groups onto the ligand structure of triple stranded helicates (*Chapter 2*). Three new complexes were synthesised through this novel method, functionalised with an ester, piperidine and thioacetate groups: $[Fe_2(L_{Ester})_3]Cl_4$, $[Fe_2(L_{Piperidine})_3]Cl_4$ and $[Fe_2(L_{Thioacetate})_3][BF_4]_4$ respectively.

It was also attempted to synthesise asymmetric ligands and ruthenium analogues with the newly functionalised aldehydes used within ligand synthesis. However, challenges were faced when purifying these compounds due to the labile nature of the imine bonds within asymmetric ligands and low yields formed for ruthenium complexes. As such only iron cylinders with di-functionalised ligands and the parent ruthenium cylinder were further analysed within this research.

These newly synthesised cylinders were then analysed for their DNA binding and cell recognition properties (*Chapter 3*). Through the use of CD and LD experiments, it was found that each of these new complexes were able to bind to ct-DNA and induce a structural change. $[Fe_2(L_{Ester})_3]Cl_4$ binds to ct-DNA in a specific manner, indicated by the ILD produced on

addition of increasing ratios of complex to DNA. This interaction results in ct-DNA becoming disorientated in solution, indicating a kinking/coiling effect. Despite this, the ester functionalised complex was least toxic towards cancer cell lines tested, indicating that the complex may not be able to access and interact with DNA in the cells.

$[Fe_2(L_{Piperidine})_3]Cl_4$ was also able to interact with ct-DNA, indicated by an ICD produced on addition of the complex to ct-DNA. This structure caused DNA to become disorientated in solution, almost to the same degree as the parent cylinder. $[Fe_2(L_{Piperidine})_3]Cl_4$ promoted least DNA 3WJ to form and was less toxic to cells than the parent cylinder. As such, it appeared that addition of piperidine functionality to the cylinder structure was not advantageous to bio-recognition.

The third new compound synthesised was functionalised with a thioacetate group, $[Fe_2(L_{Thioacetate})_3][BF_4]_4$. This complex was able to bind to ct-DNA, showing induced chirality and orientation on binding by CD and LD respectively. This complex was able to displace Hoechst from ct-DNA indicating that there was some minor groove binding interaction. Of the new compounds, this structure promoted most DNA 3WJ formation and had on par cytotoxicity to cells as the parent cylinder.

The aim of work detailed in Chapter 4 was to determine whether these metallo-cylinder structures could be attached to the surface of AuNPs. $[Fe_2(L_{Thioacetate})_3][BF_4]_4$ contained additional sulphur moieties, allowed for it to be bound to AuNPs and a gold surface. Addition of this complex to surfactant coated nanoparticles resulted in particles which were able to interact with ct-DNA and enter cancer cells resulting in cytotoxicity. Activity of this complex was however hindered on binding to AuNPs, Thio-ZAuNPs showed weaker interactions with ct-DNA by CD, LD and PAGE analysis than the ‘free’ cylinder. Through analysis of

$[Fe_2(L_{Thioacetate})_3][BF_4]_4$ attached to a gold surface, evidence indicated that the complex was lying along the surface which may have resulted in this decreased activity.

It was also attempted to attach these tetra-cationic helicates to AuNPs via electrostatic interactions. The iron parent complex appeared not to be stable in contact with the nanoparticles, but the ruthenium complex $[Ru_2(L_P)_3]^{4+}$, was attached to the surface of surfactant coated nanoparticles. In turn, Ru-ZAuNPs were able to interact with ct-DNA and induce a structural change. They also promoted DNA 3WJ formation, thought to be resulting from dissociation of the complex from the nanoparticle surface and initial results indicate that they are highly cytotoxic to cancer cell lines.

This work demonstrates that on adding new functionality to supramolecular helicates, DNA binding and cytotoxic effects can be manipulated. It also shows that such compounds could be attached to the surface of gold nanoparticles, with the ability to interact with DNA and cellular structures.

5.2 Future Work

Supramolecular helicate structures functionalised through click chemistry and gold nanoparticles coated with cylinders have been described herein.

On binding the sulphur functionalised cylinder to gold surfaces, it was found that the complex was likely lying on the gold surface through binding interactions on both ends of the complex. As a result of these sulphur moieties being present at either end of the cylinder structure, multiple interactions can occur with the AuNPs and it was shown through TEM images that the Thio-ZAuNPs were prone to aggregation.

These results indicate that it is important for future work in this area, to synthesise helicate structures which are only functionalised on one side of the cylindrical structure, Figure 1. This

would allow the cylinders to be more mobile on the gold surface and so able to interact with the major groove of ct-DNA and other DNA structures, such as the heart of a 3WJ.

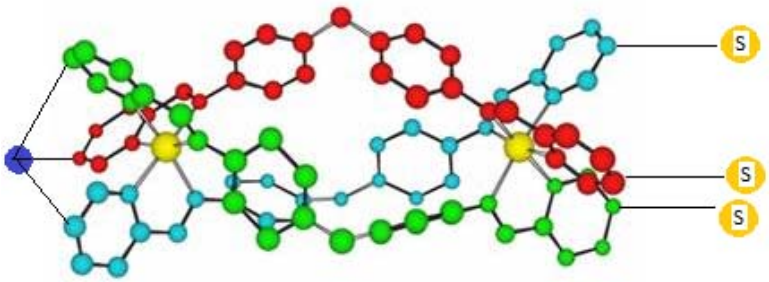

Figure 1: Capped cylinder structure functionalised on one side [adapted from ref[1]]

It was attempted to form asymmetric ligands within this research, where only one side of the ligand had additional functionality. However it was hypothesised that this would result in a mixture of helicate products forming, with the major product being a complex with 2:1 functional groups being on either side of the complex. In the case of nanoparticle binding, this would cause similar effects to those observed with $[Fe_2(L_{Thioacetate})_3][BF_4]_4$. As such, by forming one end of the complex first, or capping one end of the complex before functionalising the helicate with desired functionality, it was thought to dispel such issues. One such possible synthesis is demonstrated in Figure 2.

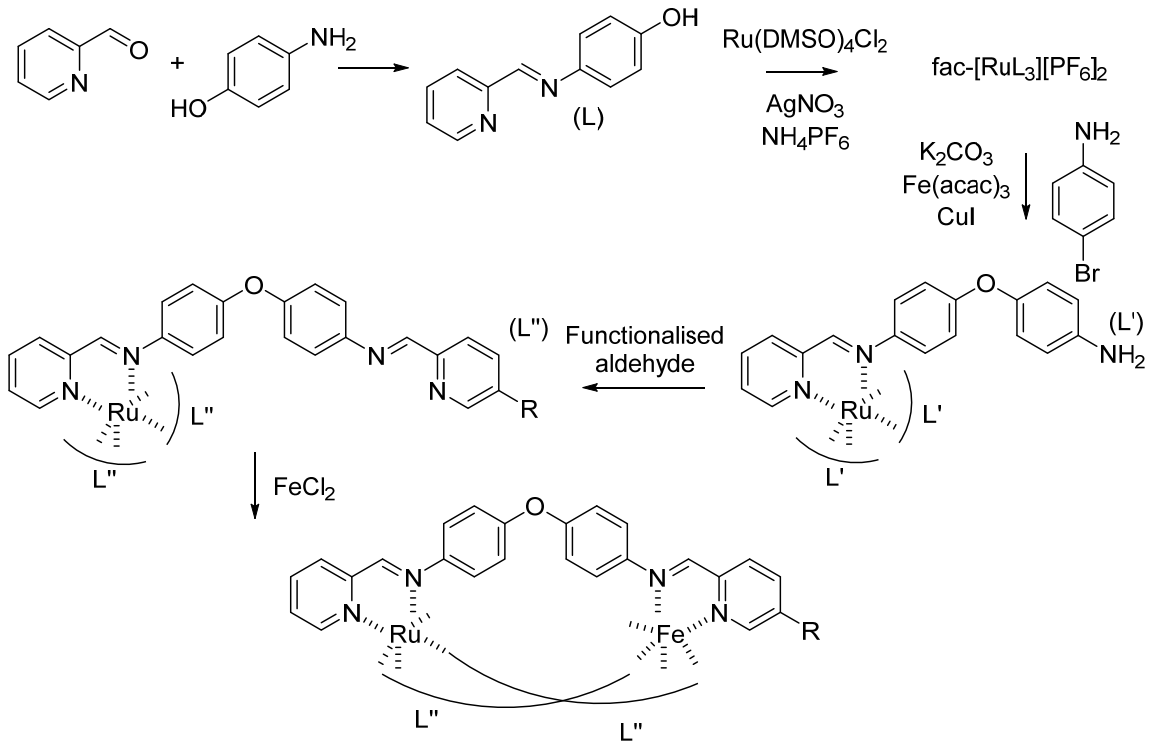

Figure 2: Proposed synthetic route to a one end functionalised triple stranded complex

Within future research, alternative metal centres of helicates can also be investigated. On binding cylinders to the surface of AuNPs, the UV-Vis spectra of the iron and ruthenium helicates were masked by the nanoparticle absorbance. As such, nickel could be investigated which are characteristically orange in colour and therefore will absorb light at a lower wavelength ~480 nm [2]. It may therefore be possible to detect whether the complex is intact on the gold surface by UV-Vis analysis, making it easier to identify and quantify the complex attached.

5.3 References

1. A. C. G. Hotze, N. J. Hodges, R. E. Hayden, C. Sanchez-Cano, C. Paines, N. Male, M-K. Tse, C. M. Bunce, J. K. Chipman and M. J. Hannon, *Chem. Biol.*, 2008, **15**, 1258-1267
2. H. Yu, X. Wang, M. Fu, J. Ren and X. Qu, *Nucleic Acids Res.*, 2008, **36**, 5695–5703

Chapter 6

Experimental

6.1 General Procedures

All solvents and commercially available reagents were bought from Sigma-Aldrich, VWR, Fisher Scientific, Fluorochem and Acros Organics and used without further purification. Deuterated NMR solvents were purchased from Goss Scientific. Water was deionized by use of an Elga Option 3 water purifier. All experiments were carried out in oven-dried glassware under atmosphere or an inert argon atmosphere, as stated.

NMR spectra were recorded using Brüker AVIII300 (300 MHz) and AVIII400 (400 MHz) spectrometers. Chemical shifts (δ) are quoted in parts per million (ppm), using residual protonated solvent as an internal standard and were assigned on the basis of chemical shift and coupling constants using COSY and HSQC experiments where necessary. Abbreviations of multiplicities are: s (singlet), d (doublet), dd (doublet of doublets), t (triplet), q (quartet), m (multiplet). Coupling constants (*J*) are quoted to the nearest 0.1 Hz.

Electrospray Ionisation (ESI) spectra were recorded on a Micromass LCT TOF Mass Spectrometer *m/z* values are reported in Daltons. Elemental analysis was obtained using a CE Instruments EA1110 elemental analyser. Analysis performed by the analytical facility at the University of Birmingham.

Infrared spectra were recorded using a PerkinElmer, Spectrum 100, FT-IR Spectrometer. Absorption maxima (ν_{max}) were recorded in wavenumbers (cm^{-1}) and are classified as strong (s), medium (m), weak (w), broad (br).Thin layer chromatography (TLC) was performed using pre-coated aluminium sheets (Silica Gel 60 F_{254}). Spots were visualised using UV fluorescence (254 nm). Retention factors (R_f) are reported with the solvent used. Flash column

chromatography was performed on Merck 60 silica gel, with a particle size of 40-63 μm, in the solvent system quoted in each case. UV-Vis spectra were recorded on a Cary 5000 Varian spectrometer using 1 cm quartz cuvettes.

CD and LD spectra were recorded on a Jasco J-810 spectropolarimeter. Dynamic Light Scattering (DLS) and Zeta Potential data was obtained using Delca Nano. DLS measurements were taken using disposable cuvettes and results are quoted with units. TEM images were obtained using JEOL 1200EX TEM, 100 kV max, using carbon on copper TEM grids.

6.2 Synthesis of Cylinders

6.2.1 Parent Cylinder

6.2.1.1 Parent Ligand, L_P

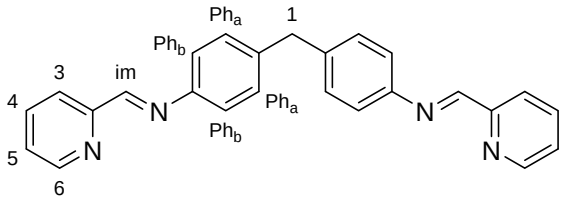

4,4'-Methylenedianiline (1.505 g, 7.59 mmol) was dissolved in EtOH (25 mL), 2-pyridine carboxaldehyde (1.40 ml, 14.71 mmol) was added via syringe followed by an excess of EtOH (35 mL) to encourage stirring. The reaction was stirred at rt for 2 hr in which time a yellow precipitate had formed in solution. Solid collected via suction filtration, washing with copious amounts of EtOH and diethyl ether, to yield a cream solid (2.542 g, 91.8 %).

^{1}H NMR: 300 MHz ($CDCl_3$): δ 8.70 (1H, d, J = 5.1 Hz, H_6), 8.62 (1H, s, H_{im}), 8.19 (1H, d, J = 8.1 Hz, H_3), 7.81 (1H, t, J = 8.1 Hz, H_4), 7.35 (1H, t, J = 6.0 Hz, H_5), 7.26 (4H, s, H_{Pha+b}), 4.04 (1H, s, H_1).

^{13}C NMR ($CDCl_3$): δ 160.30 (C_{im}), 154.91 (C_6), 149.95 (C_3), 136.90 (C_4), 130.02 (C_{Pha}), 125.30 (C_5), 121.63 (C_{Phb}), 41.32 (C_1).

Mass spectrum (+ve ESI): *m/z* 377.3 $[M]^+$, 378.3 $[M+H]^+$, 399.3 $[M+Na]^+$, 400.3 $[M+Na+H]^+$, 415.3 $[M+Na+O]^+$, 431.3 $[M+Na+MeOH]^+$, 432.3 $[M+Na+MeOH+H]^+$, 463.3 $[M+2Na+2K+2H]^+$, 464.3 $[M+2Na+2K+3H]^+$.

6.2.1.2 Parent Cylinder $[Fe_2(L_P)_3]Cl_4$

$[Fe_2(L_P)_3][Cl]_4$ L_P =

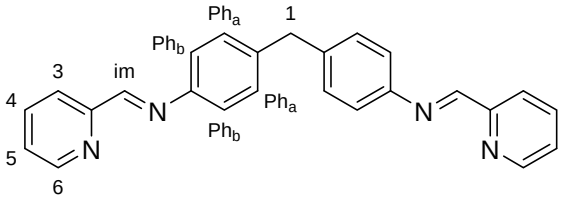

The parent ligand, L_P (1.9589 g, 5.20 mmol) was dissolved in methanol (50 mL) and heated to 50 ºC. $FeCl_2.4H_2O$ (0.7078 g, 3.56 mmol) was added to the first solution in (20 mL) methanol. The reaction mixture was heated for 2 hrs, then left to stir at room temperature overnight. Excess NH_4PF_6 was added to the now purple solution, causing the cylinder to precipitate out of solution. The product was collected by filtration and washed with copious amounts of MeOH, H_2O and Et_2O. The purple solid was then suspended in methanol and stirred with DOWEX for 2 hrs. The DOWEX and unreacted PF_6^- cylinder were collected by filtration. The chloride salt of the cylinder was then precipitated from the filtrate using ether, yielding a purple solid (2.0757g, 86.6 %).

^{1}H NMR ($CDCl_3$): δ 9.15 (1H, s, H_{im}), 8.69 (1H, d, J = 7.8 Hz, H_6), 8.49 (1H, t, J = 7.8 Hz, H_3), 7.85 (1H, t, J = 6.3 Hz, H_4), 7.44 (1H, d, J = 6.3 Hz, H_5), 7.02 (2H, s, broad, $H_{Pha/b}$), 5.61 (2H, s, broad, $H_{Pha/b}$), 4.06 (1H, s, H_1).

Mass spectrum (+ve ESI): *m/z* 310.2 $[M]^{4+}$, 425.3 $[M+Cl]^{3+}$, 467.3 $[M-L_P]^{2+}$+Cl, 592.5 $[M-Fe]^{2+}$, 775.7 $[M-2Fe-L_P]^+$+Na, 843.7 $[M-FeL_P]$+Cl

Elemental Analysis: Theoretical C: 57.63, H: 5.16, N: 10.75; Experimental C: 58.19, H: 5.10, N: 10.84. Corresponding to $[Fe_2(L_P)_3]Cl_4.10H_2O$

UV-Vis (H_2O) λ_{max} (ε_{max}/$dm^3mol^{-1}cm^{-1}$): 239 (63 799), 278 (54 654), 326 (25 120), 527 (8 779), 576 (11 759) nm.

6.2.2 Alkyne Formation

6.2.2.1 Synthesis of 5-((trimethylsilyl)ethynyl)picolinaldehyde

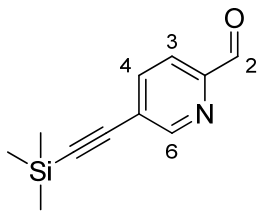

5-Bromopyridine-2-carbaldehyde (0.9662 g, 5.19 mmol), $Pd(PPh_3)_2Cl_2$ (0.1410 g, 0.20 mmol), CuI (77.1 mg, 0.40 mmol) and PPh_3 (0.1052 g, 0.40 mmol) were dissolved in THF (5 mL) in a 3 headed flask attached to a condenser and put under Argon. Triethylamine (20 mL) and THF (5 mL) were then added. Trimethylsilylacetylene (1 mL, 7.03 mmol) was then added drop wise to the reaction mixture at room temperature. The reaction mixture was then heated to 80 ºC for 5 hr. Solvent was evaporated giving a crude brown solid. Purification by silica column in DCM yielded a pale brown solid (0.90 g, 85 %).

R_f : 0. 71 (100 % DCM)

^{1}H NMR ($CDCl_3$): δ 9.83 (1H, s, H_2), 8.58 (1H, t, J = 1.4 Hz, H_4), 7.67 (2H, m, H_{3+6}), 0.08 (9H, s, H_{Me}).

^{13}C NMR ($CDCl_3$): δ 192.68 (C_2), 153.18 (C_6), 140.28 (C_4), 121.02 (C_3), 84.22 (C_{Me}).

Mass spectrum (+ve ESI): *m/z* 226 $[M+Na]^+$.

2.2.2.2 Synthesis of 5-ethynylpicolinaldehyde: Aldehyde 1

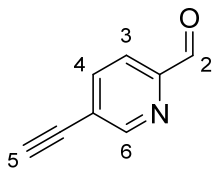

1

4-Trimethylsilylethynyl-1-formyl pyridine (0.72 g, 3.54 mmol) was dissolved in MeOH (45 mL) and K_2CO_3 was added. The reaction mixture was put under Argon and stirred at room temperature overnight. Solvent was then evaporated and the crude product was extracted with ethyl acetate, washing with water and brine. Purification on silica column in DCM yielded a white solid (0.35 g, 75 %).

R_f : 0. 63 (100 % DCM)

^{1}H NMR ($CDCl_3$): δ 10.02 (1H, s, H_2), 8.80 (1H, t, J = 1.4 Hz, H_6), 7.88 (2H, m, H_{3+4}), 3.43 (1H, s, H_5).

^{13}C NMR ($CDCl_3$): δ 192.68 (C_2), 153.19 (C_6), 140.27 (C_4), 121.02 (C_3), 77.36 (C_5).

Mass spectrum (+ve ESI): *m/z* 154 $[M+Na]^+$, 155 $[M+Na+H]^+$.

6.2.3 Synthesis of Ester Helicate

6.2.3.1 Synthesis of methyl 2-(4-(6-formylpyridin-3-yl)-1H-1,2,3-triazol-1-yl)acetate: Ester Aldehyde 2

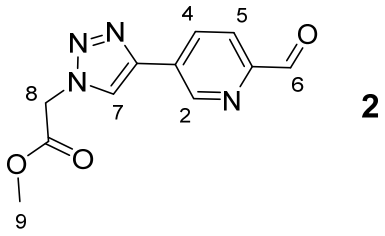

2

To a solution of 5-ethynylpicolinaldehyde (0.1998 g, 1.52 mmol) and methyl 2-azidoacetate (0.15 mL, 1.52 mmol) in *t*-butanol and H_2O (1:1, 16 mL) were added $CuSO_4.5H_2O$ (86.1 mg, 0.34 mmol) and sodium ascorbate (0.1269 g, 0.64 mmol). The resulting red/brown solution was stirred at room temperature overnight. The reaction mixture was then diluted with H_2O and the product was extracted using CH_2Cl_2. The organic layer was then dried with $MgSO_4$ and volatiles removed in vacuo to give a peach solid (283.8 mg, 76 %).

IR (solid): 3128 (m), 3003 (w), 2956 (m), 2820 (m), 1743 (s), 1712 (s), 1596 (m), 1575 (w), 1458 (w), 1434 (m), 1222 (s), 1195 (s), 830 (s), 786 (m), 689 (s), 629 (s) cm^{-1}.

^1H NMR ($CDCl_3$): δ 10.11 (1H, d, J = 0.76 Hz, H_6), 9.22 (1H, d, J = 2.0 Hz, H_2), 8.39 (1H, td, J = 8.0, 2.2, 0.76 Hz, H_4), 8.14 (1H, s, H_7), 8.06 (1H, d, J = 8.2 Hz, H_5), 5.29 (2H, s, H_8), 3.87 (3H, s, H_9).

^{13}C NMR ($CDCl_3$): δ 192.80 (C_6), 147.34 (C_2), 133.77 (C_4), 122.43 (C_7), 122.07 (C_5), 53.33 (C_9), 50.92 (C_8).

Mass spectrum (+ve ESI): *m/z* 269 $[M+Na]^+$.

Calculated mass: 269.0651, High Res mass: 269.0640 for $C_{11}H_{10}N_4O_3Na$.

6.2.3.2 Synthesis of dimethyl 2,2'-(4,4'-(6,6'-((1E,1'E)-((methylenebis(4,1-phenylene))bis(azanylylidene))bis(methanylylidene))bis(pyridine-6,3-diyl))bis(1H-1,2,3-triazole-4,1-diyl))diacetate: L_{Ester}

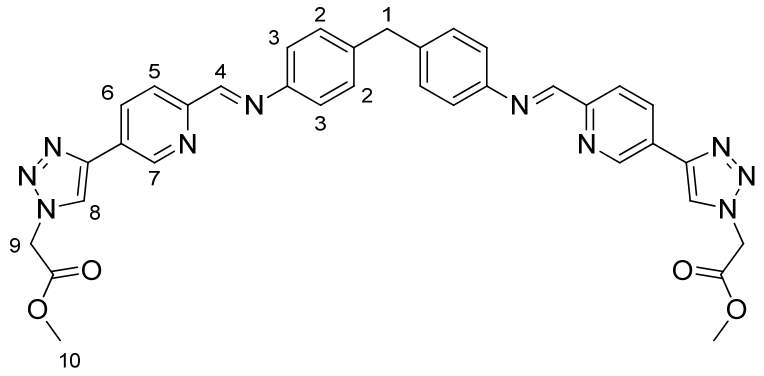

Methyl 2-(4-(6-formylpyridin-3-yl)-1H-1,2,3-triazol-1-yl)acetate (85.8 mg, 0.35 mmol) was 'dissolved' in ethanol (5 mL). 4,4'-methylenedianiline (35.5 mg, 0.17 mmol) was dissolved in ethanol (2 mL) and added dropwise. The reaction mixture was stirred under Ar, at room temperature overnight. The precipitate was then filtered and washed with ethanol and diethyl ether to give a brown solid (107.2 mg, 94 %).

IR (solid): 3373 (br, m), 3087 (w), 2953 (m), 1742 (s), 1626 (w), 1502 (w), 1456 (m), 1438 (m), 1222 (s), 821 (m), 784 (s), 704 (m), 682 (m), 635 (m) cm^{-1}.

^{1}H NMR (d_6-DMSO) (300): δ 9.22 (1H, dd, J = 2.3, 0.9 Hz, H_7), 8.82 (1H, s, H_4), 8.64 (1H, s, H_8), 8.41 (1H, dd, J = 8.1, 2.1 Hz, H_6), 8.24 (1H, d, J = 8.1 Hz, H_5), 7.35 (4H, s, H_{2+3}), 5.55 (2H, s, H_9), 4.03 (1H, s, H_1), 3.75 (3H, s, H_{10}).

^{13}C NMR: 145.84 (C_7), 132.70 (C_8), 129.23 ($C_{2/3}$), 123.78 (C_4), 121.05 ($C_{2/3}$), 120.85 (C_6), 113.61 (C_5), 55.59 (C_{10}), 52.25 (C_1), 50.17 (C_9).

Mass spectrum (+ve ESI): *m/z* 677 $[M+Na]^+$, 678 $[M+Na+H]^+$.

Calculated Mass: 655.253, High Res mass: 655.252 for $C_{35}H_{31}N_{10}O_4$.

6.2.3.3 Synthesis of $[Fe_2(L_{Ester})_3]Cl_4$

$[Fe_2(L_{Ester})_3]Cl_4$ L_{Ester} =

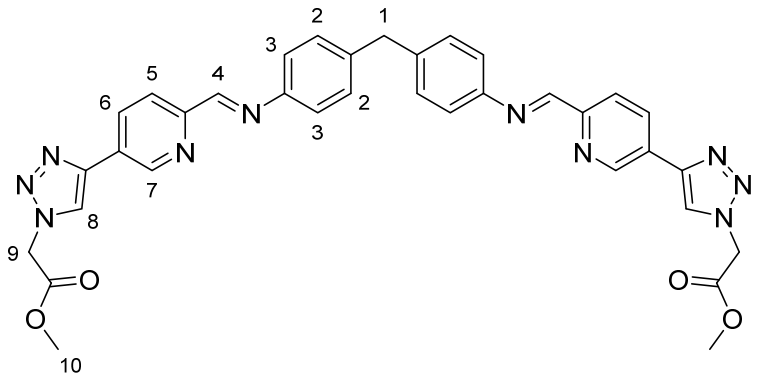

Methyl 2-(4-(6-formylpyridin-3-yl)-1H-1,2,3-triazol-1-yl)acetate (11.4 mg, 0.046 mmol) was dissolved in methanol (1.5 mL). 4,4'-methylenedianiline (4.6 mg, 0.023 mmol) was dissolved in methanol (1 mL) and added dropwise. This mixture was stirred for 15 mins, then $FeCl_2.4H_2O$ (3.1 mg, 0.015 mmol) in methanol (0.5 mL) was added dropwise, turning the solution immediately purple. The reaction mixture was stirred at room temperature overnight. The product was then precipitated out of solution with diethyl ether and washed copiously to give a purple solid (14.1 mg, 83 %).

IR (solid): 3377 (br, m), 2188 (w), 2017 (w), 1746 (s), 1601 (m), 1501 (m), 1459 (m), 1216 (s), 1048 (m), 979 (m), 786 (m), 685 (m) cm^{-1}.

^1H NMR (CD_3OD) (400): δ 9.20 (1H, s, H_7), 8.85 (1H, dd, *J* = 8.0, 1.8 Hz, H_6), 8.78 (1H, d, *J* = 8.2 Hz, H_5), 8.66 (1H, s, H_4), 8.17 (1H, s, H_8), 7.06 (2H, br s, $H_{2/3}$), 5.69 (2H, br s, $H_{2/3}$), 5.40 (2H, s, H_9), 4.08 (1H, s, H_1), 3.79 (3H, s, H_{10}).

Mass spectrum (+ve ESI): *m/z* 519 $[M]^{4+}$, 698 $[M+Na]^{3+}+H$.

UV-Vis (CH_3OH) λ_{max} ($\varepsilon_{max}/dm^3mol^{-1}cm^{-1}$): 248 (80 500), 321 (87 200), 594 (9 751) nm.

6.2.4 Synthesis of Piperidine Helicate

6.2.4.1 Synthesis of 1-(2-Azidoethyl)piperidine: Piperidine Azide

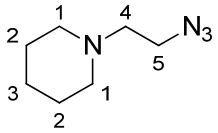

A solution of sodium azide (4.2983 g, 66.12 mmol) and 1-(2-chloroethyl)piperidine hydrogen chloride (4.0133 g, 21.80 mmol) in 30 mL H_2O was heated at 80 ºC for 17 hrs. The resulting solution was cooled in an ice bath; ether (100 mL) and then solid KOH (8 g) were added, keeping the temperature below 10 ºC. The organic layer was then separated and the aqueous

layer further extracted with ether (2 × 40 mL). The combined organic layers were dried on Na_2SO_4 and the solvent removed to give pale yellow oil (3.07 g, 91 %).

^{1}H NMR ($CDCl_3$) (300): δ 3.27 (2H, t, *J* = 6.3 Hz, H_4), 2.47 (2H, t, *J* = 6.3 Hz, H_5), 2.36 (4H, br t, *J* = 5.4 Hz, H_1), 1.52 (4H, m, H_2), 1.36 (2H, m, H_3).

^{13}C NMR ($CDCl_3$) (400): δ 57.82 (C_4), 54.60 (C_1), 48.37 (C_5), 25.87 (C_2), 24.24 (C_3).

Mass spectrum (+ve ESI): *m/z* 155.1 $[M+H]^+$

6.2.4.2 Synthesis of 5-(1-(2-(piperidin-1-yl)ethyl)-1H-1,2,3-triazol-4-yl)picolinaldehyde: Piperidine Aldehyde 3

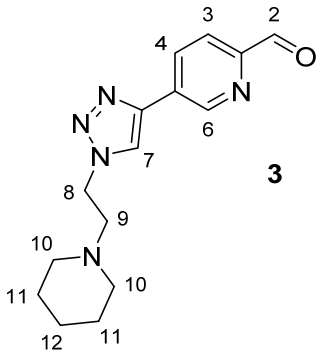

3

5-ethynylpicolinaldehyde (5.6 mg, 0.043 mmol) was dissolved in *t*-butanol (3 mL). 1-(2-azidoethyl)piperidine (6.6 mg, 0.043 mmol) was added as an oil with (1 mL) water. Aqueous solutions of $CuSO_4.5H_2O$ (2.2 mg, 8.81 μmol) and sodium ascorbate (3.8 mg, 0.019 mmol) were then added to give a resulting solvent system of (*t*-butanol/water, 1:1). The resulting red/brown solution was stirred at room temperature overnight. The reaction mixture was then diluted with H_2O and the product was extracted using CH_2Cl_2. The organic layer was then dried with $MgSO_4$ and volatiles removed in vacuo to give a yellow solid (7.2 mg, 59 %).

IR (solid): 2931 (s), 1707 (s), 1596 (m), 1576 (w), 1448 (m), 1259 (m), 1259 (s), 1082 (s), 1022 (s), 799 (s), 696 (m) cm^{-1}.

^{1}H NMR ($CDCl_3$) (400): δ 10.10 (1H, s, H_2), 9.20 (1H, d, *J* = 2.2 Hz, H_6), 8.37 (1H, dd, *J* = 8.8, 2.2 Hz, H_4), 8.20 (1H, s, H_7), 8.05 (1H, d, *J* = 8.8 Hz, H_3), 4.54 (2H, t, *J* = 6.2 Hz, H_8), 2.81 (2H, t, *J* = 6.4 Hz, H_9), 2.47 (2H, t, *J* = 4.8 Hz, H_{10}), 1.60 (2H, m, H_{11}), 1.47 (1H, m, H_{12}).

^{13}C NMR ($CDCl_3$) (400): δ 210.2 (C_2), 148.25 (C_6), 130.69 (C_7), 128.40 (C_3), 122.02 (C_4), 58.06 (C_9), 54.50 (C_{10}), 47.99 (C_8), 26.04 (C_{11}) 24.07 (C_{12}).

Mass spectrum (+ve ESI): *m/z* 258.3 $[M\text{-}CO]^+$, 286.3 $[M+H]^+$, 308.3 $[M+Na]^+$, 309.3 $[M+Na+H]^+$, 340.3 $[M+Na+MeOH]^+$.

Calculated mass: 308.1487, High Res mass: 308.1502 for $C_{15}H_{19}N_5ONa$.

6.2.4.3 Synthesis of (NE,N'E)-4,4'-methylenebis(N-((5-(1-(2-(piperidin-1-yl)ethyl)-1H-1,2,3-triazol-4-yl)pyridin-2-yl)methylene)aniline): $L_{Piperidine}$

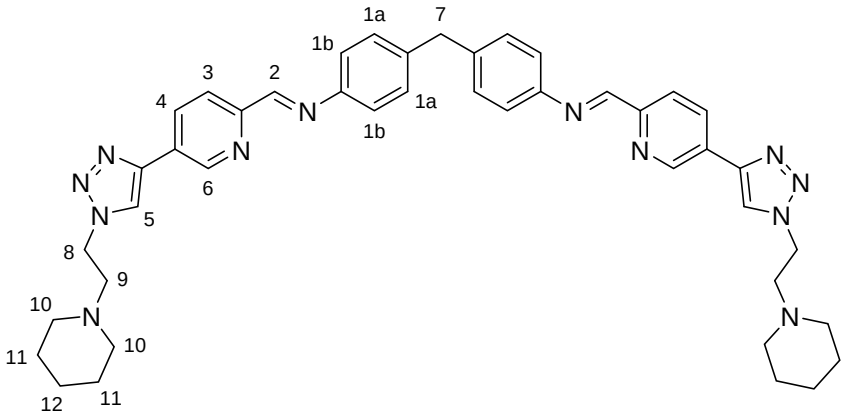

5-(1-(2-(piperidin-1-yl)ethyl)-1H-1,2,3-triazol-4-yl)picolinaldehyde, aldehyde **3** (3.1 mg, 10.9 μmol) was dissolved in methanol (1 mL) and 4,4'-methylenedianiline (1.4 mg, 7.06 μmol) was added in (0.5 mL) methanol. The solution was stirred at room temperature overnight, by which time a cream solid had precipitated out of solution. This was collected by filtration and washed with excess methanol and diethyl ether (1.1 mg, 30 %).

IR (solid): 2930 (s), 1978 (w), 1627 (m), 1503 (s), 1445 (m), 1229 (m), 1189 (m), 1108 (m), 971 (m), 816(s), 756 (m), 683 (m) cm^{-1}.

^{1}H NMR ($CDCl_3$) (400): δ 9.12 (1H, d, *J* = 2.4 Hz, H_6), 8.65 (1H, s, H_5), 8.33-8.26 (2H, m, H_{3+4}), 8.13 (1H, s, H_2), 7.28 (4H, s, H_1), 4.54 (2H, t, *J* = 6.4 Hz, H_8), 4.06 (1H, s, H_7), 2.82 (2H, t, *J* = 6.4 Hz, H_9), 2.48 (2H, t, *J* = 4.8 Hz, H_{10}), 1.60 (2H, m, H_{11}) 1.47 (1H, m, H_{12}).

^{13}C NMR ($CDCl_3$) (400): δ 210.88 (C_2), 184.93 (C_6), 179.49 (C_4), 159.49 (C_3), 146.20 (C_5), 129.75 ($C_{1a/b}$), 121.40 ($C_{1a/b}$), 58.16 (C_9), 54.52 (C_{10}), 47.98 (C_8), 26.04 (C_{11}), 24.10 (C_{12}).

Mass spectrum (+ve ESI): *m/z* 755.5 $[M+Na]^+$

Calculated mass: 755.4023, High Res mass: 755.4031 for $C_{43}H_{48}N_{12}Na$.

6.2.4.4 Synthesis of $[Fe_2(L_{Piperidine})_3]Cl_4$

$[Fe_2(L_{Piperidine})_3]Cl_4$

$L_{Piperidine}$ =

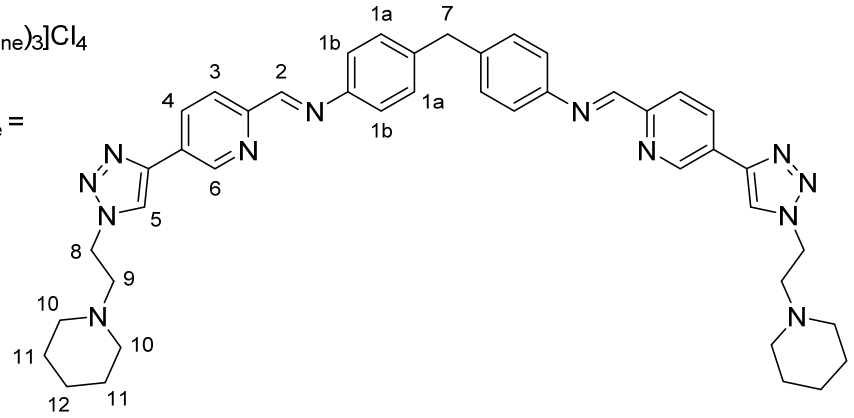

(NE,N'E)-4,4'-methylenebis(N-((5-(1-(2-(piperidin-1-yl)ethyl)-1H-1,2,3-triazol-4-yl)pyridin-2-yl)methylene)aniline) (3.3 mg, 4.50 mmol) was suspended in EtOH (1 mL) and a solution of $FeCl_2.4H_2O$ (0.7 mg, 3.52 mmol) in EtOH (0.5 mL) was added dropwise. Overnight the solution turned purple and the product was isolated by precipitation with ether, and purified by copious washing with ether to yield a purple powder (3.3 mg, 41 %).

IR (solid): 3323 (br, m), 2159 (w), 2135 (w), 1990 (w), 1609 (m), 1513 (s), 1198 (m), 1034 (m), 978 (m), 911 (m), 840 (m), 674 (m) cm^{-1}.

^1H NMR ($CDCl_3$) (300): δ 9.19 (1H, s, H_6), 8.81 (2H, m, H_{3+4}), 8.71 (1H, s, H_5), 8.14 (1H, s, H_2), 7.07 (2H, s, br, $H_{1a/b}$), 5.71 (2H, s, br, $H_{1a/b}$), 4.68 (2H, t, J = 6.3 Hz, H_8), 4.07 (1H, s, H_7), 3.07 (2H, m, H_9), 2.68 (2H, s, H_{10}), 1.62 (2H, m, H_{11}), 1.51 (1H, m, H_{12}).

Mass spectrum (+ve ESI): *m/z* 466.29 $[L\text{-Aldehyde}+2H]^{2+}$, 577.58 $[M+Cl_4]^{4+}$, 733.52 $[L]^+$, 734.53 $[L+H]^+$, 782.13 $[M+Cl]^{3+}$.

UV-Vis (CH_3OH) λ_{max} (ε_{max}/$dm^3mol^{-1}cm^{-1}$): 240 (96 900), 330 (104 000), 536 (7 200), 587 (8 400) nm.

6.2.5 Synthesis of Undecyl-thioacetate Helicate

6.2.5.1 Synthesis of 1-azidoundecan-11-ol

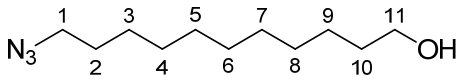

To DMF (70 mL), $Br(CH_2)_{11}OH$ (4.9310 g, 19.63 mmol) and NaN_3 (1.7082 g, 26.28 mmol) were added. The flask was put under an argon atmosphere and refluxed for 24 hrs. After cooling, the product was extracted with diethyl ether and washed with H_2O three times. The organic phase was then dried over $MgSO_4$ and the solvent removed yielding a yellow oil (6.10 g, 100 %).

IR (oil): 3404 (br), 2926 (s), 2854 (s), 2093 (S), 1668 (s), 1585 (vw), 1465 (w), 1388 (w), 1349 (w), 1417 (vw), 1256 (m), 1102 (w), 1056 (m), 904 (w), 739 (w), 722 (w), 662 (m), 625 (w) cm^{-1}.

^1H NMR ($CDCl_3$) (300): δ 3.45 (2H, q, J = 6.9 Hz, H_{11}), 3.12 (t, J = 6.9 Hz, H_1), 1.50-1.36 (4H, m, H_{2+10}), 1.28-1.12 (14H, m, H_{3-9}).

Mass spectrum (+ve ESI): *m/z* 236 $[M+Na]^+$, 186 $[M-N_2+H]^+$.

6.2.5.2 Synthesis of 1-Azidoundecan-11-methylsulfonate

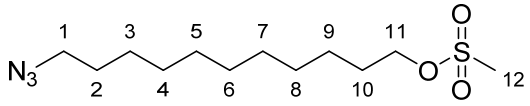

1-azidoundecan-11-ol (2.98 g, 13.97 mmol) was dissolved in THF (60 mL) and methanesulfonyl chloride (3.24 mL, 41.86 mmol) was added. In a separate vial, triethylamine (5.84 mL, 41.90 mmol) and THF (10 mL) were combined and then added slowly to the first solution over 5 mins. The reaction mixture was then stirred at room temperature for 3 hrs. Ice-cold water H_2O (50 mL) was then added to the reaction mixture and the organic phase was separated from the aqueous phase. The aqueous phase was then extracted twice with ether (2 × 35 mL) and the combined organic phases combined and washed with 1M HCl, H_2O, $NaHCO_3$ sol. and H_2O. It was then dried over $MgSO_4$ and the solvent removed yielding pale yellow oil (3.80 g, 98 %).

IR (oil): 2927 (s), 2855 (m), 2095 (s), 1722 (w), 1465 (w), 1355 (s), 1174 (s), 971 (m), 750 (m) cm^{-1}.

^1H NMR ($CDCl_3$) (300): δ 4.17 (2H, t, J = 6.6 Hz, H_{11}), 3.21 (2H, t, J = 6.9 Hz, H_1), 2.96 (3H, s, H_{12}), 1.70 (2H, m, H_{10}), 1.55 (2H, m, H_2), 1.24 (14H, m, $H_{3\text{-}9}$).

^{13}C-NMR ($CDCl_3$) (400): 70.2 (C_{11}), 52.6 (C_1), 37.4 (C_{12}), 29.4-28.8 ($C_{4\text{-}8}$), 29.0 (C_2), 28.8 (C_{10}), 26.7 (C_3), 25.4 (C_9).

6.2.5.3 Synthesis of 1-Azidoundecan-11-thioacetate

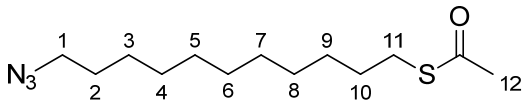

1-azidoundecan-11-methylsulfonate (1.0848 g, 3.74 mmol) and potassium thioacetate (0.8443 g, 7.39 mmol) were dissolved in MeOH (30 mL). The reaction mixture was then refluxed under Ar for 3 hrs. The solution was then cooled and water added. The product was then extracted using ether three times and the combined organic layers washed with H_2O which was then dried over $MgSO_4$ and the solvent was removed. The crude product was then purified by column chromatography (10 % EtOAc in Hexane) to give a yellow oil (188.9 mg, 19 %).

R_f : 0. 58 (EtOAc/Hexane, 1:9)

IR (oil): 2924 (s), 2853 (s), 2093 (s), 1692 (s), 1463 (w), 1351 (w), 1259 (m), 1134 (m), 953 (w), 628 (m) cm^{-1}.

^1H NMR ($CDCl_3$) (300): δ 3.21 (2H, t, J = 6.9 Hz, H_{11}), 2.82 (2H, t, J = 7.2 Hz, H_1), 2.28 (3H, s, H_{12}), 1.60-1.47 (4H, m, H_{2+10}), 1.30-1.20 (14H, m, H_{3-9}).

^{13}C-NMR ($CDCl_3$) (400): 70.3 (C_1), 51.5 (C_{12}), 37.4 (C_{10}), 29.5-28.8 ($C_{2,4-6,10}$), 26.7 (C_9), 25.4 (C_3).

6.2.5.4 Synthesis of S-(11-(4-(6-formylpyridin-3-yl)-1H-1,2,3-triazol-1-yl)undecyl) ethanethioate: Undecyl-thioacetate Aldehyde 4

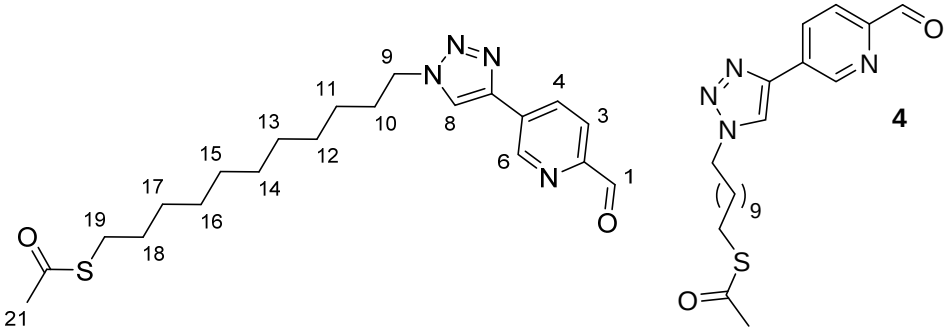

5-ethynylpicolinaldehyde (72 mg, 0.5 mmol) and 1-azidoundecan-11-thioacetate (133 mg, 0.5 mmol) in 13 mL tBuOH with 8 mL water was combined with solutions of $CuSO_4.5H_2O$ (66 mg, 0.25 mmol) and sodium ascorbate (103 mg, 0.25 mmol) in 5 mL water. After stirring at room temperature for six days the solution was diluted with 25 mL water and the light brown precipitate was collected by filtration and washed with 50 mL water, methanol and diethyl ether and dried under vacuum (189 mg, 94 %).

IR (solid): 2922 (m), 2850 (m), 1720 (w), 1694 (m), 1674 (m), 1617 (w), 1592 (w), 1575 (w), 1553 (w), 1518 (w), 1460 (w), 1405 (w), 1330 (w), 1260 (m), 1217 (w), 1168 (w), 1136 (w), 1097 (m), 1012 (s), 869 (m), 798 (s), 727 (w), 688 (w), 661 (w) cm^{-1}.

^{1}H-NMR ($CDCl_3$) (300): 10.05 (s, 1H, H_1), 9.13 (s, 1H, H_6), 8.33 (d, 1H, J = 8.1 Hz, H_4), 8.03 (d, 1H, J = 8.4 Hz, H_3), 7.89 (s, 1H, H_8), 4.38 (t, 2H, J = 7.5 Hz, H_9), 2.77 (t, 2H, J = 6.9 Hz, H_{19}), 2.25 (s, 3H, H_{21}); 1.94 (t, 2H, J = 6.9 Hz, H_{18}), 1.55 (m, 4H, H_{10+11}), 1.22 – 1.42 (m, 12H, H_{12-17}).

^{13}C-NMR ($CDCl_3$) (400): 196 (C_{20}), 192 (C_1), 152 (C_2), 147 (C_7), 144 (C_6), 134 (C_5), 131 (C_4), 122 (C_8), 121 (C_3), 51 (C_9), 31 (C_{19}), 30 (C_{21}), 26 – 30 (C_{10-18}).

Mass spectrum (+ve ESI): *m/z* 425.2 $[M+Na]^+$.

Calculated mass: 425.1987, High Res mass: 425.1972 for $C_{21}H_{30}N_4O_2Na$.

6.2.5.5 Attempted synthesis of $[Fe_2(L_{Undecyl\text{-}thioacetate})_3][ClO_4]_4$

$[Fe_2(L_{Undecyl\text{-}thioacetate})_3][ClO_4]_4$

$L_{Undecyl\text{-}thioacetate}$ =

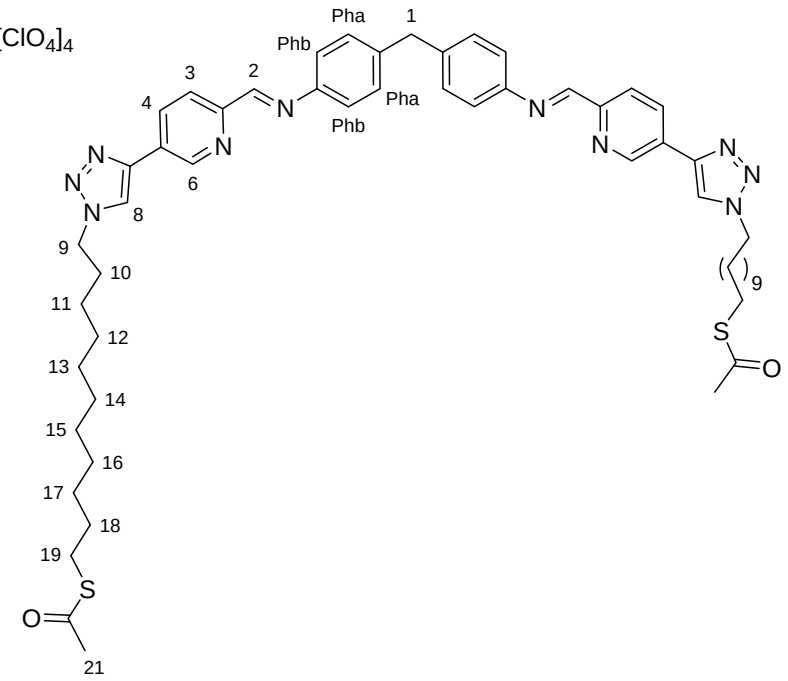

Undecyl-thioacetate aldehyde **4** (50.4 mg, 0.13 mmol) and 4,4'-methylenedianiline (12.8 mg (0.06 mmol) were suspended in methanol (15 mL), heated to 60 °C for 2 h and stirred at room temperature for additional 16 h. An off-white precipitate was formed and collected by filtration, followed by washing with copious quantities of methanol and diethyl ether (32 mg).

This highly insoluble solid could not be fully characterised as a result of insolubility, so was just taken on to the next reaction step.

$L_{Undecyl\text{-}thioacetate}$ (20 mg, 0.021 mmol) was then stirred in methanol (2 mL) with $Fe(ClO_4)_2.7H_2O$ 5 mg (0.013 mmol) and heated to reflux for 5 min. The resulting precipitate was collected by filtration, dried in vacuum and extracted with 6 mL acetone to yield a deep purple solution. Evaporation of the solvent yielded a purple solid (2 mg).

Again, this product was not very soluble, and so full characterisation was not achieved.

^{1}H NMR ($CDCl_3$) (300): δ 9.41 (1H, s, H_4), 9.14 (1H, s, H_8), 8.58 (1H, s, H3), 8.50 (1H, s, H_4), 8.22 (1H, s, H_2), 7.42 (2H, $H_{Pha/b}$), 7.09 (12H, $H_{Pha/b}$), 4.33 (2H, t, *J* = 6.8 Hz, H_9); 3.79 (1H, s, H_1); 2.69 (2H, m, H_{19}), 2.28 (3H, s, H_{21}), 1.79 (2H, s, H_{18}), 1.37 (4H, m, H_{10+11}), 1.02 – 1.22 (12H, H_{12-17}).

Educated assignment based on undecyl-thioacetate aldehyde spectra.

6.2.6 Synthesis of Thioacetate Helicate

6.2.6.1 Synthesis of 2-(2-(2-azidoethoxy)ethoxy)ethan-1-ol

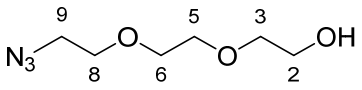

Sodium azide (3.047 g, 46.88 mmol) suspended in ethanol (30 mL) was stirred under argon at rt. to which 2-(2-(2-chloroethoxy)ethoxy)ethan-1-ol (3.4 mL, 23.39 mmol) was added slowly to, as on oil. Sodium iodide (7.00 g, 40.27 mmol) was dissolved in ethanol (20 mL) and added dropwise to the first solution. The reaction mixture was then refuxed at 79 ºC overnight. The solvent was evaporated and the residue was diluted with water (100 mL) and extracted with dichloromethane (2 × 100 mL). The combined organic phases were dried over $MgSO_4$, and the solvent removed by reduced vacuo yielding a colourless oil (3.14 g, 76%).

^{1}H NMR ($CDCl_3$) (300): δ 3.63-3.75 (8H, m, H_{2-6}), 3.57 (2H, t, *J* = 5.1 Hz, H_8), 3.37 (2H, t, *J* = 5.4 Hz, H_9), 2.52 (1H, s, H_{OH}).

^{13}C NMR ($CDCl_3$) (400): δ 50.5 (C_9), 61.5 (C_2), 69.9 (C_3), 70.1 (C_5), 70.5 (C_6), 72.5 (C_8).

Mass spectrum (+ve ESI): *m/z* 191.1 $[M\text{-}OH]^+$+MeOH, 198.1 $[M+Na]^+$, 199.1 $[M+Na]^+$+H.

6.2.6.2 Synthesis of 2-(2-(2-azidoethoxy)ethoxy)ethyl methanesulfonate

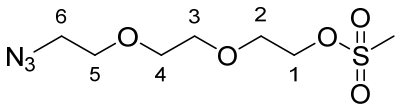

2-(2-(2-azidoethoxy)ethoxy)ethan-1-ol (1.4743 g, 8.42 mmol) was dissolved in diethyl ether, under Ar at 0 ºC. Triethyl amine (3.5 mL, 25.11 mmol) was added dropwise, followed by mesyl chloride (1.0 mL, 12.92 mmol) under a flow of Ar. Reaction mixture was left to reach rt. and stirred for 24 hrs. The reaction was then quenched with water (50 mL) and the product extracted with diethyl ether. The combined organic layers were washed with water and dried over $MgSO_4$, the solvent was removed to yield a pale yellow oil (1.58 g, 74 %).

^{1}H NMR ($CDCl_3$) (300): δ 4.38-4.34 (2H, m, H_1), 3.78-3.73 (2H, m, H_2), 3.67-3.63 (6H, m, H_{3-5}), 3.37 (2H, t, *J* = Hz, H_6), 3.05 (3H, s, H_{Me}).

^{13}C NMR ($CDCl_3$) (400): δ 72.58 (C_3), 71.58 (C_4), 70.88 (C_5), 70.31 (C_2), 69.38 (C_1), 50.90 (C_6), 37.89 (C_{Me}).

Mass spectrum (+ve ESI): *m/z* 269.2 $[M+O]^+$, 271.3 $[M+H_2O]^+$, 276.2 $[M+Na]^+$, 277.2 $[M+Na+H]^+$, 296.2 $[M+K]^+$.

6.2.6.3 Synthesis of S-(2-(2-(2-azidoethoxy)ethoxy)ethyl) ethanethioate: Thioacetate Azide

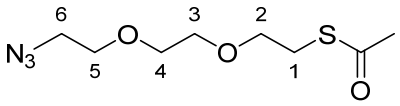

2-(2-(2-azidoethoxy)ethoxy)ethyl methanesulfonate (2.340 g, 9.24 mmol) was dissolved in ethanol (250 mL) to which a suspension of potassium thioacetate (5.80 g, 50.81 mmol) in (30 mL) ethanol was added. The reaction was heated at 80 ºC under Ar overnight. Ethanol was then

removed and the reaction quenched with water (100 mL). The product was then extracted with dichloromethane (3 × 75 mL). The combined organic layers were dried over $MgSO_4$ and the solvent removed. The resulting oil was purified via flash column chromatography (EtOAc/pentane 2:8) to yield a yellow/orange oil (2.01 g, 93 %).

^{1}H NMR ($CDCl_3$) (400): δ 3.62-3.57 (9H, m, $H_{2\text{-}5}$), 3.37 (2H, t, J = 5.6 Hz, H_1), 3.08 (2H, t, J = 6.8 Hz, H_6), 2.32 (3H, s, H_{Me}).

^{13}C NMR ($CDCl_3$) (400): δ 195.60 (CO), 70.69, 70.44, 70.17, 69.91 ($C_{2\text{-}5}$), 50.77 (C_6), 30.65 (C_1), 28.92 (C_{Me}).

Mass spectrum (+ve ESI): *m/z* 289 $[M+Na+MeOH]^+$, 272 $[M+K]^+$, 256 $[M+Na]^+$, 234 $[M+H]^+$.

6.2.6.4 Synthesis of S-(2-(2-(2-(4-(6-formylpyridin-3-yl)-1H-1,2,3-triazol-1-yl)ethoxy)ethoxy) ethyl) ethanethioate: Thioacetate Aldehyde 5

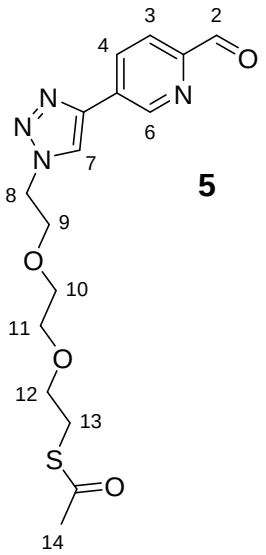

5

To a solution of 5-ethynylpicolinaldehyde (20.7 mg, 0.158 mmol) and S-(2-(2-(2-azidoethoxy)ethoxy)ethyl) ethanethioate (52.7 mg, 0.226 mmol) in *t*-butanol/water (5/1 mL) were added $CuSO_4.5H_2O$ (11.3 mg, 0.045 mmol) followed by sodium ascorbate (13.6 mg, 0.069

mmol) in water solutions, giving an overall solvent system of 1:1 *t*-butanol/water . The resulting red/brown solution was stirred at room temperature overnight. The reaction mixture was then diluted with H_2O and the product was extracted using CH_2Cl_2. The organic layer was dried with $MgSO_4$ and volatiles removed in vacuo to give a yellow solid. This was purified using column chromatography (10 % MeOH/DCM) giving a yellow solid (38.8 mg, 67 %).

IR (solid): 2893 (br, m), 2036 (w), 1694 (s), 1596 (m), 1354 (m), 1196 (m), 1101 (s), 969 (m), 841 (m), 678 (m) cm^{-1}.

^1H NMR ($CDCl_3$) (400): δ 10.09 (1H, s, H_2), 9.23 (1H, d, J = 1.6 Hz, H_6), 8.36 (1H, dd, J = 8.0, 2.4 Hz, H_4), 8.23 (1H, s, H_7), 8.03 (1H, d, J = 8.0 Hz, H_3), 4.65 (2H, t, J = 4.6 Hz, H_8), 3.92 (2H, t, J = 4.6 Hz, H_9), 3.66-3.56 (6H, m, $H_{10,11,12}$), 3.05 (2H, m, H_{13}), 2.31 (3H, s, H_{14}).

^{13}C NMR ($CDCl_3$) (400): δ 192.79 (C_2), 147.21 (C_6), 133.46 (C_4), 122.53 (C_7), 121.96 (C_3), 70.47 ($C_{10/11/12}$), 70.06 ($C_{10/11/12}$), 69.75 ($C_{10/11/12}$), 69.26 (C_9), 50.54 (C_8), 30.50 (C_{14}), 28.62 (C_{13}).

Mass spectrum (+ve ESI): *m/z* 289.1 $[M\text{-}SC(O)CH_3]^+$, 365.2 $[M+H]^+$, 366.2 $[M+2H]^+$, 381.1 $[M+OH]^+$

Calculated mass: 365.1286, High Res mass: 365.1284 for $C_{16}H_{21}N_4O_4S$.

6.2.6.5 Synthesis of S-(2-(2-(2-(4-(6-((E)-((4-(4-(((E)-(5-(1-(2-(2-(2-(acetylthio)ethoxy)ethoxy)ethyl)-1H-1,2,3-triazol-4-yl)pyridin-2-yl)methylene)amino)benzyl)phenyl)imino)methyl)pyridin-3-yl)-4,5-dihydro-1H-1,2,3-triazol-1-yl)ethoxy)ethoxy)ethyl) ethanethioate: Thioacetate Ligand, $L_{Thioacetate}$

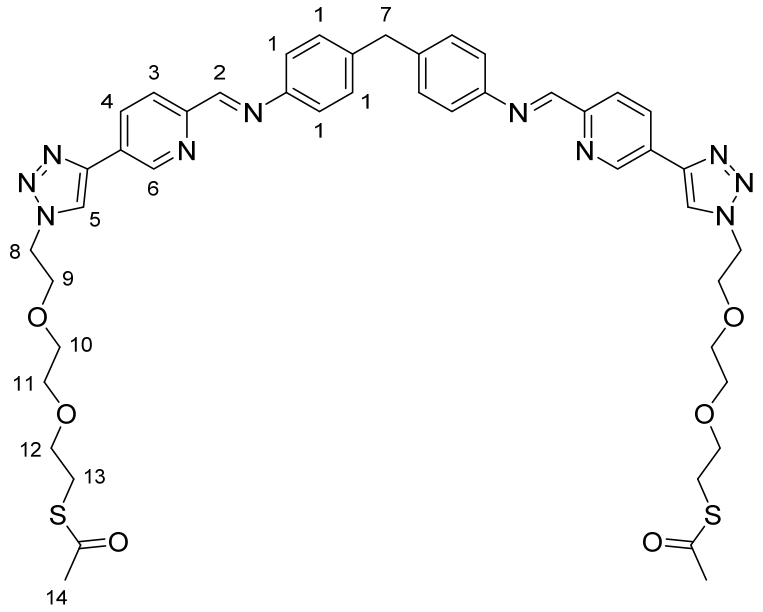

S-(2-(2-(2-(4-(6-formylpyridin-3-yl)-1H-1,2,3-triazol-1-yl)ethoxy)ethoxy)ethyl) ethanethioate, aldehyde **5** (2.0 mg, 5.49 μmol) was dissolved in methanol (1 ml) and a methanolic solution (1 mL) of 4,4'-methylenedianiline (0.7 mg, 3.53 μmol) was added. The solution was stirred at rt. overnight and the solvent removed in vacuo to yield a pale brown solid (2.1 mg, 86 %).

IR (solid): 3119 (br, w), 2866 (br, m), 2164 (w), 1689 (s), 1352 (m), 1106 (s), 973 (s), 822 (s), 783 (m), 677 (m) cm^{-1}.

^{1}H NMR ($CDCl_3$) (300): δ 9.15 (1H, s, H_6), 8.65 (1H, s, H_5), 8.31 (1H, d, J = 9.0 Hz, H_4), 8.28 (1H, d, J = 8.4 Hz, H_3), 8.17 (1H, s, H_2), 7.28 (4H, s, H_1), 4.65 (2H, t, J = 4.8 Hz, H_8), 3.94 (2H, t, J = 5.1 Hz, H_9), 3.64-3.57 (6H, m, $H_{10,11,12}$), 3.07 (2H, t, J = 6.6 Hz, H_{13}), 2.01 (3H, s, H_{14}).

^{13}C NMR ($CDCl_3$) (400): δ 159.6 (C_2), 146.9 (C_6), 133.4 (C_4), 129.8 (C_3), 121.5 (C_5), 70.6 ($C_{10/11/12}$), 70.2 ($C_{10/11/12}$), 69.5 ($C_{10/11/12}$), 28.62 (C_{13}).

Mass spectrum (+ve ESI): *m/z* 913.3 $[M+Na]^+$, 891.3 $[M+H]^+$, 567.3 $[M-(C_{16}H_{20}N_4O_3S) +H +Na]^+$, 545.3 $[M-(C_{16}H_{20}N_4O_3S) +2H]^+$, 468.2 $[M]^{2+}$ +Na, 387.2 $[M-(C_{29}H_{30}N_5O_3S) +2H+Na]^+$.

Calculated mass: 891.3434, High Res mass: 891.3441 for $C_{45}H_{51}N_{10}O_6S_2$.

6.2.5.6 Synthesis of $[Fe_2(L_{Thioacetate})_3][BF_4]_4$

$[Fe_2(L_{Thioacetate})_3][BF_4]_4$

$L_{Thioacetate}$ =

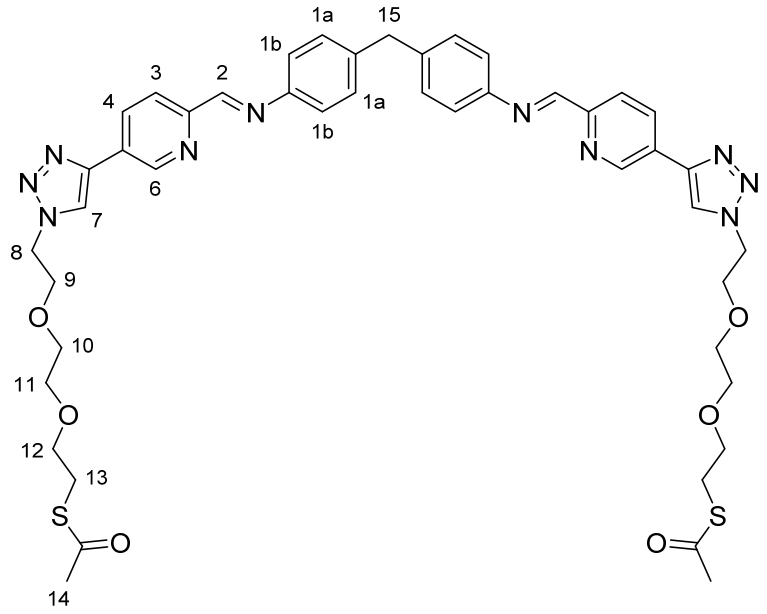

S-(2-(2-(2-(4-(6-formylpyridin-3-yl)-1H-1,2,3-triazol-1-yl)ethoxy)ethoxy)ethyl) ethanethioate, aldehyde **5** (2.6 mg, 7.13 μmol) was dissolved in methanol (1 ml) and a methanolic solution (1 mL) of 4,4'-methylenedianiline (0.8 mg, 4.03 μmol) was added. $Fe(BF_4)_2.6H_2O$ was added dropwise in methanol (1 mL), turning the reaction mixture gradually purple with time. The solution was stirred at rt. overnight. The product was precipitated out using diethyl ether and collected by filtration, yielding a purple solid (3.5 mg, 94 %).

IR (solid): 2868 (br, m), 1687 (s), 1502 (m), 1459 (m), 1352 (m), 1201 (m), 1102 (s), 973 (s), 822 (m), 674 (m) cm^{-1}.

^{1}H NMR (CD_3CN) (400): δ 8.90 (1H, s, H_6), 8.74 (1H, d, *J* = 8.0 Hz, H_4), 8.62 (1H, d, *J* = 8.0 Hz, H_3), 8.30 (1H, s, H_2), 8.04 (1H, s, H_7), 6.96 (2H, br, s, $H_{1a/b}$), 5.64 (2H, br, s, $H_{1a/b}$), 4.53 (2H, t, *J* = 6.0 Hz, H_8), 4.02 (1H, s, H_{15}), 3.84 (2H, t, J = Hz, 5.0 Hz, H_9), 3.55-3.44 (6H, m, $H_{10+11+12}$), 2.94 (2H, t, *J* = 6.0 Hz, H_{13}), 2.25 (3H, s, H_{14}).

Mass spectrum (+ve ESI): *m/z* 695.9 $[M]^{4+}$, 696.7 $[M+H]^{4+}$, 891.3 $[L_{Thioacetate}]^{+}$, 956.2 $[M+(BF_4)]^{3+}$, 1153.3 $[M+(BF_4)_4]^{3+}+Na+BF_4$, 1497.4 $[M+(BF_4)_2]^{2+}+H_2O$, 1501.5 $[M+(BF_4)_2]^{2+}+Na$.

UV-Vis (CH_3CN) λ_{max} (ε_{max}/$dm^3mol^{-1}cm^{-1}$): 237 (108200), 329 (110900), 534 (9300), 589 (13500) nm.

Elemental Analysis: Theoretical: C: 51.77 %, H: 4.83 %, N: 13.41 %; Experimental: C: 51.81 %, H: 4.92 %, N: 13.34 % for $C_{135}H_{150}N_{30}O_{18}S_6Fe_2B_4F_{16}$.

6.2.7 Synthesis of Lipoic acid Helicate

6.2.7.1 Synthesis of methyl 6-formylnicotinate

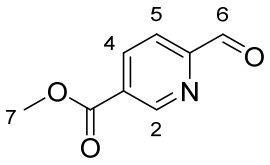

Methyl 6-methylnicotinate (4.45 g, 29.46 mmol) was mixed with iodine (7.4847 g, 29.49 mmol), and a small amount of DMSO (2 mL) to encourage mixing. After mixing for 5 min, DMSO (20 mL) was added and this solution was added to a heated solution of DMSO (35 mL) at 130 ºC. The temperature was then slowly increased to 160 ºC and the solution was stirred at this temperature for 15 min. After cooling down the reaction to room temperature, a saturated solution of aqueous Na_2CO_3 was added. The product was then extracted with diethyl ether. Volatiles were removed *in vacuo* to give a crude product, which was purified via a silica column

(CH_2Cl_2/EtOAc = 4:1) (R_f = 0.85). Product was obtained as a cream/ yellow solid (1.82 g, 37 %).

R_f : 0.85 (EtOAc/DCM, 1:4)

^{1}H NMR ($CDCl_3$): δ 10.14 (1H, d, *J* = 0.9 Hz, H_6), 9.36 (1H, dd, *J* = 2.0, 0.9 Hz, H_2), 8.47 (1H, ddd, *J* = 8.1, 2.0, 0.9 Hz, H_4), 8.03 (1H, dd, *J* = 8.1, 0.9 Hz, H_5), 4.00 (3H, s, CH_3).

^{13}C NMR ($CDCl_3$): δ 192.80 (C_6), 151.38 (C_2), 129.37 (C_4), 121.25 (C_5), 53.02(C_7).

Mass spectrum (+ve ESI): *m/z* 188 $[M+Na]^+$, 189 $[M+H+Na]^+$.

6.2.7.2 Synthesis of 6-dimethoxymethyl-nicotinate

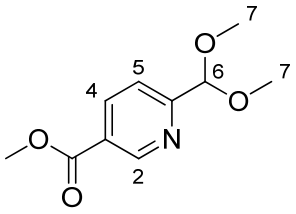

Methyl 6-formylnicotinate (1.78 g, 10.78 mmol) was dissolved in trimethyl orthoformate (46 mL), formic acid (7 mL) and sulphuric acid (5 drops). The mixture was heated to 50 ºC and stirred for 30 min. The mixture was then stirred at room temperature overnight. Water and diethyl ether were then added to the reaction mixture and the two layers were separated. The aqueous layer was further extracted with more diethyl ether. The combined diethyl ether layers were then washed with aqueous saturated Na_2CO_3 and dried with $MgSO_4$. Volatiles were removed *in vacuo* to give a crude product, which was purified via a silica column (CH_2Cl_2/EtOAc = 4:1) (R_f = 0.58). Product was obtained as yellow oil (1.15 g, 50 %).

R_f : 0.58 (EtOAc/DCM,1:4)

^{1}H NMR ($CDCl_3$): δ 9.13 (1H, dd, *J* = 2.2, 0.75 Hz, H_2), 8.26 (1H, dd, *J* = 8.1, 2.2 Hz, H_4), 7.57 (1H, d, *J* = 8.2, H_3), 5.35 (1H, s, H_6), 3.88 (3H, s, H_{Me}), 3.33 (6H, s, H_7).

^{13}C NMR ($CDCl_3$): δ 150.4 (C_2), 137.8 (C_4), 120.9 (C_5), 103.4 (C_6), 53.7 (C_7), 52.4 (C_{Me}).

Mass spectrum (+ve EI): *m/z* 210 $[M-H]^+$.

6.2.7.3 Synthesis of 6-dimethoxymethyl-nicotinic acid

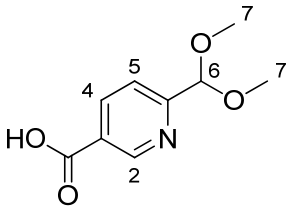

6-Dimethoxymethyl-nicotinate (1.1482 g, 5.44 mmol) was dissolved in MeOH (10 mL) and then 1M NaOH (10 mL). This mixture was then stirred at room temperature overnight. 1M HCl was then used to acidify the reaction mixture to pH 3. The product was then extracted using ethyl acetate and dried with $MgSO_4$. Volatiles were removed in *vacuo* yielding a cream/yellow solid (0.90 g, 84 %).

^1H NMR ($CDCl_3$): δ 9.35 (1H, dd, J = 2.1, 0.82 Hz, H_2), 8.45 (1H, dd, J = 8.2, 2.2 Hz, H_4), 7.73 (1H, d, J = 11.2 Hz, H_5), 5.51 (1H, s, H_6), 3.44 (6H, s, H_7).

^{13}C NMR ($CDCl_3$): δ 150.72 (C_2), 138.55 (C_4), 121.18 (C_5), 103.12 (C_6), 53.75 (C_7).

Mass spectrum (+ve ESI): *m/z* 198 $[M+H]^+$, 242 $[M+2Na-H]^+$.

6.2.7.4 Synthesis of N-(2-aminoethyl)-5-(1,2-dithiolan-3-yl)pentanamide

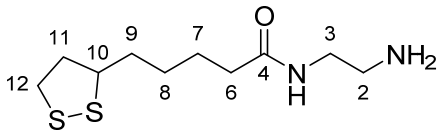

(±)-α-Lipoic acid (1.9835 g, 9.61 mmol) and 1,1'-carbonyldiimidazole (2.4465 g, 15.09 mmol) were dissolved in anhydrous chloroform (15 mL) and stirred under a flow of Ar for 30 mins at room temperature. Ethylenediamine (3.4 mL, 50.86 mmol) was cooled in an ice bath and the

lipoic acid mixture was added dropwise and the mixture was left to stir under Argon for 2 hr. The reaction mixture was then washed with brine and 10 mM NaOH solution. The chloroform layer was then dried with $MgSO_4$ and the volatiles removed *in vacuo* yielding a yellow solid/gel which was not fully dried due to the gel like nature of the compound (2.36 g, 99 % wet).

^{1}H NMR ($CDCl_3$): δ 7.75 (1H, t, *J* = 5.4 Hz, NH), 3.65-3.56 (1H, m, H_{10}), 3.24-3.10 (2H, m, H_{12}), 3.02 (2H, q, *J* = 6.6 Hz, H_6), 2.53, (2H, t, *J* = 6.6 Hz, $H_{2/3}$), 2.41 (1H, sex, *J* = 6.2 Hz, $H_{11a/b}$), 2.06 (2H, t, *J* = 7.2 Hz, $H_{2/3}$), 1.86 (1H, sex, *J* = 6.6 Hz, $H_{11a/b}$), 1.68-1.48 (4H, m, H_{7+9}), 1.34 (2H, q, *J* = 7.8 Hz, H_8).

^{13}C NMR ($CDCl_3$): δ174.21 (C_4), 56.55 (C_{10}), 42.01 (C_{10}), 41.48 (C_3), 41.03 (C_2), 40.35 (C_{11}), 38.59 (C_{12}), 36.48 (C_6), 34.72 (C_9), 29.00 (C_8), 25.50 (C_7).

Mass spectrum (+ve ESI): *m/z* 232 $[M\text{-}NH_2]^+$, 249 $[M+H]^+$, 271 $[M+Na]^+$.

6.2.7.5 Synthesis of N-(2-(5-(1,2-dithiolan-3-yl)pentanamido)ethyl)-6-(dimethoxymethyl) nicotinamide

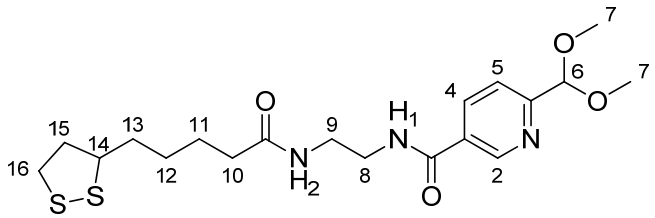

6-dimethoxymethyl-nicotinic acid (0.7845 g, 3.98 mmol), N-(2-aminoethyl)-5-(1,2-dithiolan-3-yl)pentanamide (0.84 g, 3.38 mmol) and HOBt (0.7765 g, 5.75 mmol) were dissolved in DMF (10 mL) and stirred at 0 ºC. EDC (0.9950 g, 5.19 mmol) was then added in DMF (5 mL). The reaction mixture was then left to stir at room temperature overnight. Saturated $NaHCO_3$ solution was then added and the product was extracted with EtOAc, which was washed with H_2O and brine. The organic layer was dried with $MgSO_4$ and volatiles removed *in vacuo* giving a cream

solid. Purification on silica column in 10 % MeOH in DCM yielded a cream solid (0.25 g, 17 %).

IR (solid): 3287 (s), 3084 (w), 2931 (m), 2857 (w), 1719 (w), 1634 (s), 1538 (s), 1442 (w), 683 (s), 631 (m) cm^{-1}.

^{1}H NMR ($CDCl_3$) (400): δ 9.05 (1H, d, *J* = 2.1 Hz, H_2), 8.16 (1H, dd, *J* = 8.2, 2.2 Hz, H_4), 7.66 (1H, t, *J* = 4.6 Hz, NH_1), 7.63 (1H, d, *J* = 8.2 Hz, H_5), 6.21 (1H, t, *J* = 5.6 Hz, NH_2), 5.41 (1H, s, H_6), 3.60 (2H, m, H_8), 3.54 (2H, m, H_9), 3.41 (6H, s, H_7), 3.12 (2H, m, H_{16}), 2.41 (1H, sex, *J* = 6.4 Hz, $H_{15a/b}$), 2.22 (2H, t, *J* = 7.4 Hz, H_{10}), 1.86 (1H, sex, *J* = 6.4 Hz, $H_{15a/b}$), 1.65 (5H, m, $H_{11+13+14}$), 1.43 (2H, m, H_{12}).

^{13}C NMR ($CDCl_3$): δ 147.9 (C_2), 135.5 (C_4), 121.1 (C_5), 103.5 (C_6), 56.3 (C_{14}), 53.7 (C_7), 42.1 (H_8), 40.2 ($C_{15/16}$), 39.6 (C_9), 38.5 ($C_{15/16}$), 36.3 (C_{10}), 34.5 ($C_{11/13}$), 28.8 (C_{12}), 25.3 ($C_{11/13}$).

Mass spectrum (+ve ESI): *m/z* 450 $[M+Na]^+$, 451 $[M+Na+H]^+$.

Calculated mass: 450.1497, High Res mass: 450.1474 for $C_{19}H_{29}N_3O_4NaS_2$.

6.2.7.6 Synthesis of N-(2-(5-(1,2-dithiolan-3-yl)pentanamido)ethyl)-6-formylnicotinamide: Aldehyde 6

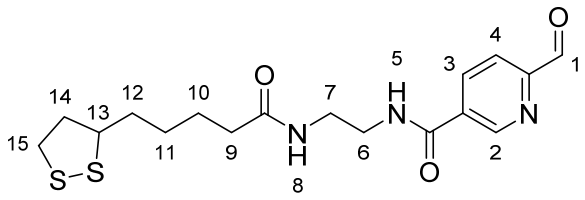

6

N-(2-(5-(1,2-dithiolan-3-yl)pentanamido)ethyl)-6-(dimethoxymethyl)Nicotinamide (237.9 mg, 0.56 mmol) was dissolved in THF (34 mL) and cooled to 0 ºC. 1M HCl (6.8 mL) was then added and the solution stirred for 5 days. The product was then extracted with EtOAc, washing

with $NaHCO_3$ solution and H_2O. The organic layer was then dried with $MgSO_4$ and volatiles removed in vacuo to give a cream solid (93.9 mg, 72 %).

IR (solid): 3284 (s), 3071 (w), 2924 (m), 2853 (m), 1720 (m), 1632 (s), 1541 (s), 1446 (w), 826 (m), 800 (m), 687 (m), 631 (w) cm^{-1}.

^1H NMR ($CDCl_3$) (300): δ 10.11 (1H, d, *J* = 0.7 Hz, H_1), 9.23 (1H, dd, *J* = 2.3, 0.7 Hz, H_2), 8.30 (1H, ddd, *J* = 7.8, 2.1, 0.7 Hz, H_3), 8.16 (1H, s, H_5), 8.02 (1H, dd, *J* = 8.1, 0.7 Hz, H_4), 6.35 (1H, s, H_8), 3.60-3.56 (4H, m, H_{6+7}), 3.10-3.05 (2H, m, H_{15}), 2.40 (1H, sex, *J* = 6.0 Hz, $H_{14a/b}$), 2.23 (2H, t, *J* = 7.8 Hz, H_9), 1.85 (1H, sex, *J* = 6.0 Hz, $H_{14a/b}$), 1.62 (5H, m, $H_{10+12+13}$), 1.36 (2H, m, H_{11}).

^{13}C NMR ($CDCl_3$): δ 192.7 (C_1), 149.1 (C_2), 135.9 (C_3), 121.3 (C_4), 43.0 (C_6), 40.3 (C_{14}), 39.3 (C_7), 38.4 (C_{15}), 36.2 (C_9), 34.5 (C_{12}), 30.3 (C_{13}), 28.7 (C_{11}), 25.2 (C_{10}).

Mass spectrum (+ve ESI): *m/z* 404.1 $[M+Na]^+$, 450.2 $[M+3Na]^+$.

6.2.7.7 Synthesis of 6,6'-((1E,1'E)-((methylenebis(4,1-phenylene))bis(azanylylidene))bis(methanylylidene))bis(N-(2-(5-(1,2-dithiolan-3-yl)pentanamido)ethyl)nicotinamide): L_{Lipoic}

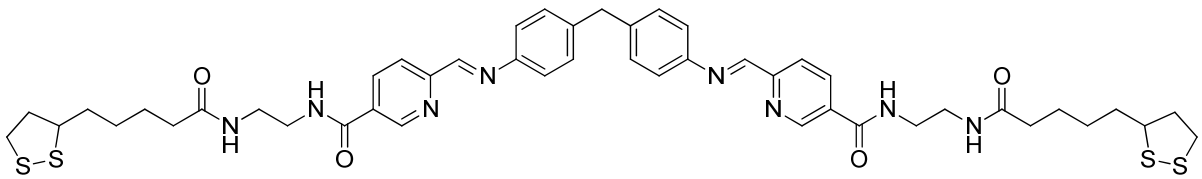

N-(2-(5-(1,2-dithiolan-3-yl)pentanamido)ethyl)-6-formylnicotinamide, aldehyde **6** (13.9 mg, 0.036 mmol) was dissolved in ethanol (3 mL). 4,4'-methylenedianaline (3.7 mg, 0.019 mmol) was then added dropwise in ethanol (2 mL). The reaction mixture was stirred at room

temperature, under Ar overnight. The precipitate was filtered and washed with ethanol and diethyl ether, giving a highly insoluble cream solid (107.2 mg, 94 %).

This compound could not be analysed due to its insolubility. It was attempted to dissolve the ligand in $CDCl_3$, CH_3CN, H_2O, CH_3OH and DMSO, but an insufficient amount of compound could be dissolve, so not data was obtained. As a result a one-pot reaction was used to form the cylinder of this ligand, straight from the aldehyde (**6**).

IR (solid): 3292 (s), 2926 (s), 1637 (s), 1541 (s), 1433 (m), 1244 (m), 1072 (w), 696 (m), 680 (m) cm^{-1}.

6.2.7.8 Synthesis of $[Fe_2(L_{Lipoic})_3][BF_4]_4$

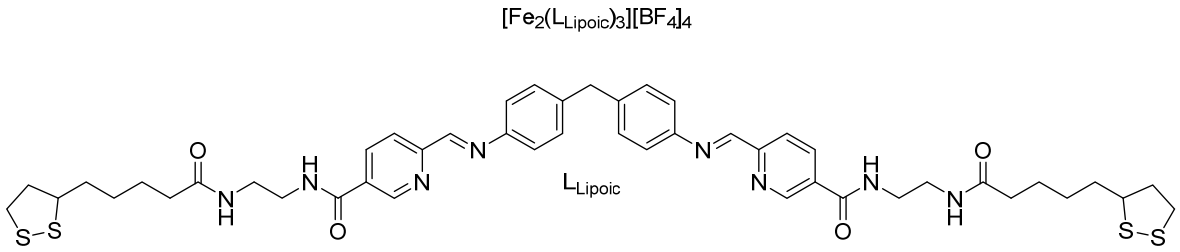

N-(2-(5-(1,2-dithiolan-3-yl)pentanamido)ethyl)-6-formylnicotinamide (8.2 mg, 0.021 mmol) was dissolved in ethanol (1 mL). 4,4'-methylenedianaline (2.4 mg, 0.012 mmol) was then added dropwise in ethanol (0.7 mL). This solution was left to stir for 10 mins, until the solution turned cloudy. $Fe(BF_4)_2.6H_2O$ (2.5 mg, 0.007 mmol) in ethanol (0.7 mL) was then added turning the solution dark blue/purple. The reaction mixture was stirred at room temperature, overnight. The precipitate was filtered and washed with ethanol and diethyl ether, giving blue/purple solid (8.5 mg, 71 %).

IR (solid): 3289 (br, m), 2928 (br, m), 2037 (w), 1638 (s), 1537 (m), 1065 (s), 811 (m), 673 (w), 658 (w) cm^{-1}.

This complex was insoluble in all solvents tested. Consisting of: MeOH, MeCN, $CHCl_3$, DCM, Acetone, H_2O, DMF, OEt_2, EtOH, EtOAc. As a result, no further analytical data could be obtained.

6.2.8 Synthesis of Half Ligand

6.2.8.1 Synthesis of S,S-Dimethyl-N-(2-pyridyl)sulfilimine

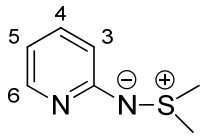

2-Aminopyridine (9.42 g, 0.10 mol) and dimethyl sulfide (8 mL) were dissolved in dichloromethane (100 mL). *N*-chlorosuccinimide (13.33 g, 0.10 mol) was dissolved in dichloromethane (250 mL) and added dropwise to the first solution over a period of 1 hr whilst maintaining the temperature at -20 ºC. The reaction mixture was the stirred at -20 ºC for 1 hr and then for 1 hr at rt. A solution of sodium methoxide in methanol (9.20 g, 0.17 mol in 75 mL methanol) was then added and stirring continued for 10 mins. Water (150 mL) was then added and stirred for 4 hrs. The organic layer was then separated and the aqueous layer extracted with water (2 × 50 mL). The organic layer was dried and evaporated to give yellow oil. The oil was recrystallised from diethyl ether to provide a cream solid (7.42 g, 48 %).

^{1}H NMR ($CDCl_3$): δ 7.98 (1H, dd, J = 5.2, 1.2 Hz, H_6), 7.32 (1H, td, J = 7.8, 1.9 Hz, H_5), 6.73 (1H, d, J = 9.0 Hz, H_4), 6.48 (1H, td, J = 6.0, 0.6 Hz, H_3), 2.73 (6H, d, J = 3.0 Hz, 2 × CH_3).

^{13}C NMR ($CDCl_3$): δ 147.0 (C_6), 136.7 (C_4), 114.1 (C_5), 111.5 (C_3), 33.7 (CH_3).

Mass spectrum (+ve EI): *m/z* 154 $[M]^+$, 139 $[M\text{-}CH_3]^+$.

6.2.8.2 Synthesis of 2-Nitosopyridine

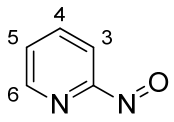

S,S-Dimethyl-N-(2-pyridyl)sulfilimine (5.54 g, 35.92 mmol) was dissolved in dry dichloromethane (35 mL). This was added to a solution of *m*-chloroperbenzoic acid (10.64 g, 61.65 mmol) in dry dichloromethane (200 mL) cooled to 0 ºC. The reaction mixture was stirred at 0-5 ºC for 2.5 h, dimethyl sulfide (2.7 mL) added and then stirring continued for 90 mins. Saturated aqueous sodium carbonate solution (200 mL) was then added to the reaction mixture. The green organic layer was separated and washed with water, dried and evaporated to dryness to give a light brown solid. The solid was recrystallised from ethanol to provide yellow crystals (1.22 g, 31 %).

The compound exists as two tautomeric forms which are denoted in the NMR data as a and b.

^{1}H NMR ($CDCl_3$): δ 8.81 (1H, dd, J = 4.5, 0.6 Hz, $H_{6a/b}$), 8.08 (1H, td, J = 7.7, 1.8 Hz, $H_{5a/b/4a/b}$), 8.01 (1H, dd, J = 4.8, 0.9 Hz, $H_{6a/b}$), 7.94 (1H, td, J = 7.8, 1.8 Hz, $H_{5a/b/4a/b}$), 7.86 (1H, d, J = 6.0 Hz, $H_{3a/b}$), 7.67 (1h, ddd, J = 12.0, 4.5, 0.9 Hz, $H_{5a/b/4a/b}$), 7.40 (1H, d, J = 6 Hz, $H_{3a/b}$), 7.31 (1H, ddd, J = 12.3, 4.8, 1.2 Hz, $H_{5a/b/4a/b}$).

^{13}C NMR ($CDCl_3$): δ 146.9 (C_6), 139.4 (C_4), 125.6 (C_5), 118.8 (C_3).

Mass spectrum (+ve EI): *m/z* 108 $[M]^+$.

6.2.8.3 Synthesis of Half-Ligand, L_{Half}

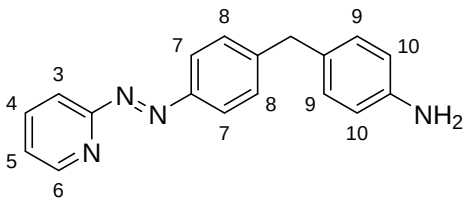

2-Nitosopyridine (1.22 g, 11.26 mmol) was dissolved in dichloromethane (10 mL). An excess of 4,4'-methylenedianiline (8.97 g, 45.24 mmol) in dichloromethane (35 mL) and glacial acetic acid were added and the orange solution was stirred at r.t overnight. The volatiles were then removed *in vacuo* to yield an orange solid which was then recrystallised from methanol (0.55 g, 22 %).

^{1}H NMR ($CDCl_3$): δ 8.73 (1H, dq, *J* = 4.8, 0.7 Hz, H_6), 7.98 (2H, d, *J* = 8.4 Hz, H_7), 7.89 (1H, td, *J* = 7.7, 1.8 Hz, $H_{4/5}$), 7.81 (1H, dt, *J* = 8.1, 1.0 Hz, H_3), 7.39 (1H, m, $H_{4/5}$), 7.34 (2H, d, *J* = 8.4, H_8), 7.01 (2H, d, *J* = 8.4 Hz, H_9), 6.65 (2H, d, *J* = 6.5 Hz, H_{10}), 3.96 (2H, s, CH_2), 3.61 (2H, broad s, H_{NH2}).

^{13}C NMR ($CDCl_3$): δ 149.5 (C_6), 138.3 ($C_{4/5}$), 129.9 (C_9), 129.5 (C_8), 125.0 ($C_{4/5}$), 123.8 (C_3), 121.4 (C_7), 115.4 (C_{10}), 41.1 (C_{CH2}).

Mass spectrum (+ve ESI): *m/z* 289 $[M+H]^+$.

6.2.9 Synthesis of Asymmetric Ligands

6.2.9.1 Synthesis of N-(2-(5-(1,2-dithiolan-3-yl)pentanamido)ethyl)-6-((E)-((4-(4-((E)-pyridin-2-yldiazenyl)benzyl)phenyl)imino)methyl)nicotinamide: $L_{Asym\text{-}Lipoic}$

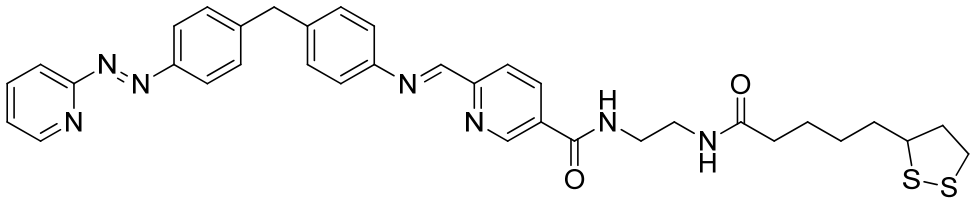

N-(2-(5-(1,2-dithiolan-3-yl)pentanamido)ethyl)-6-formylnicotinamide (7.5 mg, 0.020 mmol) was dissolved in ethanol (3 mL). Half-ligand (5.9 mg, 0.020 mmol) was dissolved in ethanol (2 mL) and added dropwise to the aldehyde solution under Ar. The reaction mixture was then left

to stir at room temperature overnight. The volatiles were then removed in vacuo, resulting in a crude orange solid (16.0 mg, 120 %).

This compound could not be purified by column chromatography, recrystallisation or by isolation through selective solubility, so could not be characterised.

6.2.9.2 Synthesis of S-(2-(2-(2-(4-(6-((E)-((4-(4-((E)-pyridin-2-yldiazenyl)benzyl)phenyl)imino)methyl)pyridin-3-yl)-1H-1,2,3-triazol-1-yl)ethoxy)ethoxy)ethyl) ethanethioate: $L_{Asym\text{-}Thioacetate}$

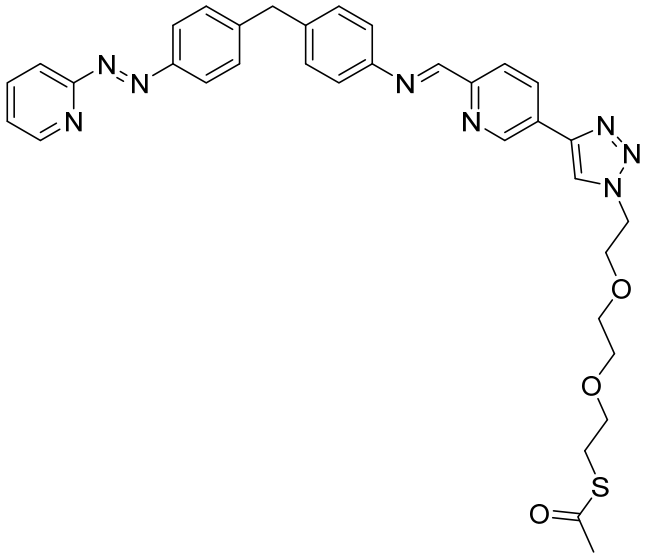

S-(2-(2-(2-(4-(6-formylpyridin-3-yl)-1H-1,2,3-triazol-1-yl)ethoxy)ethoxy) ethyl) ethanethioate, aldehyde 5 (10.3 mg, 0.028 mmol) and the half-ligand, L_{Half} (8.1 mg, 0.028 mmol) were dissolved in ethanol (3 mL) with 2 drops of glacial acetic acid. The reaction mixture was then left to stir at room temperature for 5 days. The volatiles were then removed in vacuo, resulting in a crude orange solid (17.8 mg, 100 %).

This compound could not be fully purified by column chromatography, recrystallisation or by isolation through selective solubility, so could not be characterised.

6.3 Synthesis of Ruthenium Cylinders

6.3.1 Parent Ruthenium Cylinder

$[Ru_2(L_P)_3][PF_6]_4$ $L_P =$ 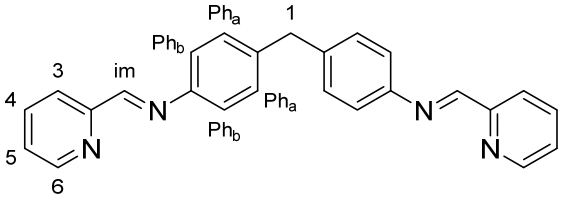

$Ru(DMSO)_4Cl_2$ was first synthesised by refluxing $RuCl_3$ (1.012 g, 4.88 mmol) in DMSO (5 mL) at 195 ºC for 5 mins. The solution was then cooled and half the DMSO removed by rotary evaporation. On addition of cold acetone, a yellow solid precipitated from solution. This was collected by filtration and washed with cold acetone. The yellow product indicated that the $Ru(DMSO)_4Cl_2$ complex was successful formed and so was used in subsequent reactions.

Parent ligand, L_P (359.6 mg, 0.955 mmol) was then added to a 50 mL microwave reaction vial containing a magnetic stirrer, degassed ethylene glycol (30 mL) and $Ru(DMSO)_4Cl_2$ (308.4 mg, 0.637 mmol). $Ar_{(g)}$ was then flushed over the reaction mixture before the vial lid was attached. The reaction vial was then placed into the microwave the reactor, where the temperature was increased to 200 ºC within 3 mins. The reaction mixture was stirred under this temperature for 4 hours, to give a dark orange/red solution. The ruthenium compounds were then precipitated out of solution using a saturated methanolic solution of NH_4PF_6. The dark brown solid was then collected by suction filtration and washed with copious quantities of water. It was then purified using column chromatography (20:1:1, $MeCN/H_2O/KNO_{3(aq)}$ on alumina) to yield a dark orange solid (5.0 mg, 0.9 %). The complex was left in the PF_6^- salt form as this was soluble in MeCN which could easily be removed from analytical samples, minimising the amount of product lost.

^{1}H NMR (CD_3CN): δ 8.72 (1H, s, H_{im}), 8.47 (1H, d, *J* = 7.8 Hz, H_6), 8.31 (1H, t, *J* = 7.8 Hz, H_3), 7.74 (1H, t, *J* = 6.9 Hz, H_4), 7.67 (1H, d, *J* = 6.0 Hz, H_5), 6.99 (2H, d, *J* = 8.4 Hz, $H_{Pha/b}$), 5.74 (2H, d, *J* = 8.4 Hz, $H_{Pha/b}$), 4.04 (1H, s, H_1).

Mass spectrum (+ve ESI): *m/z* 333.3 $[M-(PF_6)_4]^{4+}$, 444.7 $[M-(PF_6)_4]^{3+}$, 667.0 $[M-(PF_6)_4]^{2+}$.

UV-Vis (H_2O) λ_{max} (ε_{max}/$dm^3mol^{-1}cm^{-1}$): 235 (38 493), 276 (28 702), 324 (22 380), 492 (7 939) nm.

6.3.2 Thioacetate Ruthenium Cylinder

$[Ru_2(L_{Thioacetate})_3]Cl_4$

$L_{Thioacetate}$ =

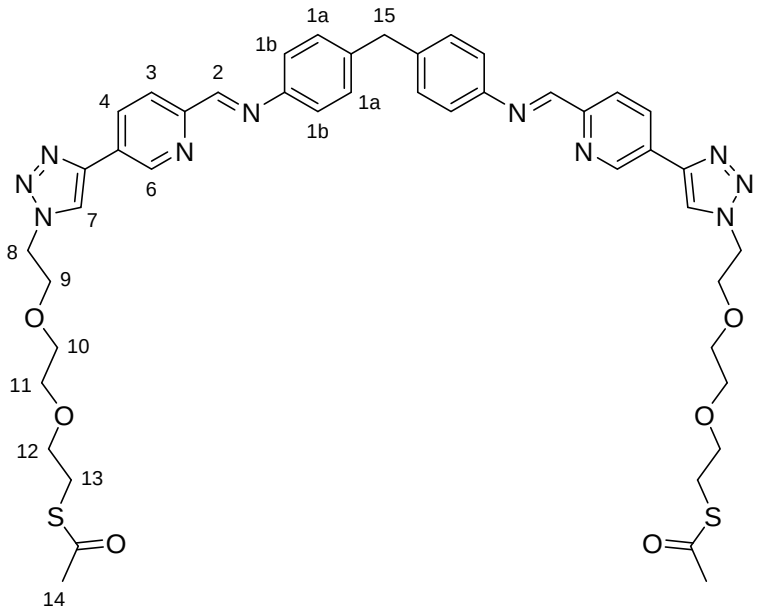

$L_{Thioacetate}$ (116.1 mg, 0.130 mmol) was added to a 50 mL microwave reaction vial containing a magnetic stirrer, degassed ethylene glycol (20 mL) and $Ru(DMSO)_4Cl_2$ (27.2 mg, 0.088 mmol). $Ar_{(g)}$ was then flushed over the reaction mixture before the vial lid was attached. The reaction vial was then placed into the microwave the reactor, where the temperature was increased to 200 ºC under 3 mins. The reaction mixture was stirred under this temperature for 4 hours, to give a dark orange/red solution. The ruthenium compounds were then precipitated out of solution using a saturated methanolic solution of NH_4PF_6. The dark solid was then collected by

suction filtration and washed with copious quantities of water. It was then attempted to purify the product using column chromatography. It was first attempted by using the same solvent system used for the parent cylinder (8:1:2, MeCN/H_2O/NH_4PF_6 solution on alumina). However after multiple columns, it was not possible to completely isolate the triple stranded product, evident by broad ^{1}H NMR spectra, impurities seen in the mass spectrum and multiple spots on the TLC. Therefore it was attempted to purify using silica column chromatography (15 mM NH_4PF_6 3:1 MeCN/H_2O) and through preparative TLCs on alumina and silica. However, pure triple stranded complex was not achieved.

^{1}H NMR (CD_3CN): Broad peaks contaminated with Ru^{3+} complex.

Mass spectrum (+ve ESI): *m/z* No peaks corresponding to $[Ru_2(L_{Thioacetate})_3]^{4+}$

6.4 DNA binding studies

All DNA binding studies were carried out using ultrapure water (18.2 MΩ) purchased from Fisher Scientific. Highly polymerised calf thymus (ct-) DNA was purchased from Sigma Aldrich, kept frozen and used without further purification. Stated concentrations of ct-DNA are calculated based on concentration of bases, as determined from the UV absorbance at 260 nm when $\varepsilon = 6600$ $mol^{-1}dm^3cm^{-1}$.

Stock solutions of ct-DNA (3000 μM) in water were prepared and kept frozen until the day of experiment. Sodium chloride (1 M) and sodium cacodylate ($Na(CH_2)_2AsO_2.3H_2O$) (100 mM) (pH 6.8) or tris-HCl (100 mM) (pH 7.2) buffer stock solutions were used to prepare final ct-DNA solutions with 20 mM Nacl and 1 mM sodium cacodylate/tris-HCl.

6.4.1 CD/LD Titrations

CD and LD experiments were recorded using a Jasco J-810 spectropolarimeter. CD experiments were performed in quartz cuvettes of 1 cm pathlength. LD measurements were recorded in a flow coquette cell (Krometek) with a 0.1 cm pathlength.

CD and LD titrations were carried out using three solutions; solution A (100 μM ct-DNA containing NaCl (20 mM) and sodium cacodylate/tris-HCl (1 mM)); solution B (167 μM complex solution) and solution C (200 μM ct-DNA solution containing NaCl (40 mM) and sodium cacodylate/tris-HCl (2 mM)). Solution A was recorded first, followed by the addition of equal aliquots of solutions B and C, keeping the concentration of ct-DNA constant throughout the titration. Increasing quantities where then added to obtain ct-DNA:complex ratios of 60:1 increasing to 4:1. A blank buffer solution was subtracted from the resulting spectra, and results are presented without any further smoothing. Each spectra shows the average signal over four scans and each experiment was repeated to ensure reproducibility.

6.4.2 Ethidium Bromide displacement

Fluorescence spectra for the ethidium bromide displacement experiments were recorded in a Shimadzu RF-5301 PC Fluorescence spectrophotometer (λexc= 480 nm; emission range:400-600 nm; resolution= 0.4 nm; speed medium; excitation split= 5; emmision split= 1.5). A solution of ethidium bromide (15 μM) with ct-DNA (12 μM) in NaCl (20 mM) and sodium cacodylate buffer (1 mM) was measured and titrated with the different complexes from ratios EB:complex 200-1 to 1-1, keeping the concentration of ethidium bromide and ct-DNA constant.

6.4.3 Hoechst 33258 displacement

Fluorescence spectra for the Hoechst 33258 (Hoechst) displacement experiment were recorded in a Shimadzu RF-5301 PC Fluorescence spectrophotometer (λexc=350 nm; emission range =400-600 nm; resolution=0.4 nm; speed medium; excitation split=5; emmision split=1.5). A solution of Hoechst (1.5 μM) with ct-DNA (12 μM) in NaCl (20 mM) and sodium cacodylate buffer (1 mM, pH 6.8) was measured and titrated with the different complexes from ratios of Hoechst:complex 200-1 to 4-1, keeping the concentration of Hoechst and ct-DNA constant.

6.5 Polyacrylamide Gel Electrophoresis (PAGE)

Polyacrylamide gel electrophoresis (PAGE) was used to identify whether three-way junction (3WJ) DNA structures where formed on interaction with new helicate structures.

6.5.1 DNA radioactive labelling

Three complementary oligonucleotide sequences were purchased from MWG Eurofin (S1: CGGAACGGCACTCG, S2: CGAGTGCAGCGTGG, S3: CCACGCTCGTTCCG). One strand (S1) was radiolabelled with ^{32}P at the 5' terminus using [γ-^{32}P] adenosine 5'-triphosphate (Perkin Elmer). Firstly milliQ water (4.8 μL), 10x T4 polynucleotide kinase buffer (1 μL), oligonucleotide S1 (1.2 μl of 100μM), bacteriophage T4 polynucleotide kinase (1 μl) (New England Biolabs) and ATP (2 μl of 3000 Ci/mmol) were incubated in an eppendorf at 37°C for an hour. The solution was then heated to 80°C for three mins, in order to deactivate the polynucleotide kinase.

To purify the radioactive labelled DNA sequences from any unreacted [γ-^{32}P]-ATP, a QIAquick nucleotide removal kit (QIAgen) was used. 10 volumes of PNI buffer to 1 volume reaction mixture were loaded onto a QIAquick spin column with a 2 mL collection tube, centrifuged at

6000 rpm for 1 minute and the flow through discarded. PE buffer (500 μL) was then added with a new collection tube, and centrifuged at 6000 rpm for 1 minute, again the flow through was put to waste and this washing with PE buffer was repeated, then centrifuged at 13000 rpm for 1 minute to remove residual buffer. The column was then transferred to a new Eppendorf, and milliQ water (30 μL) added and left for 5 minutes. After a final centrifugation at 13000 rpm for 2 minutes, the flow through was collected and diluted by half to give the radiolabelled stock solution of DNA (2 μM).

6.5.2 Polyacrylamide gel preparation

A stock solution of 15 % native polyacrylamide gel (1 L) was first prepared by mixing 40 % acrylamide (29:1, 375 mL) (Geneflow), 10x TB buffer (100 mL) containing 10.8 g tris-base and 5.5 g boric acid and HPLC grade water (525 mL). This solution was stored at 4 ºC, wrapped in foil until needed. 50 mL of this gel solution was then combined with 150 μL of 10 % (w/v) ammonium persulfate and 25 μL tetramethylenediamine (TEMED) and left to polymerise between a set of glass plates for 40 minutes. Wells within the gel were washed with running buffer (TB buffer) and the gel was pre-run at 300 V, 400 A for 10 minutes before loading samples.

6.5.3 PAGE Experiment

Sample solutions were prepared by mixing solutions of the complexes with stoichiometric amounts of the three oligonucleotides in TBN buffer (89 mM tris(hydroxymethy)amino methane, 89 mM of boric acid and 100 μM NaCl) (pH 8.3) to give a final concentration of 0.2 μM for each single strand (0.6 μM total concentration of DNA) and 0.6 μM of complex or 0.5 nM/0.5 μM of nanoparticle/complex. The sample solutions were incubated for 1 hour at room

temperature and then in ice for 15 minutes. Prior to loading samples onto the gel, 5 μL of 30 % glycerol was added to each sample, ensuring the DNA/complex solutions would fall to the bottom of the wells on loading. 13 μL of each sample was then loaded onto the 15% polyacrylamide gel.

The gel was run for 4 hours at 120 V, 300 A using Gel System equipment (Thermo Scientific UK). It was then exposed on a phosphor imaging plate for 1 hour and an autoradiogram was obtained using a Molecular Imager FX (Bio-Rad). The gel was quantified using Quantity One software.

6.6 Cell studies

All cell lines were cultured in T_{75} tissue culture flasks (Costar) at 37 ºC in a 5: 95 CO_2/Air incubator. Cells were maintained in DMEM (MDA-MB-231, A549) and RPMI 1640 (A2780) supplemented with FBS (10 % v/v), streptomycin (100 μg/mL), penicillin (100 U/mL) and L-glutamine (2 mM). Cells were sub-cultured twice each week, using a standard trypsin-EDTA protocol.

6.6.1 MTT assays

The MTT assay was used to estimate cell toxicity of the free and nanoparticle bound helicate structures over 72 hours. 15,000 cells were seeded in complete medium (100 μL) into each well of a 96 well plate. The cells were then incubated for 24 hours to allow for attachment. To treat the cells, 100 μL of compound solutions in complete media and up to 5 % MeOH/MeCN were added to the cells (10, 25, 50 and 75 μM). Following incubation for 72 hours, each well was washed with PBD and then complete media (100 μL) containing MTT (0.5mM) was added to each well. This was incubated for 2 hours (37 ºC, 5 % CO_2), after which time the media was

removed and 100 μL DMSO was added to solubilise the purple formazan product. Absorbance at 540 nm was then measured for each well against a DMSO blank, and so the IC_{50} was calculated. Each complex was tested in triplicate against a cisplatin standard. DMSO breaks down the helicate structures, so therefore was no absorbance interference from the complexes during these experiments.

6.6.2 TEM

Cells for TEM analysis with AuNPs were prepared to analyse how the nanoparticles interact with the cell structure and hence how they may induce cell toxicity.

Cells were initially seeded onto cover slips which had been sterilised in EtOH and washed with PBS. These were placed into 6 well plates where cells (150,000 in 3 mL) were suspended in media and left to adhere for 24 hours. Cells were then washed with PBS (3 mL) and treated with nanoparticles suspended in media (5 nM, 3 mL). The cell were then incubated for 24 hours (37 ºC, 5 % CO_2), before being washed with PBS. The coverslips were then transferred into a falcon tube containing glutaraldehyde in phosphate buffer, used as a fixative for the cells.

Samples were then prepared onto TEM grids by Theresa Morris, Electron Microscope Applications Technician, School of Metallurgy and Materials, University of Birmingham.

6.7 AuNP / Gold Surface Studies

For all reactions involving AuNPs, glassware was washed with aqua regia and copious quantities of distilled water prior to used, ensuring any residual particles are dissolved which may interfere with the synthesis. The nanoparticles where also synthesised and functionalised in darkness, to help maintain stability over time. All nanoparticles were filtered through an Acrodisc glass fibre membrane syringe filter, 1 μm (Sigma Aldrich) before use.

6.7.1 Citrate AuNP Synthesis

A solution of 1 mM $HAuCl_4.3H_2O$ (100 mL) was brought to 100 ºC and intensely stirred. A 38.8 mM solution of $Na_3(C_6H_5O_7).2H_2O$ (10 mL) was then added into the centre of the stirring vortex and the mixture was heated for 10 mins and then stirred without heat for 15 mins. This resulted in a deep red/purple solution.

UV absorption: 524 nm

DLS diameter by volume: 17.44 ± 6.199 nm

Zeta Potential: -43.2 ± 17.9 mV

TEM diameter: Average 16 nm

Concentration of cAuNPs: 5 nm (see Appendix, calculated using diameter observed from TEM images)

6.7.2 AuNP Functionalisation

Gold nanoparticles were functionalised with surfactant to form ZAuNPs by mixing the stock solution of cAuNPs with zonyl FSA (2 μL in 1 mL) overnight. The particles were then purified by centrifugation at 13000 rpm for 20 mins. This produced a red pellet, which was re-suspended in milliQ water, after the supernatant had been removed. This process was repeated and the nanoparticles were left suspended in milliQ water at the same concentration as the original cAuNP solution. All functionalised particles were formed over the night prior to experimental analysis.

All helicate functionalised particles were formed by reacting equal volumes of the complex solution (5 μM) with the surfactant coated particles, ZAuNPs (5 nM) overnight. They were then purified by centrifugation at 11000 rpm for 30 mins, which produced a pellet of particles which

were re-suspended in milliQ water. This purification step was repeated, and the resulting nanoparticles were used in milliQ water unless otherwise stated, at half the volume of the reaction mixture, giving 5 nM particles with 5 μM complex attached.

6.7.3 Ellipsometry

*Ellipsometry experiments were performed in collaboration with Sam Adams, Zoe Pikramenou group, University of Birmingham, with the complex solution provided.

Ellipsometry experiments were performed on Jobin-Yvon UVISEL ellipsometer with a xenon light source. The technique uses elliptically polarized monochromatic light to determine the thickness of a surface.

The surface of a thin gold film on silicon was first measured, giving the thickness of the gold surface. Gold samples were then submerged in a solution of $[Fe_2(L_{Thioacetate})_3][BF_4]_4$ (1 mg/mL in MeCN) for increasing periods of time (1, 2, 5, 10, 20 and 30 mins). Excess cylinder solution was then washed off these incubated samples with MeCN, and the gold surfaces measured. With increasing time, a maximum growth in surface height on cylinder binding was 1.69 nm.

6.7.4 Surface Plasmon Resonance

*SPR experiments were performed in collaboration with Sam Adams, Zoe Pikramenou group, University of Birmingham, with complex, buffer and DNA solutions provided.

Surface Plasmon Resonance (SPR) experiments were performed on a Reichert SR7000DC. Experiments were performed to determine whether a gold surface had affinity to various DNA solutions, bare and with the thioacetate cylinder, $[Fe_2(L_{Thioacetate})_3][BF_4]_4$ bound.

Three DNA solutions were flowed over the gold surfaces: polymeric ct-DNA (Sigma Aldrich), double stranded DNA of 26 bases: ds26 5'-CAA-TCG-GAT-CGA-ATT-CGA-TCC-GAT-TG-

3’ (MWG Eurofin) and human telomeric DNA: h-Telo quadruplex DNA 5’-AGG-GTT-AGG-GTT-AGG-GTT-AGG-G-3’ (MWG Eurofin). The two shorter DNA sequences; ds26 and h-Telo were annealed before use, heating to 90 ºC for 5 mins and slowly cooling to room temperature, to ensure that the sequences were in their helical and quadruplex structures respectively. Solutions were made to 15 μM (concentration in bases, based on their UV absorbance at 260 nm) in tris-HCl buffer (pH 8.0). (ct-DNA/ds26 ε_{260}=6600 $mol^{-1}dm^3cm^{-1}$, h-Telo ε_{260}=244 300 $mol^{-1}dm^3cm^{-1}$).

Gold surface sensor chips, bare and functionalised with the helicate were measured for bio-affinity, by first equilibrating the system for 10 minutes, then flowing the various DNA solutions (15 μM) over the gold surface by injecting into the flow cell. These solutions were washed over the surface for 30 minutes before being washed away with tris-HCl buffer (pH 8.0). Affinity of the DNA solutions to the gold surface was then analysed based on changes in the response units.

Appendix

A.1 2D NMR and Mass Spectra

A.1.1 Ester Aldehyde

COSY

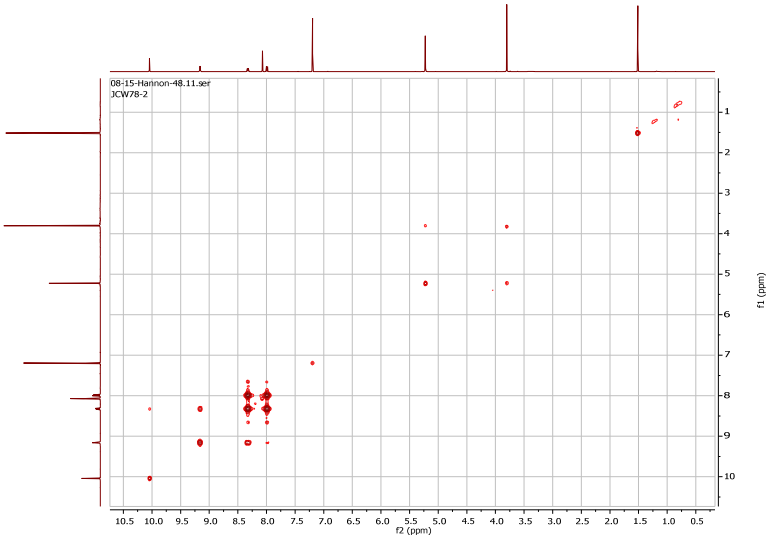

^{1}H-^{1}H COSY NMR (400 MHz, $CDCl_3$, 298 K)

HSQC

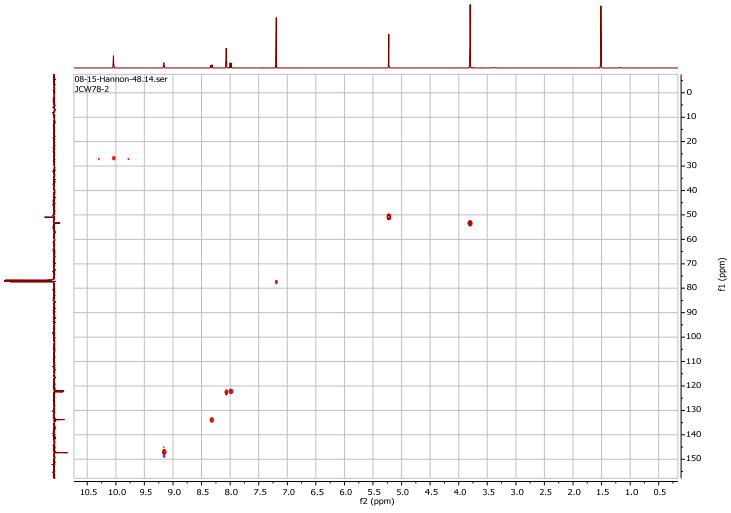

^{1}H-^{13}C HSQC NMR (400 MHz, $CDCl_3$, 298 K)

ESI Mass Spectrum

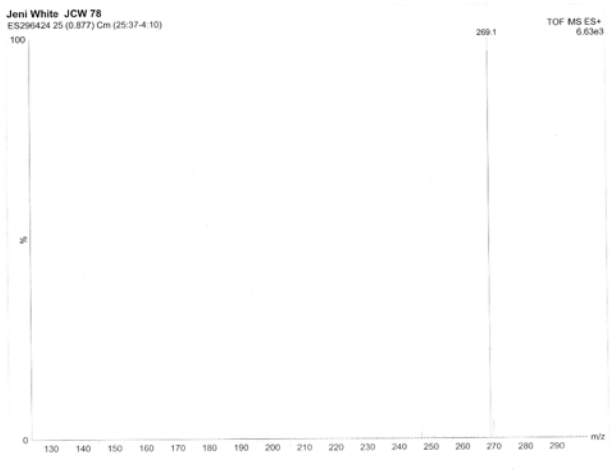

A.1.2 Ester Cylinder

COSY

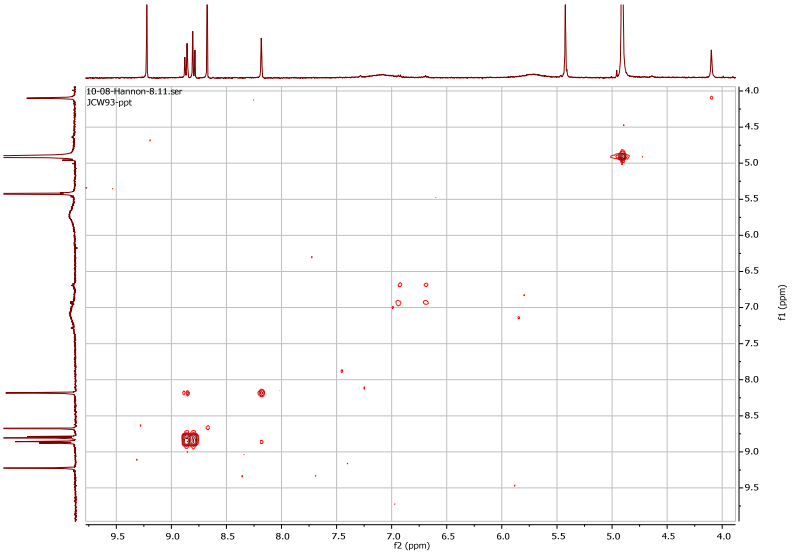

^{1}H-^{1}H COSY NMR (400 MHz, CD_3OD, 298 K)

ESI Mass Spectrum of $[Fe_2(L_{Ester})_3]Cl_4$

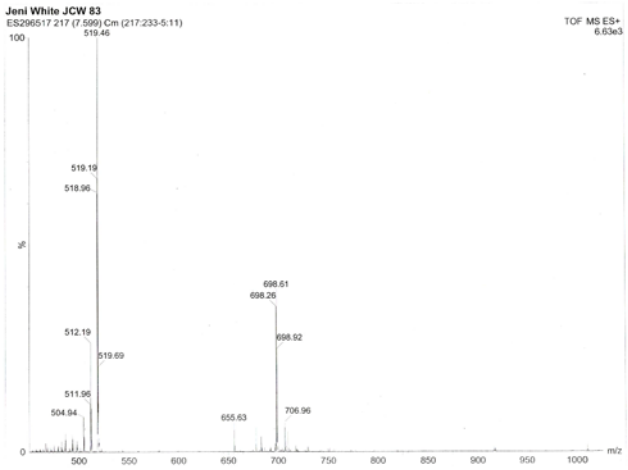

ESI Mass Spectrum of $[Fe_2(L_{Ester})_3]^{4+}$

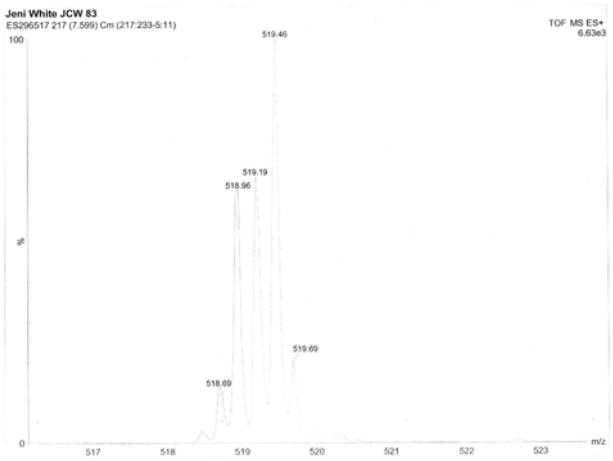

A.1.3 Piperidine Aldehyde

COSY

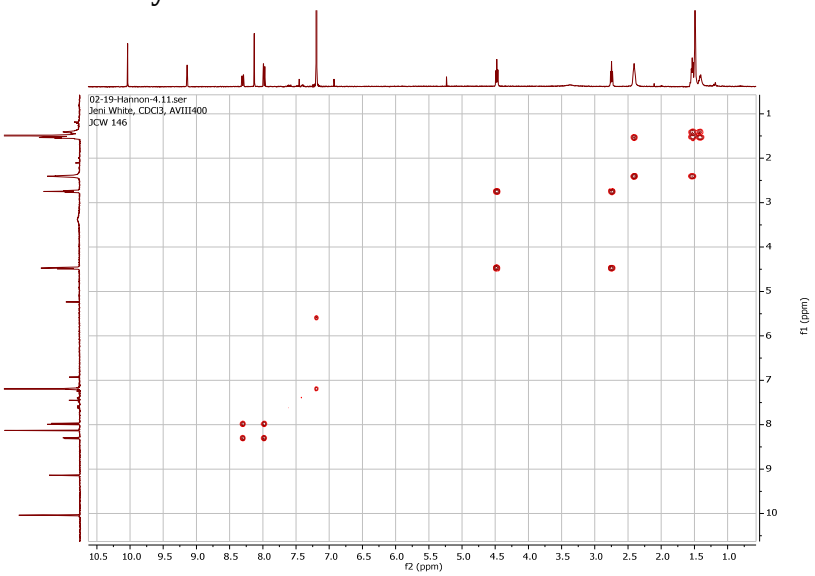

^1H-^1H COSY NMR (400 MHz, $CDCl_3$, 298 K)

HSQC

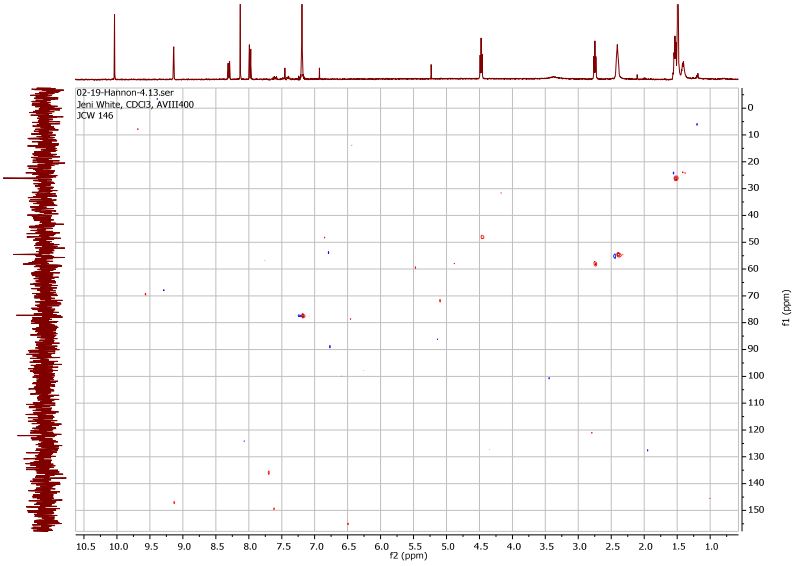

^{1}H-^{13}C HSQC NMR (400 MHz, $CDCl_3$, 298 K)

ESI Mass Spectrum

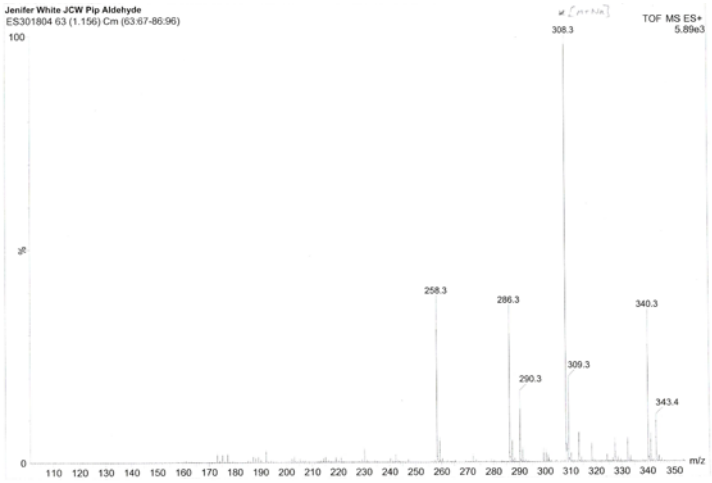

A.1.4 Piperidine Cylinder

COSY

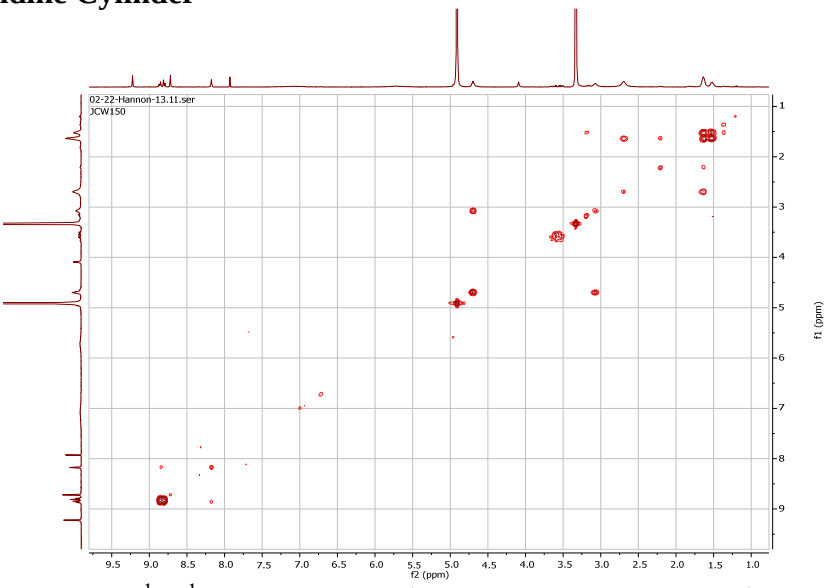

^{1}H-^{1}H COSY NMR (400 MHz, CD_3OD, 298 K)

ESI Mass Spectrum $[Fe_2(L_{Piperidine})_3]Cl_4$

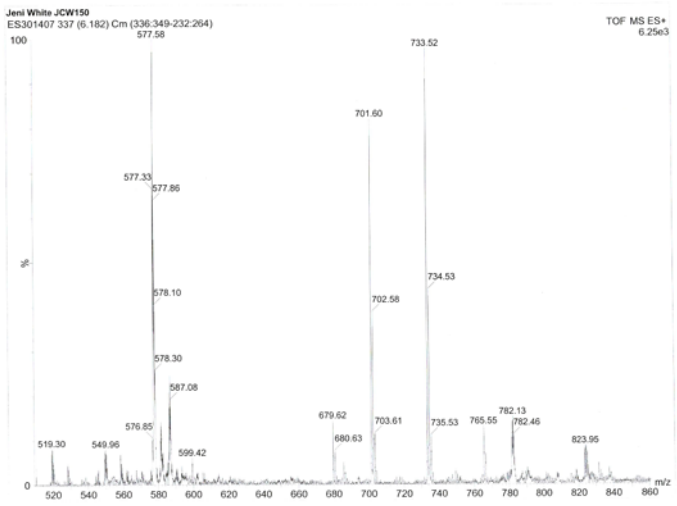

ESI Mass Spectrum $[Fe_2(L_{Piperidine})_3]^{4+}$

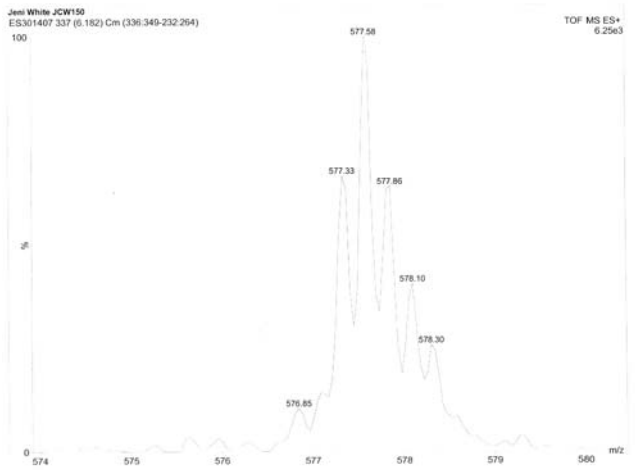

A.1.5 Thioacetate Aldehyde

COSY

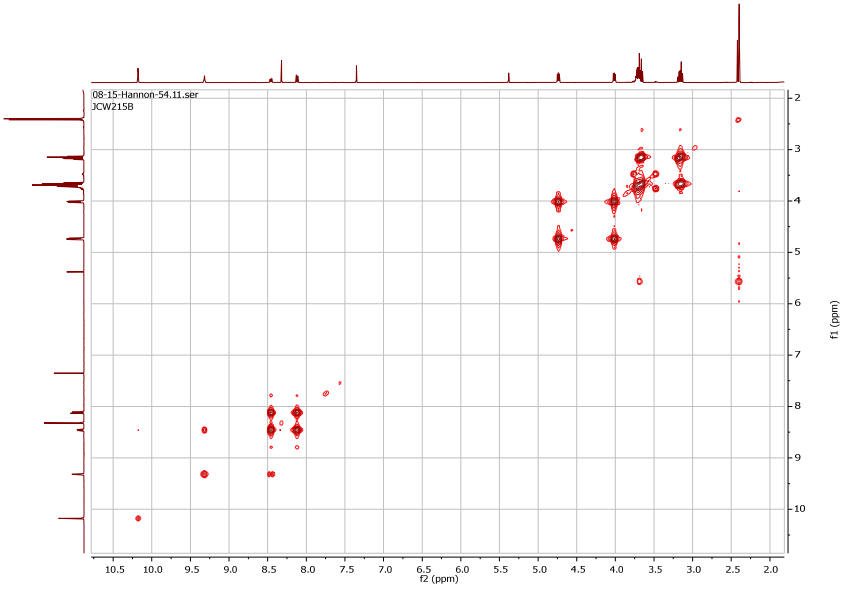

^1H-^1H COSY NMR (400 MHz, $CDCl_3$, 298 K)

HSQC

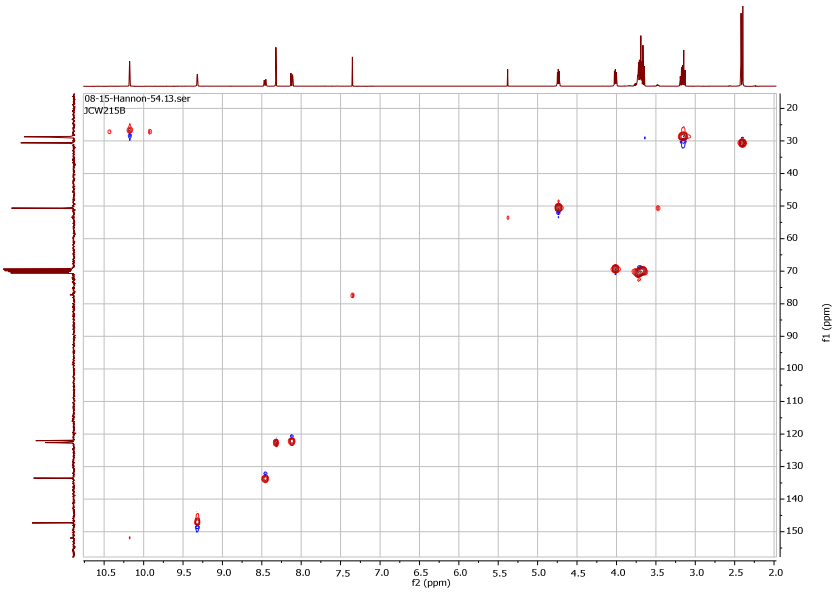

^{1}H-^{13}C HSQC NMR (400 MHz, $CDCl_3$, 298 K)

ESI Mass Spectrum

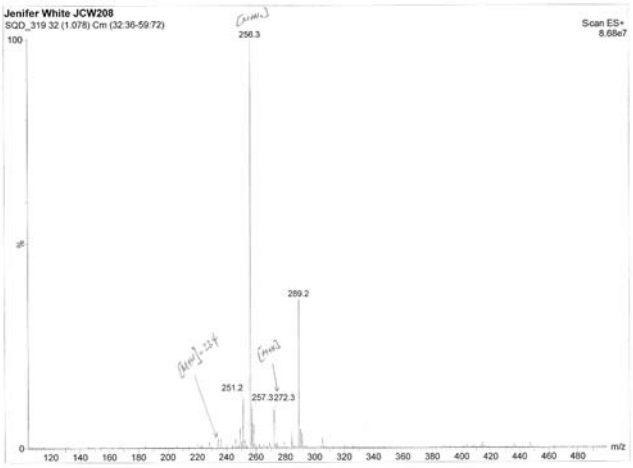

A.1.6 Thioacetate Cylinder

COSY

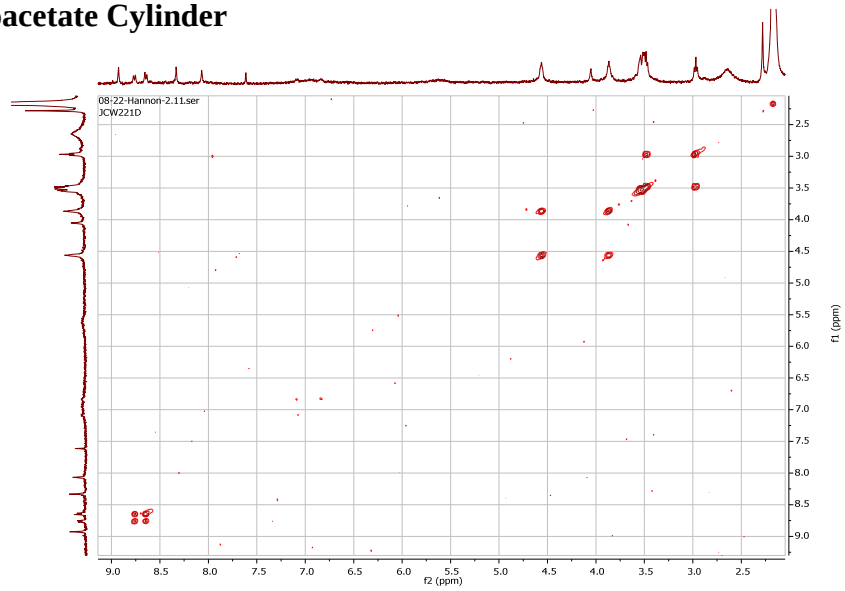

^{1}H-^{1}H COSY NMR (400 MHz, CD_3CN, 298 K)

ESI Mass Spectrum $[Fe_2(L_{Thioacetate})_3][BF_4]_4$

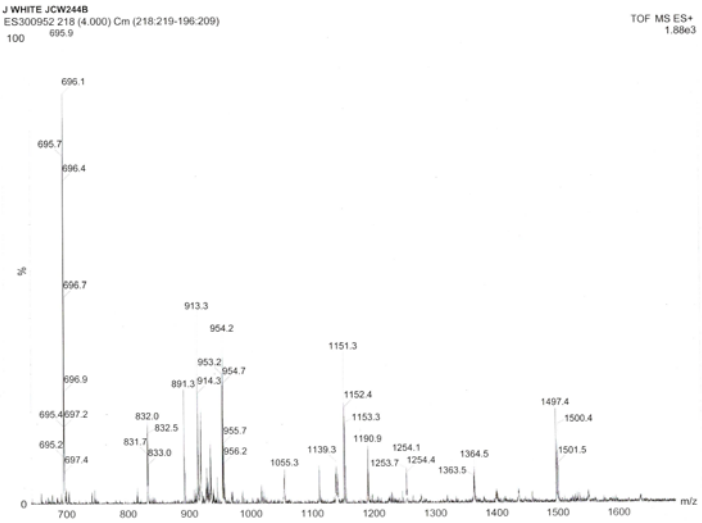

ESI Mass Spectrum $[Fe_2(L_{Thioacetate})_3]^{4+}$

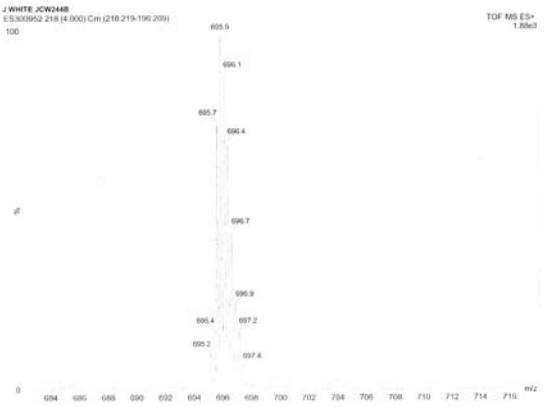

A.2 Calculation of Nanoparticle Concentration

It was possible to estimate the concentration of AuNPs from TEM experiments, using the following assumptions for large spherical metal clusters, such as a gold nanoparticle:

$V_{cluster} = NV_{atom}$ (eq. 1)

$4/3\ \pi\ (R_{cluster})^3 = N\ 4/3\ \pi\ (R_{atom})^3$ (eq. 2)

$R_{cluster} = N^{1/3}\ R_{atom}$ (eq. 3)

(V: cluster or atom volume, R: cluster or atomic radius, N: total number of atoms within the cluster)

The cluster radius is obtained from TEM imaging, so the surface (S) area of a nanoparticle can be calculated using:

$S_{cluster} = 4\ \pi\ (R_{cluster})^2$ (eq. 4)

For larger clusters, the number of surface atoms, Ns, can also be calculated by dividing the surface area of the cluster by the cross section of an individual cluster atom, and simplifying using the relationship in (eq. 3):

$Ns = (4 \pi (R_{cluster})^2) / (\pi (R_{atom})^2) = 4 N^{2/3}$ (eq. 5)

From the TEM result presented (see *Chapter 4*), we know that $R_{cluster} \approx 8$ nm, and $R_{atom} = 0.137$ nm. The number of gold atoms per nanoparticle was estimated using (eq. 3):

$N = (R_{cluster} / R_{atom})^3 = ((8 \times 10\text{-}9) / (137 \times 10\text{-}9))^3 = 199\ 107$ gold atoms per nanoparticle.

The number of surface atoms, Ns, on a single gold nanoparticle was also estimated using (eq. 5): $Ns = 4 N^{2/3} = 4 \times (199{,}117)^{2/3} = 13640$ gold surface atoms per nanoparticle.

From N, the molecular weight (Mw) of a single nanoparticle was calculated using the relative molecular mass of a single gold atom (Mgold): Mw = Mgold x N Mw = 196.97 x 199117 Mw = 39220 kDa

Calculation of the amount of nanoparticles formed (NNP) when 1 dm^3 of 1 mM HAuCl4 is reduced by citrate was then calculated: Moles of $HAuCl_4 = 1 \times 1 \times 10^{-3} = 1 \times 10^{-3}$ mol

No. of gold atoms, $Natom = 1 \times 10^{-3} \times NA = 1 \times 10^{-3} \times 6.022 \times 10^{23} = 6.022 \times 10^{20}$

$NNP = Natom / N\ NNP = (6.022 \times 10^{20}) / (199117) = 3.024 \times 10^{15}$ nanoparticles formed per 1×10^{-3} mol $HAuCl_4$.

Hence the final concentration of the gold colloid, was estimated by dividing NNP by Avagadro's number (NA):

$CAuNP = NNP / NA = (3.024 \times 10^{15}) / (6.022 \times 10^{23}) = \underline{5.022 \times 10^{-9} \text{ mol dm}^{-3}}$

All concentrations of nanoparticles presented in this thesis are calculated from the initial stock solution of citrate coated nanoparticles, cAuNPs, being 5 nM.